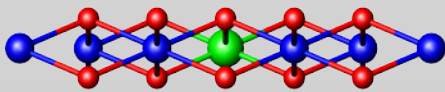# In-situ X-ray Studies
# of Model Electrode Surfaces
for Solid Oxide Fuel Cells

Navid Khorshidi

Max-Planck-Institut
für Metallforschung
Stuttgart

Institut für theoretische
und angewandte Physik
Universität Stuttgart

براى مادرم

Für meine Mutter

For my mother

In-situ X-ray Studies of Model Electrode Surfaces for Solid Oxide Fuel Cells

Von der Fakultät Mathematik und Physik der Universität Stuttgart
zur Erlangung der Würde eines Doktors der
Naturwissenschaften (Dr. rer. nat.) genehmigte Abhandlung

Vorgelegt von

NAVID KHORSHIDI

aus Tehran (Iran)

Hauptberichter:	Prof. Dr. H. Dosch
Mitberichter:	Prof. Dr. P. Michler

Tag der mündlichen Prüfung: 17.12.2010

Max-Planck-Institut für Metallforschung Stuttgart
und
Institut für theoretische und angewandte Physik
der Universität Stuttgart

2010

Table of Contents

Acronyms

AES	*Auger-Electron Spectroscopy*
AFM	*Atomic Force Microscopy*
ANKA	*Ångström-Quelle Karlsruhe*
CTR	*Crystal Truncation Rod*
DFT	*Density Functional Theory*
DW	*Static Debye-Waller Factor*
ESRF	*European Synchrotron Radiation Facility*
fcc	*Face Centered Cubic*
FWHM	*Full Width at Half Maximum*
FSZ	*Fully Stabilized Zirconia*
F-YSZ	*Fully Yttria-Stabilized Zirconia*
hcp	*Hexagonal Close-Packed*
LEED	*Low Energy Electron Diffraction*
MPI-MF	*Max Planck Institute for Metals Research*
NP	*Nanoparticle*
PSZ	*Partially Stabilized Zirconia*
PVD	*Physical Vapor Deposition*
SLS	*Swiss Light Source*
SOFC	*Solid Oxide Fuel Cell*
STM	*Scanning Tunneling Microscopy*
SXRD	*Surface X-ray Diffraction*
UHV	*Ultra-High Vacuum*
YSZ	*Yttria-Stabilized Zirconia, Fully Yttria-Stabilized Zirconia (after chapter 2)*

Symbols

[100]	*Real Space Direction*
(100)	*Reciprocal Space Direction*
{100}	*Real Space Planes / Layers*
a	*Lattice Constant*
$a*$	*Reciprocal Lattice Constant*
α_i	*Incident Angle*
α_c	*Critical Angle*
B	*Debye-Waller Factor*
F	*Structure Factor*
Γ	*Momentum Transfer 0*
λ	*Wavelength*
p	*Pressure*
Q	*Momentum Transfer*
T	*Temperature*
Θ	*Coverage*
χ_N^2	*Normalized Agreement Factor*
Z	*Atomic Number*

Deutsche Zusammenfassung

Motivation

Die Entwicklungen seit Anbeginn der Industrialisierung stellen die Menschheit heute vor eine Vielzahl von fundamentalen Problemen, die es zu lösen gilt. Der exzessive Umgang mit den natürlichen Ressourcen gekoppelt mit einem raschen Anstieg der Weltbevölkerung hat die Gesellschaft zu einem Punkt gebracht (endlich) zu realisieren, dass diese Ressourcen nicht unendlich sind und dass unsere Umwelt nicht unzerstörbar ist.

Der rasante technologische Fortschritt etwa, hat zu einem immensen Energiebedarf geführt, der notwendig ist um die Lebensqualität und den Wohlstand zu erhalten (zumindest die der Bevölkerung der G8 Staaten und der Schwellenländer).

Ein Großteil dieser Energieversorgung wird durch Kernkraftwerke und die Verbrennung fossiler Brennstoffe gewährleistet. Die Kernenergie ist trotz „des Ausstieges aus dem Ausstieg" sehr umstritten und nicht zukunftsfähig. Eine Unabhängigkeit von fossilen Brennstoffen ist wegen politischen Verhältnissen und des Restvorkommens unabdingbar. Beide Erzeugungsarten beschädigen darüber hinaus die Umwelt nachhaltig mit unvorhersehbaren Folgen. Die Notwendigkeit und der Bedarf an neuen Technologien zur Energieerzeugung sind daher unbestreitbar.

Große Hoffnung nicht nur aus wissenschaftlicher und technologischer Sicht wird in diesem Zusammenhang auf Brennstoffzellen gesetzt [1; 2; 3; 4]. Das gesellschaftliche Interesse an diesem Thema [5; 6] unterstreicht dabei dessen Bedeutung genauso wie die politische Unterstützung. Im dem 2010 veröffentlichten „Strategiepapier zum Forschungsbedarf in der Wasserstoff-Energietechnologie" des Bundesministeriums für Wirtschaft und Arbeit heißt es etwa, die Förderung von Brennstoffzellen wird intensiviert „da diese viele Einsatzgebiete auch unabhängig von einer Wasserstoffwirtschaft haben" [7].

Brennstoffzellen sind galvanische Zellen, die in der Lage sind Wasserstoff und Sauerstoff zu H_2O zu formen und die dabei entstehende chemische Energie in Elektrizität umzuwandeln, wobei H_2 als Brennstoff dient.

Die Herausforderungen bezüglich der Speicherung von Wasserstoff sowie dessen derzeitige Erzeugung aus fossilen Brennstoffen, lassen dabei der Festoxidbrennstoffzelle (SOFC aus dem englischen Solid Oxide Fuel Cell) eine besondere Bedeutung zukommen. Das besondere Merkmal der SOFCs ist ihre Fähigkeit sowohl reinen H_2 als auch Kohlenwasserstoffe als Brennstoff zu verarbeiten. Letztere werden innerhalb der Zelle zu Wasserstoff degradiert und führen zu hervorragenden Gesamtwirkungsgraden. Wegen ihrem Betrieb bei Temperaturen zwischen 600°C und 1000°C kann diese Effizienz zusätzlich gesteigert werden, wenn die SOFC in einer kombinierten Anwendung zur Kraft-Wärme-Gewinnung eingesetzt wird.

Um SOFCs konkurrenzfähig zu machen, gilt es zwei Herausforderungen anzugehen: es muss eine weitere Steigerung des Nutzungsgrades sowie eine Verlängerung der Lebensdauer der Zellen erreicht werden. Wegen der Vielzahl von möglichen Brennstoffen die von SOFCs verarbeitet werden können, spielt dabei die Brennstoff-Elektrode bzw. Anode eine herausragende Rolle. Von vielzähligen Versuchen Anoden für SOFCs zu entwickeln, hat sich ein Cermet aus Yttrium dotiertem Zirkonoxid (YSZ aus dem englischen Yttria-stabilized zirconia) und Nickelteilchen durchgesetzt, das seit ca. 50 Jahren das mit Abstand am häufigsten genutzte Anodenmaterial ist [1; 2; 8].

Die Brennstoffverarbeitung auf solch einer Anode geschieht daher zwischen den drei „Phasen": YSZ-Oberfläche, Nickelteilchen und dem Brennstoff. Diese sogenannte Drei-Phasen-Grenze (Three-Phase Boundary) spielt daher eine Schlüsselrolle und ihr Verständnis auf atomarer Ebene ist von außerordentlicher Bedeutung für die obengenannten Ziele und die Entwicklung von „next Generation" SOFCs [1; 8; 9]. Nach Meinung von Experten sind diese Ziele darüber hinaus durch strukturelle Weiterentwicklungen der Anode zu erreichen [8].

Es ist daher grundlegend zwei Wissenslücken zu schließen: YSZ-Oberflächenmodelle mit atomarer Auflösung sowie das Wachstum und die Form von Nickel-Nanoteilchen (NT) auf diesen Oberflächen. Experimentell können diese Aufgabenstellungen im Rahmen der Oberflächenphysik gelöst werden. Dabei bietet sich die oberflächensensitive Röntgenbeugung (SXRD aus dem englischen Surface X-ray Diffraction) als hervorragende Technik an, da sie nicht von den elektrischen Leitfähigkeiten des zu untersuchenden Materials abhängt, wie etwa die isolierende Eigenschaft von YSZ, die einen Großteil der Oberflächen-Untersuchungstechniken unbrauchbar macht. Zudem wurde diese Technik kürzlich sehr erfolgreich zur Charakterisierung von Metall-NT eingesetzt [10; 11] und eignet sich daher ausgezeichnet für die Untersuchung der Nickel-NTs.

Zielsetzung

Ziel dieser Arbeit ist es, atomare Modelle für SOFC-Anodenoberflächen unter betriebsrelevanten Bedingungen zu liefern. Dazu müssen

- erstens Oberflächenstrukturen von YSZ und
- zweitens die Form und Größe von Nickel NPs auf diesen Oberflächen

bestimmt werden.

Hierzu wurden YSZ-Einkristalle mit der am häufigsten benutzten Yttrium-Konzentration und der maximalen Sauerstoffionen-Leitfähigkeit - nämlich 19% - ausgewählt. Als Einkristalle dienten zwei unterschiedliche Oberflächen-orientierungen:

- die (111)-Oberfläche hat die niedrigste Energie und gilt daher als die häufigste und damit die wichtigste Facette dieses Materials [12; 13].
- die polare (100)-Orientierung. Sie hat die drittniedrigste Oberflächenenergie [12] und kann rekonstruiert sein.

Die atomare Struktur dieser Einkristalloberflächen unter UHV wurde bei zwei Bedingungen untersucht:

- nach einer einfachen Probenpräparation bei 400°C und 10^{-5} mbar Sauerstoffdruck zur Bestimmung der reinen Oberflächenstruktur und

- nach einer Behandlung bei Temperaturen über 800°C unter reduzierenden Umgebungen, die den Betriebsbedingungen von SOFCs entsprechen.

Die Charakterisierung – das heißt Größen- und Formbestimmung - von mittels physikalischer Gasphasenabscheidung (PVD aus dem englischen Physical Vapor Deposition) auf diesen Oberflächen gezüchteten Nickel-NTs wurde bei drei Zuständen durchgeführt:

- direkt nach dem Verdampfen von Nickel, um die anfängliche Form und Größe zu bestimmen

- nach einer Hitzebehandlung bei reduzierender Umgebung, um die Bedingungen eines SOFCs zu simulieren

- nach einer Sauerstoffbehandlung. Die Oxidation von Nickel-NTs führt zu einer Minderung der Anoden-Effizienz. Da dies im Betrieb eines SOFCs kein seltenes Ereignis ist [8], ist es von Interesse das Oxidationsverhalten der NTs zu kennen.

Ergebnisse

Die YSZ(111)-Oberfläche (Kapitel 5.1)

Ein besonderer Wert wurde aufgrund ihrer Häufigkeit auf die (111)-Oberfläche gelegt. Durch die Kombination von anomaler und herkömmlicher (normaler) SXRD ist hier eine besonders genaue Strukturbestimmung möglich, bei der zwischen den Elementen Y und Zr unterschieden werden kann. Diese Unterscheidung ist mit der Verwendung von herkömmlichen SXRD-Daten nicht möglich. In der Strukturverfeinerung wurden daher Positionen und Konzentrationen der obersten Metalllage auf Basis der „Zr-shift"-Modells bestimmt (siehe Abschnitt 2.4.2.2).

Die aufgelösten Oberflächenstrukturen an den zwei genannten Bedingungen sind in Abbildung 1 dargestellt. Eine erhöhte Y Konzentration auf 31% deutet bei der reinen Oberfläche auf eine Yttrium-Anreicherung hin. Gleichzeitig sinkt die Zr-

Seitenansicht Draufsicht

Reine Oberflächenstruktur

Nach Heizen bei 1000°C und reduzierenden Bedingungen
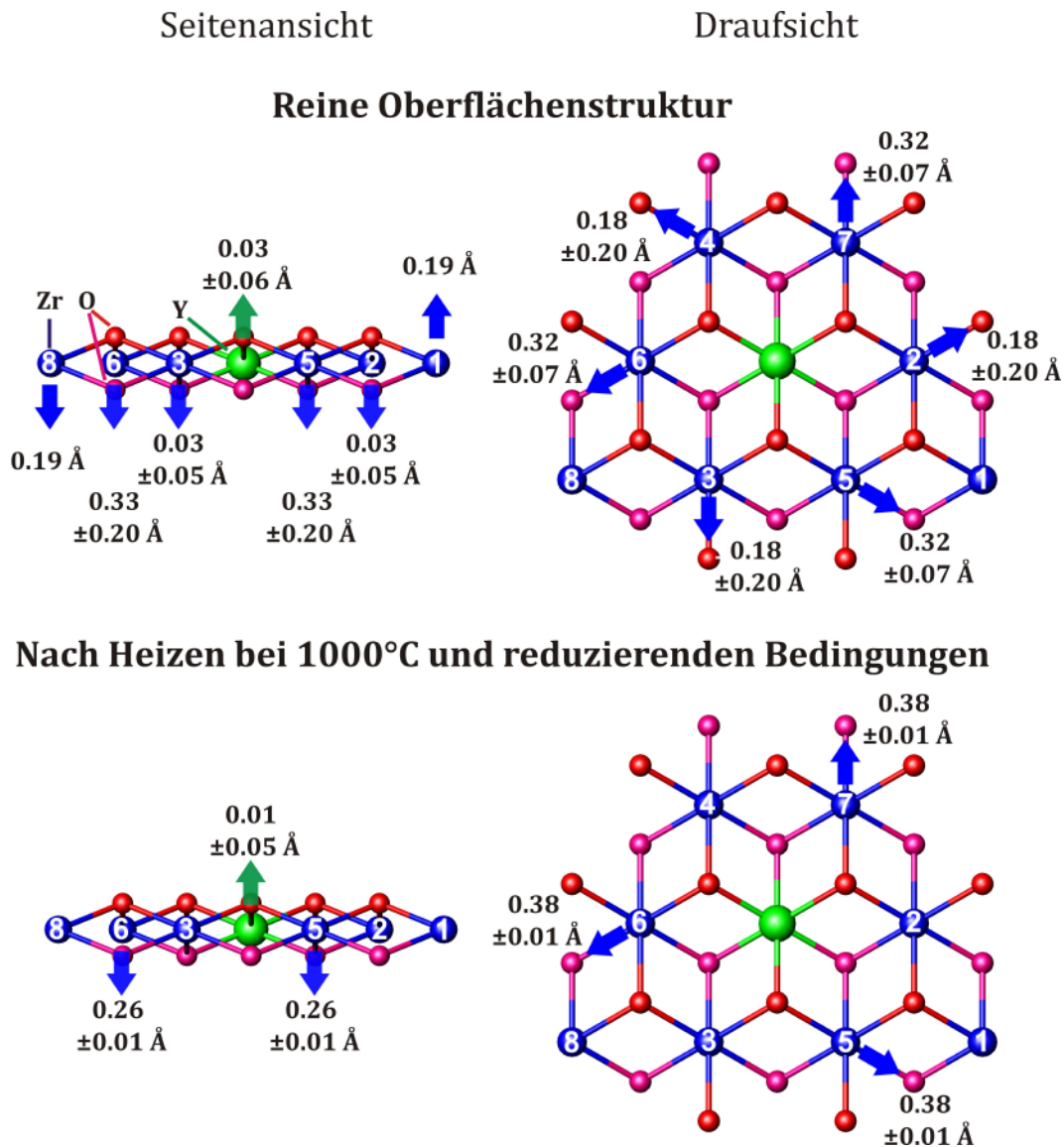
Abbildung 1: Seiten- und Draufsicht der YSZ-(111)-Oberfläche basierend auf dem „Zr-shift"-Modell. Zr: blau, O: rot (pink), Y: Grün. Die Metalle sind aus Darstellungsgründen größer als Sauerstoff. Oben: Die Zr-Atome der reinen Struktur zeigen große Auslenkungen aus den idealen kubischen Positionen. Zudem sind diese Positionen nur zu 37% besetzt, was zu einer hoch defektiven und ungeordneteren Struktur führt. Unten: nach einer Behandlung bei 1000°C und reduzierenden Bedingungen erhöht sich die Zr-Konzentration auf 50% und die Mehrheit der Zr Atome besetzt ideale kubische Positionen. Dies führt zu einer erhöhten Ordnung und weniger Defekten an der Oberfläche.

Konzentration auf 32% ab was eine Metall- und stöchiometrische Sauerstoff-

Fehlstellendichte von 37% und 40% zur Folge hat. Die reduzierte Sauerstoffkonzentration an der Oberfläche führt zu einem unausgeglichenen Bindungsverhältnis der Zr-Atome, welches diese stark aus ihren Bulk-Positionen verschiebt. Diese Oberfläche hat daher eine im Vergleich zum Bulk niedrige Ordnung und ist hoch defektiv.

Nach einer Hitzebehandlung bei 1000°C und reduzierenden Bedingungen steigt die Zr-Konzentration an der Oberfläche bei konstanter Y-Konzentration auf 50% an. Dies führt zu einer reduzierten Oberflächen Metall- und Sauerstoff-Fehlstellenkonzentration auf 21% und 24%. Der Anstieg der Sauerstoffkonzentration hat ein ausgeglicheneres Bindungsverhältnis der obersten Metalllage zur Folge und führt zu einer besser geordneten Struktur der Oberfläche bei der die Mehrheit der Zr Atome auf ideale Fluoritpositionen sitzt. Diese Behandlung führt daher zu einer hoch geordneten Oberfläche mit einer reduzierten Anzahl an Defekten.

Nickel-Nanoteilchen auf der YSZ(111)-Oberfläche (Kapitel 5.2)

Nickel wurde auf einer frisch präparierten YSZ(111)-Oberfläche mit Hilfe von PVD und einer nominellen Verdampfungsdicke von 5.7 nm hergestellt. Dies führte zu einer 60%igen Bedeckung des Substrats mit NTs, die zwei verschiedenen Epitaxien zeigen:

- (111)-orientierte NTs mit lateral koexistierenden Zwillingen und interner Verzwillingung (twinning). Diese Teilchen sind für die verschiedenen untersuchten Bedingungen in Abbildung 2 dargestellt. Sie haben mittlere Höhen und Breiten von 3,4 nm und 6,7 nm und sind aus früheren Publikationen bekannt [14].
- NTs die auf Grund der Wechselwirkung mit dem Substrat eine kohärente Neigung (coherent tilt) um 41.3° um die (111)-Orientierung zeigen. Diese Art ist in Abbildung 3 gezeigt und bisher unbekannt.

Beide Sorten von NTs zeugen von einem stark Grenzflächen-dominierten Wachstum. Ihre Form kann mit Hilfe der Wulff-Konstruktion bestimmt werden und

zeigt überwiegend (111)-orientierte Facetten und einen kleinen Anteil von (100)-Facetten.

Das Heizen der NTs bei 700°C unter reduzierenden Bedingungen für 75 Minuten, führt zum Wachstum der mittleren Größe beider Teilchensorten. Die (111)-orientierten NTs weisen dann Höhen und Breiten von 5.2 nm und 10.9 nm auf. Die geneigten NTs wachsen auf mittleren Höhen und Breiten von 5.1 nm und 8.3 nm. Dies geschieht aufgrund von Ostwald-Reifung oder das Verschmelzen von kleineren Teilchen, was in beiden Fällen zu einer reduzierten Anzahl der NTs führt.
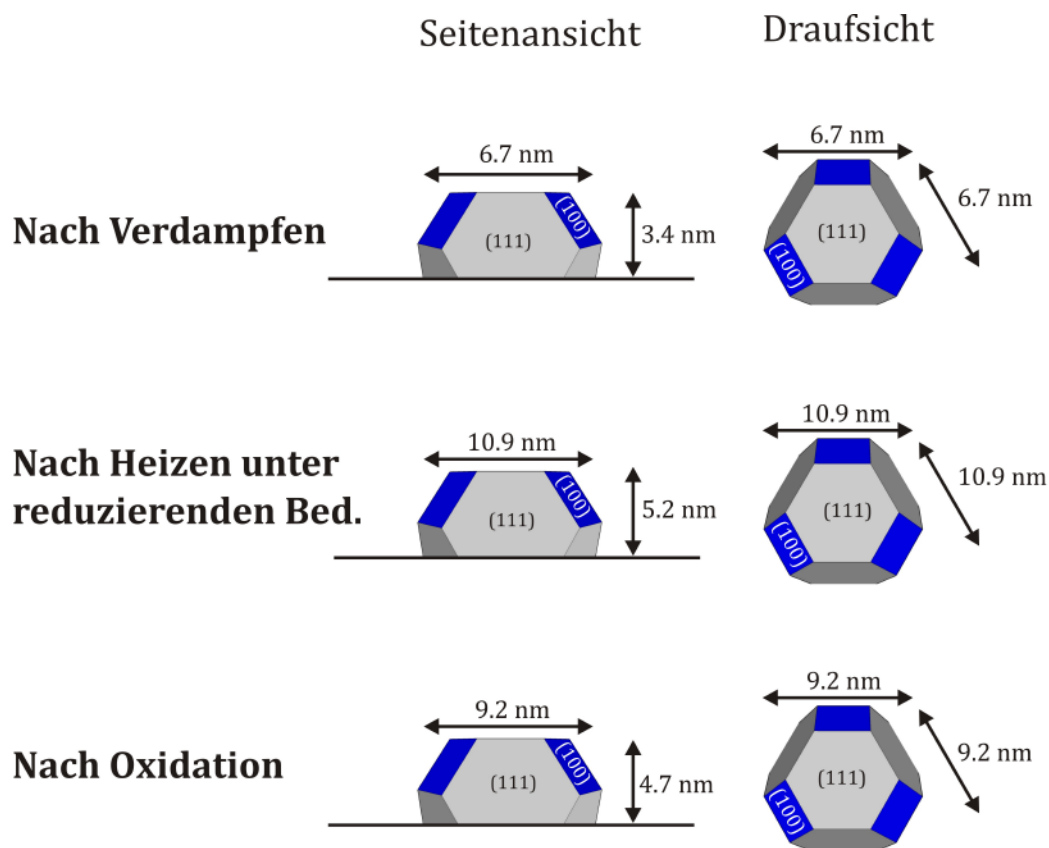
Abbildung 2: Seiten- und Draufsicht der (111)-Orientierten Nickel NTs auf der YSZ-(111)-Oberfläche. Diese Teilchen koexistieren mit lateral getrennten Zwillingen und zeigen eine interne Verzwillingung. Die Form dieser Teilchen ändert sich dabei nach den benannten Behandlungen nicht was zu einer konstanten Adhäsionskraft führt.

Die (111)-orientierten NTs behalten dabei ihre ursprüngliche Form und die geneigten NTs werden höher.

Nach einer Behandlung bei 10^{-5} mbar Sauerstoff und 300°C für 35 Minuten, wird ein Großteil beider NT-Sorten in Übereinstimmung mit Untersuchungen der jeweiligen Facetten-Einkristalle [15; 16; 17] oxidiert. Die (111)-orientierten Ni Teilchen werden dabei teilweise in Nickeloxid-NTs mit gleicher Epitaxie umgewandelt.

Bei einer schrumpfenden mittleren Größe von 4.7 nm und 9.2 nm in Höhe und Breite, behalten die (111)-orientierten Nickel NTs jedoch weiterhin ihre ursprüngliche Form. Dies deutet auf eine gleichmäßige Oxidation aller NT-Facetten über alle Teilchengrößen hinweg, wobei kleinere Teilchen gänzlich oxidiert werden können.

Die geneigten nicht oxidierten NTs behalten nach dieser Behandlung ihre
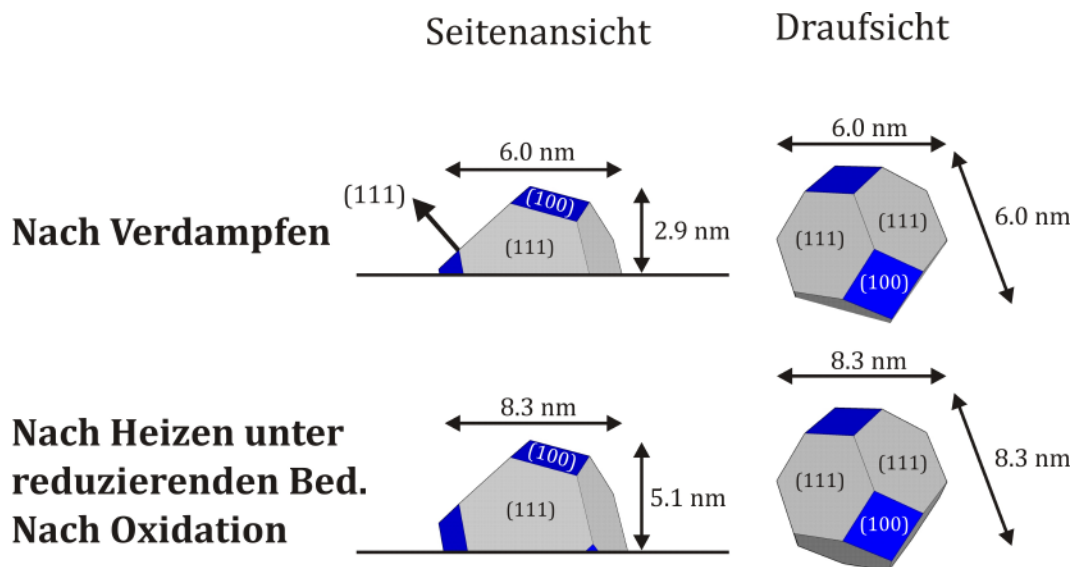
Abbildung 3: Seiten- und Draufsicht der kohärent geneigten Nickel NTs. Das Heizen bei reduzierenden Bedingungen und 700°C führt zum Wachstum dieser Teilchen wobei sich ihre Form ändert. Die anschließende Sauerstoffbehandlung hat aber keinen Einfluss auf die mittlere Größe und die Form dieser NTs.

mittlere Größe und Form. Die starke Intensitätsabnahme ihrer Braggreflexe deutet jedoch auf eine erhebliche Oxidation dieser Teilchen an. Die resultierenden mittleren Größen zeugen aber von einem andren Oxidationsmechanismus, als bei den (111)-orientierten NTs. Hier könnte der Sauerstoff durch die Grenzfläche zum Substrat in die Teilchen eindringen und diese, unabhängig von ihrer Größe, entweder gänzlich in NiO umwandeln oder gar nicht.

Die stets gleiche Form der (111)-orientierten NTs führt zu einer konstanten Adhäsionskraft von 1.99 J/m^2. Die rundlichere Form der geneigten NTs ist ein Indiz für eine niedrigere Adhäsionskraft.

Die Grenzfläche des Substrats zu den NTs wird weder beim Wachsen der NTs, noch nach den benannten Behandlungen der NTs signifikant verändert.

Die YSZ(100)-Oberfläche (Kapitel 6.1)

Zur Bestimmung der Struktur der YSZ(100)-Oberfläche standen herkömmliche (normale) SXRD-Daten zur Verfügung. Die Strukturbestimmung erfolgte daher auf Basis der Fluorit-Struktur des Bulks, die nicht zwischen Zr und Y unterscheidet, wobei intrinsische Sauerstoff-Fehstellen berücksichtigt wurden. Abbildung 4 zeigt die Modelle für beide untersuchte Bedingungen.

Die reine Oberfläche zeigt eine (1 x 1)-Rekonstruktion in Übereinstimmung mit einer früheren experimentellen Studie [18]. Eine Yttrium-angereicherte Oberfläche wird daher in Anlehnung an einer theoretischen Untersuchung dieser Facette gefolgert [12]. Die oberste Sauerstoff- und Metalllage zeigt dabei eine niedrige Besetzung von 18% und 32%. Gleichzeitig wird die Sauerstofflage in guter Übereinstimmung mit DFT-Berechnungen stark nach oben verschoben [12]. Die hohe Anzahl von Sauerstofffehlstellen an der Oberfläche führt zu asymmetrischen Bindungsverhältnissen der obersten Metalllage, die diese nach unten verschieben. Diese Struktur kann daher als ungeordnet und hoch defektiv betrachtet werden und ändert sich bis zu einer Temperatur von 600°C und oxidierenden Bedingungen nicht.
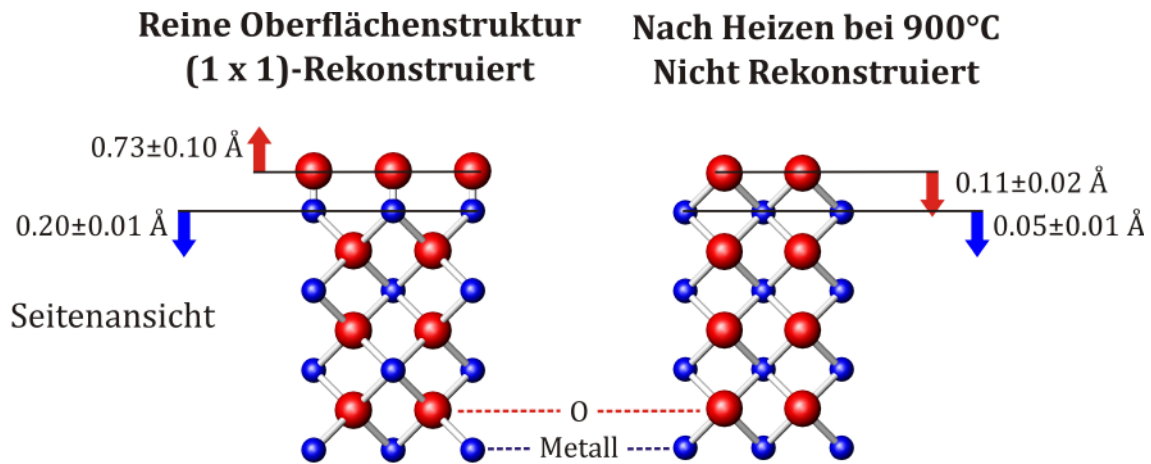
Abbildung 4: Seiten- und Draufsicht der YSZ-(100)-Oberfläche basierend auf dem Fluorit-Modell. Die reine Oberfläche auf der linken Seite zeigt eine (1 x 1)-Rekonstruktion. Die hohe Anzahl von Fehlstellen in den obersten Lagen führen dabei zu asymmetrischen Bindungsverhältnissen, die diese Atomlagen stark aus ihren Bulk-Positionen auslenken. Eine Behandlung bei oxidierenden und reduzierenden Bedingungen und 900°C führt zur auf der rechten Seite dargestellten Struktur, wobei die Rekonstruktion aufgehoben wird. Der gleichzeitige Anstieg der Konzentration in der obersten Metalllage lässt dabei auf eine Segregation von Zr aus unteren Lagen schließen. Zudem erhöht sich die Sauerstoffbesetzung in der obersten Lage, was zu einem Ausgleich der Bindungsverhältnisse und damit eine abgeschwächte Auslenkung der Atome aus ihrer Bulkposition führt.

Eine Behandlung der Oberfläche bei 900°C führt bei oxidierenden und reduzierenden Bedingungen zur gleichen Struktur. Nach dieser Behandlung steigen Metall- und Sauerstoffkonzentration in den beiden obersten Lagen stark auf 53% und 57% an. Das gleichzeitige Verschwinden der (1 x 1)-Rekonstruktion lässt dabei auf eine Segregation von Zr schließen [12]. Da für eine gute Übereinstimmung mit den Daten das Fitten der Konzentration einer zusätzlichen Metalllage auf 89% notwendig war, kann weiter angenommen werden, dass die segregierten Zr-Atome aus den unteren Lagen stammen. Der Anstieg der Sauerstoff-Konzentration an der Oberfläche sorgt für einen Ausgleich der Bindungspartner der Metallatome in der darunterliegenden Lage. Die Auslenkungen beider Lagen aus ihren idealen Bulk-Positionen reduzieren sich daher deutlich.

Nickel-Nanoteilchen auf der YSZ(100)-Oberfläche (Kapitel 6.2)

Nickel wurde im Anschluss an die oberen Behandlungen mittels PVD mit einer nominellen Dicke von 5.7 nm auf die YSZ(100)-Oberfläche verdampft und bedeckte diese anschließend zu 52%. Aufgrund der guten Übereinstimmung der Gitterparameter zum Substrat wurden (100)-orientierte NTs mit einer „cube on cube" Epitaxy erwartet. Es zeigt sich jedoch, dass

- nur ein kleiner Bruchteil der NTs eine „cube on cube" Epitaxy vorweist. Diese Teilchen haben mittlere Höhen und breiten von 3.7 nm bzw. 6.2 nm und sind in Abbildung 5 dargestellt.

- Die Mehrheit der Teilchen hat eine (111)-orientierte Texturierung wie in Abbildung 6 gezeigt. Diese flachen Teilchen bevorzugen trotz der Textur Drehungen von 15° und 30° relativ zum Substratgitter. Sie koexistieren lateral mit Zwillingsteilchen und weisen einen kleinen Anteil an internen Verzwillingungen auf. Ihre mittlere Größe beträgt 4.2 nm und 11.2 nm in Höhe und Breite und führt zu einer Adhäsionskraft von 2.27 J/m^2.

Die (111)-Textur deutet wegen der niedrigen Energie der Nickel-(111)-Oberfläche auf ein stark Oberflächenenergie-dominiertes Wachstum hin. Die Existenz und der Anteil beider NT-Sorten stimmt mit Untersuchungen von Nickel-
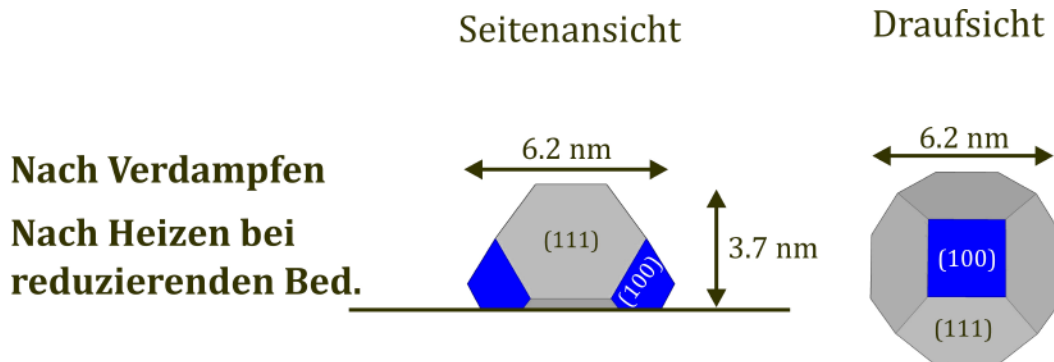
Abbildung 5: Seiten- und Draufsicht der „cube on cube" Nickel-NTs auf YSZ-(100). Diese Teilchen behalten nach einer Behandlung bei 850°C und reduzierenden Bedingungen ihre mittlere Größe und Form und verschwinden nach der Oxidation bei 850° gänzlich.
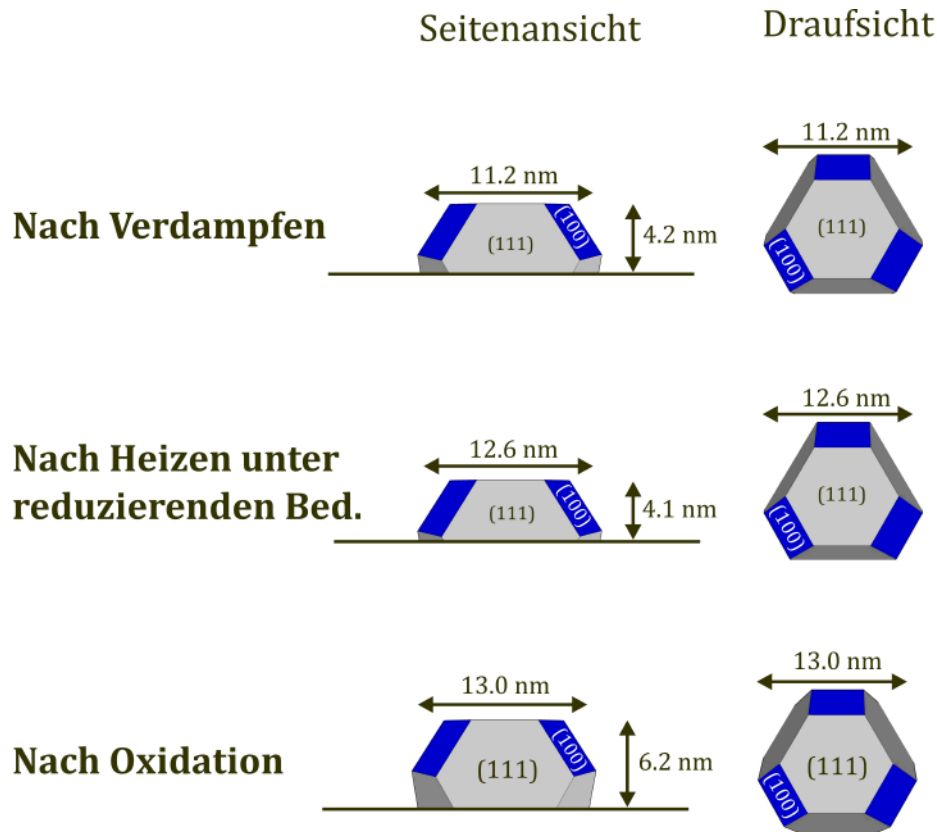
Abbildung 6: Seiten- und Draufsicht der texturierten Nickel-NTs auf YSZ-(100). Diese Teilchen koexistieren mit lateral getrennten Zwillingen, wobei beide auch interne Verzwillingungen aufweisen. Sie machen eine deutliche Mehrheit der NTs auf diesem Substrat aus. Ihre flache Form wird dabei bei einer Hitzebehandlung und reduzierenden Bedingungen weiter. Eine Sauerstoffbehandlung bei 850°C führt zur Entstehung von NiO-NTs mit gleicher Texturierung. Die nicht oxidierten Teilchen gewinnen dabei wegen des hohen Massentransfers bei den gegebenen Temperaturen an Höhe.

Inseln auf diesem Substrat überein [19; 20].

Nach einer Hitzebehandlung unter reduzierenden Bedingungen und 750°C für 45 Minuten und anschließend 850°C für 25 Minuten, ändern die (100)-orientierten Teilchen ihre Größe und Form nicht, was auf eine hohe Stabilität dieser Teilchen hindeutet. Die texturierten Teilchen werden bei einer praktisch konstanter Höhe von 4.1 nm und einem Anstieg der Höhe auf 12.6 nm etwas flacher, was zu einer nahezu konstanten Adhäsionskraft führt.

Nach einer Behandlung mit 10^{-7} mbar Sauerstoff bei 850°C für 12 Minuten und anschließend 10^{-6} mbar Sauerstoff für 13 Minuten, sind die (100)-orientierten Teilchen gänzlich oxidiert und die texturierten Teilchen größtenteils zur NiO-NTs mit gleicher Texturierung umgewandelt worden. Die nicht oxidierten texturierten NTs nehmen bei mittleren Höhen und Breiten von 6.2 nm und 13.0 nm eine höhere Form an, was auf eine niedrigere Adhäsionskraft von 2.03 J/m² schließen lässt.

Das Wechselspiel zwischen homogener Oxidation aller NT-Facetten und großer sauerstoffinduzierter Massentransfer bei den hohen gegebenen Temperaturen lässt die texturierten Ni-NTs eine höhere Form annehmen.

Die Oberfläche des Substrats ändert sich nach der Hitzebehandlung. Diese Änderung kann einem Anstieg der Zr Konzentration in den obersten Substartlagen oder die Besetzung von Substratfehlstellen durch Ni zugeschrieben werden.

Schlussfolgerungen

Die Strukturen beider Oberflächen zeigen bei den untersuchten Bedingungen ein ähnliches Verhalten. Die reinen Oberflächen sind Yttrium-angereichert und sind wegen der hoch defektiven Zusammensetzung sehr ungeordnet. Das Heizen dieser Oberflächen unter reduzierenden Bedingungen führt dabei zur Segregation von Zr und einer Reduzierung der Fehlstellen, was zu einer höheren Ordnung in der Oberfläche führt. Bedenkt man jedoch, dass gerade die Existenz von Defekten und Unordnung für die katalytische Aktivität vieler Oxide verantwortlich sind [21], so führen Betriebsbedingungen zu einer reduzierten Effizienz der SOFC-Anode (abgesehen von der Ionen-Leitfähigkeit). Die Kontrolle der Fehlstellen an der Oberfläche und die Segregation von Zr wird daher ein Schlüssel zur Steigerung der Anodeneffizienz sein. Wird Y als Ursache der Defekterzeugung und damit der Unordnung betrachtet, so könnte eine über mehrere Lagen Y-angereicherte Anodenoberfläche zu solch einer Steigerung führen. Eine kürzlich veröffentlichte Arbeit berichtet tatsächlich von solch einer Effizienzsteigerung um 50%, wenn eine SOFC-Anode mit einem Film hoher Y-Konzentration bedeckt wird [22].

Obwohl die Nanoteilchen auf den jeweiligen Substraten unterschiedlich dominierte Wachstumsmechanismen aufweisen, kann zusammengefasst werden, dass eine große Mehrheit von ihnen (111)-orientiert ist. Auch hier führen Betriebsbedingungen zu einer eher schädlichen Änderung der NT-Formen. Auf beiden Oberflächen führt die Hitzebehandlung unter reduzierenden Bedingungen zum Sintern der NTs, was zu einer Reduzierung der verfügbaren Nickeloberflächen und daher zu weniger Aktivität führt. Eine Begrenzung dieses Sinterns ist daher als eine weitere Maßnahme der Effizienzsteigerung zu betrachten.

Auch die Oxidationsmechanismen für die (111)-orientierten Nickel NTs sind auf beiden Substraten ähnlich und deuten auf die Existenz von von NiO umhüllten Ni NTs. Offen bleibt, ob die hohen Temperaturen und reduzierenden Bedingungen unter denen die Anode betrieben wird, im Anschluss der Oxidation zu einer Rücktransformation der oxidierten Teilchen zu ihrer ursprünglichen Form führt, wie es etwa für Nickel-Einkristalloberflächen der Fall ist [23]. Diese Frage gilt es in einer künftigen Arbeit zu beantworten.

Die Existenz von jeweils zwei NT-Sorten auf beiden Oberflächen kann ein Hinweis für lokale Kompositionsunterschiede auf beiden Oberflächen sein, wie sie für den Bulk von YSZ bekannt sind [24; 25]. Die hohe Sauerstofffehlstellendichte kann jedoch auch eine teils Sauerstoff- und teils Metall-Terminierung dieser Oberflächen bedeuten, was die jeweils zwei Sorten auf diesen Substraten erklären könnte. Eine weiterführende Untersuchung kann hier wertvolle Informationen liefern. Auch die lokale und angulare Verteilung der verschiedenen Nanoteilchen-Typen ist noch unbekannt und kann im Rahmen einer TEM-Studie gut erforscht werden.

Es kann zusammenfassend gefolgert werden, dass diese Arbeit atomare Modelle für die wichtigen YSZ(111) und (100)-Oberflächen liefert. Es werden weiter die Form und Formänderungen von Nickel Nanoteilchen auf diesen Oberflächen aufgelöst. Die gewonnen Erkenntnisse werden von einer Reihe theoretischer und experimenteller Studien bestätigt. Die Resultate dienen als eine fundamentale

Grundlage für weiterführende experimentelle Studien über die chemischen Reaktionen auf diesem Cermet und die Modellierung von Brennstoffzellen-Anoden.

1 Introduction

The demand for new energy concepts is undeniable. The rapid technological progress of the past decades together with an explosive development of the population, have led to an immense need of energy which is mainly provided by nuclear power or the combustion of fossil fuels today.

The risks induced by nuclear power plants are widely known and accepted and the upcoming shortage of fossil fuels makes an independent energy economy reasonable from many points of view. Moreover, both of these supply types are heavily polluting the environment with unforeseen consequences.

Fuel cells together with the hydrogen economy are considered as key technologies towards a sustainable "green" energy economy independent from fossil resources, not only amongst scientists and engineers [1; 2; 3; 4]. Their ecological-friendly energy generation makes them also widely accepted in society [26; 27] as well as by policy makers [7]. Moreover, fuel cell technology is creating an increasing number of jobs due to its economic growth [28].

Fuel cells are able to convert chemical energy into electrical power with a large scalability which makes them applicable for power plants as well as for mobile applications. The chemical conversion is done by creating H_2O out of hydrogen and oxygen with H_2 being the fuel (see Figure 1.1).

Regarding the commonly known problems with producing and storing hydrogen [29; 30], solid oxide fuel cells (SOFC) play an outstanding role. Their unique capability to use not only pure H_2 but also hydrocarbons as fuel, leads to impressive allover efficiencies. Being operated at temperatures between 600°C and 1000°C, the efficiency can be increased when SOFCs are used in combined electrical and heat production such as in a gas turbine.

In order to make SOFCs competitive, the efficiency has to be further improved and the lifecycle of the cells prolonged to reduce allover costs [8]. These requirements demand an exact understanding of the relevant physical and chemical

processes on the cathodes on a microscopic scale. The diversity of usable fuels makes the fuel cathode or anode of a SOFC to the main key for achieving the named goals.

There have been several attempts to develop and improve anodes for SOFCs. A cermet of yttria-stabilized zirconia (YSZ) and nickel particles has made it to the by far most used anode material for around 50 years now [1; 8; 31]. On this anode, the fuel is processed on a mixture of nickel particles and the YSZ surface. The so-called "three-phase boundary" between the nickel particles, the YSZ surface and the fuel is thus considered as the key element to understand on a molecular basis in order to achieve the desired properties [8; 32; 9]. Moreover, the structure of the three-phase boundary is believed to be crucial for the functionality of SOFCs [8]. Atomic resolution surface structures of YSZ surfaces and the shape and facets of Ni
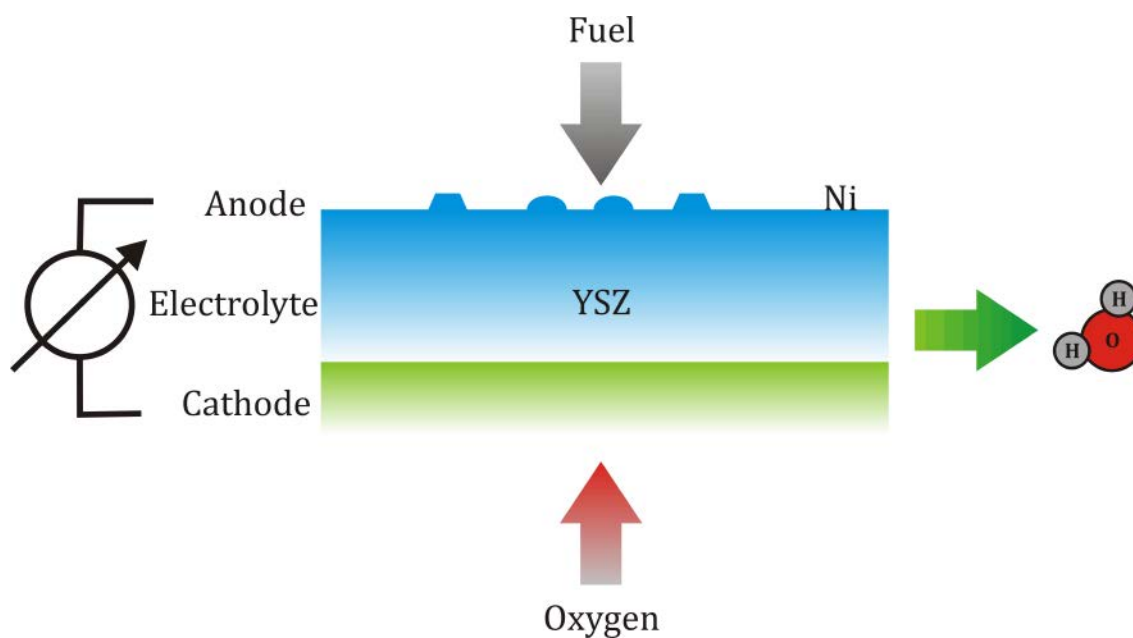
Figure 1.1: Sketch of a solid oxide fuel cell. Oxygen is ionized in the cathode and creates water with the processed fuel on the anode. The chemical energy is converted into electrical power with H_2O as the main "waist" which makes SOFCs to a "green" technology. The diversity of fuels for SOFCs makes the oxidation of the fuel and the creation of H^+ ions to the most relevant processes. These processes take place on the anode which therefore is a key to SOFC improvements and efficiency enhancements.

nanoparticles (NPs) are thus elementary for modeling and understanding the three-phase boundary. Such structures are however rare and we are facing a lack of knowledge about both, experimentally and theoretically supported models.

Surface structure models with atomic resolution have been the topic of surface science in the past decades. Here, surface driven properties as catalytic activity have been linked to structural characteristics of a material (G. Ertl was awarded the Nobel Prize for his work in this field in 2007 [33]).

The surface of a typically used material in applications shows a multifaceted shape (see Figure 1.2). Studying such faceted structures is however fairly difficult and desired atomic information hard to derive.

The frequency of these facets depends on the energy of each facet orientation. Surface energies are usually obtained by applying theoretical models as density functional theory (DFT) and have revealed the (111) surface of cubic YSZ to have the lowest energy [12].

A proper approach to deliver information about the surface structure of materials is to study single crystals and assemble the models gained for each single crystal orientation into a complete surface picture. The structure of low energy surfaces, thereby, play a major role since a large part of the surface in expected to be covered with these orientations [21].
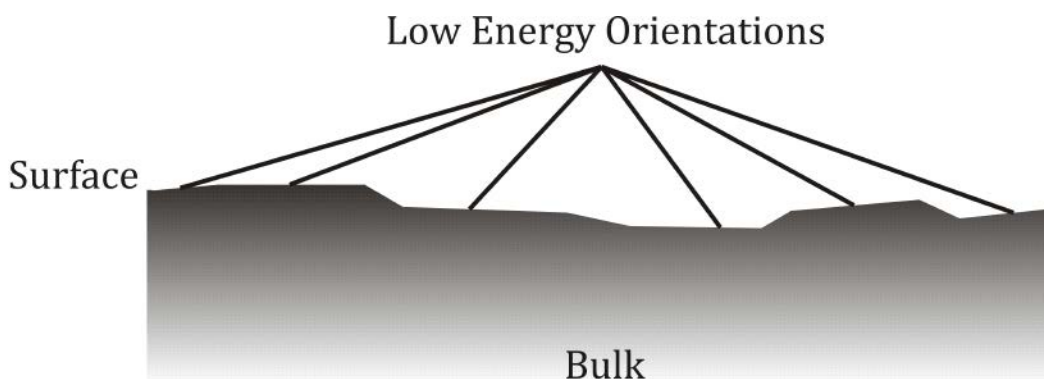

Figure 1.2: The surface of a real material often consists of facets. The frequency of theses facets is highly depending on the surface energy of the respective orientation. The major part of such a surface is thus covered by low energy facet orientations.

The structure determination of pristine surfaces under ultra-high vacuum (UHV) conditions is basal in this context. These models serve as a fundamental first step towards understanding more complicated processes in advanced experiments with the surface being exposed to reactants and under non-UHV conditions. Different, very successful techniques have been developed for this purpose with scanning tunneling microscopy (STM) being probably the most known one (the inventors received the Nobel Prize in 1986 [34]).

Most of the experimental techniques used in surface science require reasonable electrical conductivity of the studied material. Insulating materials as YSZ are thus very difficult to study with these tools. Diffraction techniques are an exception since they do not depend on conduction properties, requiring an ordered structure however. X-ray diffraction is hence a suitable tool to study the structure of YSZ and was applied to resolve the YSZ bulk structure successfully (see [35] and references therein).

Surface X-ray diffraction (SXRD) is a unique tool to resolve surface structures *in-situ* and with sub-Ångström resolution that has been employed successfully to many materials in the past years [36; 37; 38; 39; 40]. It is therefore a predestinated technique to investigate the structure of YSZ surfaces. SXRD has moreover been applied very successfully to resolve the shape and shape changes of NPs [41; 42].

The goal of this work is to use SXRD to deliver reliable atomic and compositional models of YSZ surfaces as well as the shape and size of nickel NPs grown on them as model anode surfaces for SOFCs under different conditions. Surface structure models are proposed for two pristine states. First, the structure after a simple preparation rendering a contamination free surface is discussed. The second state is after treating the surfaces at temperatures above 800°C and reductive conditions being a relevant situation for SOFC anodes. Shape changes of nickel NPs are studied at elevated temperatures as well. Although SOFC anodes are operated under reducing conditions, oxygen exposure is an important issue during startup and shutdown cycles. Since the oxidation of nickel is highly reducing the efficiency of

SOFCs and plays an important role in the design of state-of-the-art anodes, the NPs were exposed to oxygen and the structural effects studied.

Two single crystal YSZ surfaces were chosen therefore. The lowest energy surface and hence the most common orientation, namely the (111) facet is addressed in chapter 5.1. There is no experimentally derived structure model of this surface and this study delivers new insight. Chapter 5.2 deals with the growth and shape of Ni NPs on this surface and their shape changes. Although the growth of nickel on this surface has been subject of publications, the shape and shape changes of the NPs have barely been studied so far.

Chapter 6.1 treats the atomic structure of the YSZ(100) surface. This facet has the third lowest energy and is polar. It therefore plays a special role among the low index surfaces since it is reported to be reconstructed [18]. Coherent models for each of the above states are presented. Nickel NPs on this surface are discussed in chapter 6.2 which delivers insight into the growth of nickel on this substrate as well as their shape changes after the mentioned treatments.

2 Yttria-Stabilized Zirconia and Nickel Nanoparticles

It was Walther Nernst who discovered the ion-conducting property of yttria-stabilized zirconia at high temperatures over 100 years ago [43] and used it for his famous Nernst Lamp. This conductivity together with a high electrical and thermal insulation and a very high melting point of around 3000K have made YSZ a key material for a number of important applications. Today, YSZ is a widespread thermal barrier coating material like on the blades of jet turbines to protect the underlying aluminum oxide [44; 45]. The oxygen-ion conductivity is used in another important technical application, namely the sensor technology. Here YSZ is employed as a ceramic membrane. These sensors are for instance utilized in a combustion engine to reduce the emission by exhaust gas recirculation. This material is moreover widely used as a substrate for the growth of thin films and nanoparticles (NP).

A very important application and also one of the most interesting from the surface science point of view is YSZs employment in solid oxide fuel cells where YSZ is the most used material as an electrolyte for oxygen ions as well as a supporting material for metal particles on the anode side (see Figure 2.1) [1; 46]. Fuel cells are of interest for science and technology because of their low pollution production with water being the main 'waste'. They can moreover be built in a variety of scales making them useful for mobile and stationary applications. The significant advantage of SOFCs compared to other types of fuel cells, such as the proton exchange membrane fuel cell (PEMFC) or the solid polymer electrolyte fuel cell (SPEFC), is their ability to use pure hydrogen as well as hydrocarbons like methane as fuel which enables them to reach unrivaled allover efficiencies [1; 47; 2; 3].

Very frequently, nickel is chosen as a material for the anode metal nanoparticles [1; 46]. This is due to the high capability of nickel to oxidize hydrocarbons and the

low production costs. It needs to be mentioned that SOFCs function at temperatures above 600°C, which is often considered as the main disadvantage of them and has encouraged the goal to develop low temperature SOFCs.

The following will describe a SOFC and give the motivation for this work. It continues with the current knowledge about pure zirconia and YSZ and reviews its surfaces. The chapter closes with a brief summary about nickel, its surfaces and supported nickel growth.

2.1   Solid Oxide Fuel Cell

There is no better system to demonstrate the importance of the "Ni on YSZ" system than a solid oxide fuel cell (SOFC). A fuel cell in general, is a galvanic cell that converts the chemical reaction energy of a fuel with an oxidizing agent into electrical power. It consists of a cathode and an anode that are separated by an electrolyte. In case of a SOFC the fuel is hydrogen or, being the superior advantage of SOFCs, a hydrocarbon. In the latter case the anode processes hydrocarbons into H_2.

The cathode of a SOFC is usually made of a lanthanum strontium manganate (LSM) mostly being in contact with YSZ as an electrolyte. The anode is predominately a mixture of the YSZ surface and nickel particles as sketched in Figure 2.1. Since this work is about YSZ surface structures and the growth and shape of nickel NPs on them, the focus will be on the anodes hereafter

In general, there are three basic chemical reactions necessary for the fuel cell to function. On the cathode surface, oxygen molecules are adsorbed and dissociated into two O atoms which are then ionized into O^{2-} at the cathode electrolyte interface. The chemical reaction can thus be written as

$$O_2 + 4\,e^- \longrightarrow 2\,O^{2-} \tag{2.1}$$
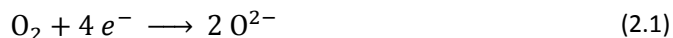
The oxygen ions migrate towards the YSZ surface. Taking pure hydrogen as a fuel, the reactions on the anode side are given by the oxidation of the fuel and the creation of free electrons
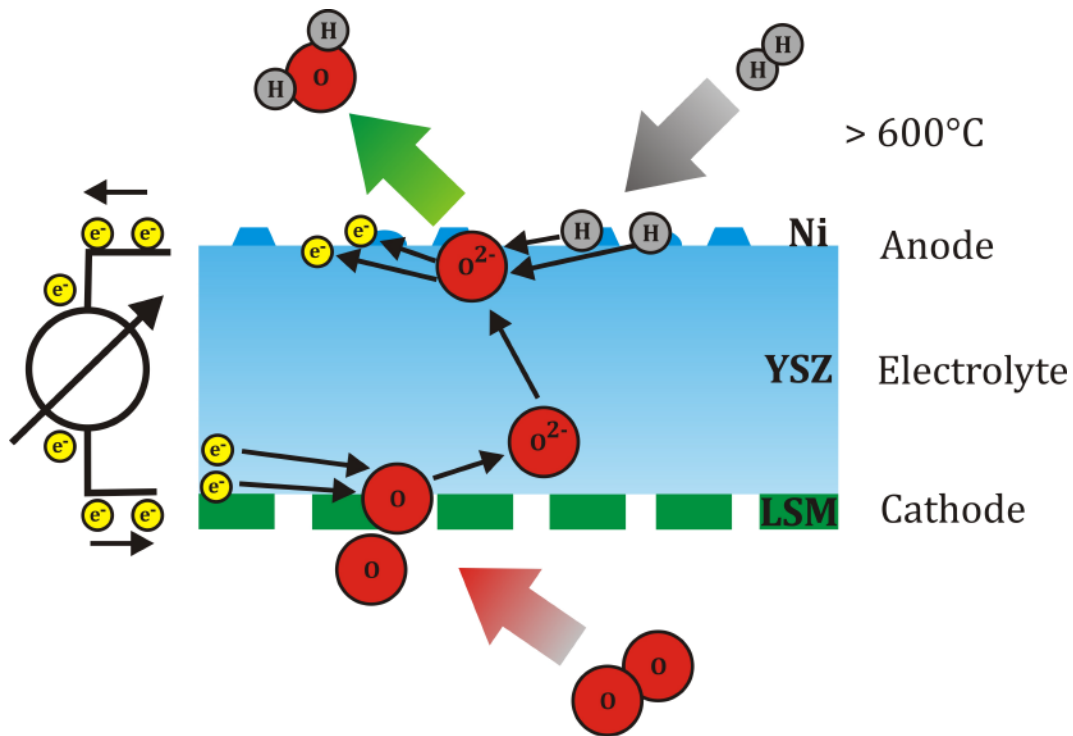
Figure 2.1: Simplified schema of a solid oxide fuel cell. The anode consists of nickel particles and the YSZ surface where H_2 is dissociated. On the cathode (usually lanthanum strontium manganate) O_2 is dissociated and ionized to O^{2-}. This O^{2-} is conducted through YSZ and creates H_2O by reacting with two H atoms and delivering two electrons.

$$2H_2 \longrightarrow 4\,H^+ + 4\,e^- \qquad (2.2)$$

and the reaction of ionized oxygen with oxidized hydrogen to create water

$$O^{2-} + 2\,H^+ \longrightarrow H_2O \qquad (2.3)$$

The electrons flow through an external circuit connecting anode and cathode and delivering electrical power.

Taking hydrocarbons into account, the oxidation of CH_x and the creation of CO_2 are additional reactions on the anode and have to be taken into account.

In order to improve the efficiency of SOFCs it is necessary to understand the following procedures on the anode:

- Where is the fuel adsorbed? On the NPs, on the YSZ surface or at the boundary between YSZ and nickel?

- Where and how is the fuel oxidized? The dissociation could be a cooperation between the NPs and the YSZ surface with spillovers of the reactants playing a major role [32; 9].

- Where and how is water created? Here, spillovers are supposed to play an important role again.

- In case of hydrocarbons as fuel, where and how does the creation of CO_2 take place?

2.2   Motivation

The supreme importance of the three-phase boundary between the YSZ surface, Ni nanoparticles and the fuel for the SOFCs anode is unchallenged [32; 48; 8] and spillovers between these phases were shown to play a major role for the functioning in theoretical studies [32; 9]. Hence knowledge about the atomic structure of YSZ surfaces and the shape of nickel NPs grown on them is a key to understand chemical reactions on the SOFCs anode on a fundamental level [1]. This model system delivers fundamental knowledge about the composition and coordination of the YSZ surface and the facets of nickel all being dominating the above mentioned reactions. Moreover, this knowledge will serve as a base for future modeling of SOFCs and is essential for the development of more efficient anodes in the future.

The above considerations give the motivation for this work to study the pristine atomic structure of two important surfaces of the most used YSZ composition with 9.5% mol yttria (see section 2.4): the most stable (111) surface and the polar (100) surface [12]. Thereafter the shape and size of nickel NP grown on these surfaces where explored *in-situ*.

Looking at the operating conditions of SOFCs at above 600°C, the surface structures of YSZ were studied at elevated temperatures as well. Segregation of yttrium to the surface has been discussed recently [49; 50; 51]. Such a segregation changes the chemical potential of the YSZ surface and the interface with the nickel NPs noticeably and was reported to change the efficiency of SOFCs significantly [22]

very recently. Moreover, the shape change of the NPs at these temperatures and the influence of oxygen and methane on the NPs were subjects of this work in order to deliver structural information about the system under realistic conditions.

The electrical insulating property of zirconia and YSZ severely hinders experimental techniques involving an electron current such as STM and LEED . STM images of the YSZ(111) surface were measures recently by making use of the ion-conducting property at elevated temperatures [52]. This experiment, however, is far from atomic resolution and thus unable to deliver a structural model. To the best of my knowledge, there exists only one single experimental paper about the atomic structure of an YSZ surface using high resolution ion scattering up to date [18]. Experimental data about all other surfaces are missing and the validity of the model mentioned before [18] has to be proved with other techniques. Moreover, there are only very few publications using theoretical calculations such as DFT [53; 12]. This is due to the additional insertion of yttrium atoms and O vacancies to the "supercells" used for the calculations and the partially polar surfaces of zirconia that complicate such studies and make them time consuming.

Considering these facts, surface X-ray diffraction (SXRD) is an outstanding experimental tool to study YSZ surfaces and gain atomic-resolved knowledge about their structures. (see section 4.1). Moreover, SXRD is recently being used very successfully to determine the shape of NPs and their changes during chemical reactions [11; 41]. These reasons have motivated the use of SXRD as a main tool for studying the Ni/YSZ system.

In order to understand the surface of a crystal, it is essential to know its bulk. The following will give a short summary about what is known about the bulk structures of pure zirconia in the different phases. It continues with the bulk structure of YSZ and gives an overview about the few publications on the surface structures of YSZ.

2.3   Pure Zirconia

Zirconia undergoes three phase transitions with temperature. It is monoclinic at room temperature and changes to the more dense tetragonal structure above 1440 K. Finally a cubic phase is stable in a very small temperature range between 2640 K and close to the melting point at 3000 K. These transitions, especially the first one, are accompanied by a big volume change that very often causes the material to crack which is a severe drawback for the use of pure zirconia in real applications. In the next sections, the structures of pure ZrO_2 are discussed.

2.3.1   Cubic ZrO_2

The cubic phase of zirconia is stable at temperatures above 2640K and has a lattice constant of [54]

$$a = 5.07 \text{ Å} \tag{2.4}$$

The space group symmetry is Fm3m (see International Tables of Crystallography for symmetry group information [55]) and the unit cell contains four ZrO_2 molecules with the metals on (4a) and oxygen on (8c) positions. Figure 2.2 shows the unit cell
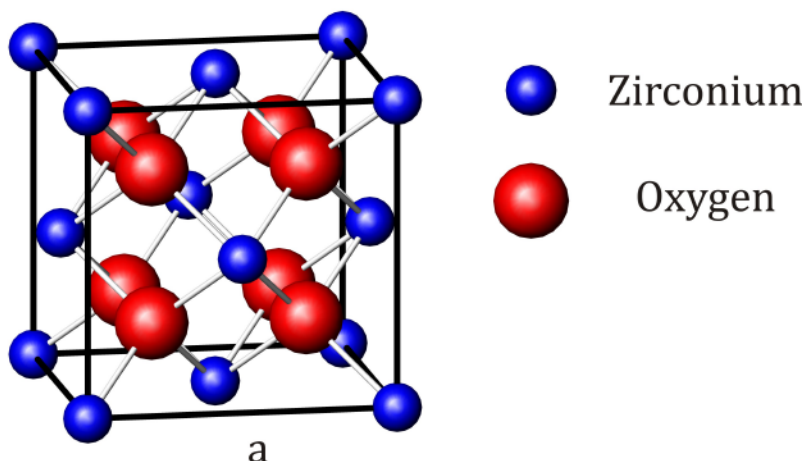

Figure 2.2: Fluorite structure of pure zirconia in the cubic phase: the red oxygen atoms are surrounded by a tetrahedron of blue zirconium atoms sitting on the fcc sites of the unit cell with a lattice constant of 5.07 Å

of the cubic phase in a stick and ball model. In this fluorite (CaF_2) structure, the oxygen atoms are surrounded by a tetragon of zirconium atoms with the bonding length 2.91 Å sitting on the fcc sites where Zr atoms are eight-fold coordinated.

2.3.2   Tetragonal ZrO_2

This phase is stable between 1440K and 2640K. It has the symmetry group $P4_2$/nmc [55] and contains two Zr and four O atoms sitting on 2(a) and 4(d) positions in a unit cell with the dimensions [56]:

$$a = b = 3.64 \text{ Å}, c = 5.27 \text{ Å and } \alpha = \beta = \gamma = 90°.$$

The phase transition from the monoclinic to the denser tetragonal structure is accompanied with a large density change from $5.7 g/cm^3$ to $6.1 g/cm^3$ which often causes the material to crack.

The tetragonal phase can be thought of as an ideal cubic fluorite structure where altering {111} oxygen planes are displaces along [011] directions by ∼0.3 Å.

2.3.3   Monoclinic ZrO_2 (Baddelyite)

The monoclinic phase of ZrO_2 is the lightest phase of pure zirconia with a density of 5.7 g/cm^3. It is stable up to a temperature of 1440 K. The unit cell is dimensioned as [57]:

$$a = 5.169 \text{ Å}, b = 5.232 \text{ Å and } c = 5.341 \text{ Å with } \alpha = \gamma = 90° \text{ and } \beta = 99°.$$

It has the space group symmetry $2P_1$/c [55] with two ZrO_2 in the unit cell where the atoms sit on (4e) positions. This phase is not used in applications because of its phase transition at relatively low temperatures.

In this phase, the coordination of Zr reduces to four and a irregular polyhedron of seven oxygen atoms builds up the baddelyite structure.

2.4   Yttria-Stabilized zirconia

The most common way to stabilize one phase of zirconia over a large temperature range is yttria doping. This dopant stabilizes ZrO_2 at concentrations

above 2% mol where zirconia is partially stabilized at concentrations between 2% and 8% mol and fully stabilized there above. Moreover, the oxygen-ion conductivity is introduced by oxygen vacancy creation, due to the replacement of ZrO_2 by Y_2O_3. The oxygen-ion conductivity has been subject to some studies. It was found that the ion conductivity is showing an Arrhenius-equation behavior over wide ranges of yttria concentration [58]. Another study reported the ion conductivity to become maximal at concentrations between 9% and 10 % mol and drop rapidly for higher concentrations [59].

For thermal protection applications like in the jet turbines, partially stabilized zirconia (PSZ) is more beneficial since it is more resistant to sudden and massive temperature changes. Heterogeneous catalysis and SOFCs however use fully stabilized zirconia (FSZ) because of its higher ion-conductivity. Today, the most used yttria concentration for catalytic applications including SOFCs is 9.5% mol. Therefore, a sample with a 9.5% mol yttria concentration was studied in this work.

A look into literature shows that the surfaces of PSZ are investigated both experimentally and theoretically [13; 60; 61; 62; 53] to some extent. However, there are only very few publications about FSZ despite the numerous applications and the undisputed importance of its surface structures for many applications, especially catalysis as well as the growth of nanoparticles and thin films.

This chapter gives an overview about partially stabilized and fully stabilized zirconia. The focus will be on fully stabilized zirconia, since this phase was studied in this work. Detailed information about PSZ are to be found under [63; 64].

The macroscopic structure of YSZ was controversially discussed in the past (see [65; 66] and references therein). A systematical study [24] revealed that tetragonal clusters of YSZ form upon yttria doping coexisting with small cubic clusters. With increasing concentration of the yttria dopant, the number and stability of the cubic clusters grow. It is also shown that the small cubic clusters are mainly responsible for the oxygen-ion conductivity. This model is hence able to explain why the oxygen-ion conductivity increases up to the limit of yttria concentration to fully stabilize zirconia and drops with further addition of yttria [24; 25].

2.4.1 Partially-Stabilized Zirconia (PSZ)

Partially stabilized zirconia also called tetragonal stabilized zirconia, can be obtained by ceria or yttria doping. In case of yttria, concentrations between 2% and 6% mol are necessary. PSZ is a mixture of the tetragonal phase and a metastable cubic phase due to the lack of stabilizers [64; 24].

It is a highly physical- and thermal-shock resistant material that finds applications whenever sudden and drastic thermal changes have to be resisted like in the aerospace industry where it is used as a thermal barrier coating material. There are three different theories that explain the high physical resistance of PSZ.

The thermal expansion theory [67] assumes the presence of yttria-free ZrO_2 clusters to reduce the thermal expansion compared to FSZ. The second theory expects microcracks at the grain boundaries to prevent the material from further breaking [68] . The last theory uses the slipbands in the material and derives an intrinsic stress-relieve theory [69].

There are a few studies about some of the low index surfaces of PSZ or tetragonal zirconia. While an experimental investigation on polycrystalline samples using TEM and Fourier transform infrared (FTIR) spectroscopy finds the (101) surface to be the most common one [60], theoretical calculations find the (111) surface to have the lowest surface energy and thus to be the most stable orientation [13].

The (011) surface is reported to be oxygen terminated and unreconstructed [61]. The (101) surface was studied more extensively applying DFT and suggests a stoichiometric oxygen termination and no reconstruction [53]. This investigation moreover predicts yttrium atoms far from the (001) while an accumulation of yttria in the (101) surface region is stabilizing this orientation.

2.4.2 Fully-Stabilized Zirconia (FSZ)

Zirconia is stabilized fully in the cubic phase at room temperature by yttria doping concentrations above 7% mol. This doping has two consequences. First, replacing Zr^{4+} with Y^{3+} causes the lattice constant of the cubic unit cell to grow because of the difference in ionic radii [70]. Second, replacing two zirconia

molecules $2 \cdot \text{ZrO}_2 = \text{Zr}_2\text{O}_4$ with one yttria molecule Y_2O_3 will create one oxygen vacancy. Thus, the concentration of yttria equals the intrinsic oxygen vacancy concentration.

The growth of the lattice constant of the fluorite-like structure can be described by Vegard's law over wide ranges of dopant concentration and is given by [71]

$$a\,(\text{Å}) = 0.200x + 5.1063\,(\text{Å}) \qquad\qquad (2.5)$$

where x is the yttrium concentration in the chemical formula

$$(1-x)\text{ZrO}_2\,x\text{YO}_{1.5} \qquad\qquad (2.6)$$

including the intrinsic oxygen vacancy caused by yttria doping.

Assuming the most common yttria concentration used in this work

$$\text{Y}_2\text{O}_3 = 9.5\,\%\,mol = 19\%\,mol\,\text{YO}_{1.5} \qquad\qquad (2.7)$$

the composition of the sample given by equation (2.6) becomes

$$\text{Zr}_{0.81}\text{Y}_{0.19}\text{O}_{1.905} \qquad\qquad (2.8)$$

and thus

$$x = 0.19. \qquad\qquad (2.9)$$

The theoretical lattice constant of the sample is then resulting from equation (2.5) and is

$$a = 5.1443\,\text{Å}. \qquad\qquad (2.10)$$

There are two models for the bulk structure of fully yttria-stabilized zirconia (F-YSZ). These models are presented in the following.

2.4.2.1 Fluorite-like Model

In a first approximation, the bulk structure of F-YSZ can be considered as an ideal fluorite structure where the metal and oxygen atoms of the YSZ composition sit on the ideal (4a) and (8c) fluorite positions with the respective concentrations. This model will be referred to as the 'fluorite-like' model hereafter.
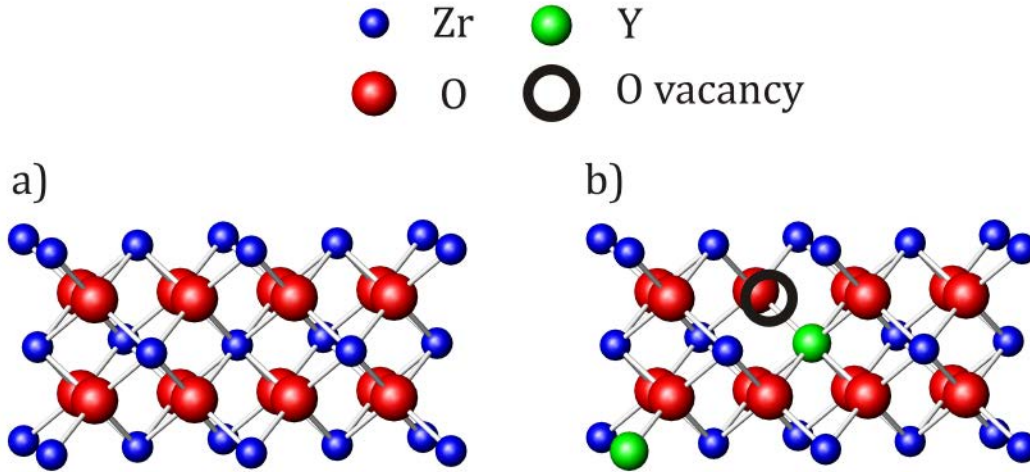
Figure 2.3: Construction of the fluorite-like model: a) shows two unit cells of the pure cubic zirconia structure. b) to construct the fluorite-like model, two zirconium atoms (blue balls) are replaced by two yttrium atoms (green balls) creating one oxygen vacancy (black circle).

Figure 2.3 a) shows two unit cells of pure ZrO₂ in the cubic phase. To construct a fluorite-like model with an yttria concentration of 9% mol, two blue zirconium atoms are replaced by green yttrium atoms in part b). This results in the creation of one oxygen vacancy illustrated by the black circle. This model is used for all theoretical calculations of F-YSZ.

2.4.2.2 Zirconium-shift Model

It was mentioned above, that the structure of YSZ is a mixture of tetragonal and cubic clusters [24; 25]. Hence a microscopic description of this structure has to

Table 2.1: Static Debye-Waller factors B of the atoms in the fluorite-like structure as given in equation (4.10). The mean spacial deviation u(Å^2) is taken from [42].

	$u(\text{Å}^2)$	$B(\text{Å})$
Zirconium	0.0179	1.41
Yttrium	0.0179	1.41
Oxygen	0.029	2.28

contain both elements, the tetragonal and the cubic phase. This is achieved by a distortion of the ideal fluorite unit cell where oxygen atoms of the tetragonal structure are shifted along [011] directions and metals along [111] directions.

Several studies have proved the existence of such a F-YSZ structure with different yttria concentrations using a variety of experimental techniques [72; 73; 74; 75; 76; 77; 78; 79; 35]. They all indicate that the metal and oxygen atoms are shifted from their ideal fluorite position due to the strain caused by yttria doping and the resulting oxygen vacancies [24; 25].

A microscopic picture is motivated by the fact that oxygen atoms surrounding an oxygen-vacancy position will tend to move towards the vacancy. These displacements are thus along the [001] directions as shown in Figure 2.4. On the other hand, metals around an oxygen vacancy are attracted more strongly by their surrounding oxygen atoms which displace them along the diagonal [111] directions, away from the oxygen vacancies.

Although discussed for some time, consensus has been found on the so-called "Zr-shift" model resulting from an experimental study of the bulk structure of a F-YSZ sample with an yttria concentration of 13.9% mol using a combination of normal and anomalous X-ray diffraction at the yttrium K-edge (see section 4.1.1 for description) together with extended X-ray adsorption fine structure (EXAFS) [35]. The normal diffraction data could be fitted quite well by modifying the Debye-Waller factors of pure cubic ZrO_2 in a fluorite-like model. The Debye-Waller factor B of an atom in a crystal is defined as the mean spacial deviation $\langle u \rangle$ of this atom from its perfect position in the crystal given by (see section 4.1.1).

$$B = 8\pi^2 \cdot \langle u^2 \rangle \tag{2.11}$$

The resulting Bs of the metal and oxygen atoms in the fluorite-like model for normal diffraction are given in Table 2.1 and show relatively large values.

Much better agreement was achieved using the so-called "Zr-shift" which allows the additional shifts of oxygen and zirconium atoms from their ideal fluorite positions. Figure 2.4 shows the displacements in this model in a cubic unit cell. Every Zr atom is surrounded by eight neighboring Zr atoms. When yttrium is doped,
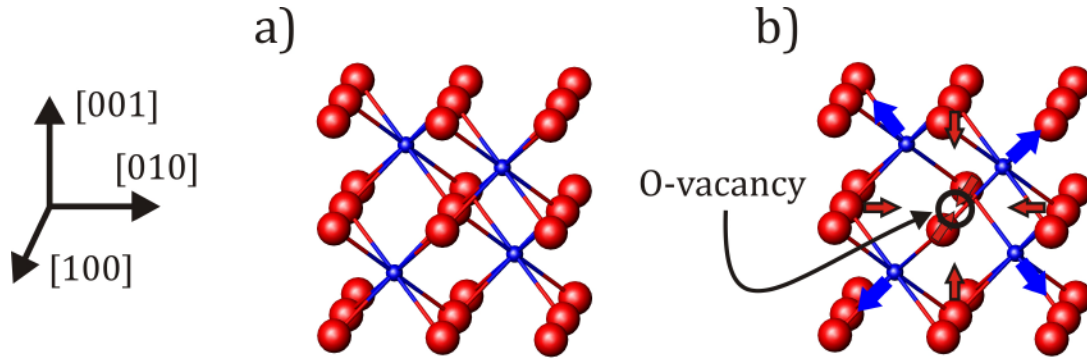
Figure 2.4: a: ideal fluorite structure. b: displacement directions in the zirconium-shift (Zr-shift) model. Oxygen atoms surrounding an oxygen vacancy are displaced towards this vacancy along the [001] directions (red arrows). Metals around the vacancy are attracted from their surrounding oxygen atoms and displaced towards [111] directions (blue arrows), away from the vacancies. Since Y has a lower coordination than Zr, a neighboring oxygen vacancy does not influence its bonding relations and it remains at (4a) positions.

it goes to the ideal (4a) positions. These yttrium atoms create oxygen-vacancies which force the eight surrounding Zr atoms to move along the [111] directions by 0.19 Å.

Moreover, there are two types of oxygen atoms differing in crystallographic position. The first type, called O1 hereafter, is displaced along the [001] directions by 0.31 Å representing the tetragonal clusters. The second type (O2) remains at the original fluorite position, making up 43% and 48% of the oxygen atoms in equation (2.6) respectively. The remaining oxygen atoms are reported to sit on interstitial positions. The resulting Debye-Waller factors for both types of diffraction are listed in Table 2.2.

Note that this model is in line with the requirements given by the tetragonal and cubic clusters, since a part of the oxygen atoms are shifted by 0.31 Å along [001] direction, which is exactly the difference between the cubic and the tetragonal phase as described in section 2.3. The occupation of (4a) sites by Y atoms and the shift of all Zr atoms can be understood by the following. First, oxygen vacancies around Zr forces these atoms o shift. The lower coordination of Y^{3+}, moreover, makes this species less sensitive to surrounding O vacancies than Zr^{4+} and keeps them at (4a)

Table 2.2: Static Debye-Waller factors B resulting from the Zr-shift model [42] using equation (4.10) for normal and anomalous diffraction at the Y K-edge. O1 denotes oxygen atoms displaced from their ideal fluorite position and O2 those remaining on these positions.

	Normal Diffraction		Anomalous Diffraction at Y K-edge	
	$u(\text{Å}^2)$	$B(\text{Å})$	$u(\text{Å}^2)$	$B(\text{Å})$
Zr	0.0087	0.69	0.0101	0.80
Y	0.0059	0.47	0.0005	0.04
O1	0.0169	1.33	0.0163	1.29
O2	0.015	1.18	0.019	1.50

sites. Second, at yttria concentrations stabilizing the cubic phase and thus high oxygen-vacancy concentrations, it can be assumed that all Zr atoms are affected by the mechanism responsible for the shifts illustrated in Figure 2.4.

Symmetry considerations lead to displacements along the equivalent $\pm[001]$, $\pm[100]$ and $\pm[010]$ directions for O1 atoms and along the $\pm[111]$, $\pm[\bar{1}11]$, $\pm[\bar{1}\bar{1}1]$ and $\pm[1\bar{1}1]$ directions for the Zr atoms. Thus a unit cell containing all of the displaced atoms along these directions can be defined to describe this model in a crystallographic way. Since all atoms displaced along equivalent directions are equal, they all have the same occupancy. These occupancies are determined by x given in equation (2.6), and hence by the yttria concentration.

For the shifted Zr, there are eight equivalent atoms with the occupancy Occ_{Zr}

$$\text{Occ}_{Zr} = \frac{1-x}{8} \tag{2.12}$$

The oxygen occupancies are not only depending on x, but also on the partial distribution between the two types O1 and O2 (OccP_{O1}, OccP_{O2}). In case of the O1 atoms, we have six equivalent atoms each with the occupancy

$$\text{Occ}_{O1} = \frac{(2-0.5x) \cdot \text{OccP}_{O1}}{2 \cdot 6}. \tag{2.13}$$

The occupancy of the O2 atoms is accordingly given by

$$Occ_{O2} = \frac{(2 - 0.5x) \cdot OccP_{O2}}{2}. \tag{2.14}$$

Figure 2.5 shows a cubic unit cell originating from the fluorite structure and illustrating the crystallographic description of the Zr-shift model. In this unit cell, each yttrium atom sitting on the (4a) site is surrounded by eight blue zirconium atoms shifted along symmetry equivalent [111] directions. Each O2 atom (red) sitting at the ideal fluorite position is surrounded by six equivalent O1 atoms (pink) that were displaced along [001] directions. It is important to note, that none of the positions shown in Figure 2.5 is fully occupied; it illustrates a statistical average as determined by X-ray diffraction.

Considering the sample studied in this work $Zr_{0.81}Y_{0.19}O_{1.905}$ and hence $x = 0.19$, and assuming an equal partial distribution of both oxygen atom types, i.e. $OccP_{O1} = OccP_{O2} = 0.5$, the occupancies become

$$Occ_{O1} = \frac{(2 - 0.5 \cdot 0.19) \cdot 0.5}{2 \cdot 6} = 0.0794 \; \hat{=} \; 7.94\% \tag{2.15}$$
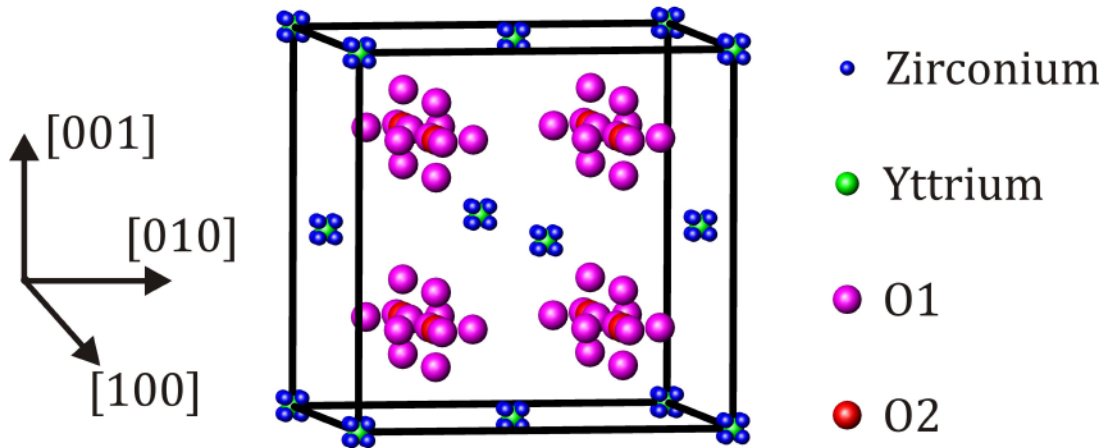
Figure 2.5: Crystallographic illustration of the Zr-shift model: the zirconium atoms (blue) are shifted from the (4a) sites along the [111] and symmetry equivalent directions. There are pink oxygen atoms, O1, being displaced from their ideal fluorite position along the [001] and symmetry equivalent directions while other oxygen atoms, O2, remain here. The yttrium atoms remain at the fcc sites. Note that none of the positions is fully occupied in this crystallographic description of Zr-shift model.

and

$$Occ_{O2} = \frac{(2 - 0.5 \cdot 0.19) \cdot 0.5}{2} = 0.4763 \; \triangleq 47.63\% \tag{2.16}$$

using equations (2.13) and (2.14) respectively.

The occupancies of the metals become

$$Occ_{Zr} = \frac{1 - 0.19}{8} = 0.1013 \; \triangleq \; 10.13\% \tag{2.17}$$

and

$$Occ_Y = 0.19 \; \triangleq \; 19.00\%. \tag{2.18}$$

2.5   Fully Yttrium-Stabilized Zirconia Surface Structures

Very little is known about the F-YSZ (the acronym YSZ instead of F-YSZ will be used for fully or cubic stabilized zirconia hereafter for convenience) surface structure on an atomic scale. To the best of my knowledge, there are only two publications dealing with the atomic structure of YSZ surfaces. The only experimental work with structural information is dealing with the (100) surface [18].

A theoretical study using DFT was published recently [12]. In this study the low-index surfaces (100), (110) and (111) are investigated at T=0 K using a pure zirconia model and a fluorite-like model with an yttria concentration of 14% mol for the calculations. Their calculations of surface energies show that the (111) surface

Table 2.3: Energies of low-index F-YSZ surfaces determined by DFT calculations [18]. The (111) facet has the lowest energy followed by the (110) and (100) surfaces.

YSZ Surface Orientation	Surface Energy (meV / $Å^2$)
(111)	65
(110)	90
(100)	109

has by far the lowest energy followed by the (110) and (100) surfaces (see Table 2.3). Accordingly, the (111) surface is the most stable and is thus expected to be the most common surface of YSZ.

The results of the above mentioned two publications are summarized in the following.

2.5.1 The (111) Surface

This surface is the most frequent one of YSZ and thus the most common facet of YSZ due to its low energy [12].

Using the transformation matrix

$$M = \begin{pmatrix} 1/2 & 0 & -1/2 \\ -1/2 & 1/2 & 0 \\ 1 & 1 & 1 \end{pmatrix} \tag{2.19}$$

to transform to a [111] oriented hexagonal unit cell, results in the P3m1 symmetry group [55] with metals on the (1a), (1b) and (1c) positions and oxygen atoms on the (6e) sites. The axes lengths a_s, b_s and c_s of the new cell are then given by

$$a_s = b_s = \frac{a}{\sqrt{2}}, c_s = \sqrt{3} \cdot a, \alpha = \beta = 90°, \gamma = 120° \tag{2.20}$$

A structural model for this surface was calculated using DFT [12]. Figure 2.6 shows their results assuming a fluorite-like structure of the bulk. The proposed model shows no reconstruction and is oxygen terminated with the truncation indicated in Figure 2.6 a). The surface atoms of the resulting structure in Figure 2.6 b) remain on their bulk positions, except for the topmost oxygen and metal layers that move 0.01 Å inwards and outwards each, indicated by the red and blue arrows respectively. The very small deviation of the surface atoms from the ideal bulk positions is a hint for the high stability of this surface.

It is possible to obtain STM measurements of this surface when the sample is annealed to temperatures above 200°C by making use of the ion conductivity [52]. These STM images show a high density of defects on the surface. Since atomic
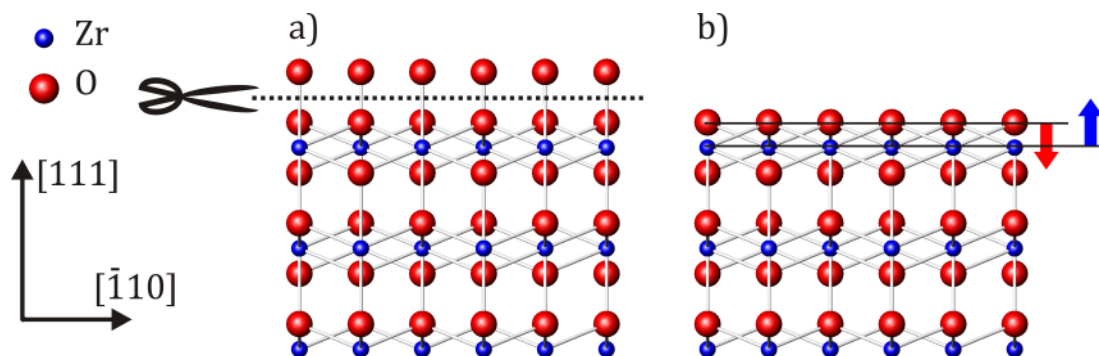
Figure 2.6: Proposed structure for the (111) surface using DFT [10]. a) the bulk fluorite-like structure is oxygen terminated with the truncation illustrated by the dashed line and the scissor. b) the resulting model shows no reconstruction and the atoms remain at their bulk positions. Only the topmost oxygen and metal layer are displaced slightly by 0.01Å inwards and outward, respectively, indicated by the red and blue arrows.

resolution is not achieved by this method, these images are not capable of delivering atomic structural models.

Theoretical studies predict the accumulation of yttria at the YSZ(111) surface [49; 80]. Upon heating at reducing conditions, zirconia is experimentally and theoretically shown to segregate to this surface [49; 51].

2.5.2 The (110) Surface

The (110) surface is a non-polar surface that has the second lowest energy among the YSZ surfaces. The only available structural information was proposed using DFT [12] which reports the surface to be unreconstructed and oxygen terminated, similar to the (111) face. However, the subsurface oxygen layer is distorted with respect to the ideal fluorite-like positions and causes the surface oxygen atoms to relax outward more strongly by 0.08 Å. Moreover, surface oxygen atoms close to oxygen vacancies tend to show an increased relaxation by up to 0.7 Å.

The surface metal atoms are displaced as well. The two topmost metal layers show noticeable shifts by moving 0.2 Å and -0.09 Å respectively.

2.5.3 The (100) Surface

 The only experimental based surface model for an YSZ surface exists for the (100) surface using high-resolution medium energy ion scattering (HRMEIS) [18]. Since HRMEIS does not allow distinguishing between Zr and Y, the proposed model is based on a pure cubic zirconia structure. In this work a single crystal with 9.5% mol yttria concentration is investigated under UHV conditions [18]. The surface is prepared by chemical etching and annealing in oxygen under UHV conditions.

The authors suggest an oxygen terminated surface that shows a (1 x 1) reconstruction. Figure 2.7 shows an illustration of the model. The upper left part shows a top view of the oxygen terminated bulk-like structure. In order to construct the suggested (1 x 1) reconstruction, the surface oxygen atoms (orange) have to be rotated by 45°. The resulting structure is shown in the right part of Figure 2.7: here the topmost reconstructed oxygen atoms lie above the zirconium atoms in the lower layer, which have a twofold coordination compared to a fourfold coordination in the bulk. The reconstruction of polar surfaces is not unusual and is reported to occur in order to eliminate the polar moment and stabilize the surface (see also section 3.2.4). In addition to the reconstruction, the topmost oxygen and metal layers are shifted outwards by 0.11 Å and 0.045 Å, respectively, compared to the bulk layer distance. Moreover, an improvement of the fit was reported, when a surface oxygen vacancy concentration of 10% was introduced.

This model was tested in a DFT which proposes a removal of half of the surface oxygen atoms as an alternative to neutralize the surface polarity [12]. Taking the (1 x 1) reconstructed surface and the surface with oxygen vacancies as a starting point for the calculations, it is shown that the surface structure transfers back to a bulk-like structure (left part of Figure 2.7) in both cases.

A similar but more distorted (1 x 1) reconstruction was only achieved when a fluorite-like structure was used and an yttrium-rich surface was implied. The resulting structure reveals two different displacements of oxygen atoms. The topmost oxygen layer creating the reconstruction is shifted downward towards the underlying metal layer, while the subsurface oxygen layer is shifted upwards
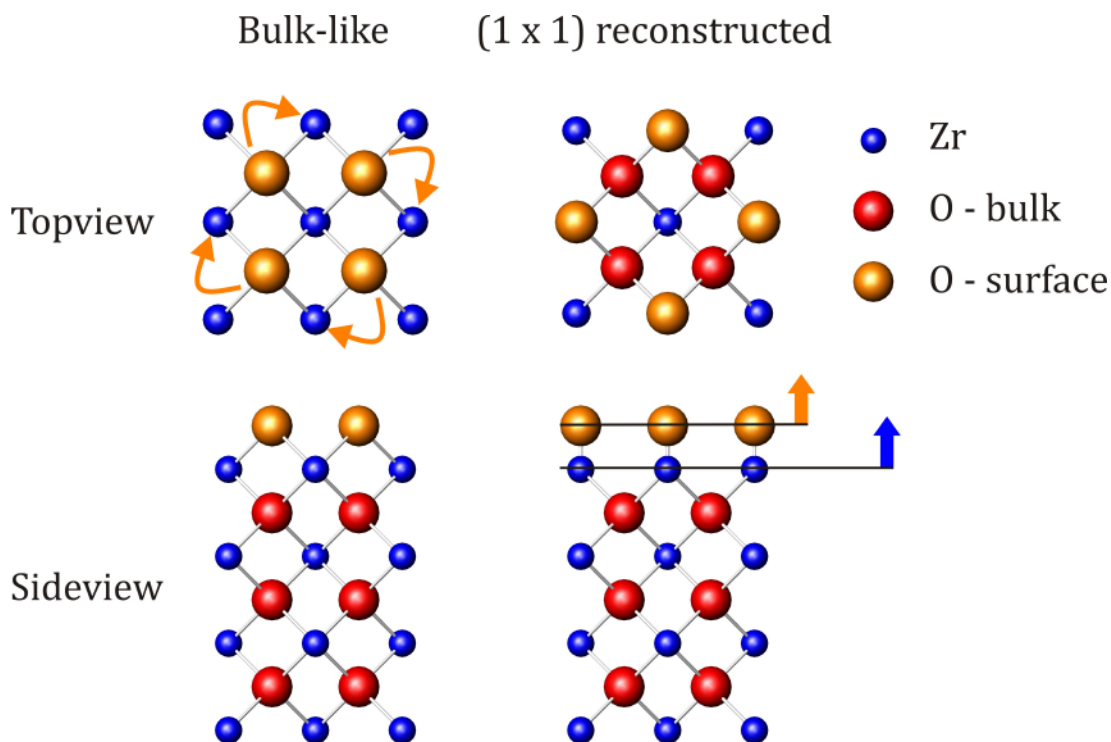
Figure 2.7: (1 x 1) reconstructed surface proposed by [17]. The left part shows a bulk-like, oxygen terminated structure. The reconstruction is created when the topmost oxygen layer, illustrated as orange balls, is rotated by 45° as indicated with the orange arrows in the top view. The resulting structure is shown in the right part. Here the surface oxygen atoms sit above the underlying metal atoms. It is moreover reported that the topmost oxygen and Zr layer move up by 0.11Å and 0.045Å respectively with a 10% oxygen vacancy concentration in the reconstruction layer.

towards the same metal layer by 0.55 Å. The average shift of the oxygen atoms is then determined to be 0.59 Å still much larger than the value identified by the HTMEIS experiment (0.11 Å). These heavy displacements are attributed to the massive increase of strain in the yttria enriched surface region.

2.6 Nickel Growth

Nickel is a ferromagnetic transition-metal with a melting temperature of 1728K which is chemically inactive at standard conditions. It is a cheap metal with a high capability to adsorb hydrocarbons [81; 82; 83] and a high catalytic activity to oxidize them at elevated temperatures [84; 85; 86]. Nickel nanoparticles are very easy and cheap to produce, which makes them the ultimate choice as an anode metal in SOFCs [87].

Nickel is easily oxidized at slightly elevated oxygen pressures and temperatures with nickel oxide being a rather inert material. Thus, avoiding oxidation of nickel is always an issue in state of the art SOFCs.

This section gives an overview about the structure of nickel and nickel oxide and the equilibrium shape of nickel using its surface energies. Finally, recent findings about nickel growth are summarized.

2.6.1 Bulk Structure of Nickel and Nickel Oxide

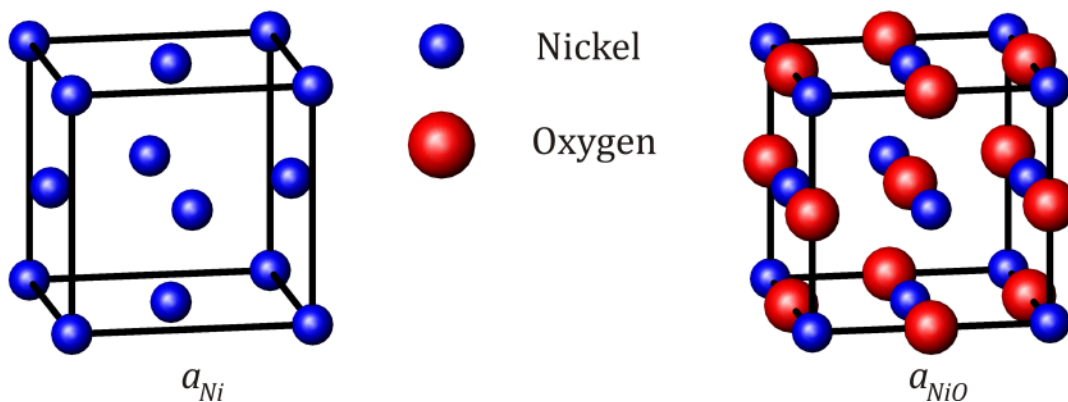Nickel and nickel oxide have cubic unit cells with the lattice parameters [88]

Figure 2.8: fcc structure of nickel on the left and rock salt structure of nickel oxide on the right side. Both have a cubic unit cell with lattice parameters a_{Ni} = 3.54 Å and a_{NiO} = 4.20 Å where Ni sits on fcc (4a) sites within the Fm3m symmetry group. The oxygen atoms of NiO sit on (4b) positions.

$$a_{Ni} = 3.54 \, \text{Å} \qquad\qquad (2.21)$$

and [89]

$$a_{NiO} = 4.20 \, \text{Å} \qquad\qquad (2.22)$$

The nickel atoms sit on fcc (4a) sites within the symmetry group Fm3m [55] for both cases, while the oxygen atoms sit on (4b) position in the rock salt structure of NiO. Figure 2.8 shows the structure of Ni and NiO on the left and right, respectively.

Considering the stacking sequence of successive {111} planes of an fcc metal, an interesting behavior is observed. The {111} planes allow different stacking sequences. Starting with the arrangement depicted "A" in Figure 2.9, either arrangement "B" or "C" are possible follow-ups to build a crystal structure [90; 91]. Possible stacking sequences along the (111) direction are ABCABC or CBACBA. If a stacking inversion within the same crystal occurs, the crystal is called to be twinned with the stacking sequence at the interface being ABCBA. The sequence ABCBA is linked with the creation of defects at the interface between the two sequences [92]. The other possibility is laterally coexisting twins, i.e. crystals with the sequence ABCABC and other crystals with the sequence CBACBA.

Stacking sequence inversions within a crystal and thus twinning as well as twins give rise to additional Bragg peaks [90] in the diffraction pattern of a crystal and
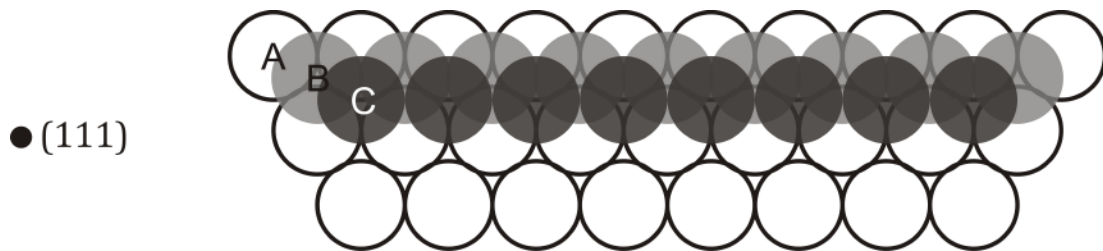
Figure 2.9: Looking at the {111} planes of a metal fcc structure, the following can be observed. A {111} plane called "A" can be followed by a plane that has the arrangement of the layer called "B", but as well of a layer called "C". Crystals with the stacking sequences ABCABC and CBACBA can laterally coexist and are called twins. If a stacking inversion leads from one sequence to the other, i.e. ABCBA, within one crystal, internal twinning is present.

should hence be considered when studying the growth of Ni.

2.6.2   Equilibrium Shape

The catalytic activity of nickel surfaces in hydrogenation and oxidation reactions has motivated a number of experimental and theoretical studies [93; 94; 95; 96; 97]. This property has made nickel surfaces to one of the most studied from the beginning of surface science.

Table 2.4 shows some theoretically calculated energies of low-index Ni surfaces. They show that the (111) surface has by far the lowest energy, followed by the (100) and (110) orientations [98; 99]. This fact explains the stability of the two first surfaces upon adsorption of hydrogen at room temperature, whereas the (110) surface forms a (2 x 1) reconstruction after a certain coverage[85].

The low energy of the (111) and (100) surface compared to the (110) surface leads the equilibrium shape of Ni crystals to be a truncated octahedron using the Wulff-construction [100] and shown in Figure 2.10. The Wulff-shape of Ni is hence mainly covered with (111) facets having a regular-hexagon shape and some square-shaped (100) facets.

The equilibrium shape of supported particles is given within the so-called "Wulff-Kashiev" theorem better known as the "Winterbottom" theorem [101]. A similar scheme as the Wulff-construction can be applied. Here the surface energy γ is replaced by an effective surface energy γ^* defined as the difference between the interface energy $\gamma_{\mathrm{interface}}$ and the energy of the substrate surface $\gamma_{\mathrm{substrate}}$ [101]

Table 2.4: Energies of low-index Ni surfaces determined theoretical calculations [89]. The (111) surface has the lowest energy followed by the (100) and (110) orientations.

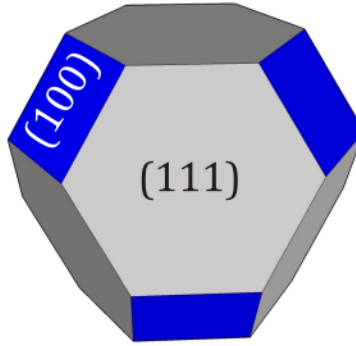| Ni Surface Orientation	Surface Energy (meV / Å^2)
(111)	94
(100)	103
(110)	112

Figure 2.10: The equilibrium shape of a Ni crystal is given by a truncated-octahedron using the Wulff-construction. It mainly consists of (111)-oriented facets (grey) and some (100) facets (blue). This shape can be used to derive the shape of nanoparticles on a substrate.

$$\gamma^* = \gamma_{\text{interface}} - \gamma_{\text{substrate}} \qquad (2.23)$$

Note that the interface energy and the growth of particles on a support depend on the adhesion behavior, and thus the work of adhesion W_{adh}. The effective surface energy can thus be used to determine the adhesion work [102]

$$W_{\text{adh}} = \gamma_{NP} - \gamma^* \qquad (2.24)$$

2.6.3 Supported Nickel Growth

Metal NPs grown on oxides are used in many applications including catalysis and thus of high importance for science and technology. A collection of different NPs grown on a number of substrates has been investigated in the past decades and the results are collected in review articles as [103].

The growth of NPs or thin films upon deposition starts with the nucleation of the first atoms followed by the upcoming atoms upon the initial arrangement. Two types of mechanisms are classified in order to describe the initial nucleation [104].

If the first case atoms nucleate on defects on the surface and following atoms arrange upon these. This mechanism is called heterogeneous nucleation. Homogenous nucleation is present if the first atoms nucleate on regular sites on the

surface and the following atoms arrange in a regular way upon the initial arrangement once a critical cluster size is exceeded.

The system Ni on YSZ is most frequently used as the anode of SOFCs. In the following the most relevant results on the growth of Ni NPs and thin films are presented briefly.

The initial growth of nickel on MgO-(001) was extensively examined at different temperatures and after oxidation using X-ray scattering [105]. A rather complex growth of a Ni-(001) film that is dominated by the small mismatch of the cube on cube epitaxy was the outcome of this study.

The system Ni on YSZ surfaces has been subject to a number of investigations. Experimental studies lead to the conclusion that major orientation relationships for this system are (111)-oriented Ni on YSZ(111) and YSZ(100) [106; 14]. It has moreover been reported that the metallic Zr-Ni bonding is important for the stability of Ni(111) on YSZ(100)[19].

Theoretical calculations were performed to determine the favorable termination of the YSZ substrate for Ni growth. While an oxygen-terminated substrate was reported to be energetically more suitable for the growth of (111)-oriented Ni on YSZ(111) [107], there is no consent about the right termination for a cube on cube growth of (100)-oriented Ni on YSZ(100) and both Zr and O are reported to advantage such an epitaxy [108; 109; 110].

The changes of the interface between the YZS-(100) surface and Ni was the topic of a transmission electron microscopy (TEM) investigation [20]. The formation of an yttria layer between the substrate and nickel, which is breaking up regularly and leads to different orientations of the nickel growth, was revealed.

Nickel NPs grown on YSZ have also been the topic of some publications. A high-resolution TEM study reports the epitaxial growth of (111)-oriented nickel NPs on a YSZ(111) surface [14]. The NPs were grown at 1073K using pulsed laser deposition [111].

Using XRD and different electron diffraction techniques, it was found that nickel prefers to grow in the (111) orientation on YSZ(100) substrates. A second

orientation of nickel with a much smaller fraction was found that shows an epitaxial cube on cube (i.e. (100) on (100)) growth. Both types of orientations were found to be homogeneously distributed over the substrate [19]. Nickel films grown for this work were prepared by molecular beam epitaxy (MBE) [112].

3 Physics of Metal Oxides

Today, oxides are used in a huge variety of applications, from food to sun cream, from solar cells to fuel cells, from self cleaning surfaces and pollution reducing surfaces to thermal barriers and many more. These numerous and increasing applications of metal oxides in the last decades have raised the effort to understand the structure and properties of these materials. Many experiments have been performed and theories have been developed to describe the bulk structure of oxides with numerous textbooks and reviews [113; 114]. While the bulk structure of oxides is quite well understood, there is no clear theory to describe the structure and properties of oxide surfaces.

Metal oxides usually have band gaps larger than 3eV, which make them to poor semiconductors or mostly insulators. Doping is often used to manipulate the band gaps of oxides to reach desired properties, especially the catalytic.

This chapter discusses the key points of oxides bulk structures and properties as well as theories to describe general mechanisms in the surface formation. Detailed information can be found in the cited publications and textbooks.

3.1 Bulk Oxides

Most of the information given in this section stems from the book of P. Cox "Transition Metal Oxides" [113]. The interested reader is referred to this book and the following citations for detailed information and helpful illustrations.

An oxide consists of metals acting as electron donors (cations) and oxygen acting as electron acceptors (anions). The chemical structure of most oxides can thus be described by an ionic bonding between the cation and an O^{2-} anion (note that this is an approximation and the real electronic distribution is more complicated) . In the so-called "hard-sphere" model, these ions are all assumed to have fixed spherical

shapes with the size given by the ionic radius. In almost all oxides the ionic radius of an O^{2-} is larger than that of the cations. The crystal structures of oxides can thus be described of metals surrounded by anions and vice versa. These structures are very well known and recorded in textbooks as Wyckoffs "Crystal Structures" [54] with the most common ones being:

- Fluorite
- Rutile
- Rock salt
- Wurtzite
- Corundum.

An alternative way to describe an oxide is to start with close-packed structures of oxides. All of the above structure can be described either as an fcp or hcp arrangement of oxide ions with metals cations sitting between them on interstitial positions. This description is helpful when the limits of the hard-sphere model are achieved and the electronic configuration of metal ions starts to play a noticeable role.

The important properties to determine a crystal structure are stoichiometry and coordination. The stoichiometry of a material gives the ratio of the element numbers present. The coordination gives the number of on type of ions surrounding the other type and their geometrical arrangement, with the six-fold metal-ion coordination being the most common one.

3.1.1 Defects

Although oxides can nowadays be produces in an almost perfect crystal structure with reasonable impurities compared to alloys, defects play an important role. They are required for some applications and necessary to describe a number of properties. From the thermodynamical point of view small defect densities stabilize a crystal at non-zero temperatures, since the gain of entropy decreases the free energy [113].
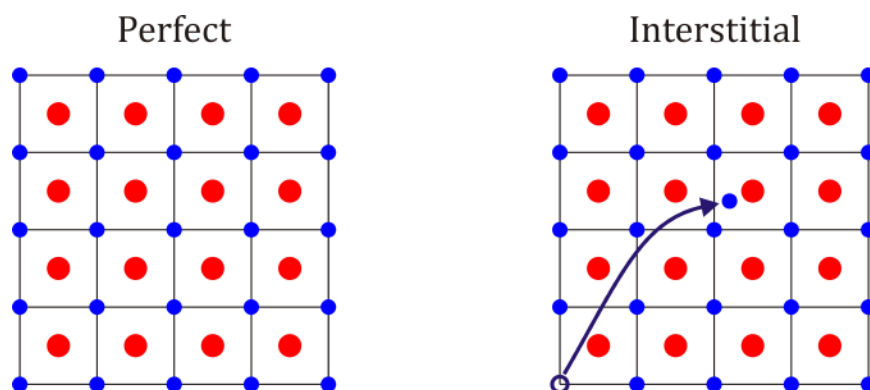
Figure 3.1: The left part show the arrangement of blue and red atoms in a perfect crystal. If a blue atom moves from its original site to a new, non-crystallographic position leaving behind a vacancy and creating an interstitial, a "Frenkel" defect is present.

Defects can be classified in two general types: "point" defects and "extended" defects. As extended defects are not important for this work, the focus will be on point defects. A point defect is affecting a certain position in the crystal structure. The main point defects are vacancies in the lattice, and interstitials that might be occupied either by the crystal specimen or dopants and impurities. The last two can also occupy original crystal structure sites. Interstitials change the band gap of metal oxides and are shown to play a major role in the catalytic activity of oxides, when they segregate to the surface and react with adsorbates [115].

In order to keep the overall charge neutrality of a crystal, defects are assumed to occur in pairs in the defect theories. In this sense, two types of defect couples can be distinguished. In the first case, a vacancy of one type of ion is compensated by the according number of vacancies of the other ion, called a "Schottky" defect. A "Frenkel" defect is present if a vacancy is present but the missing atom is sitting on an interstitial position. Impurities then can be assigned to either a Schottky or a Frenkel defect.

The left part of Figure 3.1 shows a perfect arrangement of atoms in a crystal. For a Frenkel point defect, a blue atom on the right part is moved to a non-

crystallographic position. It thus creates a vacancy at its original position and an interstitial at the position it moved to.

Two other possibilities can be thought of to keep the charge neutrality in case of a point defect. First, the electronic rearrangement of the neighboring sites of a defect or second by the change of the charge of an ion.

If the defect concentration overcomes certain limits, defects will start to interact with each other. As they do so, they might start forming clusters within the crystal. These clusters are able to cause crystallographic shear planes, which are the most prominent extended defects [116].

An experimental probing of defects is rather complicated and thus theoretical tools are required to reasonably describe defects in crystals. Density functional theory (DFT) is one of these tools [117]. It is also broadly used to examine the structure of surfaces.

3.2   Oxide Surfaces

Metal-oxide surfaces have been subject of a number of textbooks, reports and reviews [21; 118; 119; 120] and detailed information about the content of this section might be found there.

A surface is generated, if a bulk is truncated. The direction of the cleavage in the bulk gives the orientation of the produced surface. The energetically stable configuration of the surface and the arrangement of its atoms depend on the environment. The environment includes thermodynamic- as well as kinetic considerations. In other words, the surface structure of a material can differ under different conditions.

The first step giving information about the stability of the surface is its termination. That is, at which positions within a unit cell is the crystal cleaved to have a stable configuration. There are two models predicting a stable termination: the "Tasker" model and the "dangling bonds" model which are discussed briefly in the following.

3.2.1 Tasker Model

Tasker proposed a model for "the stability of the ionic crystal surfaces" in the late seventies [121]. In his model he assumed the single layers of a crystal to have a charge. For an ionic crystal, the different layers can only have charges that are a multiple of each other.

With this assumption, three different so-called Tasker surfaces can be distinguished and are shown in Figure 3.2. Thus, a type-a Tasker surface is a surface, where the single layers of the crystal are electrically neutral due to charge compensation of the cations and anions. A type-b Tasker surface is present, if two layers with a negative charge are followed by a layer with double positive charge. Finally, a c-type Tasker surface is around if positively and negatively charged layers with the same magnitude alter.

To derive information about the stability of these surfaces, electrostatic considerations are used. Assuming the distance between the layers z to be larger than a few interionic spacings, the electrostatic potential $V(z)$ of a layer is given in terms of the layer charge q [121]:
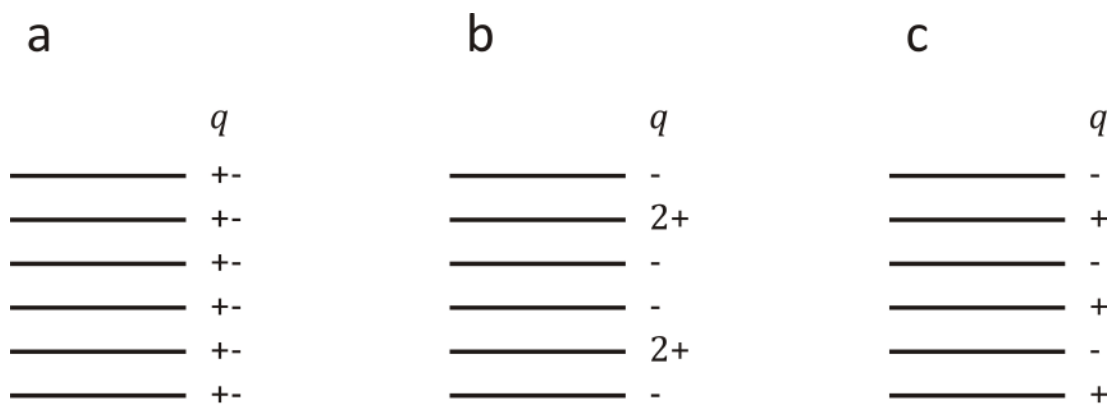

Figure 3.2: Dividing a crystal into single layers and assuming a charge density of the layers, there different type of so-called Tasker surfaces can be distinguished. Type a and b are stable surfaces according the Tasker model and type c is unstable due to its polarity.

$$V(z) = \frac{1}{4\pi\epsilon_0} \cdot \frac{2\pi \cdot q \cdot z}{A} \qquad (3.1)$$

where A is the area of the unit cell in the layer. The stability of the surface is then given by taking into account dipole moments perpendicular to the surface in a Madelung sum.

Above considerations lead to the following surface stability conditions: type a and b are stable. This is due to a compensated dipole moment either within the layer itself (type a) or within a sequence of three layers (type b). Type c, however, results in an infinite dipole moment between a couple of layers and is un- or metastable according the Tasker model. Reconstructions and faceting are thus expected for this surface type.

3.2.2 Dangling-Bonds Model

The auto compensation of a surface is the central idea of the dangling-bonds model which was originally developed for semiconductors and introduced by LaFamina in the nineties [122]. According to this model, a surface is stable if it is autocompensated. The basic idea thereby is to consider the dangling bonds produced by a truncation of the crystal. These broken bonds create anion and cation excess-charges on each side of the cleaved crystal that have to be compensated in order to stabilize the surface. If the surface is able to compensate this charge excesses itself, a surface stability condition is fulfilled.

In other words: if the number of dangling bonds from anion to cation equals the number of dangling binds from cation to anion, the surface excess-charges are autocompendated and the surface is stable. Hence, the termination of the surface having the lowest difference between cation-anions and anion-cation dangling bonds is the most stable one. According LaFamina, the autocompensation determines the stoichiometry of a surface and the redistribution of dangling bond densities of a surface determines how surface atoms displace [122].

It is important to note that there is no general model to derive the stable termination of oxide surfaces. Both, the Tasker- and the dangling-bond model

describe conditions for such a termination. However, fulfilling them does not guarantee the existence of a stable surface and vice versa.

3.2.3 ZrO$_2$(111) and (100) Termination

The above models can now be applied to the orientations of zirconia surfaces studied in this work to find the most stable termination. We start with the (111) orientation, which is shown in Figure 3.3. Following symmetry considerations, three different orientations denoted A, B and C are possible. A look at the coordination of the cations and anions of Zr^{4+} and O^{2-} reveals the {111} planes to have altering plane changes q (for this cutout) of 16+ of the metallic layer followed by two 8- oxygen planes. Hence, according the Tasker model, it is a b-type Tasker surface and Termination B is the stable one.

The numbers of broken cation to anion bonds and vice versa, important for the dangling-bonds model are given in Table 3.1. It shows that the termination predicted to be most stable by the Tasker model also has equal numbers of positive and negative excess charges due to dangling bonds. Hence this termination is able to
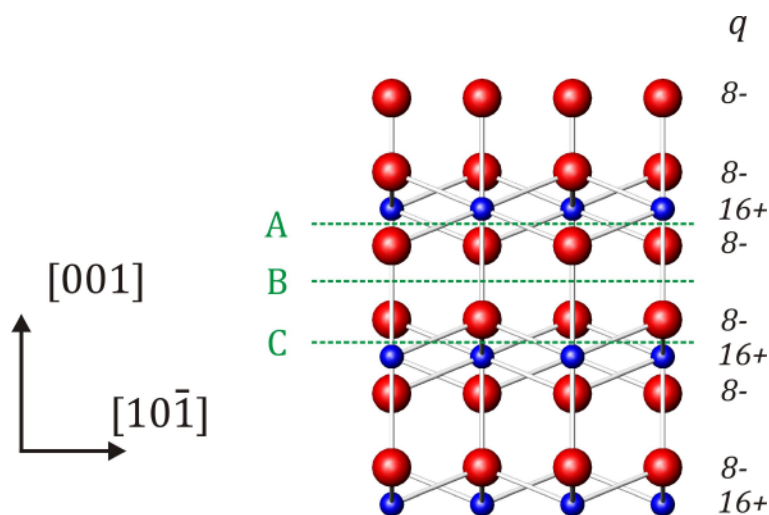

Figure 3.3: Symmetry considerations lead to three possible terminations of the cubic ZrO$_2$(111) surface. Looking at the {111} planes, a type-b Tasker surface is recognized, which predicts the termination called B to be the most stable one. The same termination is proposed by the dangling-bonds model.

Table 3.1: The number of broken cations-to-anion and anion-to-cation bonds, of the three terminations possible for the cubic ZrO2(111) surface.

Termination	Broken cation to anion bonds	Broken cation to anion bonds
A	0	8
B	2	2
C	8	0

autocompensate and the most stable termination.

In summary the termination called B here that is an oxygen termination just above a metal layer is the stable one according to the Tasker and the dangling-bonds model. This result is also in agreement with a theoretical study which finds this termination to be the most stable one [12].

A look at the {100} planes of cubic ZrO_2 displays a different situation. Figure 3.4 shows a side view of these planes. Two different terminations, an oxygen and a metal termination, called A and B are possible for this surface.

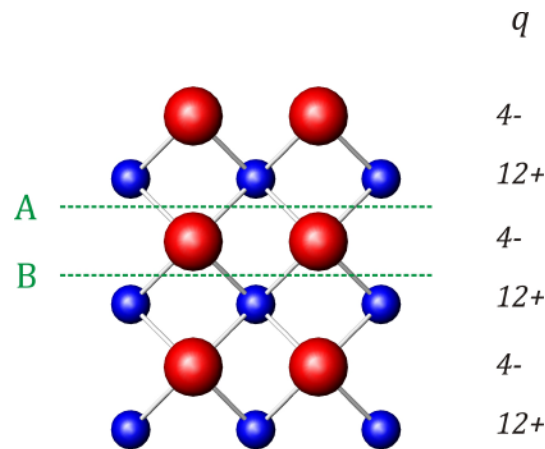The charge sequence of the planes corresponds to a type-c Tasker surface which is

Figure 3.4: Two terminations are possible for the cubic ZrO2(100) surface. Both terminations do not fulfill the autocompensation requirements necessary for a stable surface according the dangling-bonds model. This surface is also a c-type Tasker surface and thus unstable due to its polarity. However, an oxygen termination (termination A) results from theoretical calculations [48].

Table 3.2: No autocompensation is possible for the terminations of the ZrO2-(100) surface, since the number of broken bonds between cations and anions does not equal the number of broken anion to cation bonds.

Termination	Broken cation to anion bonds	Broken cation to anion bonds
A	0	4
B	4	0

a polar surface and predicted to be unstable. The dangling-bonds model predict an unstable surface as well, since none of the terminations has the same number of broken cation-to-anion and anion-to-cation bonds as shown in Table 3.2.

Although both models predict this surface to be unstable and no termination can be deduced, it is possible to determine a termination with *ab-initio* calculations. These calculations predict the oxygen termination of the (100) surface to be the stable one of cubic ZrO_2 and YSZ [13; 12].

Thus an oxygen termination of the ZrO2(100) surface can be assumed and was used in the progress of this work.

3.2.4 Surface Reconstructions and Defects

Energetic reasons can lead to a considerably different arrangement of the surface atoms compared to their bulk positions. A well known source for such mass transports is a polar surface as given by the type-c Tasker surface and hence the (100) orientation of ZrO_2. These polar moments can lead to an interaction of the surface with the bulk charge densities and hence changes in the surface structure. Rearrangements leading to a changed periodicity of the surface or a change in the direction of periodicity compared to the bulk are called reconstructions. Depending on their symmetry, reconstructions are denoted "p" and "c" indicating a primitive and a centered arrangement. Numbers in brackets give the multiple periodicities as compared to the bulk. A c-(2 x 1) reconstruction, for instance, is a centered reconstruction that has a doubled periodicity along *a*.

Talking considering surface defects (in this thesis), only point defects are taken into account. These point defects can either be cation or anion vacancies or the presence of ad atoms. Defects with a high influence on surface properties such as chemi- or physisorption and dissociation are oxygen vacancies [21]. They are present on almost every metal-oxide surface and often act as nucleation centers [123; 124]. This is due to the creation of under-coordinated metal cations in the vicinity of oxygen vacancies that are known to be responsible for the activity of metal-oxide surfaces [125]. Moreover, an increasing concentration of vacancies is reported to lead to reconstructions and self-organized defect clusters [126; 127].

Quantitative work on the position of neighboring atoms to a vacancy position is rare and hence proposed models often neglect the structural influence of vacancies. However, their importance on the electronic structure of surfaces, especially on the creation of states in the band gaps of oxides is without question and has be subject to an increasing number of studies [128; 129].

Regarding the main preparation techniques in surfaces science being ion bombardment or sputtering and subsequent annealing, segregation of impurities from the bulk to the surface becomes an important issue and is another type of surface defect. These contaminations can be of great influence for the surface structure and properties and have to be excluded prior to the study of a pristine surface. Several experimental tools are available for such a characterization of the surface components. Auger electron spectroscopy (AES) is one of them that was used in this work and described in section 4.2. AES is improper for insulating materials or at least very hard to use and inaccurate.

4 Experimental Techniques

Considering the insulating property of YSZ, surface X-ray diffraction (SXRD) is a supreme experimental method that allows deriving a surface model on an atomic level. Hence, this technique was chosen as the main tool for this work.

Reflectivity measurements as well as atomic force microscopy were used to characterize sample surfaces and nickel nanoparticles complementary to SXRD. Auger electron spectroscopy was applied to qualitatively check the cleanness of the surface by applying very low electron currents.

This chapter describes the experimental tools employed in this work with a focus on surface X-ray diffraction.

4.1 Surface X-ray Diffraction (SXRD)

Surface X-ray diffraction is a very powerful technique in surface science to determine surface structures with sub- Ångström resolution. SXRD is independent from the electric conductivity of a material and allows *in-situ* experiments over wide ranges of pressures and temperatures. This section gives an introduction to surface X-ray diffraction by first describing X-ray diffraction. More detailed descriptions of SXRD and XRD in general are to be found in standard textbooks [90; 130; 131; 132] and well known publications [133; 134; 135] .

4.1.1 X-ray Diffraction (XRD)

The first resolved crystal structure of a material was delivered by William Henry Bragg and his son William Lawrence Bragg using X-ray diffraction (XRD) [136] who received the Nobel Prize in 1915 [137].

XRD can be understood as the scattering of electromagnetic waves from the electron density of a crystal. In the kinematic approximation [138] which only

considers single scattering events, the structure factor $F(\mathbf{Q})$ can be defined as a structure specific quantity given by

$$F(\mathbf{Q}, E) = \sum_j f_j(\mathbf{Q}, E)\, e^{-i\mathbf{Q}\mathbf{r}_j} \cdot \sum_{\mathbf{R}_n} e^{i\mathbf{Q}\mathbf{R}_n} \qquad (4.1)$$

In this equation the structure factor is a function of $\mathbf{Q}$, the momentum between an incident wave and a diffracted wave with the wave vectors $\mathbf{k}_i$ and $\mathbf{k}_f$ respectively (see Figure 4.1)

$$\mathbf{Q} = \mathbf{k}_f - \mathbf{k}_i \qquad (4.2)$$

The first sum in the equation (4.1) is the diffraction contribution of all j atoms in a unit cell given by the atomic form factor $f(\mathbf{Q}, E)$, which is summed up coherently with the phase difference given by the positions $\mathbf{r}_j$ of the atoms in the unit cell. The
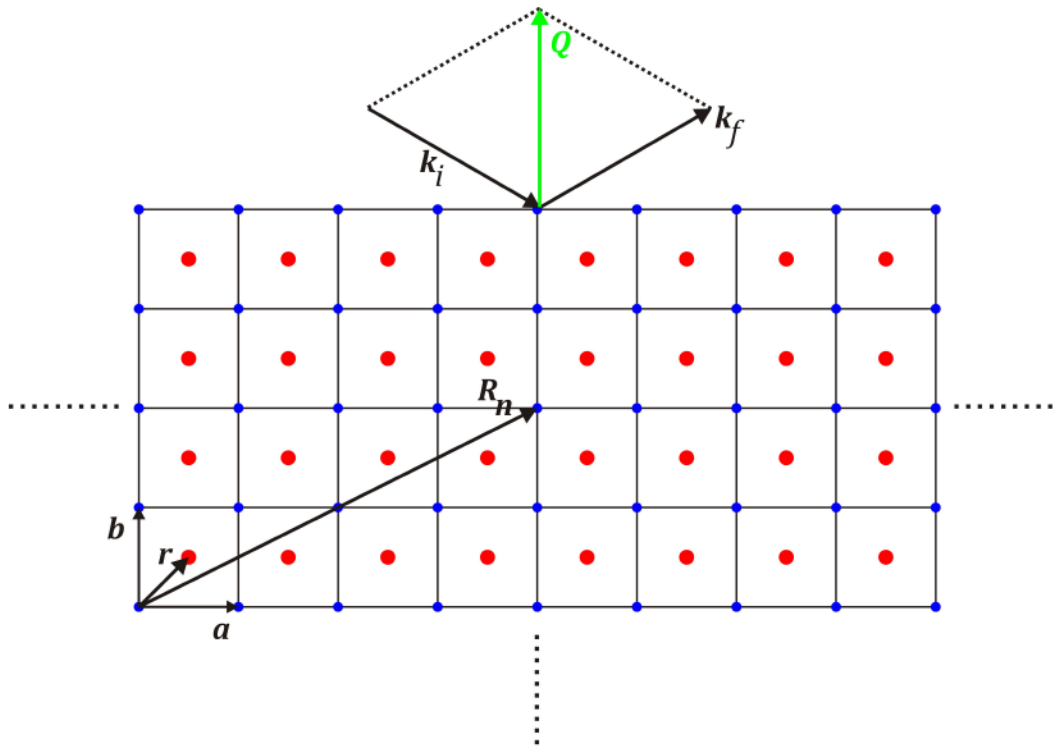

Figure 4.1: Scheme of a two dimensional crystal lattice: the incident beam $\mathbf{k}_i$ results in the diffracted beam $\mathbf{k}_f$ with a momentum transfer of $\mathbf{Q}$. The lattice itself consists of unit cells containing atoms sitting at positions $\mathbf{r}$. The translation invariance of the unit cells makes the real space transition vector $\mathbf{R}_n$ to be a multiple of the lattice vectors $\mathbf{a}$ and $\mathbf{b}$.

X-ray-energy dependent atomic form factor $f(\boldsymbol{Q}, E)$ is of importance for anomalous scattering and discussed more detailed in section 4.1.3.

The second sum is known as the lattice sum and counts for the coherent superposition of the single unit cell contributions translated by the vector $\boldsymbol{R_n} = n_1\boldsymbol{a} + n_2\boldsymbol{b} + n_3\boldsymbol{c}$, where $\boldsymbol{a}$, $\boldsymbol{b}$ and $\boldsymbol{c}$ are the axis of the unit cell [139], as shown in Figure 4.1 for a two dimensional rectangular case.

Assuming an infinite crystal lattice, the structure factors are non-zero only if

$$\boldsymbol{R_n} \cdot \boldsymbol{Q} = 2 \cdot \pi n \ \text{ with } n \in \mathbb{Z}, \tag{4.3}$$

which determines the selection rules for a certain structure and gives rise to the so-called Bragg peaks.

Introducing the reciprocal unit cell defined by

$$\boldsymbol{a}^* = 2\pi \frac{(\boldsymbol{b} \times \boldsymbol{c})}{\boldsymbol{a} \cdot (\boldsymbol{b} \times \boldsymbol{c})} \tag{4.4}$$

and permutative, where $\boldsymbol{a}^*$, $\boldsymbol{b}^*$ and $\boldsymbol{c}^*$ are the corresponding reciprocal lattice axis to $\boldsymbol{a}$, $\boldsymbol{b}$ and $\boldsymbol{c}$, a translation in reciprocal space is given by the reciprocal space vector

$$\boldsymbol{G} = h\boldsymbol{a}^* + k\boldsymbol{b}^* + l\boldsymbol{c}^*, \tag{4.5}$$

with h, k and l as the miller indices. Using equations (4.4) and (4.5) the selection rule in equation (4.3) becomes the famous Laue condition

$$\boldsymbol{Q} = \boldsymbol{G}. \tag{4.6}$$

The structure factor can thus be written as a function of h, k, l and the position of the atoms in the unit cell x_j, y_j and z_j

$$F(\boldsymbol{Q})_{hkl} = \sum_j f_j(\boldsymbol{Q}, E)\, e^{2\pi i(hx_j + ky_j + lz_j)} \tag{4.7}$$

The selection rules for all symmetry groups can be determined from the above given equation and are collected in the international tables of crystallography [55].

Cubic ZrO_2 has the symmetry group Fm3m with the metal atoms sitting on the (4a) fcc positions surrounded by the oxygen atoms sitting on the (8c) fcc positions. The selection rules are thus given by [55]:

$$h, k, l = even$$

$$h, k, l = odd \tag{4.8}$$

for this structure.

In an experiment, the measureable quantity is intensity. Hence, the structure factor has to be set into a relation to the measured diffracted intensity I_m. Supposing the mostly true plane-wave-approximations for distances between sample and detector being much larger than the coherent length of the X-rays, this relation is given by [90]:

$$I_m(\boldsymbol{Q}) = |F(\boldsymbol{Q})|^2 \cdot \prod_{i=1}^{3} \frac{sin^2\left(\frac{N_i \cdot \boldsymbol{Q} \cdot \boldsymbol{a}_i}{2}\right)}{sin^2\left(\frac{\boldsymbol{Q} \cdot \boldsymbol{a}_i}{2}\right)} \cdot I_o \cdot cor \tag{4.9}$$

for a parallelepiped sample where N_i is the number of unit cells in the direction i, $\boldsymbol{a}_i$ the corresponding lattice vector in that direction, I_0 the incident intensity and cor a factor for possible polarization corrections.

Assuming an infinite lattice, i.e. $N_i \rightarrow \infty$, the measured intensity adopts a δ-function shape when the selection rules are fulfilled and is zero else being equivalent to the Bragg peaks.

An important damping factor for the intensity is the thermal vibration $\langle u \rangle$ of the atoms around their perfect position. This effect was integrated in the structure factor calculations by Debye [140] and Waller [141] with

$$B = 8\pi^2 \cdot \langle u^2 \rangle \tag{4.10}$$

as the so-called Debye-Waller factor.

Looking at equation (4.9), it becomes apparent that only a perfect crystal leads to a δ-like shape of the measured intensity. Any deviation from that perfect structure would result in slightly different h, k and l values and thus in a broadening of the detected signal. The integrated intensity method [90; 132] is the solution to this issue since no crystal structure is absolutely perfect and defects are present in every material [113] (see also section 3.1.1).

This method aims to collect the signal for a small volume around the optimal diffraction geometry, leading to an integrated detected signal. One way to realize

this is by rocking the sample around its surface normal with a certain rotation speed and measure the whole intensity during that time [90; 134].

4.1.2   Surface X-ray Diffraction

The δ-shape of the Bragg peaks following from equation (4.9) as shown in the left part of Figure 4.3 is only true if an infinite crystal in three dimensions is assumed. Real crystals, however, are truncated and the infinity condition is broken along the surface-normal +z as illustrated in Figure 4.2. The intensity given in equation (4.9) has thus to be modified for a semi-infinite crystal.

This is done by keeping the delta-characteristics along the reciprocal directions corresponding to the infinite x and y directions, i.e. along H and K, and changing the last product in equation (4.9) resulting in [135]:

$$I_{rod}(\boldsymbol{Q}) \propto \left(\delta(\mathrm{H}x - 2\pi v) \cdot \delta(\mathrm{K}y - 2\pi w) \right) \frac{1}{2sin^2\left(\frac{1}{2}\mathrm{L}z\right)}, \qquad (4.11)$$

$$v, w \in \mathbb{Z}$$

Hence, while the common Bragg peaks are observed along the H- and K-directions in reciprocal space, the Bragg peaks along the L-direction are broadened
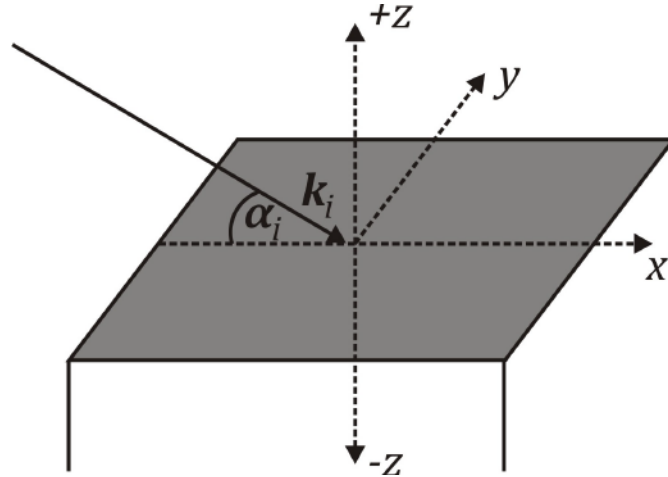

Figure 4.2: An incoming X-ray beam $\boldsymbol{k_i}$ sees an infinite lattice along the ±x and ±y directions. This infinity is however broken along the +z direction resulting into the crystal truncation rods (CTR).

and linked to each other as shown in the right part of Figure 4.3. This fact was first discovered and mentioned by von Laue. A nice and elegant derivation was given in the 1980s [135], and the name "crystal truncation rod" (CTR) was established.

It is important to notice that the signal of a CTR in the minimum between two Bragg peaks originate only from the topmost layers of the surface and is very sensitive to sub- Ångström changes of the surface atoms. Thus, the measurement of CTRs delivers a very powerful tool to examine surface structures. However, X-ray diffraction is only able to deliver this sort of information for an average over a few thousand unit cells and is restricted to periodic structures only.

A typical ratio of the Bragg peak to CTR signal of 10^5 [135] requires X-rays with a high brilliance necessary for this types of measurements. High brilliance beams are available at numerous synchrotron facilities nowadays, such as the European synchrotron radiation facility (ESRF), Ånström-Quelle Karlsruhe (ANKA), the Swiss light source (SLS) and many more.

In order to reduce the background signal mainly caused by the bulk defect structure, SXRD measurements are usually performed at incident X-rays angles α_i (see Figure 4.2) around the critical angle α_c.
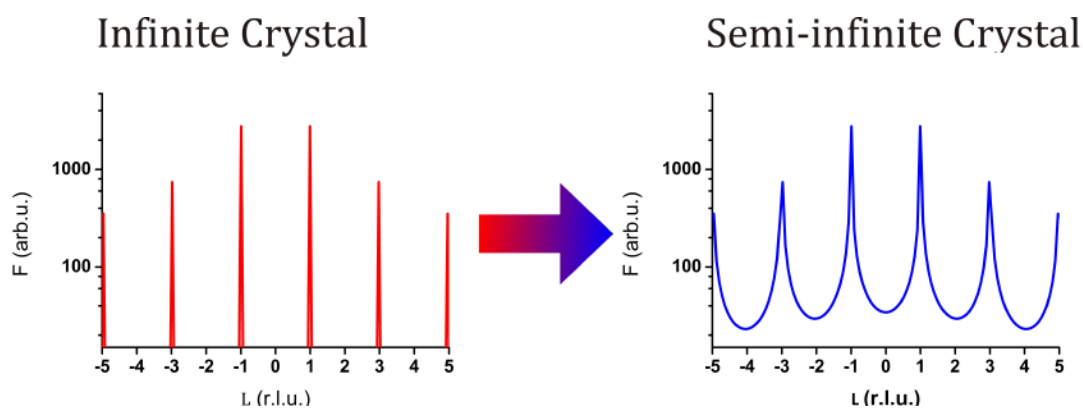

Figure 4.3: Left side: an infinite crystal leads to δ-shaped Bragg peaks and thus structure factors F at the Bragg peak positions in the kinematic approximation. If this condition is relaxed along one direction, say +z, it lead to a broadening of the Bragg peaks along that corresponding reciprocal direction L and finite structure factor values in-between the Bragg peaks, as shown on the right side. The plot shown here is called a "crystal truncation rod" [135].

4.1.3 Non-anomalous and Anomalous X-ray Diffraction

The element specific parameter in the structure factor is the X-ray energy- and momentum transfer- dependent atomic form factor $f(\boldsymbol{Q},E)$ defined as the effective number of electrons of an element contributing to diffraction given by

$$f(\boldsymbol{Q},E) = f_0(\boldsymbol{Q}) + f'(E) + if''(E) \tag{4.12}$$

where $f_0(\boldsymbol{Q})$ is the contribution from the electrons of a certain element defined as

$$f_0(\boldsymbol{Q}) = \int \rho(\boldsymbol{r})e^{i\boldsymbol{Q}\boldsymbol{r}}d\boldsymbol{r} \tag{4.13}$$

with $\rho(\boldsymbol{r})$ as the electron density of that element and thus the number of its electrons or the atomic number Z.

$f'(E)$ and $f''(E)$ are counting for the energy dependent dispersion and adsorption, respectively. Figure 4.4 shows the characteristics of $f'(E)$ and $f''(E)$ [142] for Zr and Y around the K-edges of these elements, i.e. at 17.9976 keV and 17.0384 keV respectively. It is clear to see that $f'(E)$ is only considerably different from zero around the resonant energies and $f''(E)$ only deviates from its common characteristics around the same energies. Bearing in mind atomic numbers of 39
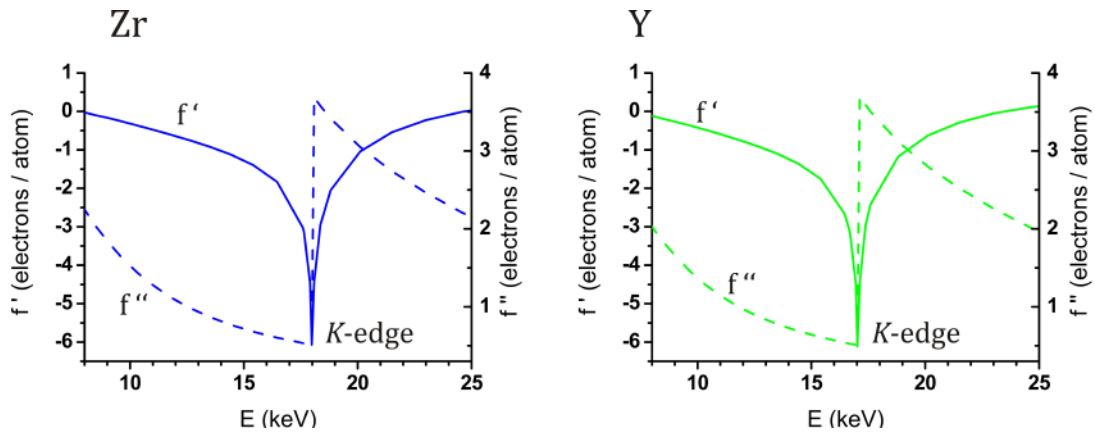

Figure 4.4: f' and f'' values for Zr and Y around the K-edges at 17.8876 keV and 17.0384 keV. Considering Z values of 39 and 40 for Y and Zr, it becomes clear that f' and f'' only have to be taken into account for energies around the K-edges and can be neglected elsewise.

and 40 for Y and Zr, it is obvious that these values have to be considered only for energies around the excitation edges and can be neglected elsewise. Thus, for non-resonant energies

$$f(\boldsymbol{Q}, E) \xrightarrow{yields} f(\boldsymbol{Q}) = f_0(\boldsymbol{Q})$$ (4.14)

is a reliable approximation.

For X-ray energies at which no dispersion and adsorption effects have to be taken into account, i.e. for energies far away from the edges, the so-called non-anomalous diffraction is valid. Anomalous diffraction is present if X-ray energies are close to an excitation edge of the elements and adsorption and dispersion effects cannot be neglected. The values for f' and f'' for the energies at the Y- and Zr-edge can be extracted from the graphs given in Figure 4.4 or well known databases as the NIST [142] and are listed in Table 4.1. These values were used for the structure refinements using anomalous data in chapter 55.1.

Non-anomalous diffraction is very restricted in distinguishing between elements with similar numbers of electrons. This is certainly the case for yttrium and zirconium with 39 and 40 electrons. Anomalous diffraction is very helpful when trying to increase the contrast between two elements that have similar numbers of electrons, by changing the effective number of electrons contributing to the diffraction. Thus, measuring at the K-edges of Zr and Y provides a powerful tool to gain structural information about the metallic compounds of YSZ.

Figure 4.5 shows the $(1, 1)$ CTR of an oxygen terminated surface of (100)-

Table 4.1: f' and f'' values for Zr and Y around the K-edge at 17.8876 keV and 17.0384 keV. These values are taken from the database of NIST [142].

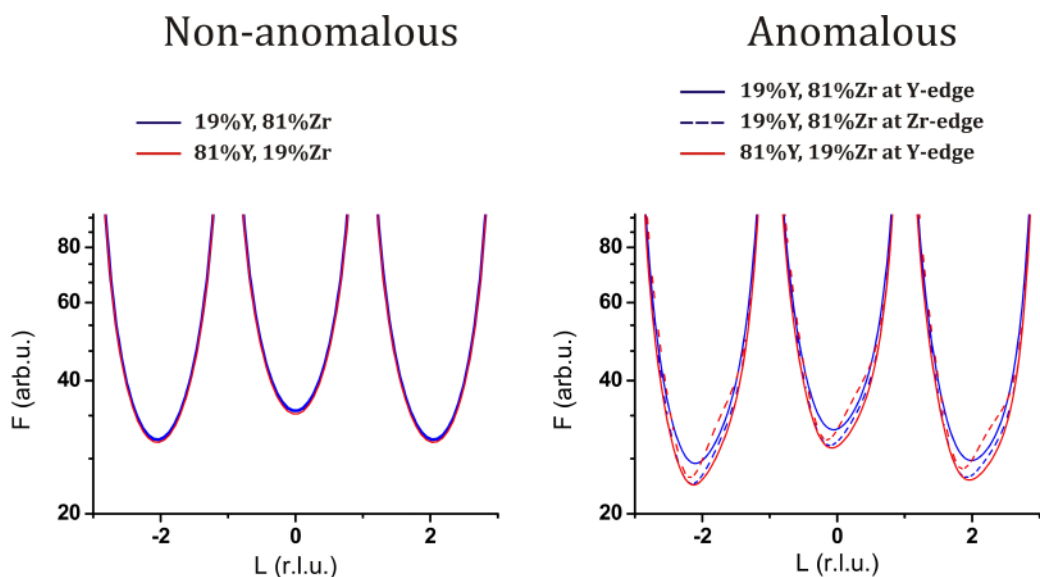|		f'	f''
Zr-edge	Zr	-5.79	1.05
	Y	-2.01	3.38
Y-edge	Zr	-2.44	0.57
	Y	-5.85	1.02

Figure 4.5: Simulated (1, 1) CTR of an oxygen terminated YSZ(100) crystal. The blue lines show the CTRs for a composition of 81% Zr and 19% Y, the red lines the opposite concentrations. Non-anomalous diffraction shows two identical CTRs, i.e. non-anomalous diffraction is unable to distinguish between these elements. Anomalous diffraction at the Y- and Zr-K-edges shows major differences in the minima of the two compositions and is thus able to distinguish between these elements.

oriented YSZ in the fluorite-like structure (see section 2.4.2.1) with two different metal concentrations: the blue lines corresponds to an 81% Zr and 19% Y concentration and the red lines illustrates the opposite composition. While normal diffraction shows no difference between these two vastly different compositions (left part of Figure 4.5) there is a noticeable difference observable between the anomalous CTRs at the yttrium and zirconium K-edge (right part of Figure 4.5).

This example illustrates the advantage of anomalous diffraction experiments and warrants the use of this technique for this work.

4.1.4 Experimental Setups

The SXRD experiments of this work were mainly performed at the surface X-ray diffraction beamline of the MPI-MF at ANKA at the Karlsruhe institute for technology (KIT). The beamline can operate at X-ray energies between 6 keV and

20 keV with energy resolutions around 0.03% and monochromatic X-ray fluxes around 10^{10} photons/s (at 10 keV). The setup of the beamline is shown in Figure 4.6 [143].

The synchrotron beam is monochromatized with a Si(111) double monochromator. The size of the resulting focused beam is typically 500µm in the horizontal and 350µm in the vertical direction and can be modified by slits.

Figure 4.7 shows a sketch of the Huber diffractometer [144] of the MPI-MF beamline in the vertical geometry which was used for the measurements of this work. It was operated in the six-circle/z-axis mode [145], where two circles are used to align the sample-normal perpendicular to the beam, one circles determines the incident angle and the remaining three are free for measurements. The diffractometer is controlled by the software "SPEC" [146], which is able to transform reciprocal space positions into rotations of the free diffractometer circles once two reciprocal points and the orientation are known [147]. There are slits before the sample and in front of the detector that allow cutting the incoming and diffracted signal which are needed to set the reciprocal resolution.
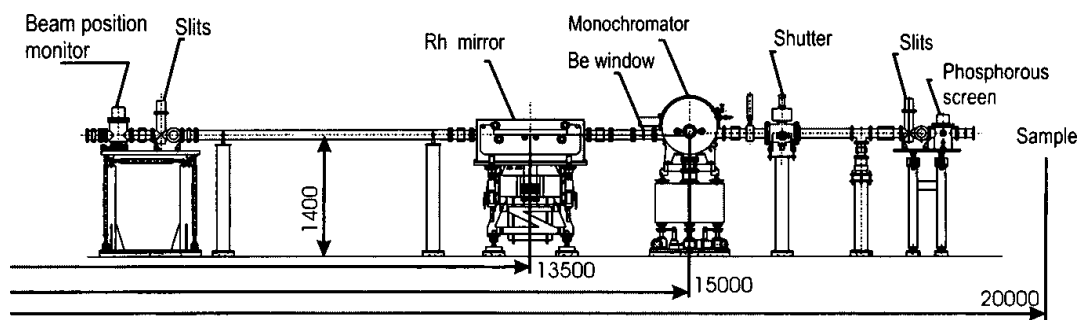

Figure 4.6: [143] Setup of the MPI-MF beamline at ANKA. The white beam of the synchrotron is directed through the beamline optics and monochromatized by a silicon double monochromator with an energy resolution of $3 \cdot 10^{-4}$ keV. The monochromatic beam has a size of typically 500 µm horizontally and 350 µm vertically.
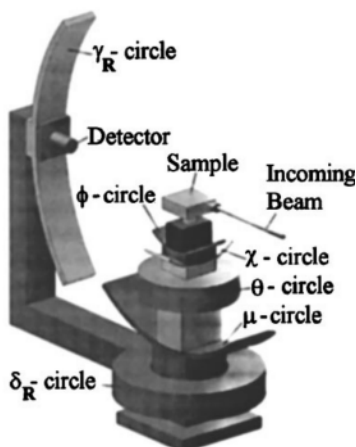
Figure 4.7: [143] Diffractometer of the MPI-MF beamline at ANKA in the vertical setup. Six circles are used to move the sample: two for aligning the sample-surface normal perpendicular to the incoming beam, one for the incident angle and three for the measurements.

Two dedicated mobile UHV chambers with beryllium windows were used for the measurements (see Figure 4.8). These chambers can be mounted on the diffractometer of a beamline. Both chambers are equipped with a turbo-pump and an ion-pump to guarantee UHV conditions. Different sensors allow precise pressure measurements at different pressure ranges. A gas system allows exposing the sample to different gases. An open module on the top of the chambers allows mounting different extensions such as a sputter gun or an evaporator. While the high pressure chamber is equipped with a ceramic heater and able to operate at up to atmospheric pressures and temperature of about 650°C, the electron beam heater of the high temperature chamber allows temperatures of over 1400°C but is restricted to pressure of maximum 10^{-5} mbar at these temperatures. These features of the chamber allow *in-situ* measurement during and after sample preparation and reactions.

The signal is detected either with a sodium iodide (NaI) point detector or a Pilatus-II 2D pixel detector [148]. Pilatus-II has a CMOS chip and is able to process in the so-called "single photon mode". It has 486 × 195 pixels each with a size of 172
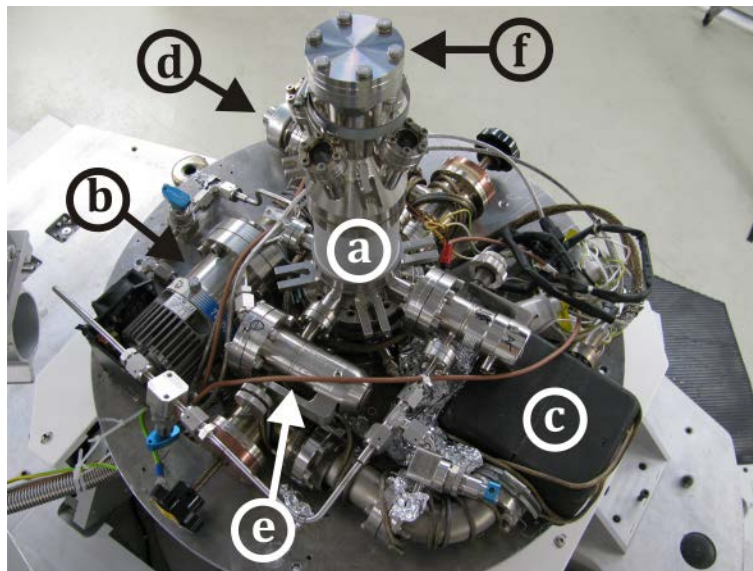
Figure 4.8: Mobile chamber used for the SXRD experiments. a: beryllium window, b: turbo pump, c: ion pump, d: pressure sensor, e: leak valve, f: module for expansions.

x 172 μm². The chips can be read out within $\sim 3ms$ giving the time resolution of this detector. The size of the 2D detector of 83.592 × 33.540 mm² allows the measurement of integrated intensities in the so-called "stationary mode" at higher
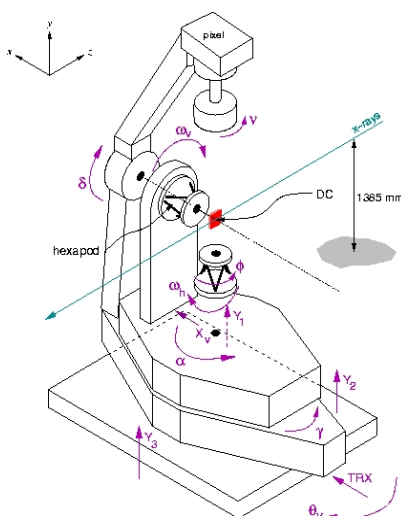

Figure 4.9: [115] Diffractometer of the material-science surface diffraction beamline at SLS. The (2+3)-circle diffractometer was operated in the z-axis mode. The sample is tilted with a hexapod.

reciprocal L values due to the known size of the diffraction signal with the Ewald sphere [145]. In the stationary mode the integrated intensity signal can be measured without rocking the sample and the whole signal is detected at once.

All anomalous diffraction experiments were carried out at the material-science (MS) surface diffraction beamline [149] of the SLS at the Paul Scherer Institute. This beamline has a (2+3)-circle Newport Micro-Control [150] diffractometer with a hexapod (see Figure 4.9 [151]) which is controlled by "SPEC" as well. The diffractometer was used in the vertical z-axis mode. Similar optics to that of the MPI-MF beamline at ANKA are used to monochromatized the beam from 4 keV to 40 keV with a resolution of 0.014% and typical beam sizes of 450 x 160 μm^2 and fluxes around 10^{13} photons/sec (at 10 keV). The MS surface diffraction beamline provides a Pilatus-II detector [148] for the measurements.

4.1.5 Data Analysis

4.1.5.1 Corrections

When deriving a structure factor from measured intensity signals, different corrections have to be taken into account. These corrections can be written as functions of the diffractometer angles as given in Figure 4.7. They were derived in two publications [145; 152] and are listed and explained in the following.

- **Lorentz factor**: this correction is necessary to correlate resolutions in real- and reciprocal space where the finite angular resolution in real space has to be considered.

    The Lorentz factor for rocking scans is:

    $$\frac{1}{\sin \delta \cos \alpha \cos \gamma} \tag{4.15}$$

    And for the stationary mode:

    $$\frac{1}{\sin \gamma} \tag{4.16}$$

- **Polarization factor**: the detected intensity is in general depending on the polarization of the incident beam. For vertically X-rays present at the SXRD experiments of this work performed at the synchrotrons

$$P_{\text{ver}} = 1 - \sin^2 \delta \cos^2 \gamma \qquad (4.17)$$

the polarization factor is given by

$$P = (1 - p_h)P_{\text{ver}} \qquad (4.18)$$

- **Transmission correction**: if the beam is going through materials before hitting the sample and arriving at the detector, the transmission through these material have to be considered. In our case, the beam goes through a beryllium window.

  With $T_0(E)$ as the X-ray energy dependent transmission at angles 0, the transmission correction for the incoming beam is given by:

$$T(E)_{0,\text{in}}^{\left(\frac{1}{\cos \alpha} - 1\right)} \qquad (4.19)$$

  while the transmission for the outgoing beam is given by

$$T(E)_{0,\text{out}}^{\left(\frac{1}{\cos \gamma} - 1\right)} \qquad (4.20)$$

- **Area correction**: the size of the incident beam and the slits in front of the detector will determine the active area of a sample, i.e. the area that diffracts into the detector. Ignoring footprint and sample size this correction is

$$\frac{1}{\sin \delta} \qquad (4.21)$$

- **Beam profile and finite sample size correction**: the beam has a certain shape and profile that affect the detected signal. Usually a Gaussian beam shape is assumed. The finite size of a sample can also reduce the detected signal. This correction is determined numerically as given in [145].

- **Rod interception**: includes the angular range in which a rod is detected and a possible cut by the angular resolution. This correction is given by

$$\cos \gamma \qquad (4.22)$$

4.1.5.2   Structure Factors

Software that derives structure factors from integrated intensity measurements must integrate the above corrections. Two different programs were used to calculate structure factors from the experimental data.

When using the point detector, rocking scans can deliver integrated intensity data. For these data the program "ana" [152] in the software package "ana-rod" [153] was used to determine structure factors.

Figure 4.10 show a typical rocking scan of an integrated intensity measurement. ana first normalizes all rocking scans with respect to the number of incoming photons measured by a monitor. This normalization has to be performed in order to keep different data comparable as the synchrotron beam has an intrinsic fluctuation due to refill cycles of the ring. As a next step, the background is determined as the average signal left and right of the main peak and subtracted from the detected signal. The above mentioned corrections are executed subsequently with the following required information:

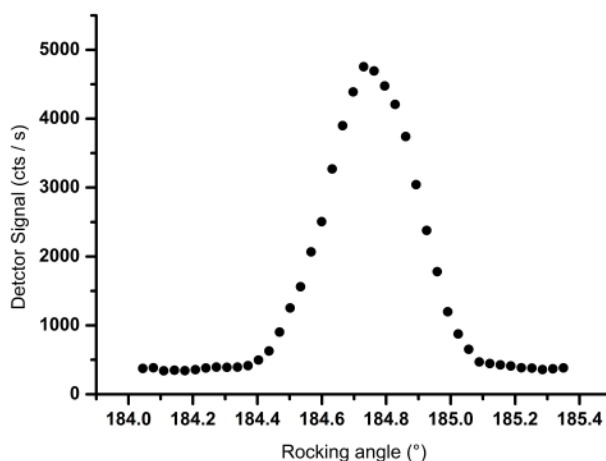- Transmission factors of the incoming and outgoing beam.

Figure 4.10: Rocking scan: ana integrates the signal by first subtracting a background. This background is determined from the signal left and right of the main peak. The subtracted signal is then corrected and integrated to deliver structure factors.

- The slit sizes

- The size of the sample

- The beam size

Structure factors are calculated subsequently by integrating the corrected intensities.

All of the above features were implemented in a self-made program using IDL (interactive data language) [154] which allows to determine structure factors from the signal of an 2D detector.

The left part of Figure 4.11 shows a typical diffraction image measured with the Pilatus-II detector. The integration is done as follows: the right part of Figure 4.11 shows a cutout of the region with the diffracted signal. Two different areas are marked here: the red rectangular is placed around the diffracted signal and is called region of interest (ROI) hereafter. Two dashed rectangles, which we call the background boxes, have the same height as the ROI and are placed left and right to the ROI. After monitor normalization, the integrated signal is background subtracted by determining the average pixel intensity in the background boxes and subtracting it from each pixel in the ROI. The structure factors are then determined after
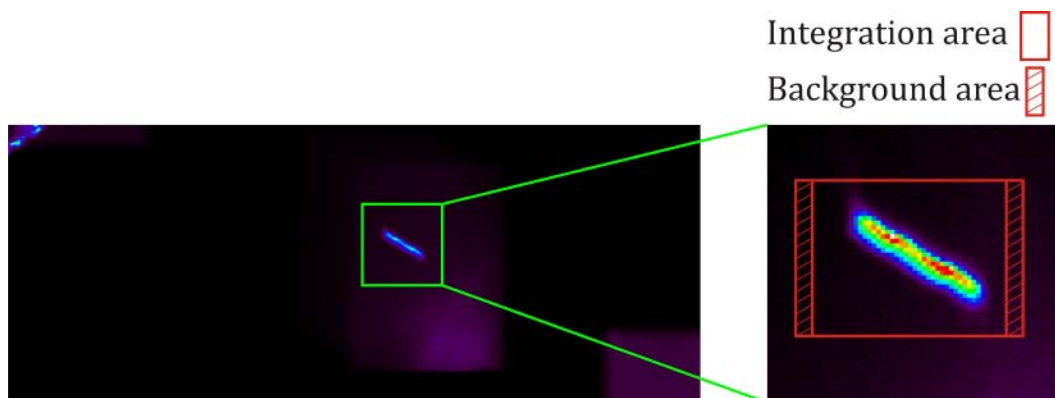

Figure 4.11: A typical diffraction image measured with the Pilatus detector. The red box marks the region of interest (ROI) and the red-dashed boxes determine the background. The background per pixel is subtracted from each pixel in the ROI. The signal is normalized to the monitor and corrected subsequently. Integrated intensities deliver structure factors thereafter.

applying the routine corrections given in section 4.1.5.1).

4.1.5.3   Averaging

A common way to obtain reliable error bars for the structure factors is to measure several symmetry equivalent structure factors and average them. ana-rod provides the program "ave" for this propose.

Once all measured structure factors are read in, ave needs to know the symmetry group of the measured crystal. With this information, ave is able to identify equivalent structure factors and average them [152]. A weighted error σ_{hkl} is then calculated for each structure factor defined as [152]:

$$\sigma_{hkl} = \sqrt{\epsilon^2 F_{hkl}^2 + \sigma^2},$$
(4.23)

with σ as average agreement of the entire dataset and ϵ as the statistical error of each structure factor. This type of averaging allows determining reasonable errors for the structure factors without equivalents as well.

4.1.5.4   Structure Refinement

In order to improve the agreement of a dataset with a structure model, several structure refinements were performed in this work. Refinements were performed by the variation of parameters contributing to the CTRs and comparing the resulting CTRs with the experimental data.

All fits in this work were done using the program "rod" [155] in the software-package "ana-rod" including the "Robach"-extension [156]. rod calculates structure factors from a given structure, included in a bulk- and a surface file. Parameters of all atoms in the surface file can be changed within a given range in the fit.

The "Levenberg-Marquardt" [157; 158] method was used to fit the data. A fit was finished, when the squared agreement factor

$$\chi^2 = \sum_{hkl} \frac{\sqrt{\left(F_{hkl}^{exp} - F_{hkl}^{mod}\right)^2}}{\sigma_{hkl}}$$
(4.24)

i.e. the summed difference between the structure factors of the model F_{mod} and the experiment F_{exp} reached a minimum value.

As an increasing number of fitting parameters simplifies finding a good agreement between experiment and model (As Johnny von Neumann once said [159], "with four parameters I can fit an elephant, and with five I can make him wiggle his trunk") introducing a normalized agreement factor is necessary to prevent this. A normalized agreement factor χ_N^2 penalizes using too many fitting parameters with respect to the available experimental data points. It is defined as

$$\chi_N^2 = \frac{1}{N - P} \sum_{hkl} \frac{\sqrt{\left(F_{hkl}^{exp} - F_{hkl}^{mod}\right)^2}}{\sigma_{hkl}} \tag{4.25}$$

where N is the number of available structure factors and P the number of parameters used for the fit.

The error of a parameter used for the structure refinement implemented in the rod fitting procedure is defined as the variation of this parameter to cause a 0.1 change of χ_N^2 with all other parameters fixed.

In order to simultaneously using anomalous and non-anomalous data for the structure refinements, an extension to rod was programmed [160]. It includes the energy dependent atomic form factors $f(\boldsymbol{Q}, E)$ as described in section 4.1.3. This extension allows fitting non-anomalous and anomalous data measured at one energy, i.e. either a set of non-anomalous and anomalous data at Zr-edge or non-anomalous and anomalous data at the Y-edge could be used. The remaining data was taken to cross validate the accuracy of the fit and served as a prediction error by contributing to the normalized agreement factor for the combined datasets which is calculated as

$$\chi_N^2 = \frac{\chi_{\text{Y-edge}}^2 + \chi_{\text{Zr-edge}}^2 + \chi_{\text{non}}^2}{N_{\text{Y-edge}} + N_{\text{Zr-edge}} + N_{\text{non}} - P} \tag{4.26}$$

with $\chi_{\text{Y-edge}}^2$, $\chi_{\text{Zr-edge}}^2$ and χ_{non}^2 as given in equation (4.24).

Following parameters were used for the fits of this work and can be fitted at once:

- **Scaling factors**: allows scaling the structure factors of the model to achieve better agreement. Two scaling factors are used when handling two datasets, where one scaling factor is used for each dataset.

- **Displacements**: all atoms in the surface file can be displaced and the displacements can be linked in order to keep the surface symmetry.

- **Roughness**: one roughness parameter in the so-called β- model.

- **Debye-Waller factors**: static Debye-Waller factors of the surface atoms can be fitted.

- **Occupancy**: the crystallographic sites are not always fully occupied. The occupancy of the sites in the surface can hence be refined.

4.2   Complementary Characterization Techniques

4.2.1   X-ray Reflectivity

X-ray reflectivity is an excellent technique to determine thicknesses of single and multilayer systems and their roughness with Ångström resolution as well as the electron densities and has been used successfully in the past (see for instance [161; 162; 163] and references therein).   It was used in this work to determine the roughness of the studied surfaces. By deriving the thickness and the effective electron density of a nickel film, the height and coverage of the nickel nanoparticles were estimated (see section 5.2.1.)

The idea to derive the above mentioned magnitudes from reflectivity measurements is based on the optical considerations given within electrodynamics [132; 164]. The main features of this technique are discussed in the following.

The index of refraction n of a material is smaller than unity for X-rays and can be written as

$$n = 1 - \delta + i\,\beta \tag{4.27}$$

for plane X-ray waves [132]. In this equation the dispersion and absorption terms δ and β are given by [164]

$$\delta = \frac{\lambda^2}{2\pi} r_e \rho \sum_{j=1}^{N} \frac{f_j^0 + f_j'}{Z} \tag{4.28}$$

and

$$\beta = \frac{\lambda^2}{2\pi} r_e \rho \sum_{j=1}^{N} \frac{f_j''}{Z} = \frac{\lambda}{4\pi} \mu \tag{4.29}$$

where λ is the wavelength of the X-rays, r_e the classical electron radius, ρ the electron density, N the atom density per volume, μ the linear absorption coefficient and f', f'' the dispersion and adsorption terms as given in equation (4.12).
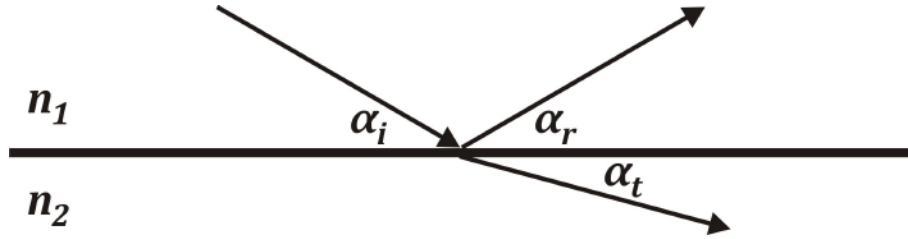
Figure 4.12: According to electrodynamics, an electromagnetic beam propagating through a medium with refraction index n_1 and hitting a medium with refraction index n_2 with the angle α_i can be reflected with the angle α_r and transmitted with the angle α_t.

Figure 4.12 shows a sketch of the optical parameters important for reflectivity. If an incident electromagnetic wave hits a material with angle α_i, reflection and transmission with the angles α_r and α_t are possible according the boundary conditions of the Maxwell equations [165]. For the specular geometry, the incident angle equals the reflected angle ($\alpha_i = \alpha_r$) and the incident and the transmission angles α_i and α_t are connected by the refraction indices n_1 and n_2 through

$$n_1 \cos(\alpha_i) = n_2 \cos(\alpha_t). \tag{4.30}$$

Hence, there is a critical incident angle α_c at which α_t becomes zero and total reflection occurs.

The reflection and transmission functions for X-rays, R and T are then given as [164]

$$R = \left| \frac{\sin(\alpha_i) - \sin(\alpha_t)}{\sin(\alpha_i) + \sin(\alpha_t)} \right| \tag{4.31}$$

and

$$T = \left| \frac{2 \cdot \sin(\alpha_i)}{\sin(\alpha_i) + \sin(\alpha_t)} \right| \tag{4.32}$$

which are plotted in Figure 4.13.

Recursive Fresnel equations can be used to derive the amplitude of the reflected beam [165]. For multilayer systems a formalism suggested by Parratt is used to calculate amplitudes where incoming waves are assumed to be refracted only once
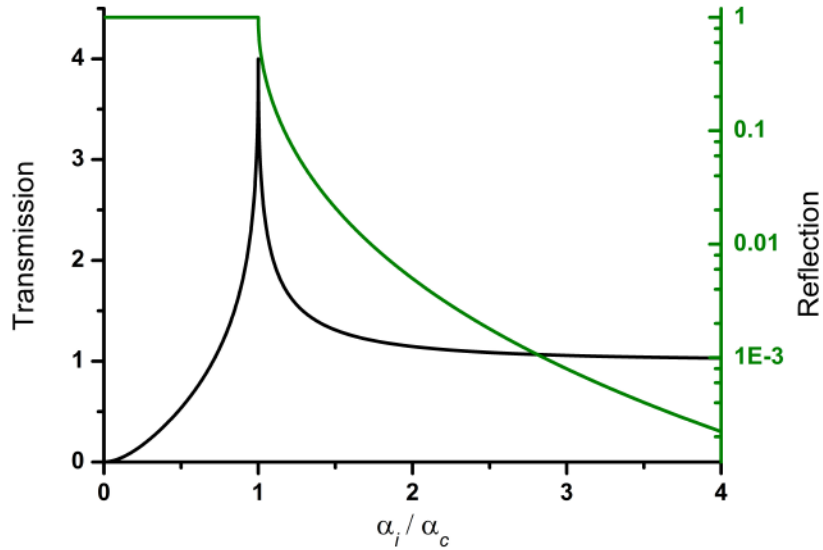
Figure 4.13: Transmission and reflection functions for X-rays as a function of the incident angle α_i. Total reflection is present up to the critical angle α_c. The transmission grows to amplified values around α_c and decreases towards one with increasing incident angle.

[166]. Following Parratts formalism and introducing the root mean square (rms) roughness σ_n of the n-th layer [167] the reflectivity function $R_{n,n-1}$ becomes

$$R_{n,n-1} = e^{\left(\frac{-i}{2} Q_n d_n\right)} \frac{R_{n,n+1} + F_{n-1,n}}{R_{n,n+1} F_{n-1,n} + 1} \tag{4.33}$$

with

$$F_{n-1,n} = \frac{f_{n-1,n} - f_n}{f_{n-1} + f_n} \, e^{-\frac{1}{2}Q_{n-1}Q_n\sigma_n^2} \tag{4.34}$$

and

$$f_n = \sqrt{\sin^2(\alpha_i) - 2\delta_n - 2i\beta_n}, \tag{4.35}$$

where Q_n and d_n are the momentum transfer and the thickness of the nth layer, respectively. The reflectivity function can thus only be calculated numerically and several programs are available to fit reflectivity data. The fits in this work were performed using the program "Fewlay" [168].

4.2.2 Atomic Force Microscopy (AFM)

Atomic force microscopy (AFM) is a technique to obtain topological information about surfaces. Its big advantage compared to electronic probe microcopies such as STM is its independence on the electronic conductivity of the sample of interest. AFM has become an indispensable tool in surface science and has established its status within the scientific community through numerous conclusive publications as [169; 170; 171]. Regarding the insulating properties of YSZ, AFM is one of the very few tools to deliver surface information, yet, it is not routine to achieve atomic resolution [172; 173] and only few groups were able to obtain AFM images with this resolution just recently [174; 175].

AFM was used in this work to get topographical information about nickel nanoparticles grown on the YSZ surfaces and comparing them to the results derived from SXRD and reflectivity. The basic principles of AFM are discussed in the following. A detailed description can be found in the book of Bhushan [176].

Figure 4.14 shows the schematic setup of an AFM machine: the probing tip is attached to a cantilever which can be moved very precisely by a piezoelectric tube. A Laser is emitting light that hits the cantilever just above the tip. A photodiode, divided into two equal parts A and B, is aligned to be equally radiated in both parts.

An AFM can be operated in two modes: the contact mode and the non-contact or tapping mode. In the contact mode, the tip is brought in contact with the surface and scanned along it. Topographical changes of the surface will lead to a deflection of the cantilever and thus to a displacement of the reflected light. The photodiode detects these displacements by comparing the reflected intensities in part A and B and converts them into height differences and thus a topological image. The disadvantages of this mode are possible scratches of the surface or film being scanned and the damage of the tip.

A nicer way to scan the sample is given by the tapping mode which was used for the measurements of this work. In this mode the cantilever is oscillated with its resonant frequency and a certain amplitude. The tip is approached to the surface to
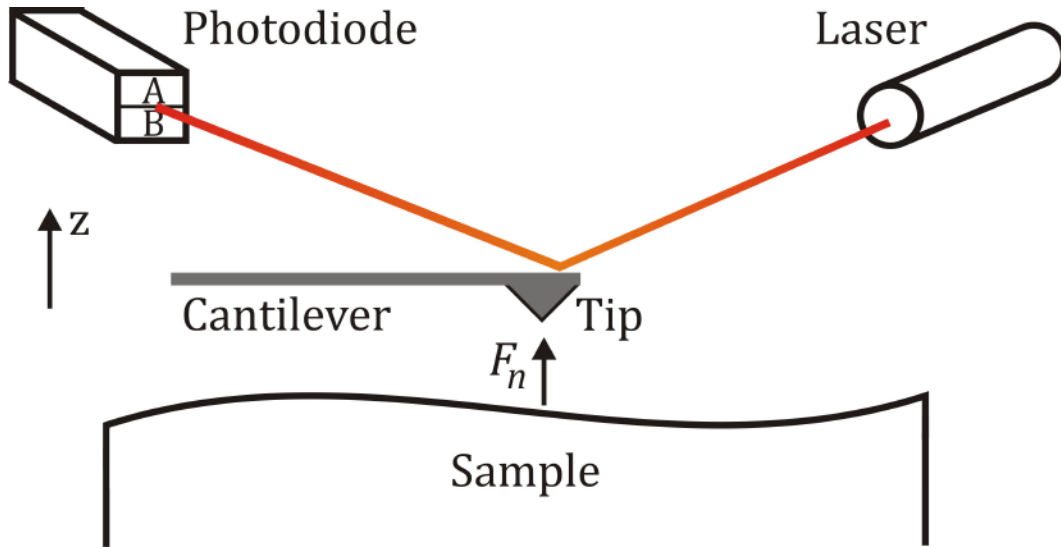
Figure 4.14: A typical setup of an AFM machine. The tip is hold by a cantilever which reflects the light of a Laser into a detecting photodiode. The photodiode is divided into two parts (A and B) and thus able to detect deflections of the reflected light caused by movements of the cantilever and transform them into a topological image.

have distances in the nm range. The basic idea is that there is a normal force F_n of the surface interacting with the tip and changing the oscillation:

$$F_n = k \cdot \Delta z, \tag{4.36}$$

where k is the spring constant of the cantilever in the z-direction and Δz the deflection caused by the interaction. The normal force can include different interactions such as van der Waals, magnetic and electrostatic.

With the resonant frequency f_{res} being

$$f_{\text{res}} = \frac{1}{2\pi} \sqrt{\frac{k}{m}}, \tag{4.37}$$

where m is the mass, changes in the amplitude and frequency of the oscillation detected by the photodiode can be linked with the interaction with the surface and a surface topography can be derived.

The tapping mode is only reasonable for surfaces with small height variations or rather for surfaces with height variations smaller than the oscillation amplitude of

the cantilever. If this condition is not fulfilled, the tip might hit the sample and the results are distorted.

The AFM measurements in this work were analyzed using the software package "WSxM" [177].

4.2.3 Auger Electron Spectroscopy (AES)

Auger electron spectroscopy (AES) is based on the so-called Auger effect, which predicts the emission of an electron from an excited atomic state [178]. The mechanisms of this effect are illustrated in Figure 4.15: the atoms of the sample are excited externally for instance by a primary electron (photons are able to cause the same effect) . The primary electron creates a hole in an inner orbital of an atom, which is filled by an electron of a higher orbit thereby emitting radiation. There is a finite probability of this radiation to release another electron with a lower binding energy from the atom, called the Auger electron, with a characteristic kinetic energy.

AES measures the energy of the Auger electrons, which have known element-specific spectra [179; 180] , and thereby identifies the chemical composition of the irradiated material. A more detailed description of AES with experimental details can be found in [181].

The electron energy of the primary electrons is typically in the range of a few keV. The resulting mean free paths of the Auger electrons only allow the detection of electrons created in the surface area and make AES to a surface sensitive tool. AES
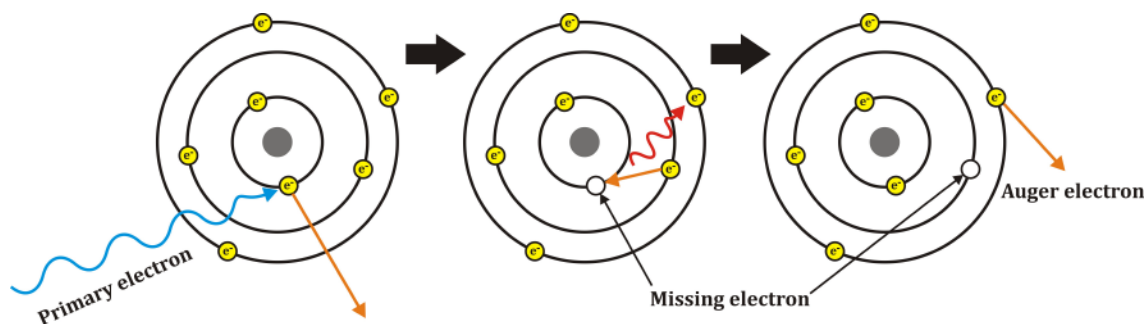

Figure 4.15: Principal of the Auger effect. From left to right: an external excitation of an atom is done by a primary electron (or photon). The primary electron removes an electron from the inner orbital leaving behind a hole. This hole is filled by an electron in a higher shell releasing radiation. The generated radiation can release another electron with a lower binding energy from a higher shell, called the Auger electron. The Auger electron has a very element specific kinetic energy and its measurement delivers information about the chemical composition of a sample.

was used in this work to characterize the chemical composition of the studied surfaces prior to the X-ray experiments.

Being unsuitable for insulating materials is the big disadvantage of AES. An insulating sample leads to charging of the surface through the primary electrons which rejects following electrons. However, using a very low primary electron current, it was possible to collect qualitative information about the chemical composition of the surfaces. Hence the accuracy of quantitative results has to be handled with care. An alternative solution is to measure AES at elevated temperatures which excites some electrons from the valence band into the conduction band.

The AES experiments were performed in the preparation chamber of our department shown in Figure 4.16. The main chamber, denoted a, is separated from a transfer chamber, denoted b, by a valve, denoted c. This construction allows keeping
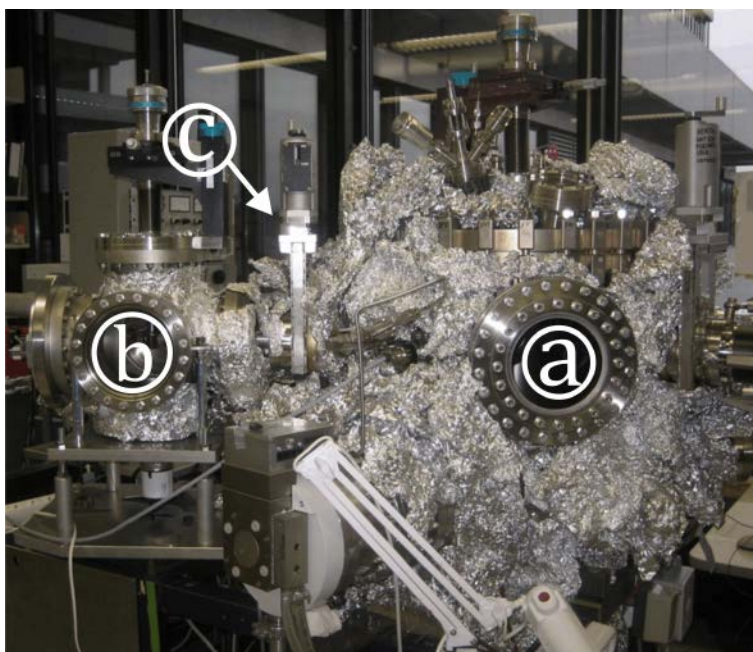

Figure 4.16: Setup of the preparation chamber at the MPI-MF, denoted a. It is separated from a transfer chamber (b) by a valve (c). A pumping system ensures very good UHV pressures in the 10^{-10} mbar range. A gas system allows experimenting with different gases and the samples can be characterized using AES and LEED. Several extensions are available for surface sputtering as well as the growth of thin films and nanoparticles.

very good pressures in the low 10^{-10} mbar range in the preparation chamber which is pumped by a system of an oil-free pump, a turbo- and an ion-pump. The preparation chamber is equipped with a sputter gun, AES, LEED and different extensions such as evaporators can be mounted. Windows on two opposite sides of the chamber ensure viewing the sample which can be translated and rotated on a manipulator. A gas system allows the introduction of different gases.

4.3   Physical Vapor Deposition (PVD)

The nickel NPs were grown on the YSZ surfaces using the physical vapor deposition (PVD) method [182]. Figure 4.17 shows a sketch of the used electron beam evaporator. A nickel rod is mounted into a hollow shroud. This shroud can be heated in order to anneal the rod. A cathode is creating electrons that are accelerated towards the tip of the rod by a bias of 600-1000V. This electron beam hits the tip of the nickel rod and evaporates nickel. Nickel ions among the evaporated particles are sorted out using a positive bias. The so produced current is a measure for the nickel flux that is leaving the evaporator towards the sample. Thus this quantity will give a magnitude for the evaporation rate.
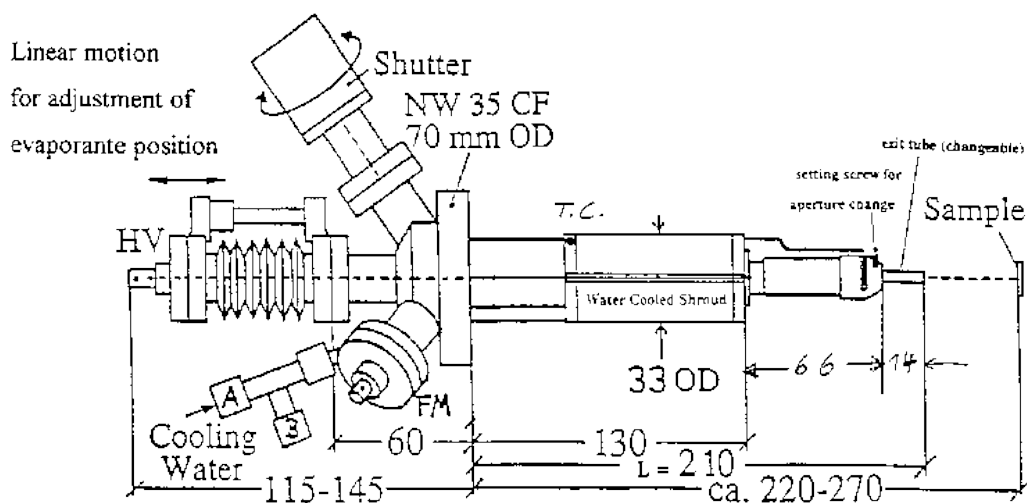

Figure 4.17: Sketch of the electron beam evaporator used for the nickel NP growth. An electron beam with energies between 600 and 1000 eV hits the tip of a nickel rod mounted in a hollow shroud, creating nickel atoms and ions. The ions are sorted out using a positive bias and causing a flux. This flux is a measure of the nickel atoms leaving the evaporator. The shroud is cooled with water and a shutter can stop the nickel atoms from leaving the aperture.

Figure 4.18 shows the evaporator on the top of the mobile UHV chamber both mounted on the diffractometer of the MPI-MF beamline. The evaporator is cooled with water and has a shutter that allows starting and interrupting the evaporation. The latter one is important for the experiment preparation. In order to have a pure nickel flux, the rod was annealed for several days during the bake out of the UHV chamber. Prior to the evaporation, the evaporator was operated for several hours to clean the rod tip from contaminations. The evaporation was only started when the flux was constant over several tens of minutes.

A thick nickel layer was grown on a sapphire substrate in the preparation chamber shown in Figure 4.16 prior to the experiments. Measuring the reflectivity of this film, the deposition rate could be determined. This rate was taken as a growth control during the evaporation of the nickel NPs.
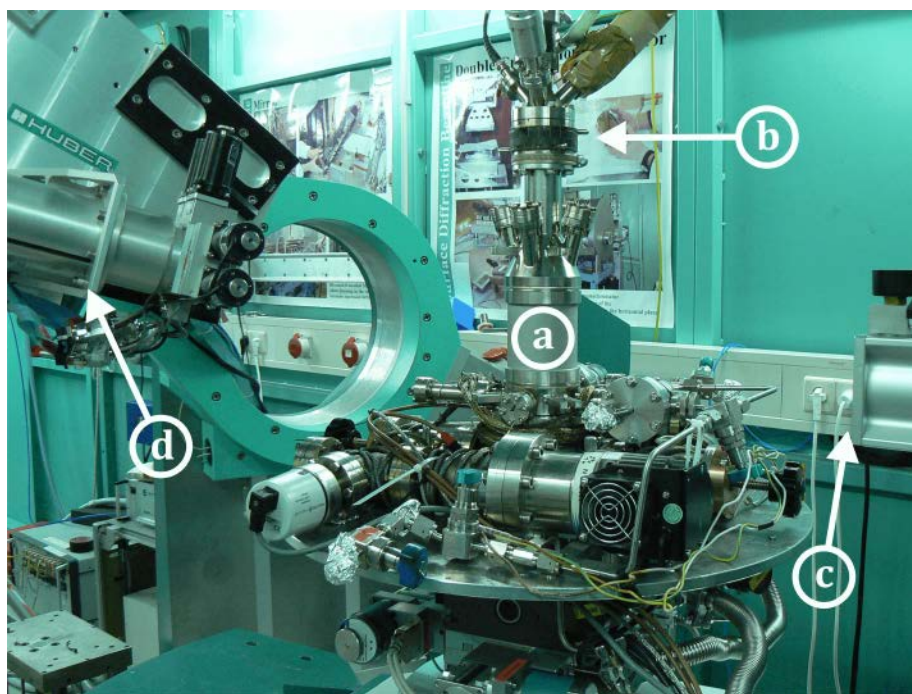

Figure 4.18: Mobile UHV chamber (a) as shown in Figure 4.8 with the PVD evaporator (b) mounted on top. The picture shows the setup used at the MPI-MF beam line at ANKA for the experiments where monochromatized X-rays leave the optics at (c) and the diffracted signal is measured with the detectors at (d).

5 The YSZ(111) Surface

The (111) surface of cubic ZrO_2 is a non-polar type-b Tasker surface with the lowest surface energy among the low-index orientations [13] (see also section 3.2.3). DFT calculations proved this statement to be also true for YSZ [12].

Using the most common composition of YSZ with an yttria content of 9.5% mol, the surface studied here is expected to be the most widespread facet of YSZ to confront. In terms of SOFC anodes and YSZ thin films, this orientation predominantly covers the surface and is hence the most important to investigate.

The structure of the YSZ(111) surface was studied by making use of a combination of anomalous and non-anomalous SXRD. This combination allows distinguishing between Y and Zr within the surface structure model where the composition is of great interest for applications like SOFCs as part of the three-phase boundary which is believed to be a key for the future development of anodes [8]. It also influences the growth of nanoparticles and thin film considerably by interacting with the deposited material. Regarding operation temperatures of SOFCs of typically above 600°C under reductive conditions, the surface structure was examined after a heat treatment at 1000°C and under reductive conditions as well.

The anode of an SOFC is covered by nickel nanoparticles, the shape and size of which have a great impact on the performance. Hence, the growth and shape of Ni nanoparticles on the YSZ(111) surface was studies as well. Shape changes after a heat treatment at 700°C and reductive conditions as well as exposure to methane and oxygen were also subjects of this study.

This chapter first presents the results of the surface structures of YSZ using the ideal fluorite- and the Zr-shift model (see section 2.4.2). It continues with the results about the growth of nickel nanoparticles grown on this surface and how the shape changes when the system is annealed and exposed CH_4 and O_2. All experiments were performed *in-situ* and the measurements done *ex-situ* are explicitly mentioned.

5.1   Surface Structure

5.1.1 Sample Preparation

The single crystal samples used for this study were purchased from Crystec GmbH and have miscuts below 0.1° with the chemical declaration 9.5% mol Y_2O_3. They were roundly shaped with the dimensions 10x1 mm or 15x1 mm.

The singles crystals are (typical for oxides) transparent and the optical transparency did not change during the experiments meaning a negligible change in the oxygen vacancy concentration [183]. For the experiments performed under UHV, the samples were mounted on a molybdenum sample holder using tantalum foils as shown in Figure 5.1. Temperatures were determined using a calibration curve with an error of ±100°C.

Before starting with SXRD experiments, it is important to know the state of the studied surface in terms of contaminations and surface roughness. A contamination-free and smooth surface is desirable for SXRD and a method to achieve this was found. The preparation tests and the AES experiments were performed in the preparation chamber of our department shown in Figure 4.16. As a first characterization step, AFM measurements of the as-received sample surface were performed in air. At the given miscut and step heights of 3.68 Å, a step is expected at distances of 211 nm (=3.68 Å/sin(0.1°)). The AFM images show huge terraces over several hundred of nm with height variations smaller than the resolution of the
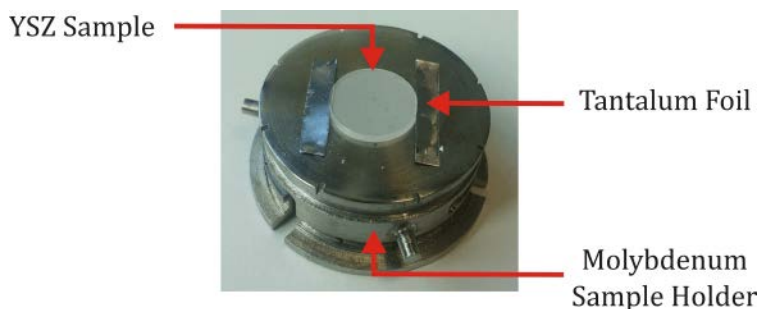

Figure 5.1: The transparent samples were mounted on molybdenum sample holders using tantalum foils that are inserted into slits on the sample's sides and spot-welded.
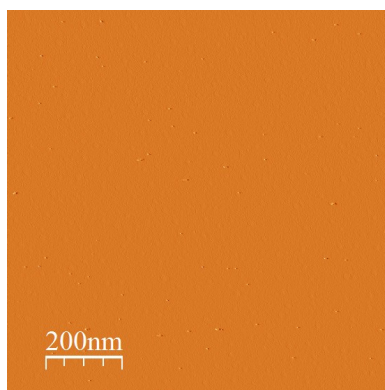
Figure 5.2: AFM images of the as-received sample show very big terraces pointing to a high quality of the samples which makes them capable for SXRD measurements.

AFM-machine as seen in Figure 5.2. This points to a smooth and clean state of the surface, even in the as-received state.

The next characterization step was to measure the reflectivity of an unprepared, as-received sample in air. This reflectivity curve is shown in Figure 5.3 (black dots). It shows a rather rapid decay in intensity and a broad feature around 0.5 Å^{-1} being an indication for a thin layer on top of the single crystal. A measurement beyond a Q value of 0.62 Å^{-1} is not possible, altogether pointing to reflective properties unsatisfactory for SXRD measurements. This qualitative information is indeed approved by the fit. It delivers a big root-mean-square (rms) σ-roughness (see section 4.2.1) value of 4.3 Å. In order to get satisfactory fitting results an additional layer with a thickness of 10.1 Å has to be added to the single crystal surface (see appendix B for fitting details). This layer is most probably hydrocarbon physisorbed on the surface and has to be removed for proper experimental conclusions.

The insulating property of YSZ makes AES measurements very difficult (see section 4.2.3). However, AES spectra were obtained by using very low electron currents and long counting times. The AES spectrum measured directly after transferring the sample into the preparation chamber confirm the additional layer to be hydrocarbons. Figure 5.4 shows the measured AES spectrum. Three peaks at the energies 141eV, 272eV and 510eV are observed which can be assigned to Zr, C and O respectively [184] (the Y peaks are outside the measurement range). Hence,
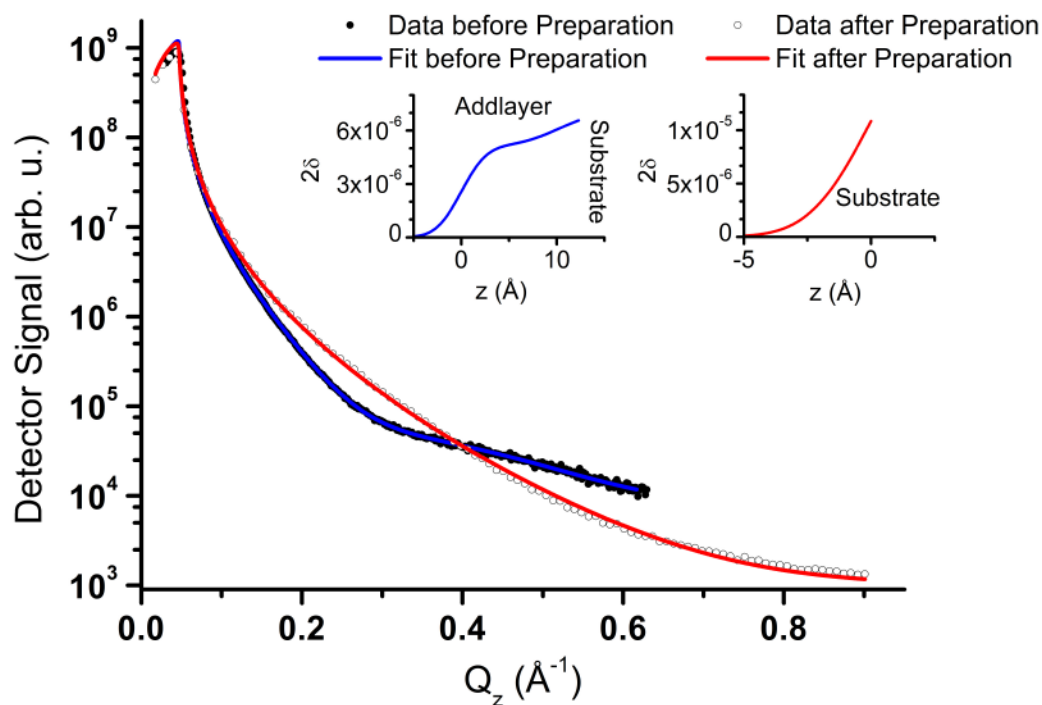
Figure 5.3: Reflectivity curve of an YSZ(111) crystal "as received" and unprepared (black dots) and after the preparation (white dots). The curve before the preparation decays rather fast and no signal is detected above 0.62 Å^{-1} pointing to insufficient reflective properties for SXRD. It also has a feature around 0.5 Å^{-1} indicating a thin additional layer on the surface. The fit results approve these statements and require layer with the thickness of 10.1 Å. After the preparation the reflectivity shows textbook characteristics for a clean and smooth single crystal. The insets show the electron density profiles resulting from the fits. The roughness of the unprepared surface is 4.3Å which reduces to 1.9 Å after the preparation.

the only contamination to deal with is carbon or hydrocarbons and the surface is clean elsewise even in the as-received state.

In order to generate a clean and smooth surface the sample was prepared as follows:

- Annealing at T = 400°C
- at an oxygen partial pressure of $p_{O2} = 10^{-5}$ mbar
- for 120 minutes

which is a typical preparation to clean the surface of hydrocarbons and water.
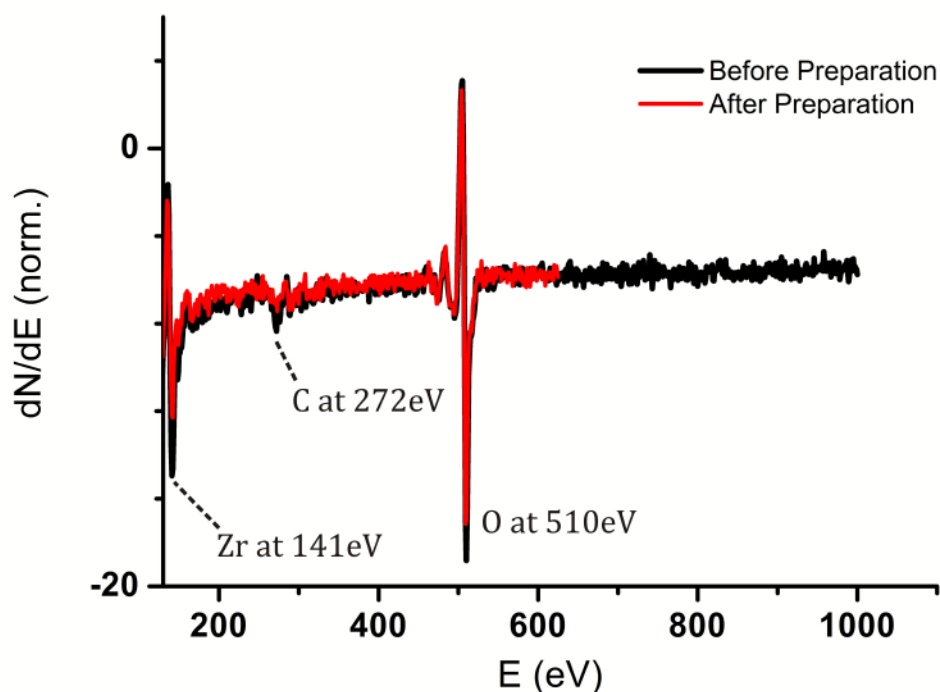
Figure 5.4: AES spectrum of an unprepared "as-received" (black line) and prepared (red line) YSZ(111) sample. The characteristic peaks at 141eV, 272eV and 510eV arise from Zr, C and O. Hence, carbon is the only contamination and is removed by the preparation. The Y peak is expected at energies outside the measurement range.

A look at the AES spectrum after three cycles of this preparation (red line in Figure 5.4) indeed shows an improvement and the carbon content decreases to a negligible amount indicating a vanish of the hydrocarbon layer. The reflectivity curve measured after the preparation shows an improved (textbook) characteristic for a clean and smooth single crystal (white dots in Figure 5.3). The improved optical properties of the surface are also found in the Q value up to which the reflected signal was detectable. This visible improvement is confirmed by the values delivered by the fit. No additional layer is necessary to fit the data and the rms roughness of the surface is determined to have a very good value of 1.9 Å. A clean and smooth surface with very large terraces could therefore be prepared. The achieved state of the surface is excellently qualified for SXRD measurements.

5.1.2 Surface X-ray Diffraction Experiments

The data for the structure determination of this surface were collected during two beam times at two different beam lines and from two different samples using the dedicated high-temperature mobile chamber. Description of the beam lines and the chamber can be found in section 4.1.4.

All data were collected at room temperature and UHV conditions. Base pressures in the upper 10^{-10} mbar range were achieved by baking the chamber prior to all experiments at the beam lines. One beam time at the MPI-MF beam line at ANKA was used to measure non-anomalous data after the cleaning preparation described in the previous section. This data was collected at an X-ray energy of 10 keV and an incident angle of 0.28° slightly above the critical angle of 0.26°, using a point detector. Figure 5.5 shows the in-plane reciprocal space map of the hexagonal (111)-oriented YSZ crystal. The triclinic arrangement is marked with the in-plane Bragg peaks, which can be determined considering the P3m1 symmetry group with atoms on the (4a) and (8c) positions [55]. The black rectangles mark the CTRs that have been measured during the beam time. A total of 373 structure factors included
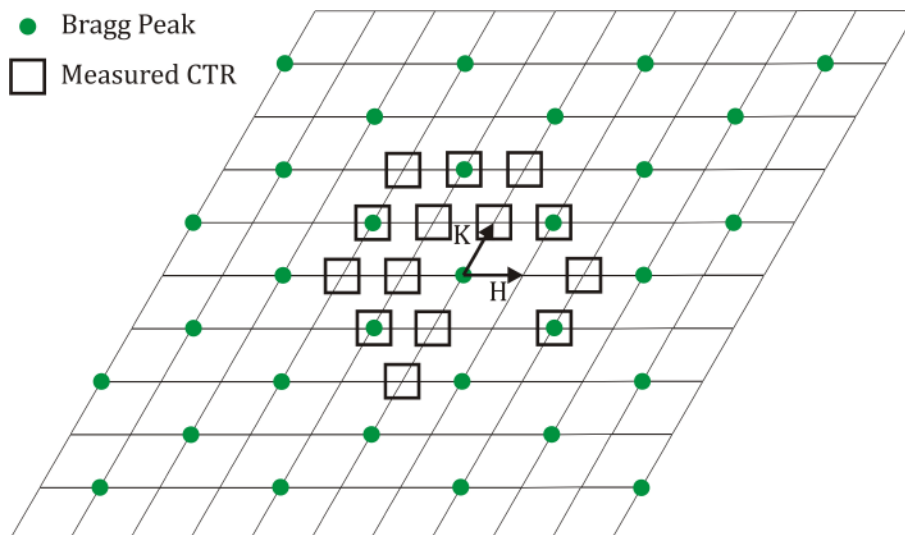

Figure 5.5: In-plane reciprocal space map of YSZ(111) with Bragg peaks marked with green dots and the measured non-anomalous CTRs during the ANKA beam time marked with black rectangles.

in 14 CTRs resulted from the measurements.

The threefold symmetry of the structure makes the 14 measured CTRs to reduce to three, when averaging over symmetry-equivalent CTRs as (0, 1 ,L) and (-1 ,0, L). After data integration and averaging using ana and ave (see section 4.1.5), the CTRs (1, 0, L), (1, 1, L) and (2, 0, L) remain, as shown in Figure 5.8. The indices in brackets give the H and K value of the respective CTRs. These CTRs include 125 non-equivalent structure factors with an average error of 14%.

In order to distinguish between Y and Zr, anomalous data was measured (see section 4.1.3). These data were collected at the materials-science beamline of the SLS after the same cleaning preparation but using another sample than that of the ANKA beam time. An incident angle of 0.3° was chosen to measure all the data at the SLS which is about double the critical angles at the used energies. This high incident angle was chosen to avoid transmission variations of the incoming beam caused by unreliability of the hexapod at this beamline (see Figure 4.13). The increased incident angles leads to the loss of some intensity and the increase of the background, however. Figure 5.6 shows an in-plane map of YSZ(111) with the CTRs
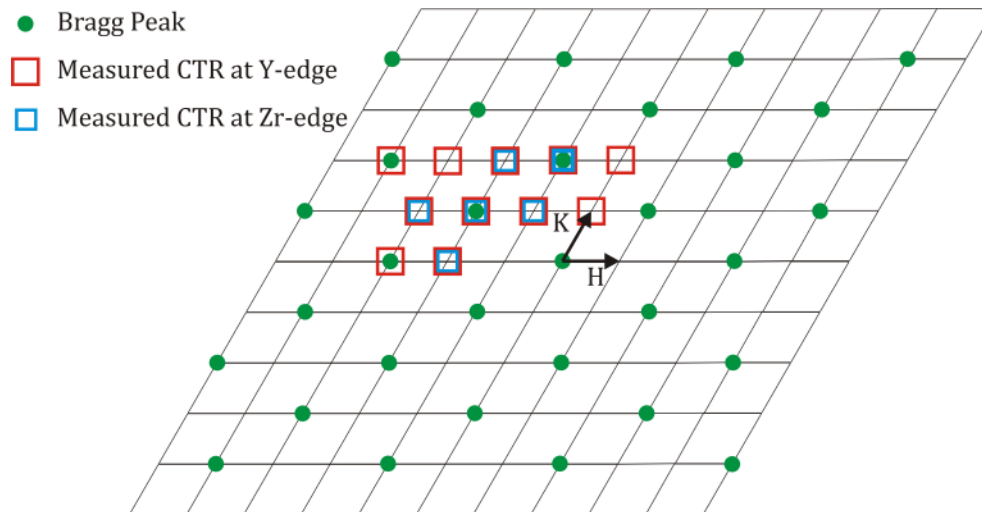

Figure 5.6: In-plane reciprocal-map of YSZ(111) with Bragg peaks marked with green circles and the anomalous measured CTRs during the SLS beam time after the cleaning preparation marked with red and blue rectangles for the data at the Y- and Zr-edge, respectively.

measured at the Y- and Zr-edge.

Since anomalous measurements include adsorption effects which result in a fluorescent radiation and thus a high background-signal level, some difficulties had to be faced during data integration. The high background level was especially distinctive for the data measured at the Zr-edge due to the higher content of Zr in the material. This fact leads to declined signal to background ratios and specially diffraction signal in the CTR minima become hard to detect. In such cases, the following procedure was applied in order to estimate the value of structure factors:

- If a structure factor has a detectable neighboring structure factors along a CTR, the value of this structure factor was estimated to be 30% less than that of the mean of the neighboring structure factors. The error was estimated to be 50%.

- If several structure factors in a row could not be detected, their value was set to the mean of the next detectable structure factors and the error was set to 100% since the signal could be 0 here as well.

The latter step is reasonable, because an estimation of the upper limit of these structure factors allows two respect changes between the data measured at the different conditions instead of ignoring them.

The resulting CTRs shown in Figure 5.9 and Figure 5.10 indeed show that the last step is predominantly necessary for the data measured at the Zr-edge. Such a procedure results in rather high average errors of the anomalous datasets.

Considering operation conditions of SOFCs of typically above 600°C and reductive conditions, another dataset was collected after the sample was undergoing a heat treatment as follows:

- Annealing temperature T= 1000°C

- Annealing time: 145 minutes

- Pressures during the heat treatment up to p = 10^{-8} mbar

After the sample was cooled down, more datasets were measured at the Y- and Zr-edge and non-anomalously. All of these data were measured at the MS beamline of the SLS with the non-anomalous data measured at X-ray energies of 16 keV.
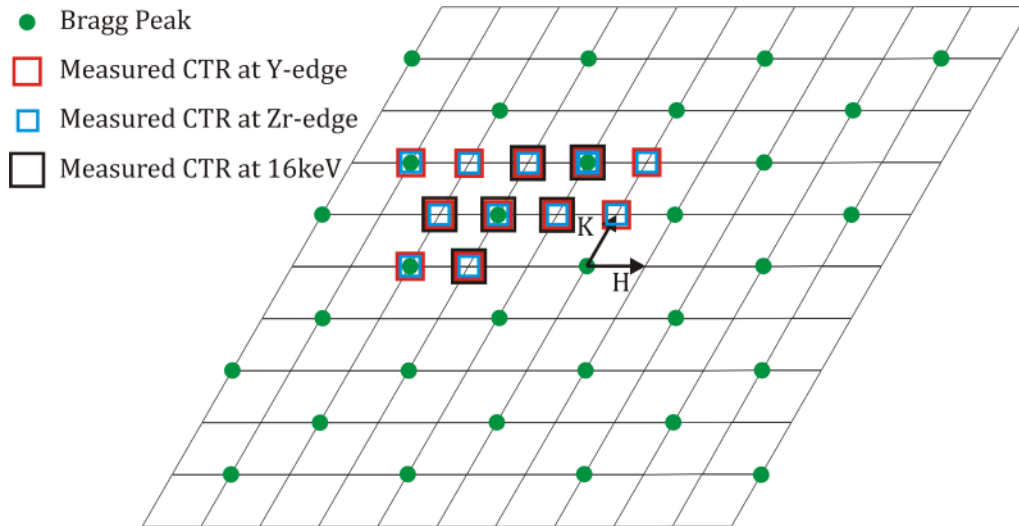
Figure 5.7: Measured CTRs after the heat treatment. Black rectangles indicate CTRs measured non-anomalous at 16 keV. Red and blue rectangles indicate CTRs measured anomalous at the Y- and Zr-edge respectively.

Figure 5.7 shows an in-plane map of YSZ(111) with the measured CTRs marked. Undetectable structure factors of these datasets have been treated with the same procedure as described above.

The threefold symmetry of the crystal reduces the number of available structure factors and CTRs for the refinements, when averaging over equivalent data. This

Table 5.1: Total number of datasets available for structure refinements after averaging over symmetry-equivalent structure factors. The high mean errors of the anomalous datasets arise from the high background signal caused by the increased incident angle resulting in low signal-to-background ratios.

		Dataset	Measured at	# F	#CTR	∅ ΔF
After Cleaning Preparation		Normal	ANKA	125	3	14.6%
		Y-edge	SLS	141	5	33.6%
		Zr-edge	SLS	153	4	22.9%
After Heat Treatment		Normal	SLS	95	3	14.2%
		Y-edge	SLS	142	5	19.6%
		Zr-edge	SLS	124	5	23.0%

leads to a total of datasets as given in Table 5.1 available for structure refinements.

Note that all data were measured during the same beam time using the same sample except the non-anomalous data after the cleaning preparation which was collected at the ANKA beam line from another sample.

The resulting CTRs are all shown in Figure 5.8, Figure 5.9 and Figure 5.10. Note that the single CTRs after the cleaning preparation and after the heat treatment are plotted in the same graph for comparison reasons using different scaling factors with the CTRs measured after the heat treatment in the upper part.
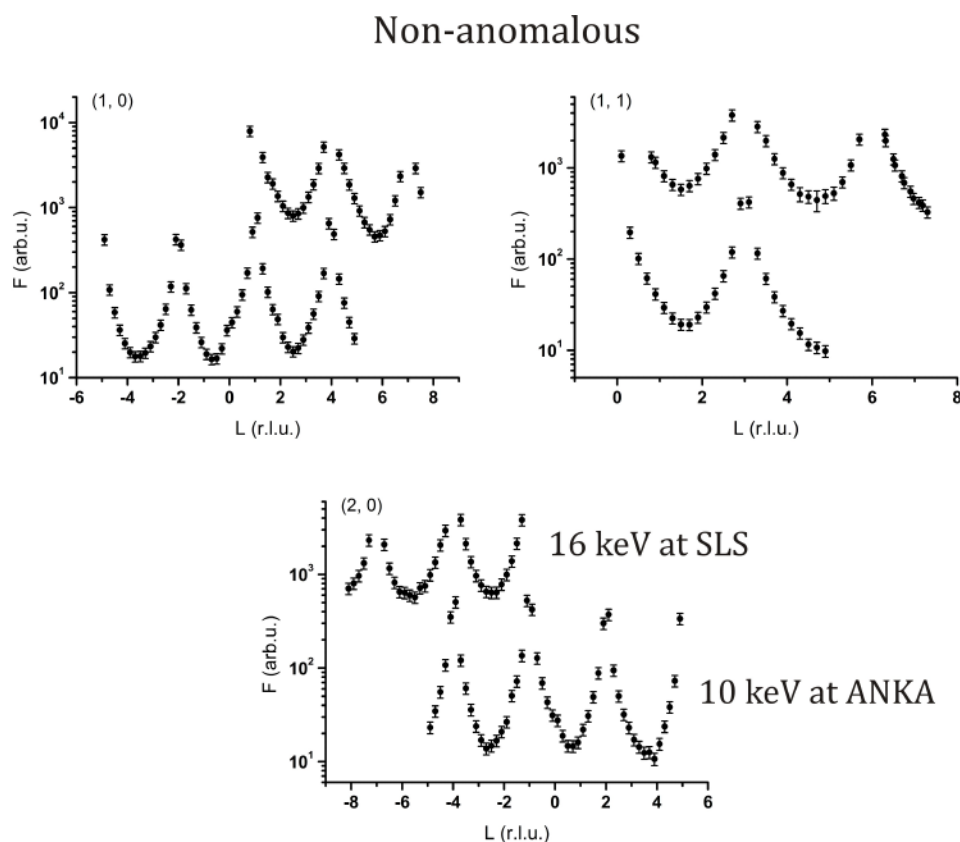

Figure 5.8: Non-anomalous data. The upper CTRs measured after the heat treatment are scaled in order to plot each CTR after the two studied conditions in one plot. Note that these data were measured from two samples during two beam times at different beam lines.
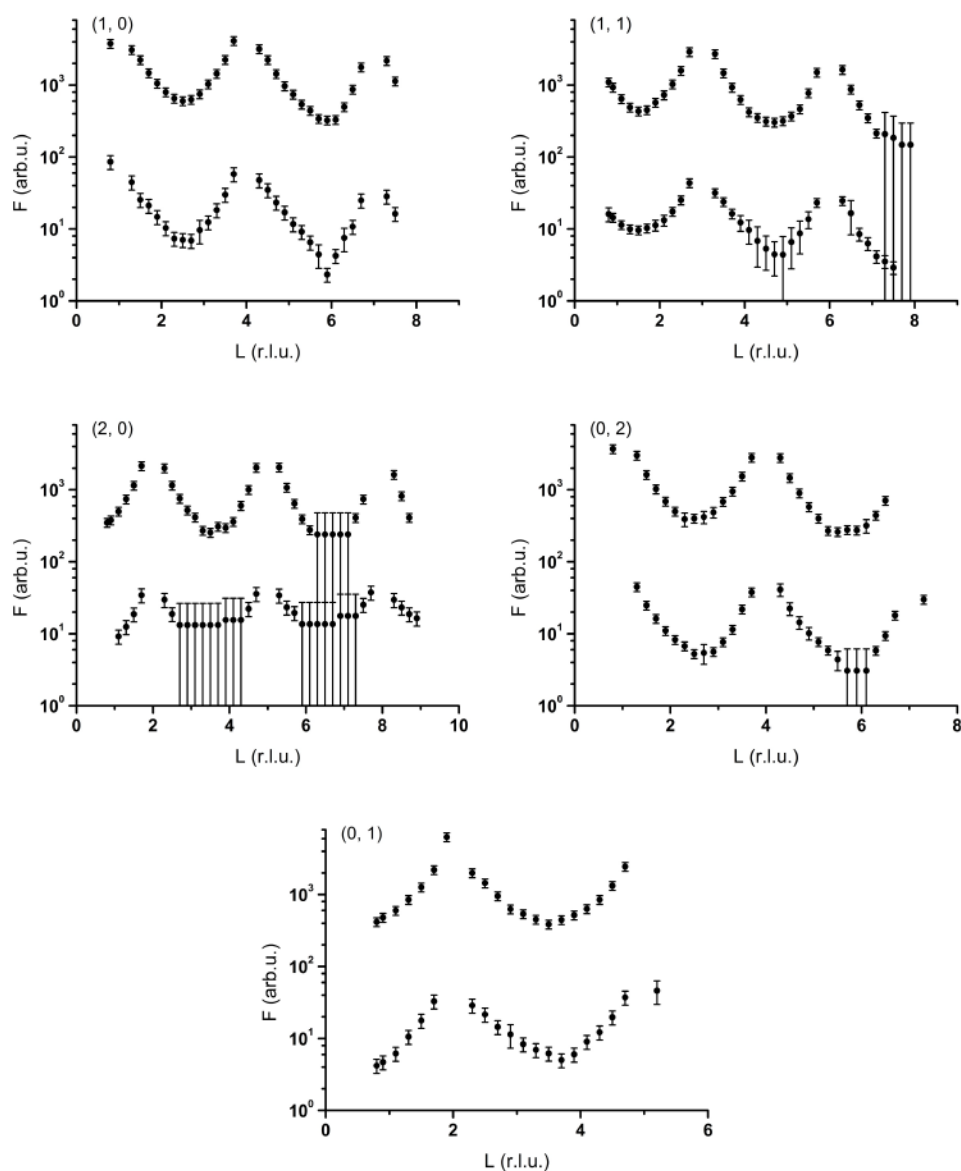
Figure 5.9: Anomalous data measured at the Y-edge. Using two different scaling factors for the CTRs measured at the two conditions both CTRs are plotted in the same graph with the CTRs after the cleaning preparation in the lower part.
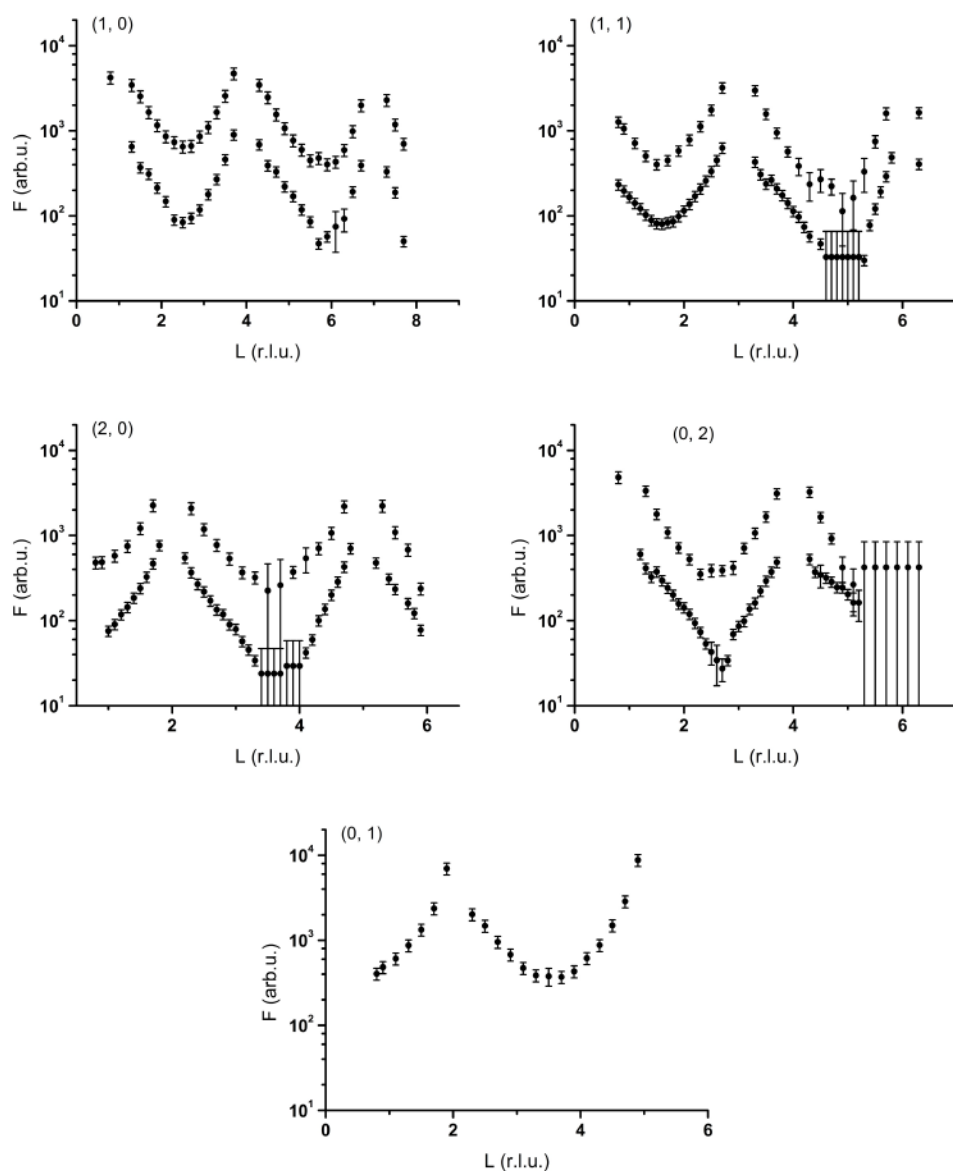
Figure 5.10: Anomalous data measured at the Zr-edge. Here again, the CTRs for both conditions are plotted in the same graph with the upper CTRs being measured after the heat treatment.

5.1.3   Structure Refinement

Before discussing the refinement results, it is important to mention that the SXRD measurements did not show an indication for a reconstruction of the surface when high-symmetry reciprocal directions were scanned.

The tools used for the structure refinements were introduced in section 4.1.5. Fits were performed using two different models for the bulk structure: the ideal fluorite structure and the Zr-shift model (see sections 2.4.2.1 and 2.4.2.2). An oxygen terminated surface as derived in section 3.2.3 was chosen as a starting point for the structure refinements. The results using both models are presented in this section.

5.1.3.1   Refinements Using the Fluorite Model

Figure 5.11 shows the oxygen-terminated surface of YSZ in the ideal fluorite model. As a first step it was tried to fit the data with the fluorite model using only the non-anomalous dataset after the sample preparation. It is important to emphasize that these non-anomalous data does not resolve differences between Y
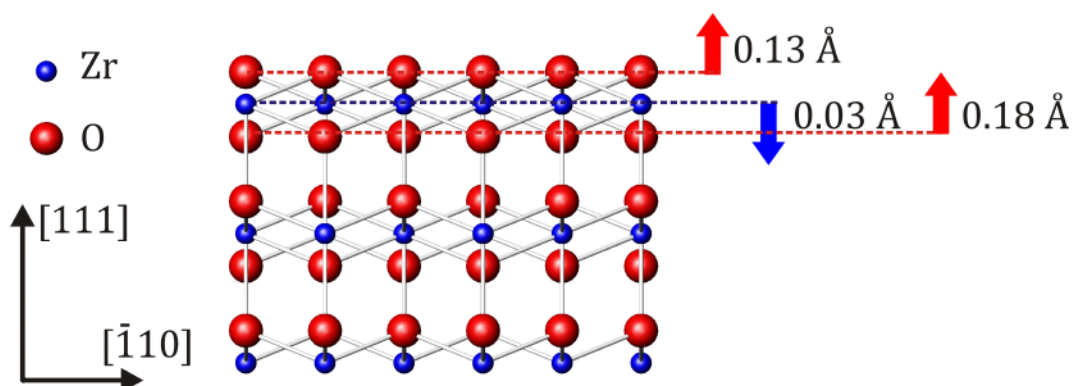

Figure 5.11: Oxygen terminated YSZ(111) surface in the fluorite model where Y atoms have been replaced by Zr, since a discrimination between them is not possible when non-anomalous data is used only. The arrows indicate the out-of-plane displacements of the three topmost layers resulting from the best fit with for the state after the cleaning preparation.

and Zr, since these elements almost have the same atomic form factors $f_0(\boldsymbol{Q})$ (see section 4.1.3). A triclinic unit cell with the dimensions

$$\alpha = \beta = 90°, \gamma = 120° \tag{5.1}$$

and

$$a' = b' = 3.63 \text{ Å}, c' = 8.91 \text{ Å} \tag{5.2}$$

by combining equations (2.10) and (2.20) was used for this fit.

Starting with Debye-Waller factors (DW) as given for a fluorite model in Table 2.1 and [35] an agreement factor of

$$\chi_n^2(N) = 6.5 \tag{5.3}$$

was achieved for a bulk termination of the atoms. A very good fit was achieved, when the following parameters were fitted:

- Out-of-plane displacements of the three topmost layers, that is, two oxygen layers and the Zr-layer in-between.
- Statistic DW-factor B_{Zr} of the topmost metal layer.
- Roughness of the surface.

The results are discussed in the following.

The displacements of the topmost atom layers are shown in Figure 5.11. Both oxygen layers move outwards by 0.13 Å and 0.18 Å, while the metal layer is slightly displaced inwards by 0.03 Å. The latter displacement is in line with the DFT calculations predicting a minor displacement of the metallic surface layer by 0.01 Å [12] (see also section 2.5.1). The oxygen displacements, however, clearly disagree with the results of that study.

The concentration of the topmost atom layers was not necessary to be fitted in order to get a very good agreement. Instead, the roughness of the surface has to be taken into account. The refinement delivers a β-roughness of 0.41 and thus 1.4 Å which is in a very good agreement with the σ-roughness of 1.8 Å found from reflectivity data.

A noticeable increase of the statistic DW-factor B_{Zr} of the topmost metal layer gives hints for the surface composition. It is fitted to be 2.23 Å² compared to the
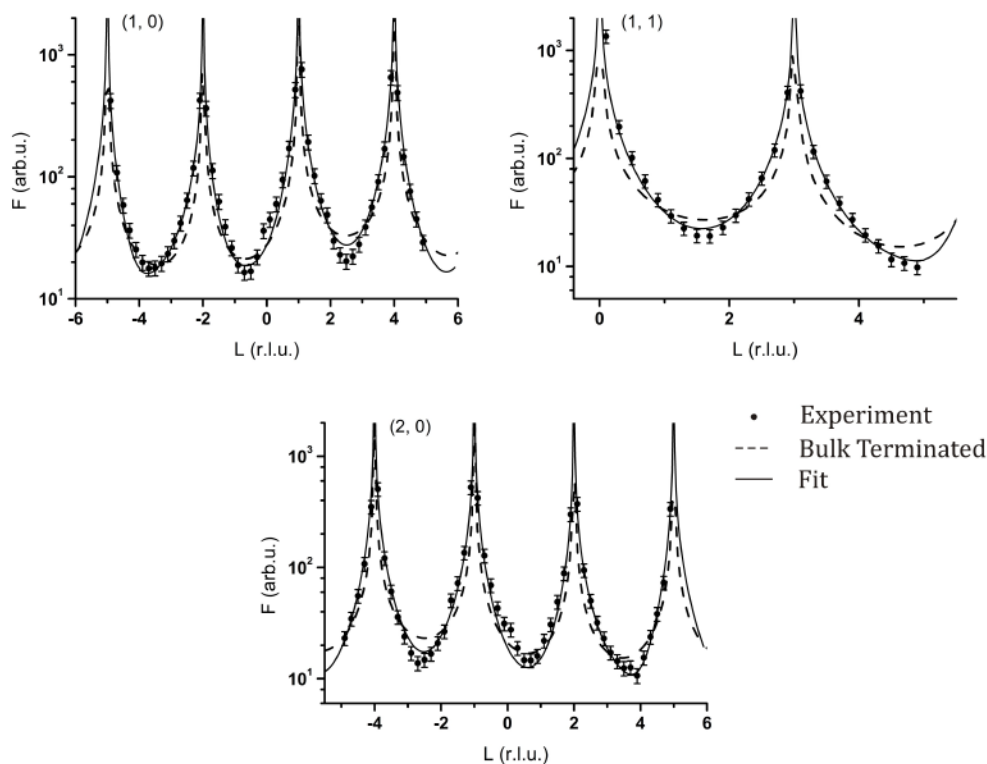
Figure 5.12: Resulting CTRs after fitting with non-anomalous data collected after the cleaning preparation using the fluorite model. The dashed lines show the CTRs of the bulk terminated surface. Straight lines show the CTRs for the best fit. An improvement through the fit is clearly visible. This improvement is also given by the change of the normalized agreement factors from 6.5 to 1.1.

bulk value of 1.41 $Å^2$, which is an increase of 158%. As explained in section 4.1.1, B gives the mean spatial deviation of an atom from its ideal position within the crystal. Keeping that in mind and considering that the presence of Y in the lattice causes the displacements of Zr atoms [35; 25; 24], this is an indication for a considerable increase of yttrium content in the surface compared to the bulk. This interpretation is in line with DFT calculations [49]. It also agrees with another DFT study which predicts the stabilization of the (101) surface of the tetragonal YSZ phase through yttrium accumulation in the surface area [53]. This surface has a similar structure as the (111) orientation of the cubic phase.

The fit parameters lead to a very good normalized agreement factor of

$$\chi_n^2(N) = 1.1 \qquad\qquad (5.4)$$

which is also seen in the resulting CTRs shown in Figure 5.12.

The disadvantages of the fluorite model become obvious when anomalous data is taken to refine the structure. As described in section 4.1.5.4, a combination of either a set of Y-edge and normal data (Y+N) or Zr-edge and normal data (Zr+N) was used for the structure refinements with the values of f' and f'' given in Table 4.1. Debye-Waller factors were taken from [35] given in Table 2.2.

Trying to fit the data after the cleaning preparation, the best agreement was achieved when the same parameters as for the above fit were used. The resulting parameters for the fits using the (Y+N) and (Zr+N) datasets will be discussed in the following.

The displacement of the topmost layers showed differing behavior depending on the used dataset. While both fits are not sensitive to the oxygen displacements, the yttrium atoms show opposite movements of -0.26 Å and 0.044 Å for the (Y+N) and (Zr+N) datasets, respectively. The Zr atoms show agreeing inwards displacements of 0.01 Å and 0.07 Å.

Resulting roughness parameters also affirm the disadvantage of the fluorite model to describe this surface when using anomalous data. β values of 0.36 and 0.27 for the (Y+N) and (Zr+N) datasets lead to roughness values of 1.22 Å and 0.97 Å. However, considering the sensibility of CTRs to roughness parameters, this is an immense contradiction between the fits.

The final prove for the disadvantage of this model is delivered by the static DW factors. The DW factors of Zr are fitted with values of 2.42 and 2.50 in very good agreement and are an indication for an increasing strain in the surface. However, both datasets deliver very big errors for the yttrium DW-factor of 3900% for the (Y+N) dataset and 51% for the (Zr+N) dataset. These contradictory outcomes are also present in the poor resulting normalized agreement factors of

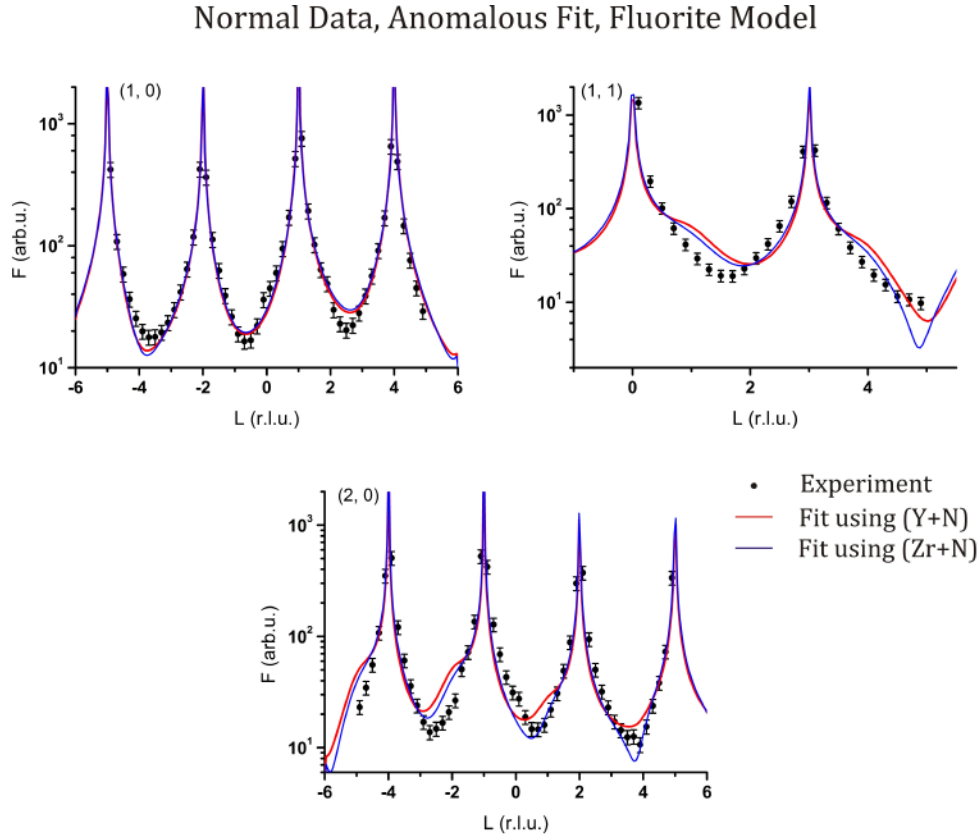$$\chi_n^2(Y+N) = 4.0 \qquad\qquad (5.5)$$

Figure 5.13: CTRs after fitting with a combination of either (Y+N) or (Zr+N) dataset. The red lines show CTRs resulting from the refinement using (Y+N) data and the blue lines CTRs using the (Zr+N) data. Major discrepancies not only in the value but also in the shape of the CTR minima are visible.

and

$$\chi_n^2(\text{Zr} + \text{N}) = 3.6 \qquad (5.6)$$

using equation (4.26) compared to

$$\chi_n^2(\text{Y} + \text{N}) = 5.2 \qquad (5.7)$$

and

$$\chi_n^2(\text{Zr} + \text{N}) = 8.7 \qquad (5.8)$$

for a bulk terminated surface.

The calculated CTRs shown in Figure 5.13, Figure 5.15 and Figure 5.14 also show deviations not only in the values but also in the shapes in case of the non-anomalous
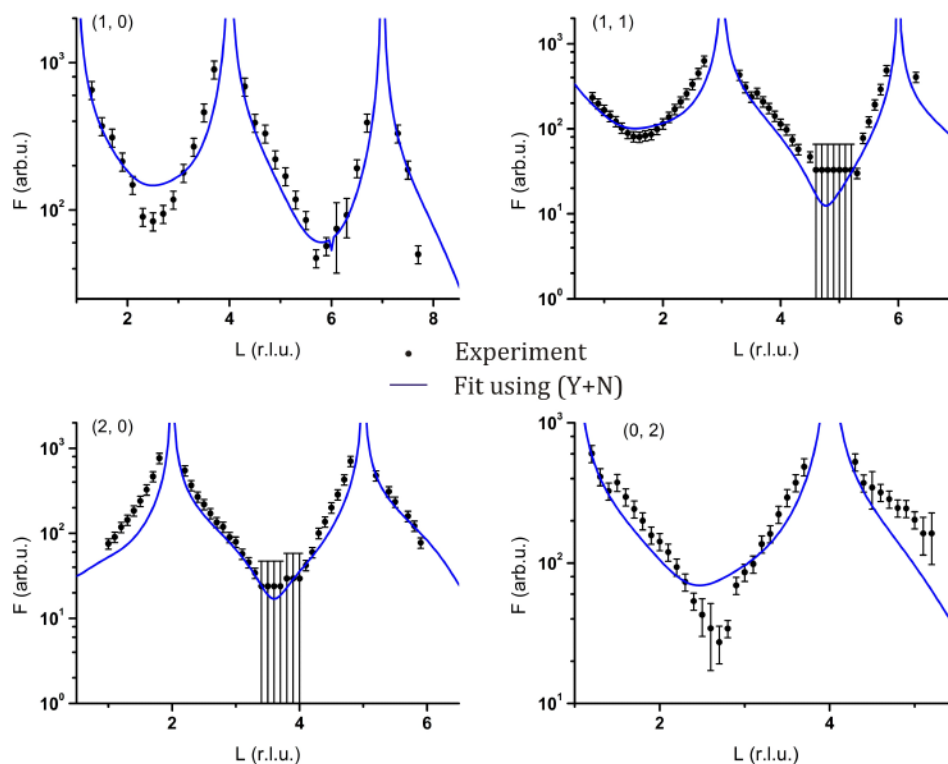
Figure 5.14: The data measured at the Zr-edge after sample preparation (black dots) show deviations from the fit results using a set of Zr-edge and normal data (Zr+N).

data. Looking at the non-anomalous CTRs resulting from the fits, distinct oscillations in the minima are observed especially in the (1, 1) and (2, 0) CTRs. Moreover, the positions of the minima are shifted for almost all CTRs compared to the non-anomalous and anomalous data.

These major differences between experimental data and fit clearly point to a failure of the fluorite model to deliver a proper surface-structure model when using the anomalous data. Hence the Zr-shift model will be the subject of the following.

Figure 5.15: Fits using a set of (Y+N) data (red lines) compared to the experimental data (black dots). A disagreement between fit and experimental data is clearly present, particularly in the minima of the rods.
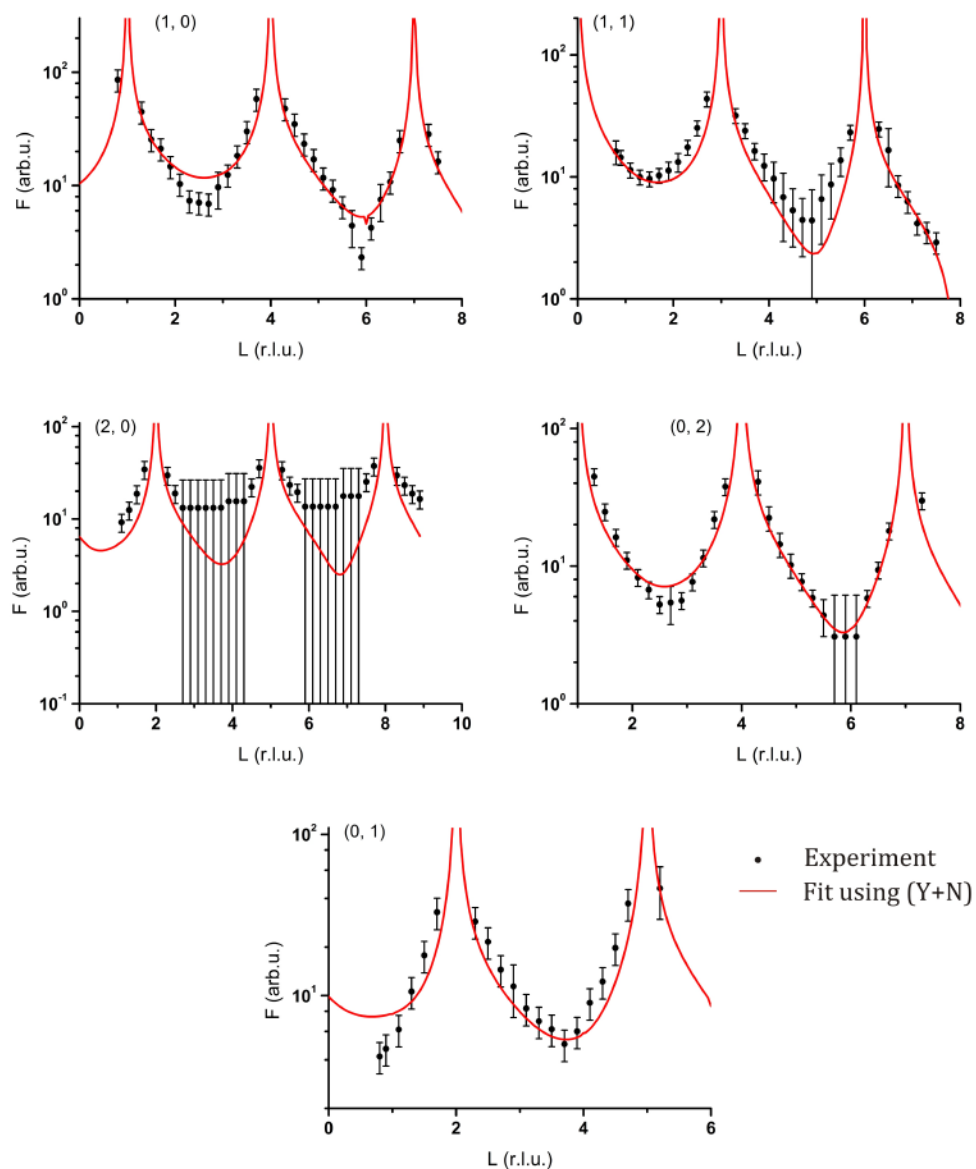
5.1.3.2   Refinements Using the Zr-shift Model

A more consistent description of the surface structure is achieved when the Zr-shift model (see section 2.4.2.2) is used as a starting point instead of the simpler fluorite model. The displacements of the Zr atoms along the [111] directions and the oxygen atoms along the [100] directions lead to eight equivalent Zr atoms and six equivalent oxygen atoms around their original (4a) and (8c) positions, as described in section 2.4.2.2 and illustrated in Figure 2.5. Using the transformation matrix $\mathcal{M}$ given in equation (2.19) to construct a (111)-oriented unit cell and the matrix

$$\mathcal{H} = (\mathcal{M}^T)^{-1} = \begin{pmatrix} 2/3 & 2/3 & -4/3 \\ -2/3 & 4/3 & -2/3 \\ 1/3 & 1/3 & 1/3 \end{pmatrix} \tag{5.9}$$

to transform the coordinates of the atoms [185], the crystallographic unit cell shown in Figure 5.16 results.
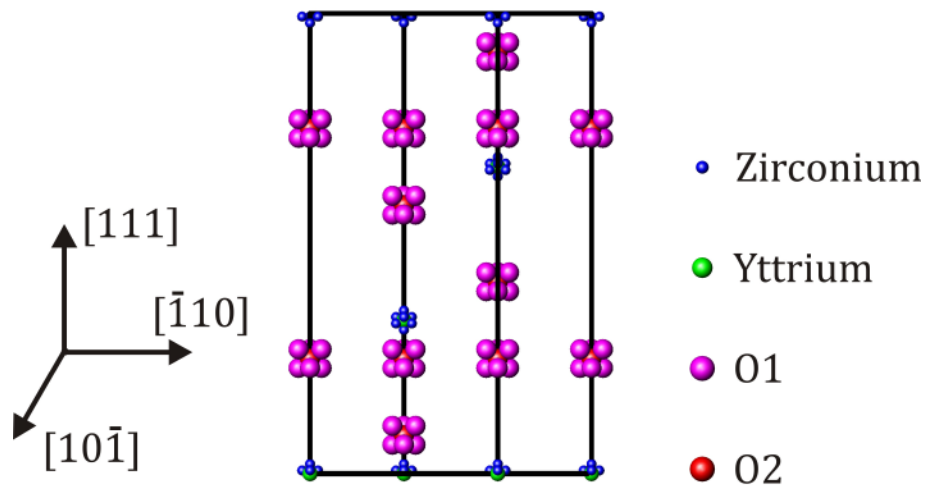

Figure 5.16: Crystallographic way to describe the YSZ(111) unit cell of the Zr-shift model. Eight equivalent Zr and six equivalent O (O1) surround their ideal fluorite positions. This is a quite complicated way to illustrate the structure. Hence the ideal fluorite illustration is used hereafter.

Since this is a fairly complicated way to demonstrate and discuss the coming results, the fluorite structure will be used in the following where oxygen atoms are smaller than metals for illustrating reasons. It is however important to keep in mind that using the Zr-shift model includes dealing with eight equally distributed Zr as well as six additionally and equally distributed O atoms at any position of the coming fluorite illustrations. Note that the eight directions of Zr-shifts are also present at the surface, since the metallic layer is sandwiched between two oxygen layers and the vacancies of these oxygen layers cause the displacements (see section 2.4.2).

The following presents the results for the structure of the YSZ(111) surface after both studied conditions using this model. The oxygen terminated surface shown in Figure 5.17 leads to following normalized agreement factors when using the DW-factors and f' and f'' as given in Table 2.2 and Table 4.1, respectively :

$$\chi_n^2(Y + N) = 5.1 \tag{5.10}$$

and

$$\chi_n^2(Zr + N) = 8.3 \tag{5.11}$$
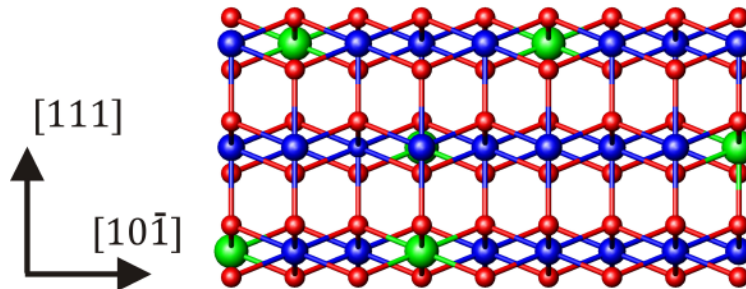
Figure 5.17: Oxygen terminated surface of YSZ(111) used for the fit using the Zr-shift model. The Topmost surface metal layer is sandwiched between two oxygen layers. Hence, all displacements of the Zr atoms present in the bulk are also present at the surface. Note that oxygen vacancies and shifted Zr and O atoms are not drawn. However, they were used for the structure refinements. Moreover, metals are plotted bigger than oxygen atoms for illustration reasons.

for the data after the cleaning preparation and

$$\chi_n^2(Y + N) = 4.1 \qquad\qquad (5.12)$$

and

$$\chi_n^2(Zr + N) = 4.2 \qquad\qquad (5.13)$$

for the data after the heat treatment

Before starting with the refinement results, it is important to point out the origin and direction of the displacements. As the surface-oxygen atoms were not used for the refinements due to a negligible contribution to the SXRD data, the shifts of Zr atoms are discussed here. The types of oxygen atoms O1 and O2 are taken into account for the fits however. As described in section 2.4.2.2, every Zr atom in the
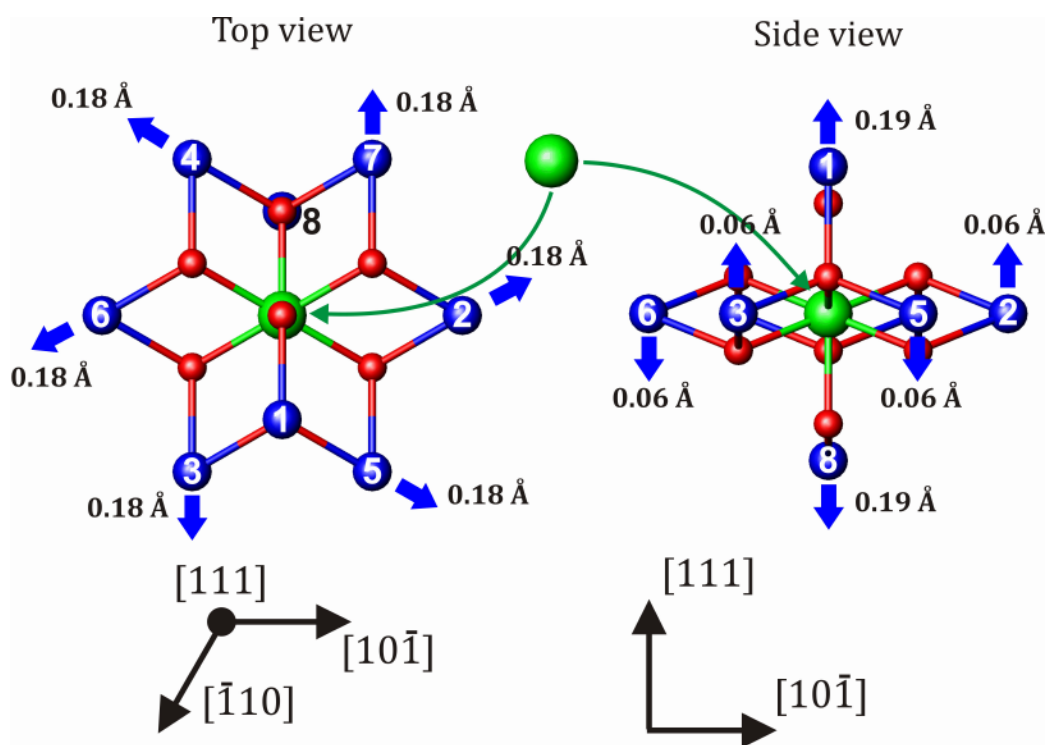
Figure 5.18: Origin of the Zr atoms displacements. When doping with Y, yttrium goes to ideal crystal positions. The surrounding eight Zr atoms which are numerated here, are shifted by 0.19 Å along [111] directions, indicated by blue arrows. Atoms 1 and 8 are only displaced out-of-plane in a (111) surface unit cell. Atoms 2, 3, 4 and 5, 6, 7 are each at the same height and all have the same radial displacement, bearing a threefold symmetry.

cubic ZrO_2 structure is surrounded by eight neighboring Zr atoms as illustrated in Figure 5.18. The replacement of Zr with Y creates oxygen vacancies (and produces strain) which shift the neighboring Zr atoms along [111] directions. These eight neighboring Zr atoms are enumerated in Figure 5.18 and their shifts are discussed briefly, in order to understand the allowed displacements in the fit.

Although all of these atoms are shifted along equivalent directions by 0.19 Å, a distinction is possible when a (111) unit cell is considered. First, it becomes obvious that atoms 1 and 8 are only displaced out-of-plane. The second important point is that atoms 2, 3, 4 and 5, 6, 7 are displaced to the same height each and all have the same radial displacement. Looking at these shifts, it also becomes clear that they bear a three-fold symmetry. In order to conserve the symmetry the same directions of displacement of the according Zr atoms have to be allowed. Yttrium atoms are only allowed to shift out-of-plane. There are therefore seven displacement parameters to fit the positions of one metal layer:

- One parameter for the out-of-plane displacement of Y
- Two for the out-of-plane displacements of Zr atoms 1 and 8
- Two for the out-of-plane displacements of atoms 2, 3, 4 and 5, 6, 7
- Two for in-plane displacements of atoms 2, 3, 4 and 5, 6, 7

Another important point to mention is that no reasonable fitting results were obtained, when surface roughness was taken into account. This means that we are not dealing with a random distribution of atom densities on the surface. Conclusive outcomes were achieved, when the concentration of the topmost metal layer was fitted, meaning that atomic concentrations are proper to describe the surface structure and we are dealing with monolayer variations of densities. Two concentration parameters were used therefore: one for the yttrium and one for the zirconium content of the topmost layer. The zirconium concentration was equally distributed among all eight equivalent Zr atoms, meaning that each position is occupied by

$$\frac{81\%}{8} = 10.125\% \qquad\qquad (5.14)$$

in the bulk.

The low sensitivity of the data to the oxygen concentration and displacements in the surface, made fitting these parameters unnecessary. Statement about the oxygen content in the surface can be made however, as discussed later.

This leads to the following summary for the structure refinement details:

- Roughness does not deliver acceptable results
- Only the topmost metal layer is used
- Nine parameters are necessary therefore:
  - 3 scaling factors for the datasets measured at the three energies
  - 7 displacement parameters
  - 2 concentration parameters for Y and Zr.

5.1.3.2.1 Surface Structure after Cleaning Preparation

The concentration of the metals in the surface region highly correlates with the surface properties of YSZ and is of major interest for understanding processes on the SOFC anode. A modification of the yttria content in the surface was recently reported to increase the activity of a SOFCs anode considerably [22]. For the samples studied here after the cleaning preparation, significant changes of the concentrations and positions of the metallic layer as given in Table 5.2 and Figure 5.18 result.

The fit results deliver a heavily increased yttrium concentration in the topmost layer to 31% compared to a bulk value of 19%. At the same time, they virtually stay at their fluorite position by being displaced 0.03±0.06 Å. This accumulation of yttria at the surface is supported by recent DFT calculations: a systematical study of the surface composition of YSZ and yttria segregations to the surface for several yttria concentrations in the bulk [49], also predicts an yttria enriched surface for the composition and state studied here. It was moreover found that the accumulation of yttrium atoms in the near surface area of (101)-oriented tetragonal-stabilized zirconia stabilizes this surface having a very similar structure to that of (111)-oriented cubic YSZ studied here [53]. A very recent study using the reactive force-field (ReaxFF) Monte Carlo method, also predicts an Y enrichment of the YSZ(111)

surface to be energetically favorable [80] with results in were good agreement with the values found here.

At the same time the Zr concentration dramatically drops to 32% compared to a bulk value of 81% meaning a decrease of 49%. This leads to a metal vacancy concentration Vac_M of

$$Vac_M = 100\% - \text{Concentraion}_Y - \text{Concentration}_{Zr} = 32.3\% \qquad (5.15)$$

A statement about the oxygen concentration at the surface can be made, when considering the chemical composition formula of YSZ given in equation (2.6) as well as those of yttria and zirconia, namely $YO_{1.5}$ and ZrO_2. This leads to a stoichiometric oxygen concentration of

$$Oxy_{stoich} = 0.31 \cdot 1.5 + 0.32 \cdot 2 = 1.105 \qquad (5.16)$$

compared to a value of 1.905 in the bulk given by $Y_{0.19}Zr_{0.18}O_{1.905}$ and thus an oxygen vacancy concentration of

$$Vac_{Oxy} = \frac{1.905 - 1.105}{2} = 0.40 \ \hat{=} \ 40\% \qquad (5.17)$$

Such high oxygen vacancies are supported by recent publications. An STM study of this surface clearly shows a high density of dark spots at the surface [49] that is correlated to defects. Since the bright imaged spots are oxygen atoms, the dark defects can be attributed to oxygen vacancies. A reduction of anions on the surface under this condition is also reported by DFT calculations [49].

The displacements of the atoms in the topmost metal layer are illustrated in Figure 5.19. Since we have eight Zr atoms to deal with, these are numerated in the figure as well, indicating their original displacements. Note that a total Zr occupancy of 32% leads to a concentration of 4% of each of the eight positions in the crystallographic unit cell (see Figure 5.16). The shifts are always given with respect to the ideal (4a) position in the fluorite structure. As displacements of Zr atoms 1 and 8 did not influence the fits, these two atoms were fixed at their bulk positions at a distance of 0.19 Å from the ideal (4a) positions. All other Zr atoms were displaced in the fits with the following results.

Table 5.2: Concentrations of metals after the preparation and resulting metal-vacancy and stoichiometric oxygen-vacancy concentrations. The given results are an average of both fits made with the (Y+N) and (Zr+N) datasets

	Fit (Y+N)	Fit (Zr+N)	**Result**
Y Concentration	26.8%	34.9%	30.8±4%
Total Zr Concentration	46.4%	17.6%	32.3±14%
Metal Vacancy Concentration	26.8%	47.5%	36.8±10%
Stoich. Oxygen Vacancy Concentration	28.8%	51.5%	39.9±11%

Atoms 5, 6 and 7 are shifted further away from their ideal positions compared to the bulk, both in-plane and out-of-plane which results in a distance of 0.46 Å to the (4a) sites. Atoms 2, 3 and 4, however, are shifted less pronounced and the distance to the ideal position of 0.18 Å is virtually remaining as in the bulk. Hence, 20% of the Zr atoms rest at their bulk positions while 12% are shifted further away. It is interesting to mention that those Zr atoms being below the ideal position in the bulk, meaning atoms 5, 6, and 7 (see Figure 5.18) are shifted further away in the surface while the rest is more or less static. This is due to the much lower oxygen concentration in the topmost layer, while the concentration of the oxygen layer below the topmost metallic layer remains at bulk level. Hence, those Zr displacements caused by the topmost oxygen vacancies, i.e. Zr atoms shifted towards the bulk are displaced more distinct.

These displacements indicate a more disordered arrangement in the surface than in the bulk. Moreover, the average displacement of 0.29 Å of the Zr atoms is bigger than 0.19 Å in the bulk pointing to a higher strain and oxygen vacancy concentration.

Considering the presence of Y to be responsible for the strain and the creation of oxygen vacancies as described before (see for instance sections 2.4.2.2 and 5.1.3.2), the increased shifts of Zr atoms compared to the bulk consistently correlate with the increase of yttrium concentration in the surface.

It is important to point out that the data used for the fits at this condition, were collected at two different beam lines from two different samples. Although the
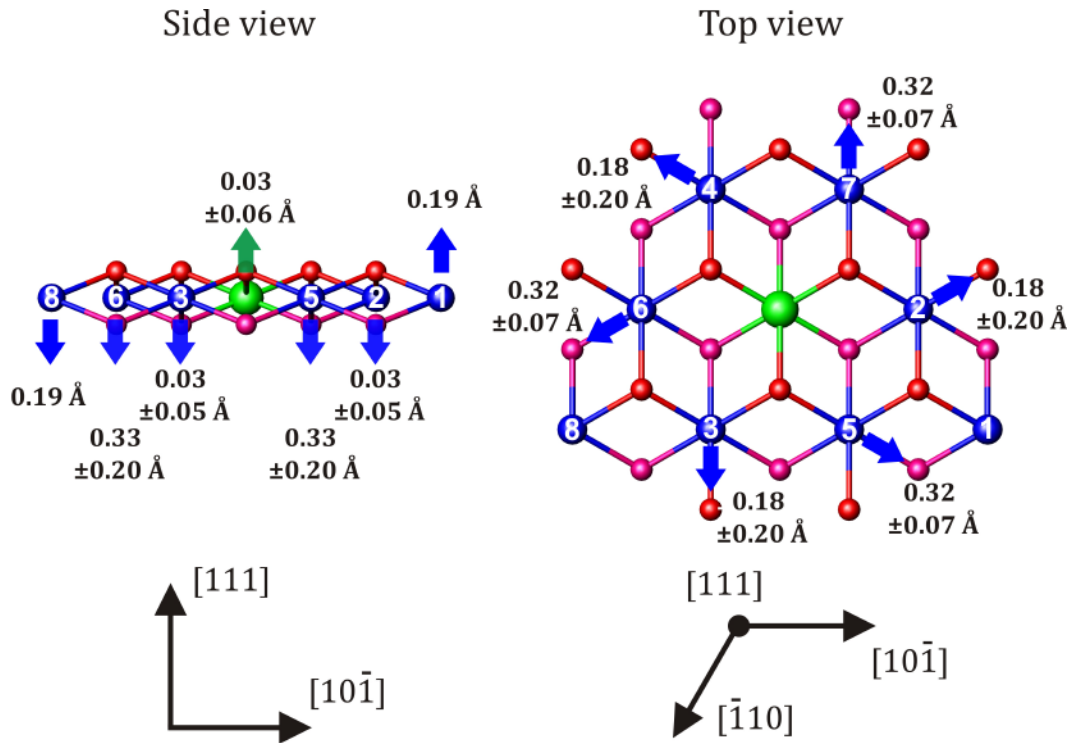
Figure 5.19: Displacements of the atoms in the topmost metallic layer after the cleaning preparation. The lower oxygen layer is painted pink for illustration reasons. The shifts are given with respect to the ideal fluorite (4a) positions. Five Zr atoms, namely 1, 2, 3, 4 and 8 keep their bulk positions and have distances of 0.19 Å (within the errors) to the ideal positions. The other three Zr atoms are shifted further away, both out-of- and in-plane. The average displacement of the Zr atoms is consistent with the increase of yttrium, which remains at its (4a) position.

samples were prepared following the same recipe given in section 5.1.1, the resulting agreement factors of

$$\chi_n^2(Y + N) = 2.7 \qquad (5.18)$$

and

$$\chi_n^2(Zr + N) = 3.0 \qquad (5.19)$$

using equation (4.26) for the (Y+N) and (Zr+N) fits, respectively, affirm the surfaces studied during the beam times to be slightly different which also leads to rather big errors of the resulting fitting parameters. The agreement factors are nevertheless superior to those achieved by the refinements using the fluorite structure.

The small deviations of the two surfaces are also obvious when comparing the resulting CTRs from the two fits shown in Figure 5.21, Figure 5.22 and Figure 5.23. Major statements within the errors can be made however and show the surface to be significantly different in composition and structure compared to the bulk.

5.1.3.2.2 Surface Structure after Heat Treatment

In order to study the compositional and structural changes of the surface under conditions relevant for SOFCs, the sample was heated to 1000°C under reductive conditions. After this treatment the surface structure changes considerably.

Table 5.3 shows the metal concentrations and the resulting vacancies. The concentration of yttrium remains virtually constant within the error bars. This result is in agreement with an experimental study on the macroscopic bulk changes of YSZ. In this study, yttria clusters within the YSZ bulk are discovered to be nearly static when the material is exposed to temperatures up to 1500°C [24]. Hence yttrium atoms in the bulk are not mobile when the material is heated. The results obtained point to the same behavior for surface Y atoms. This statement is supported by the displacement of the yttrium atoms of 0.01±0.05 Å and thus no shift from the initial position.

At the same time, the Zr concentration is rising considerably to a value of 50%. The segregation of Zr to the surface under reductive heating conditions has been reported before in both, experimental and theoretical studies [49; 51]. The increase of Zr in the surface area after the heat treatment is also qualitatively observable in

Table 5.3: Concentrations of metals after the heat treatment and resulting metal-vacancy and stoichiometric oxygen-vacancy concentrations. While the Y concentration is remaining almost constant, there is a considerable increase of the Zr concentration.

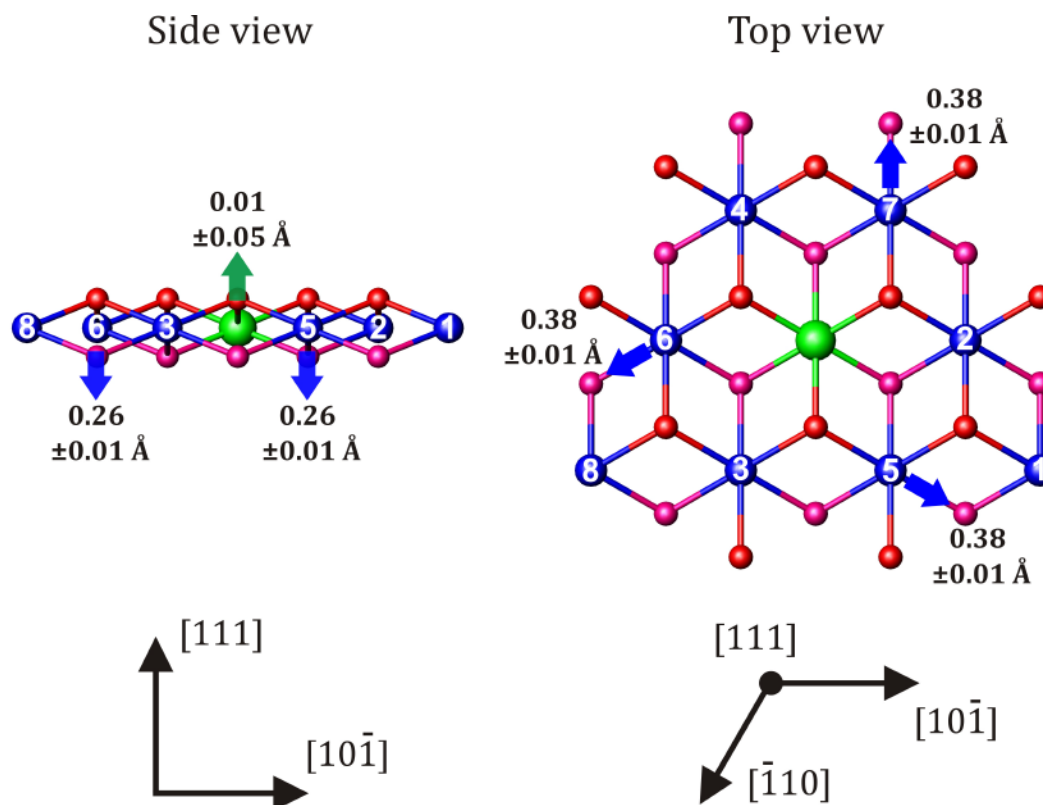|	Fit (Y+N)	Fit (Zr+N)	**Result**
Y Concentration	31.2%	24.9%	28.1±3%
Total Zr Concentration	49.6%	50.4%	50.0±0.4%
Metal Vacancy Concentration	19.2%	24.7%	21.9±3%
Stoich. Oxygen Vacancy Concentration	22.3%	26.2%	24.2±2%

Figure 5.20: Displacements of the atoms in the topmost metallic layer after the heat treatment. The shifts are given with respect to the ideal fluorite (4a) positions. The Y atoms at the surface virtually remain at their bulk positions. On the contrary significant changes of the Zr positions are observed. Zr atoms 1 to 4 and 8 occupy ideal fluorite (4a) sites, while atoms 5, 6, and 7 move closer to the (4a) sites out-of-plane and keep their distances in-plane, compared to the situation after the sample preparation. The average shift of the Zr atoms is thus decreased notably.

the measured anomalous data. Taking a look at Figure 5.9 showing the data measured at the Y-edge after the initial cleaning preparation (lower CTRs) and the heat treatment (upper CTRs) a clear increase of the intensity in the minima is observable. Neglecting dispersion effects and thus f'' in equation (4.12) and knowing that roughness does not explain the data, this is an indication for the increase of the non- anomalously diffracting atoms in the surface and thus a distinct increase of Zr concentration.

Although the segregation of Zr has been reported before, the results of this fit are able to deliver a physical reason for such a behavior. At the state before the heat

treatment a high number of metal vacancies at the surface are present. This leads to a decrease of strain in the surface layer compared to the bulk which makes the surface energetically more favorable for Zr atoms. Once Zr atoms have a sufficient mobility, as they do in this case through thermal energy, they prefer to migrate to the surface. Moreover, the oxygen-ion-conducting property of YSZ at elevated temperatures leads to a compensation of oxygen vacancy sites in the topmost oxygen layer which allows the creation of zirconia. This simple train of thoughts delivers a satisfying explanation for the increase of Zr in the surface region.

The motivation for the Zr atoms to segregate to the surface is fully supported by the positions of the Zr atoms shown in Figure 5.20. The eight different types of shifted Zr atoms present after the cleaning preparation reduce to four after the heat
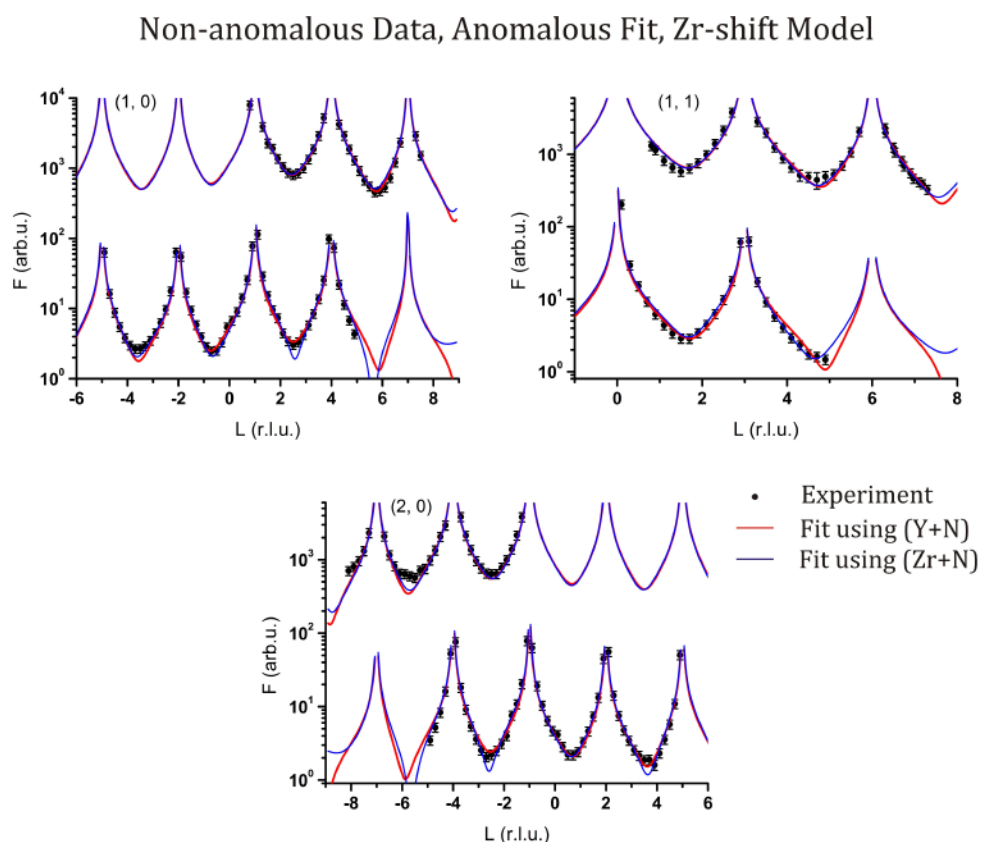

Figure 5.21: Non-anomalous CTRs using the Zr-shift model and either the (Y+N) (red lines) or (Zr+N) (blue lines) dataset. The lower and upper CTRs and data correspond to the conditions after the cleaning preparation and the heat treatment, respectively.

treatment. Atoms 1 to 4 and 8 thereby occupy ideal fluorite (4a) positions, which is consistent with the above argumentation basing on reduced strain and increasing oxygen concentration in the topmost layer. Consequently, the remaining Zr atoms, namely atoms 5, 6 and 7 are moving closer to the (4a) positions out-of-plane and nearly keep the distance in-plane compared to the state before. Hence, these atoms have also moved closer to the (4a) positions due to a decrease of oxygen vacancies. Thus the remaining strain and oxygen vacancies in the surface, do not allow all of the Zr atoms to move back towards their ideal positions. These displacements point to a higher order in the surface than in the state before and even than in the bulk.

The yttrium and zirconium concentrations of 28.1% and 50.0%, respectively, lead to a reduced metal vacancy concentration of 22% in the topmost layer using equation (5.15). This leads to a reduced stoichiometric oxygen vacancy concentration of 24% in the surface, calculated following the same steps as in equations (5.16) and (5.17) and in line with the above argumentation.

The very good agreement of the results derived from the fits using (Y+N) and (Zr+N) datasets, leads to small errors of the fitting parameters and excellent normalized agreement factors of

$$\chi_n^2(\text{Y} + \text{N}) = 1.3 \tag{5.20}$$

and

$$\chi_n^2(\text{Zr} + \text{N}) = 1.2 \tag{5.21}$$

using equation (4.26). These results support the assumption that the rather high errors of the fits after the sample preparation originate from two slightly different surfaces studied during two different beam lines. The supremacy of the fitting results for the condition after the heat treatment is also visible in the resulting fits shown in the upper part of the graphs in Figure 5.21, Figure 5.22 and Figure 5.23.

Note that at X-ray energies of 16 keV anomalous diffraction effects have to be taken into account. Since the surface is mainly covered with Zr and the anomalous form factor corrections lead to an effective decrease of one electron per atom (see section 4.1.3), non-anomalous diffraction can be assumed here within the errors.

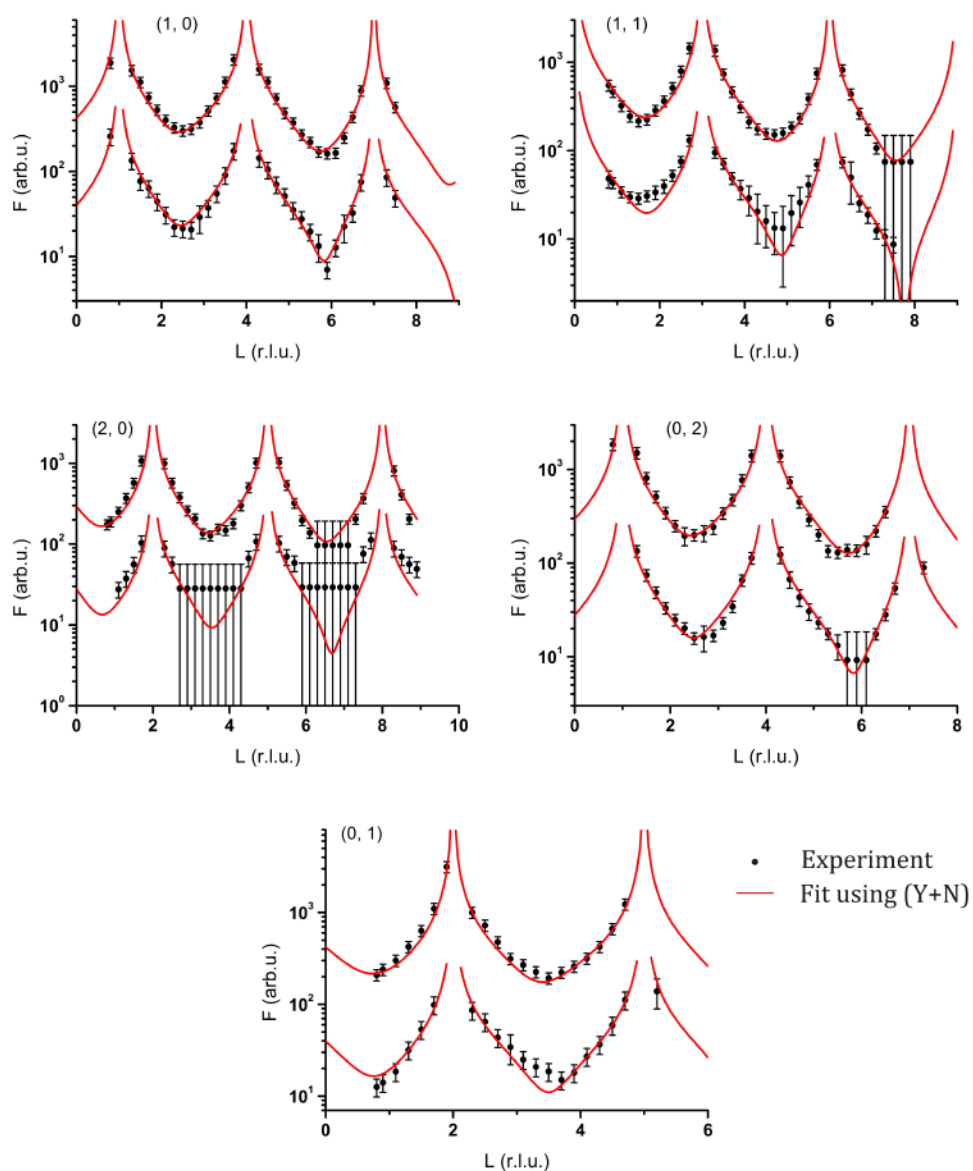Y-edge Data, Anomalous Fit, Zr-shift Model

Figure 5.22: A very good agreement between the data (black dots) and simulated CTRs (red lines) is observed, when using the set of (Y+N) data and the Zr-shift model, for both conditions: after the cleaning preparation (lower part of graphs) and after the heat treatment (upper part of graphs).
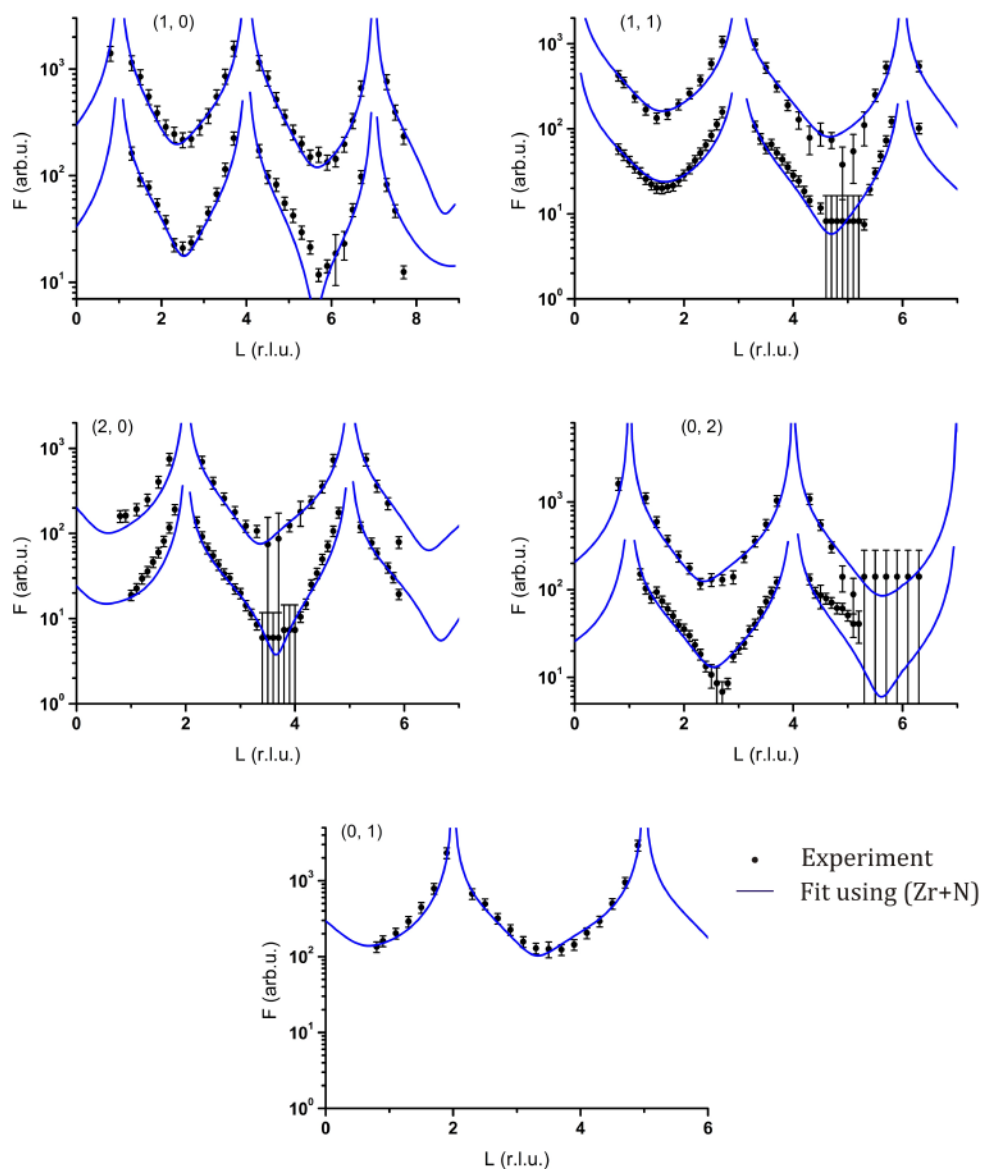
Figure 5.23: The excellent agreement using the Zr-shift model is also true when taking the (Zr+N) data set. There are very small deviations between the experimental data (black dots) and the simulated CTRs at the conditions after the cleaning preparation (lower part of graphs) and after the heat treatment (upper part of the graphs).

5.1.4   Summary

Non-anomalous and anomalous SXRD measurements at the Y- and Zr-edge were performed to resolve the atomic structure and composition of the YSZ(111) surface. Two oxygen terminated models were chosen as starting points for structure refinements: the ideal fluorite model and the Zr-shift model (see section 2.4.2).

The ideal fluorite structure delivers a good fit, when only non-anomalous data is taken into account. This fit points to an accumulation of Y at the surface through an increased static Debye-Waller factor of the topmost metallic layer. When including anomalous data, this structural model is unable to deliver satisfying results.

Consistent and much more precise results are achieved, when using the Zr-shift model as a starting point and refining the concentration and position of the topmost metallic layer. For the state after the cleaning preparation where the sample is annealed at 400°C and 10^{-5} mbar O_2 for 120 minutes, a significant increase of Y concentration from 19% in the bulk to 31% is found, indicating an yttria enriched surface. At the same time a depletion of Zr to 32% compared to 81% in the bulk results in a high metal vacancies concentrations of 37% and thus a stoichiometric oxygen vacancies of 40%. A high distorted structure of the surface follows from the big displacements of the Zr atoms which can be explained by the weaker bonding of the zirconium atom to the topmost oxygen layer and an increased strain due to the accumulation of yttria.

After a heat treatment at 1000°C and reductive conditions, the structure changes significantly. While the Y concentration remains constant, the Zr concentration rises to a value of 50%. This increase is explained by the mobility of Zr atoms at such high temperatures that allow them to occupy sites at the surface where a lower strain than in the bulk is present. The reduced strain also results in a higher order, meaning that all of the Zr atoms move towards ideal (4a) fluorite sites and most of them indeed occupy these positions. The increased metal concentration at the surface leads to a decrease of oxygen vacancy concentration. This fact nicely demonstrated the oxygen ion conductivity of YSZ that allows oxygen atoms in the bulk to move to the surface. The increased oxygen concentration can also be used as

an argument to explain the decreased displacements of the Zr atoms due to a more balanced bonding to the two oxygen layers below and above the topmost metallic layer.

It is important to point out that the result using the fluorite model and non-anomalous data, does not disagree with the more precise results gained by using the whole datasets and the Zr-shift model. The main result of the first fit is the increase of the static Debye-Waller factor of topmost Zr atoms. This statement is supported by the latter refinement through an increase of the Y content and a more distorted arrangement of Zr atoms.

5.2   Growth and Shape Change of Nickel Nanoparticles

Nickel (nano) particles grown on oxide substrates are of interest as model systems in science [105]. They are also used in a number of applications with nickel nanoparticles (NP) on a YSZ substrate being one of the most important model system for SOFC anodes [1; 3]. In most of these systems, Ni is grown on the substrate under vacuum or UHV conditions [186].

This part of the work is about the growth of nickel NPs on the previously studied YSZ(111) surface under UHV condition. After the characterization of the PVD grown nickel NPs, the results about the shape changes after a heat treatment and the exposure to methane and oxygen are discussed.

5.2.1 Growth

The data presented in the following were collected during two experiments under UHV conditions at ANKA using an X-ray energy of 10 keV (see section 4.1.4) and YSZ(111) samples with 9.5% mol yttria with a miscut smaller than 0.1° which have the dimensions 10x10x1 mm. Data used for the initial shape determination and growth of the NPs were collected with the Pilatus detector and data used for the shape changes were measured with the point detector (see section 4.1.4).

Nickel was grown using an electron beam evaporator as described in section 4.3. Prior to each evaporation, the samples were prepared just as described for the surface structure measurements at 400°C and 10^{-5} mbar O_2 for 120 minutes, resulting in the same surface structure, as CTR measurements prove (see Figure 5.24).

The procedure to grow nickel NPs was the same at both experiments

- Substrate temperature: T = 350°C
- Evaporation time: 30 minutes
- Flux current: ~25 nA
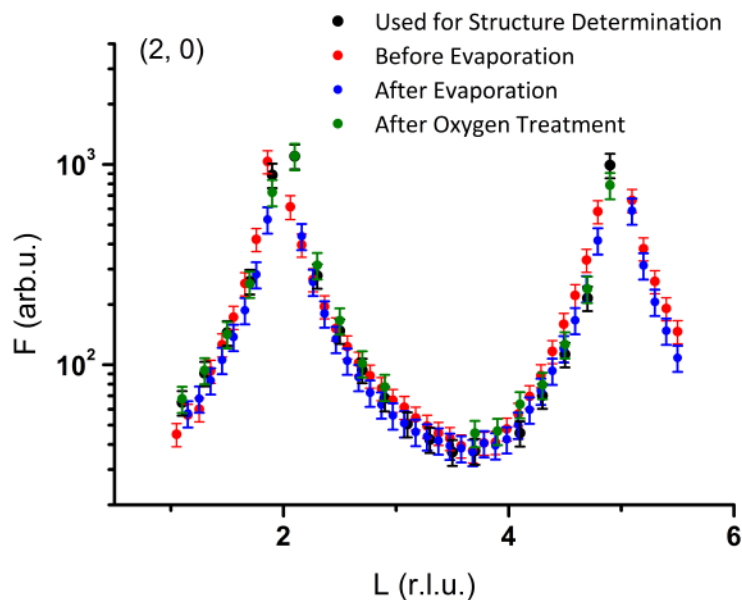- Growth rate: ~0.19 nm/minute

Figure 5.24: (2, 0) CTR measured for the structure determination and prior to nickel growth show no difference. Hence we are facing the same surface structure as determined in the previous section. The same CTR after evaporation and the oxygen treatment (see section 5.2.3.3) also shows no changes. This means that the nickel NPs do not cause a structural change at the interface.

CTR measurements after evaporation and after the oxygen treatment described in section 5.2.3.3 do not indicate considerable changes of the YSZ(111) surface as shown in Figure 5.24 meaning that Ni NPs do not displace the surface atoms of the substrate.

5.2.2 Particle Shape

AFM images taken *ex-situ* after the SXRD experiments prove the growth of nickel nanoparticles on the YSZ(111) surface. Such an image is shown in Figure 5.25. Particles are clearly observed and typical heights of 3 nm can be derived from line profiles along them.

Another indication of the existence of NPs is given by nice and clear thickness oscillations of the reflectivity measurements after the growth of nickel as shown in Figure 5.26. The coverage of the surface can be determined by not only fitting the
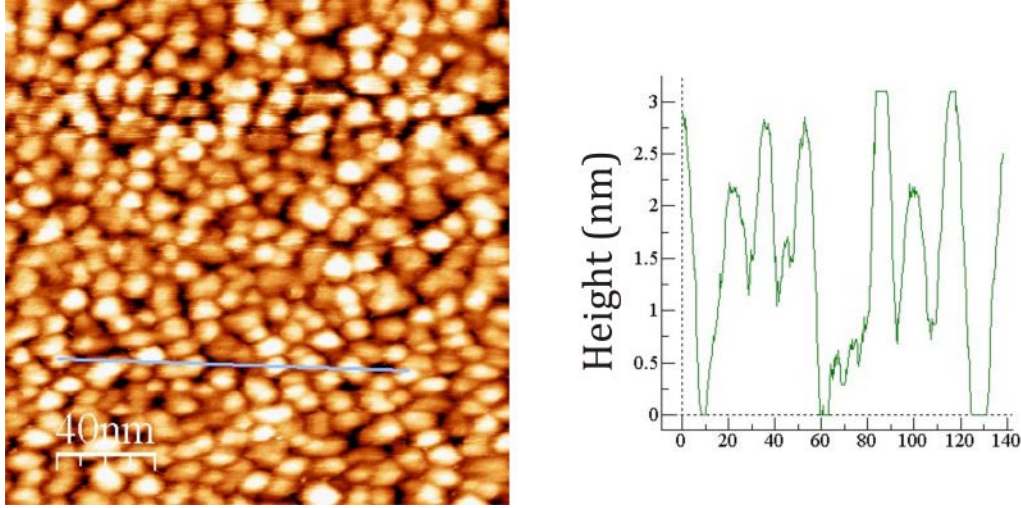
Figure 5.25: Left: AFM image of a nickel evaporated YSZ(111) surface (left). Nanoparticles are clearly visible. Line scans along the NPs (right) reveals particle heights in the range of 3 nm.

thickness of a Ni layer on the YSZ surface, but also its electron density given by δ in equation (4.28). The 2δ value of Ni at X-ray energies of 10 keV is

$$2\delta_{\mathrm{Ni}}(10 \,\mathrm{keV}) = 3.44 \cdot 10^{-5} \tag{5.22}$$

The coverage Θ of the surface with NPs can thus be determined by

$$\Theta: \frac{2\delta_{\mathrm{Fit}}}{2\delta_{\mathrm{Ni}}} \tag{5.23}$$

A very good fit of the reflectivity curve was obtained with a model of two nickel layers with a total thickness d of (see appendix B for reflectivity fitting parameters)

$$d = 36.3 \,\text{Å} \tag{5.24}$$

and the 2δ value of (see appendix B)

$$2\delta_{\mathrm{Fit}} = 2.06 \cdot 10^{-5} \tag{5.25}$$

Combining equations (5.22) to (5.25) leads to a coverage of
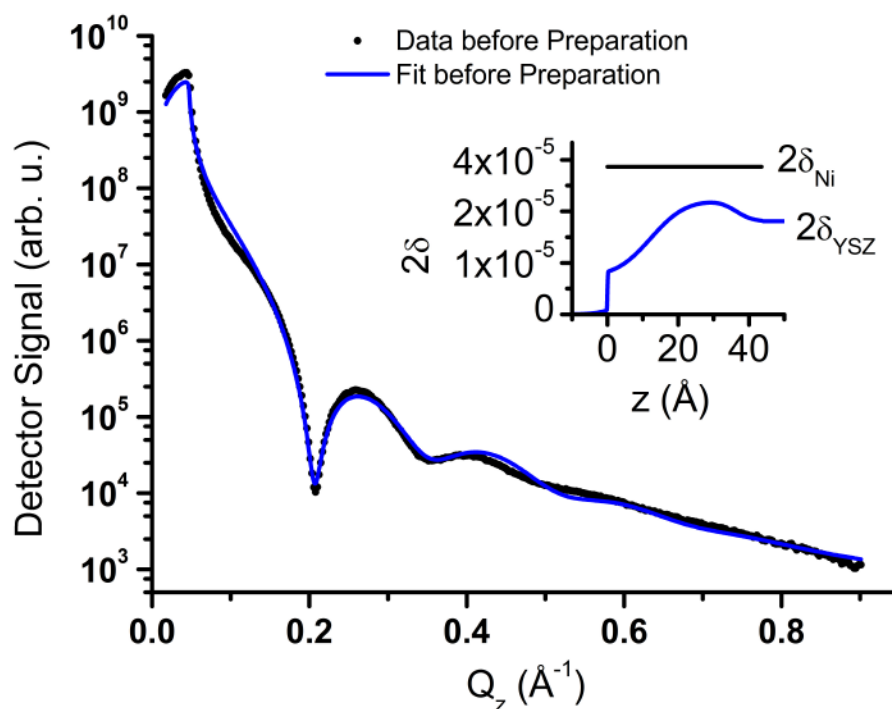
$$\Theta = 59.7\% \tag{5.26}$$

Figure 5.26: Reflectivity curve measured after nickel evaporation. The oscillations are a clear indication for a nickel layer on the YSZ surface. The thickness and coverage of this layer are determined to be 36 Å and 60%, respectively, in very good agreement with the AFM measurements. The inset shows the density profile resulting from the fit.

The thickness derived from this fit is thus in a very good agreement with the results from the AFM. Moreover, the coverage of about 60% is also consistent with the AFM images as shown in Figure 5.25. Hence, these values are supported by two different experimental methods and can be considered correct.

A top view at the (111) surface oriented unit cell of YSZ with the axis lengths of 3.61 Å suggests a cubic growth of nickel with a small mismatch of

$$\text{Mismatch} = \frac{3.54 \text{ Å}}{3.61 \text{ Å}} \triangleq 4.4\% \tag{5.27}$$
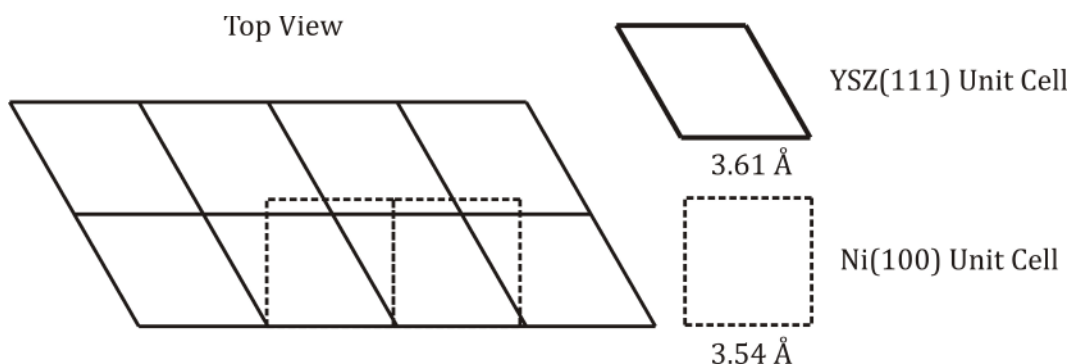
Figure 5.27: Top view on the YSZ(111) (solid) and Ni(100) (dashed) unit cells. The lattice lengths of 3.61 Å and 3.54 Å for YSZ(111) and Ni(100) lead to a lattice mismatch of 4.4% and suggest a cubic growth of (100)-oriented nickel NPs. This epitaxy is not present however.

where the lattice constant of Ni is 3.54 Å, and hence a (100) orientation of the NPs. Such a scheme is shown in Figure 5.27.

For simplifying the identification in the following, peaks will be subscripted with:
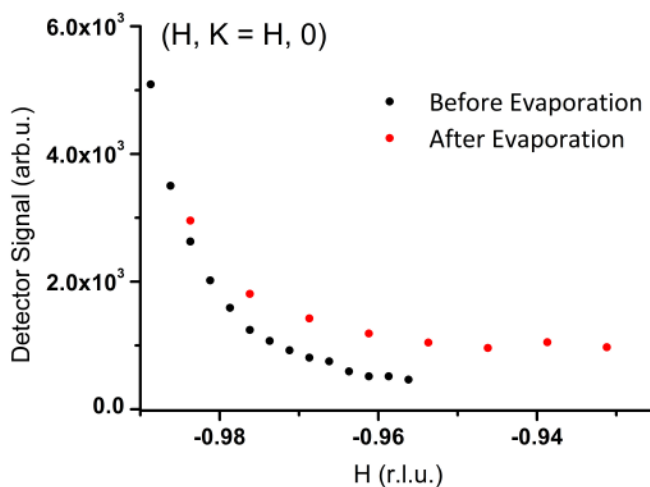
Figure 5.28: Line scans along the H-direction where the $(-1, -1, 0)_{Ni-bul}$ Bragg-Peak is expected at H = −0.98, before starting with the evaporation and after the evaporation. No peak is observed at −0.98 meaning that nickel is not growing (100)-oriented. The increase of signal in the left part is due to the substrate (−1, −1, 0) Bragg-Peak. The allover increase of signal after the evaporation is caused by nickel fluorescence.

- Ni-bul, if the Ni bulk coordinates are used

A Ni $(-1, -1, 0)_{Ni\text{-}bul}$ Bragg-Peak is hence to be expected at the reciprocal coordinates $(-0.98, -0.98, 0)$ of the YSZ(111) substrate since the reciprocal ratio of the used substrate coordinates and the bulk Ni coordinates is

$$\frac{1/3.61\,\text{Å}}{1/3.54\,\text{Å}} = 0.98 \qquad (5.28)$$

Hence, scans along the H-K-direction close to L=0 were performed to observe the growth of this orientation. The scans before starting with the evaporation and after the evaporation are shown in Figure 5.28. They indicate that although there is a small lattice mismatch between (100)-oriented Ni and the substrate, such an orientation does not grow. The allover increase of the intensity after the evaporation is due to fluorescence of Ni at 10 keV X-ray energies.

The $(-1, -1, 0)_{Ni\text{-}bul}$ Bragg peak is instead found at the substrate reciprocal
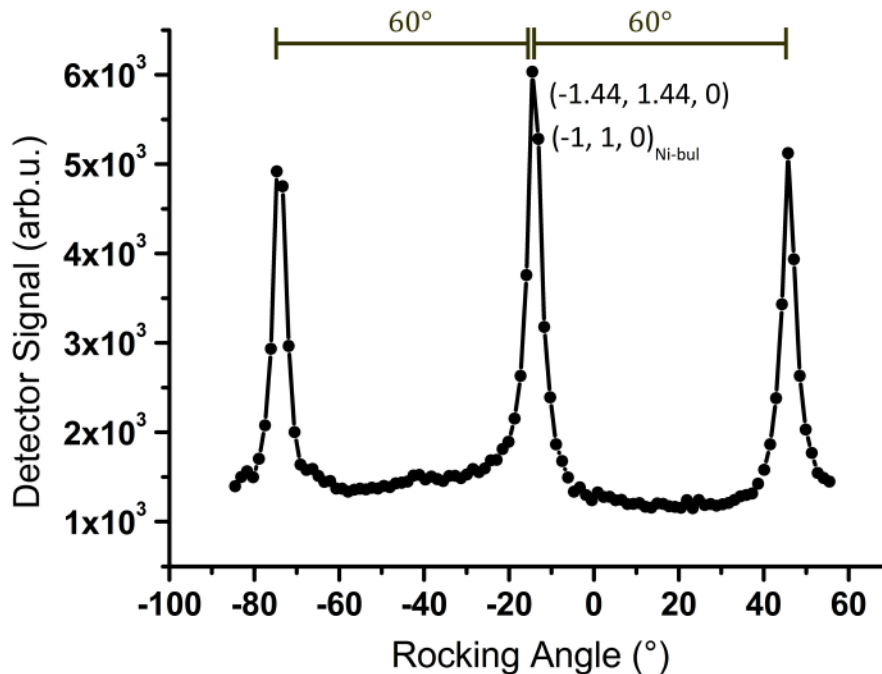
Figure 5.29: Rocking scan around the $(-1, 1, 0)_{Ni\text{-}bul}$ Bragg peak reveals further peaks at 60° distances pointing to a (111) orientation of the grown nickel NPs.

position (-1.44, -1.44, 0). A rocking scan around this peak shows further peaks at 60° distances (see Figure 5.29) pointing to the existence of (111)-oriented NPs. A (111)-oriented Ni unit cell has the dimensions

$$a_{Ni(111)} = b_{Ni(111)} = \frac{a_{Ni}}{\sqrt{2}} = 2.503 \text{ Å}$$

(5.29)

$$c_{Ni(111)} = \sqrt{3} \cdot a_{Ni} = 6.13 \text{ Å}$$

and

$$\alpha = \beta = 90°, \gamma = 120°$$ (5.30)

The ratio of the reciprocal (111)-oriented Ni lattice and the YSZ(111) substrate lattice is hence

Reciprocal In-plane Map

Figure 5.30: Reciprocal in-plane map of (111)-oriented nickel grown epitaxially on the YSZ(111) substrate.

$$\frac{1/2.503\,\text{Å}}{1/3.61\,\text{Å}} = 1.442 \qquad\qquad (5.31)$$

and thus in prefect agreement with the Ni peak found at the (-1.44, 1.44, 0) substrate coordinates.

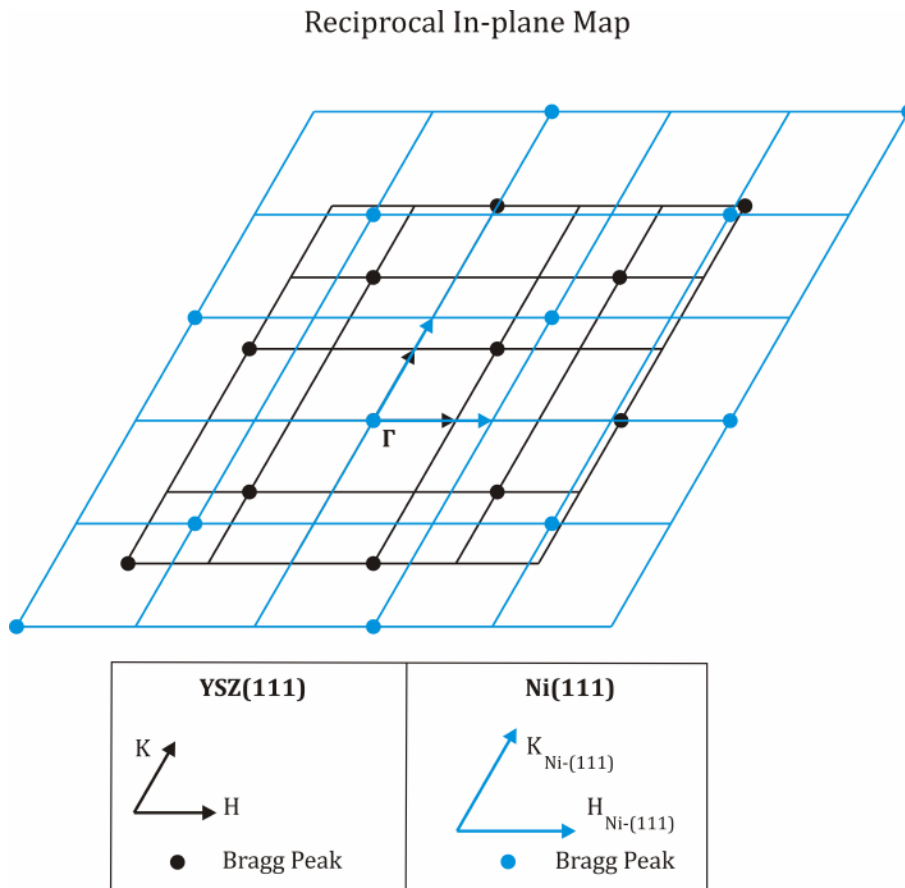Introducing a new set of coordinates for (111)-oriented Ni shown in the reciprocal in-plane lattices of YSZ(111) and (111)-oriented Ni in Figure 5.30, subscribed with Ni(111) results in three reciprocal coordinates for a simple identification:

- no subscription is applied for the YZS-(111) substrate coordinates used for the measurements
- Ni-bul subscription is used for the Ni bulk coordinates
- Ni(111) subscription is used for the coordinates of (111)-oriented nickel.

The epitaxy of the (111)-oriented Ni grown on the YSZ(111) surface is depicted in Figure 5.31. The structure of both, the substrate and Ni(111), lead to the same lattice mismatch along both in-plane directions. As illustrated, three unit cells of Ni(111) fit on two unit cells of YSZ(111) with a mismatch of

$$\text{Mismatch} = \frac{3 \cdot 2.503\,\text{Å}}{2 \cdot 3.61\,\text{Å}} \,\hat{=}\, 4.0\% \qquad\qquad (5.32)$$

along both directions and thus lower than for the (100)-oriented epitaxy.
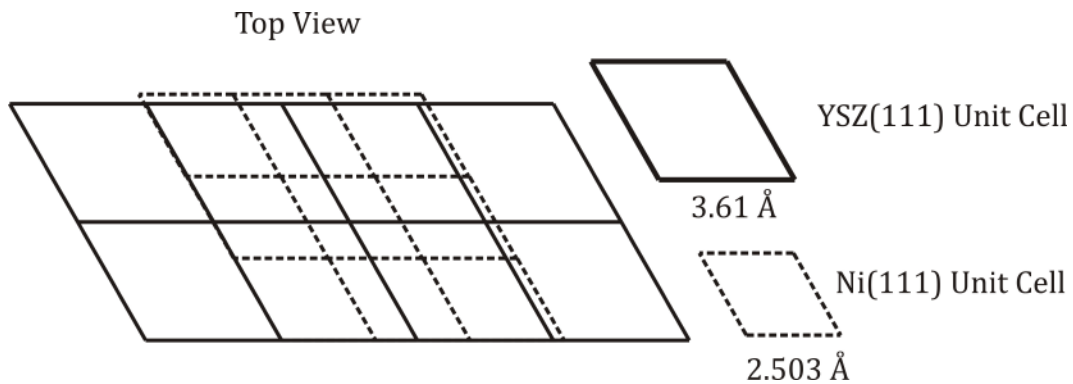

Figure 5.31: Illustration of the epitaxy of Ni(111) on YSZ(111). Three unit cells of Ni(111) fit on two unit cells of YSZ(111) with a mismatch of 4% along both in-plane directions.

The (111) orientation of the nickel NPs is indeed supported by a number of measured reciprocal maps. One of these maps is shown in Figure 5.32. A Bragg peak is detected at the reciprocal position (0, −1.44, 1.44) which correspond to the (0, −1, 1)$_{Ni(111)}$ Bragg peak of (111)-oriented nickel.

An additional peak is observed at the position (0, −1.44, 2.88), which is a (0, −1, 2)$_{Ni(111)}$ Bragg peak and can be assigned to laterally coexisting (111)-oriented nickel twin NPs with an inverse stacking sequence [90]. There are thus particles with the stacking sequence ABCABC and coexisting particles with the stacking sequence CBACBA (see section 2.6.1).

Figure 5.33 shows another reciprocal map measured with the Pilatus detector where six peaks are observed. The peaks appearing at (−1.44, 0, 1.44) and (−1.44, 0, 2.88) can be assigned to the (−1, 0, 1)$_{Ni(111)}$ and (−1, 0, 2)$_{Ni(111)}$ Bragg peaks of (111)-oriented Ni and its twin. The intense peak at (−1, 0, 2) is the according Bragg peak of
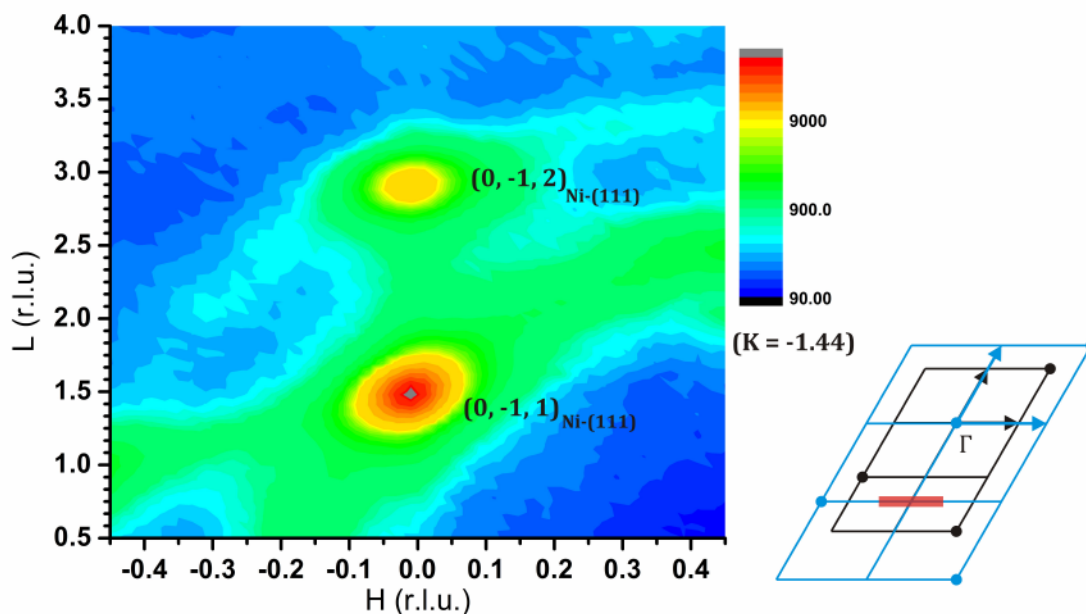
Figure 5.32: Reciprocal H-L mesh scan at K = -1.44. The color code gives the measured intensity. The sketch on the right side gives the in-plane projection of the measured area. Peaks are observed at the positions (0, −1.44, 1.44) and (0, −1.44, 2.88) which are assigned to a (0, −1, 1)$_{Ni(111)}$ and a (0, −1, 2)$_{Ni(111)}$ Bragg peaks. There are hence two laterally coexisting twins with inverse stacking sequences.
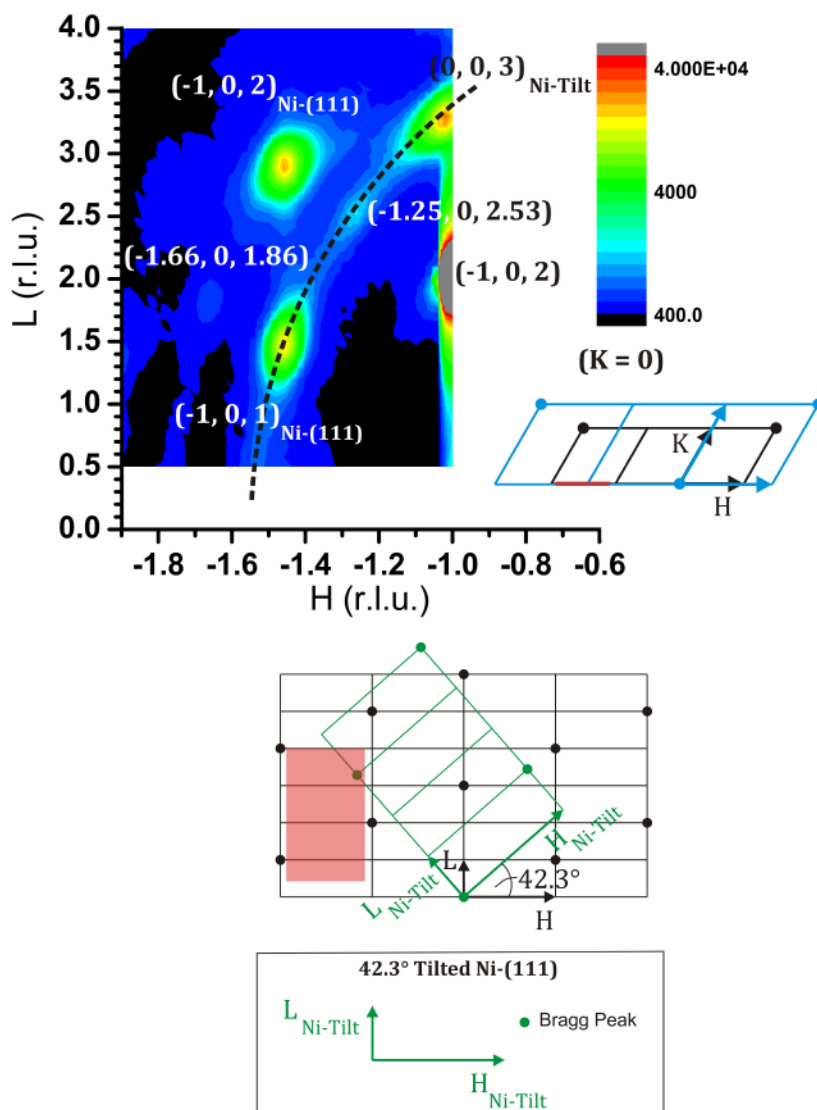
Figure 5.33: Reciprocal H-L map at K = 0 measured with the Pilatus detector. Beside the (-1, 0, 1)$_{Ni(111)}$ and (-1, 0, 2)$_{Ni(111)}$ Bragg peaks from the known (111) orientation of Ni and the substrate (-1, 0, 2) Bragg peak, two peaks at (-1.25, 0, 2.53) and (-1.66, 0, 1.86) are observed. They result from an internal twinning within the (111)-oriented Ni NPs. The reaming peak at (-1.02, 0, 3.28) lies on a circle with the (-1, 0, 1)$_{Ni(111)}$ Bragg peak and hence originates from 41.3° tilted (111)-oriented nickel NPs and can be assigned as the (0, 0, 3)$_{Ni-Tilt}$ Bragg peak using the coordination system of these particles as indicated in the lower part.

the substrate. Beside these, two peak are observed at (−1.25, 0, 2.53) and (−1.66, 0,

1.86) which cannot be assigned to (111)-oriented or (100)-oriented nickel. These peaks are identified considering the internal stacking sequence inversion (see section 2.6.1) within the single (111)-oriented NPs and thus an internal twinning within these NPs [90]. From the measured intensities of the peaks, it can be qualitatively concluded that while (111)-NPs and their laterally coexisting twins cover an equal fraction of the surface, the internal twinning plays a minor role.

The remaining peak at (−1.02, 0, 3.28) lies on a circle centered at the Γ point and going through the $(-1, 0, 1)_{Ni(111)}$ Bragg peak of (111)-oriented nickel. Thus, the new peak originates from the same planes of nickel which, however, are tilted with the tilting angle

$$\arctan\left(\frac{1.02 \cdot 2 \cdot \sqrt{2}}{3.28}\right) = 41.33° \tag{5.33}$$

The existence of the tilted NPs was checked at several other reciprocal positions

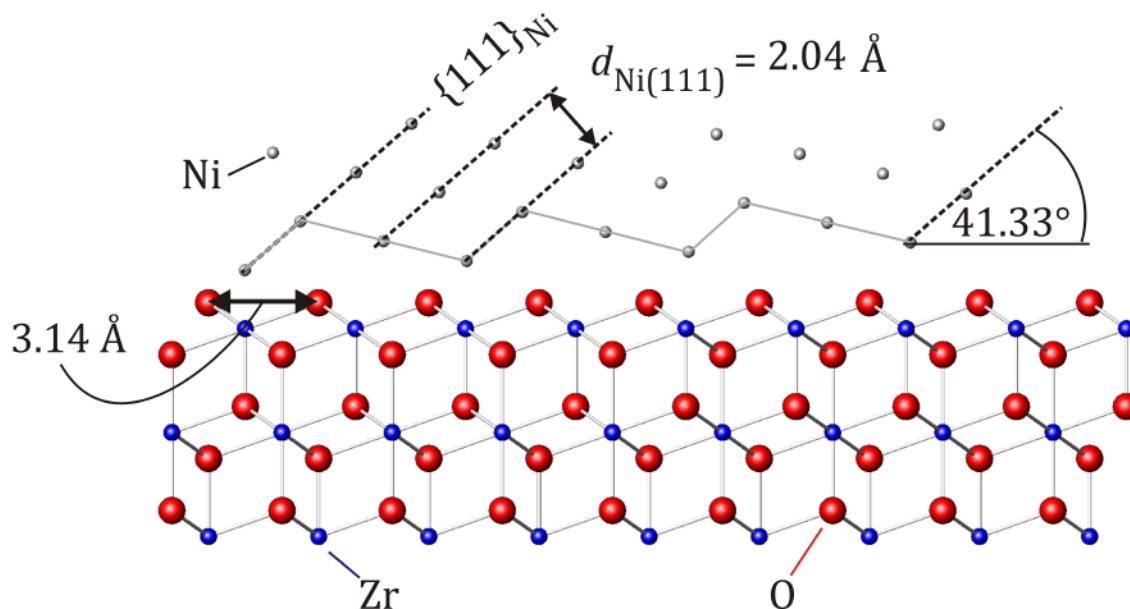**Figure 5.34:** Side view of the tilted Ni(111) epitaxy on YSZ(111). Ni {111} planes order such that the projection of the d-spacing $d_{Ni(111)}$ fits on the substrate lattice. The tilt leads to a stepped edge of the NPs at the interface with the substrate indicated with the solid grey line. Having a tilting angle of 41.33°, results in a small mismatch of 1.6%. Such a growth mechanism is known as "coherent tilt".

and proved. There are hence two types of nanoparticles. The first type is a (111) orientation laterally coexisting with twins and having a small fraction of internal twinning. The second type shows a 41.33°-tilted (111) orientation which will be called (111)-NP and tilted-NP hereafter. The new peak can therefore be assigned as the $(0, 0, 3)_{\text{Ni-Tilt}}$ Bragg peak of a 41.33° tilted Ni(111) orientation, introducing the subscription "Ni-Tilt" for the 41.33°-tilted coordination (see low part of Figure 5.33).

The epitaxy of the tilted orientation is illustrated in Figure 5.34. It shows a side view of the YSZ(111) unit cell. The dashed lines illustrate nickel {111} planes with a d-spacing $d_{\text{Ni}(111)}$ of 2.04 Å. The tilted nickel orientation grows such that the projection of $d_{\text{Ni}(111)}$ fits on one substrate atomic distance of 3.14 Å along this direction. This results in a stepped edge of the NPs at the interface with the substrate as depicted with the grey solid line. The tilting angle of 41.33° leads to a very small mismatch of

$$\text{Mismatch} = \frac{d_{\text{Ni}(111)}}{\sin(41.33°) \cdot 3.14 \text{ Å}} \triangleq 1.6\% \tag{5.34}$$

Such tilted orientations of the nickel growth to match the substrate lattice are an indication for an interface driven growth mechanism of these NPs. This kind of growth is known for hcp rare earth metals in order to relief long-range epitaxial strain and is called "coherent tilt" [187].

The average size of the two types of NPs can be determined by analyzing reciprocal scans across their Bragg peaks. Such a scan along the reciprocal L-direction of the $(-1, 0, 2)_{\text{Ni}(111)}$ Bragg peak of (111)-NP is shown in the left part of Figure 5.35. The peak shows a Gaussian shape and a fit of it delivers an FWHM_{L} value of 0.258. The used slit settings lead to an angular acceptance of the detector of around 0.6° and thus to ΔL errors around 6%. The average height of (111)-NPs can thus be calculated as

$$\text{Height} = \frac{1}{\text{FWHM}_{\text{L}} = \Delta L} \cdot c \tag{5.35}$$
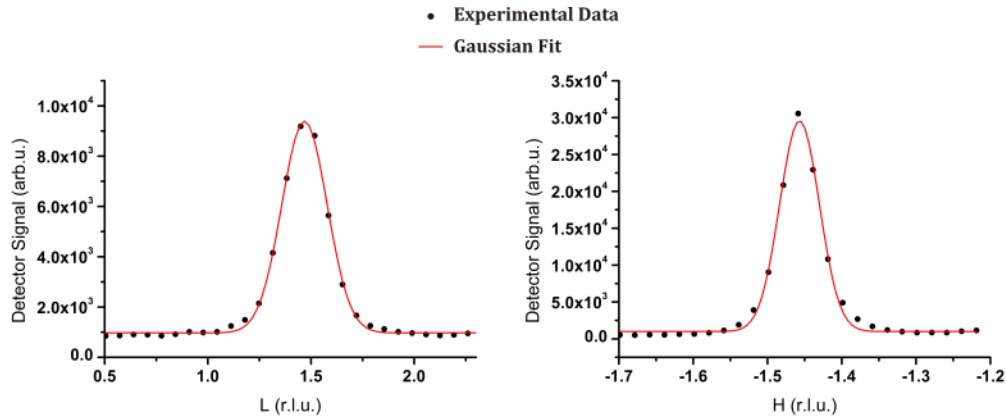
Figure 5.35: Left: L-scan through the (−1, 0, 2)$_{Ni(111)}$ Bragg-Peak of (111)-oriented Ni shows a Gaussian shape. A Gaussian fit delivers an FWHM$_L$ value of 0.258 which can be used to determine an average size of the (111)-oriented NPs of 34 Å in excellent agreement with reflectivity and AFM measurements. Right: H-scan through the same Bragg peak delivers an FWHM$_H$ value of 0.062 and hence an average width of the (111)-NPs of 67 Å.

where c is the according lattice constant to L and thus the height of the YSZ(111) unit cell. With $c = 8.90$ Å and FWHM$_L$ = 0.258, the average height is determined to be

$$\text{Height}_{(111)-NP} = \frac{1}{0.258} \cdot 8.9\text{ Å} = 34\text{ Å} \pm 2\text{ Å} \tag{5.36}$$

in almost perfect agreement with the reflectivity and AFM measurements (see equation (5.24) and Figure 5.25).

An analogous procedure leads to a FHWM$_H$ value of the same peak of 0.062 as shown in the right part of Figure 5.35. Considering the hexagonal structure, the width of the (111)-NPs is given by

$$\text{Width}_{(111)-NP} = \frac{2}{\sqrt{3} \cdot 0.062} \cdot 3.61\text{ Å} = 67\text{ Å} \pm 4\text{ Å} \tag{5.37}$$

using the in-plane lattice constant of 3.61 Å. Hence, the (111)-NPs are 3.4 nm high and 6.7 nm broad on average which indicates a rather flat shape.

Corresponding measurements through Bragg peaks of the tilted-NPs (see appendix C for the scans) deliver values of

$$\text{Height}_{\text{Tilted-NP}} = \frac{1}{0.301} \cdot 8.9 \text{ Å} = 29.5 \text{ Å} \pm 1.8\text{Å} \tag{5.38}$$

and

$$\text{Width}_{\text{Tilted-NP}} = \frac{2}{\sqrt{3} \cdot 0.069} \cdot 3.61 \text{ Å} = 60.4 \text{ Å} \pm 3.6 \text{ Å} \tag{5.39}$$

The dimensions of both NP types are thus in the same range.

Summarizing the results so far, NPs are grown on a YSZ(111) substrate. Two types of NPs are discovered which equally cover the surface as indicated by the intensities of their Bragg peaks:

- (111)-oriented nickel NPs ((111)-NP)
    - Average height: 34 Å
    - Average width: 67 Å
- 41.33° tilted (111)-oriented NPs (tilted-NP)
    - Average height: 29 Å
    - Average width: 60 Å

In order to determine the shape of the NPs, the Wulff-construction [100] of Ni as described in section 2.6.2 is used. The Wulff-shape is predominantly covered by (111)-oriented hexagonal facets, while a smaller fraction are (100) facets. This base shape can now be taken as a starting point to describe the shape of the two NP types. Knowing the dimensions and orientation of each type, the Wulff-shape has to be cut at the according positions [101].

Starting with the (111)-oriented NPs, the Wulff-shape is given in the top part of Figure 5.36. The width of 6.7 nm and a height of 3.4 nm require a cut of the Wulff-shape as shown in the lower part of Figure 5.36. The (111)-NPs are hence having a top (111)-oriented facet and six (111)-oriented facets on the sides in contact with the substrate. Two of the side facets are thereby almost fully present while the remaining four are cut slightly above the bisectors.

Similar considerations can be used to construct the shape of the tilted-NPs. This shape is however looking rather uncommon. It is constructed taking the same Wulff-shape as for (111)-NPs and rotate it by 41.33° around the (111)-direction which

Figure 5.36: Side- and top-view of the (111)-NP. The top parts show the Wulff-shape. The determined dimensions of 6.7 nm width and 3.4 nm height require a cut through the Wulff-shape as shown in the lower part. This cut results in six (111)-oriented side facets. Two (111) facets are almost completely present while the remaining four are cut slightly above the bisector.

results in the shape in the upper left part of Figure 5.37. This shape is then set on the substrate respecting the determined dimensions. The resulting side view is shown in the lower left part of Figure 5.37. The unusual shape of the tilted-(111) is the result of a strong interface driven growth which forces a tilted (111) orientation. The tilted-NPs have both (111) and (100)-oriented facets facing up. There are two (100)-oriented and four (111)-oriented side facets.

It is important to note that both NP types are also growing along all symmetry-equivalent in-plane directions as the ones shown in Figure 5.36 and Figure 5.37.

Another important fact to mention is that while the (111)-NPs and thin films are found as the major orientation to grow on this surface [14], the tilted-NPs have not
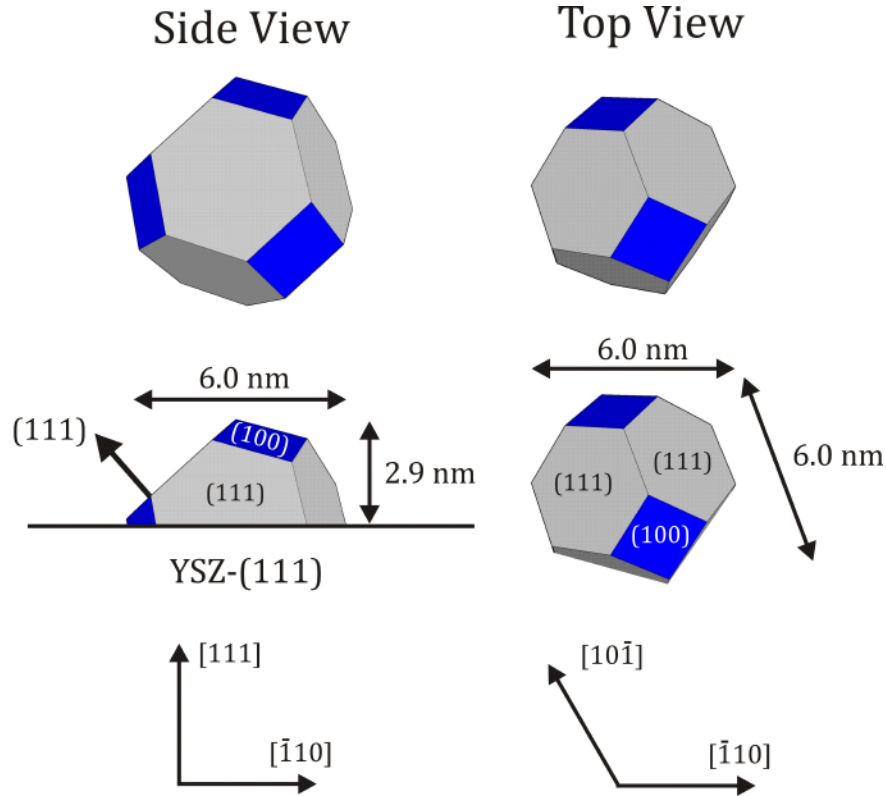
Figure 5.37: Shape of the tilted-NPs. For this construction, the same Wulff-shape used before is rotated by 41.33° and cut with respect to the dimensions of 6.0 nm width and 2.9 nm height. The NPs show an uncommon round shape which result from the coherent tilting growth dominated by interface interactions.

been reported before. Hence this works presents the first observation of coherent-tilt growth of Ni on YSZ(111).

Knowing the surface energies and the size of (111)-oriented NPs, it is possible to derive the work of adhesion W_{adh} for their growth using [102]

$$W_{adh} = 2 \cdot \gamma_{111} - \sqrt{\frac{3}{2} \cdot \frac{\text{Height}}{\text{Width}}} \cdot \gamma_{100} \qquad (5.40)$$

where γ_{100} and γ_{111} are the surface energies of the Ni-(100) and (111) surfaces. Using the surface energies given in Table 2.4 and the dimensions of (111)-NPs given in equations (5.36) and (5.37) leads to a work of adhesion

$$W_{adh} = 2 \cdot 94 \frac{meV}{\text{Å}^2} - \sqrt{\frac{3}{2} \cdot \frac{34 \text{ Å}}{67 \text{ Å}}} \cdot 103 \frac{meV}{\text{Å}^2} = 124 \frac{meV}{\text{Å}^2}$$

$$= 1.99 \frac{J}{m^2}$$

(5.41)

compared to a value of 9.8 J/m² derived from contact angle measurements and assuming a spherical shape of the NPs [188]. A value of 2.8 J/m² was derived from Pd NPs grown on Al_2O_3 on NiAl(110) which is in the same range as the value derived here [102]. The more rounded shape of the tilted-NPs indicates a lower work of adhesion for these particles.

5.2.3 Shape Changes

Shape changes of the above observed NPs were studied after three different treatments.

- Heating at T = 700°C
- for 75 minutes

After this treatment the sample was exposed to

- p = 10⁻⁵ mbar methane (CH_4)
- at T = 300°C
- for 30 minutes

and finally the NPs were exposed to

- p = 10⁻⁵ mbar O_2
- at T = 300°C
- for 35 minutes.

All measurements were preformed after the sample was cooled down and the according gases were pumped out, in order to prevent further shape changes during the characterization. The results are presented in the following

5.2.3.1 Heat Treatment

Figure 5.38 shows the reflectivity curve measured after the NPs were annealed at 700°C for 75 minutes. It clearly differs from the one measured after the evaporation

shown in Figure 5.26 indicating a change of the NPs. A fit of the curve delivers a film of the thickness

$$d = 48.1 \text{ Å} \tag{5.42}$$

and the 2δ value of

$$2\delta_{\text{Fit}} = 1.74 \cdot 10^{-5} \tag{5.43}$$

Using equations (5.22) and (5.23) leads to a coverage of

$$\Theta: 42.8\% \tag{5.44}$$

Hence, the heat treatment results in higher NPs and a lower coverage conserving the total amount of material.
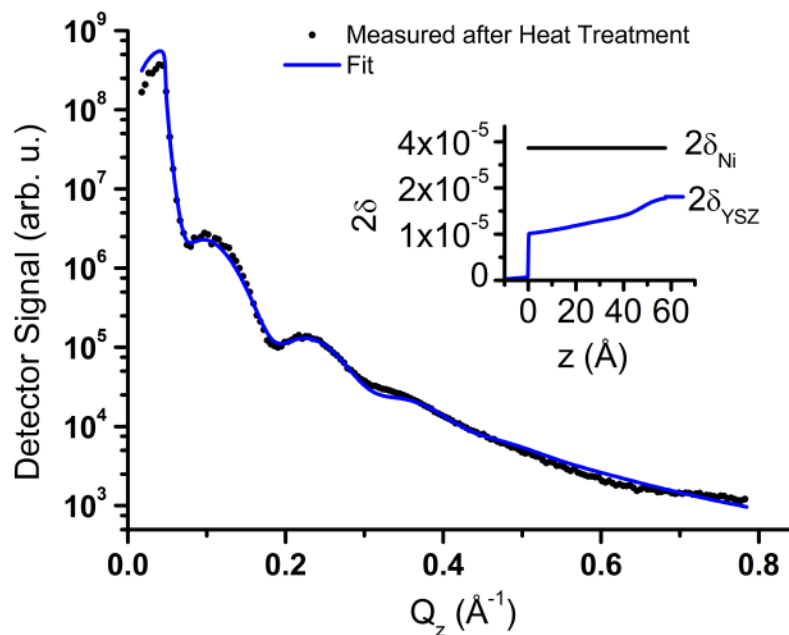

Figure 5.38: Reflectivity curve measured after the heat treatment indicates a change of the NPs since it differs from the curve measured before this treatment (see Figure 5.26). The analysis of the curve delivers a nickel layer with the thickness of 48 Å, in good agreement with the values derived from the SXRD reciprocal maps, and a coverage of 43%.

Figure 5.39 shows a reciprocal H-L map measured with the point detector and revealing the same peaks as shown in Figure 5.33 measured after the evaporation. The creation of new particle type or the total decomposition of the known particle types can thus be excluded. Note that a comparison of the intensities of both maps is not directly possible since two different detectors were used.

The dimensions of the NPs can however be determined the same way as in the previous section and show considerable changes. The (111)-NPs dimensions have changes to

$$\text{Width}_{(111)-\text{NP}} = \frac{2}{\sqrt{3} \cdot 0.038} \cdot 3.61 \text{ Å} = 109.7 \text{ Å} \pm 6.6 \text{ Å} \qquad (5.45)$$

and

$$\text{Height}_{(111)-\text{NP}} = \frac{1}{0.173} \cdot 8.9 \text{ Å} = 52.0 \text{ Å} \pm 3.1 \text{ Å} \qquad (5.46)$$
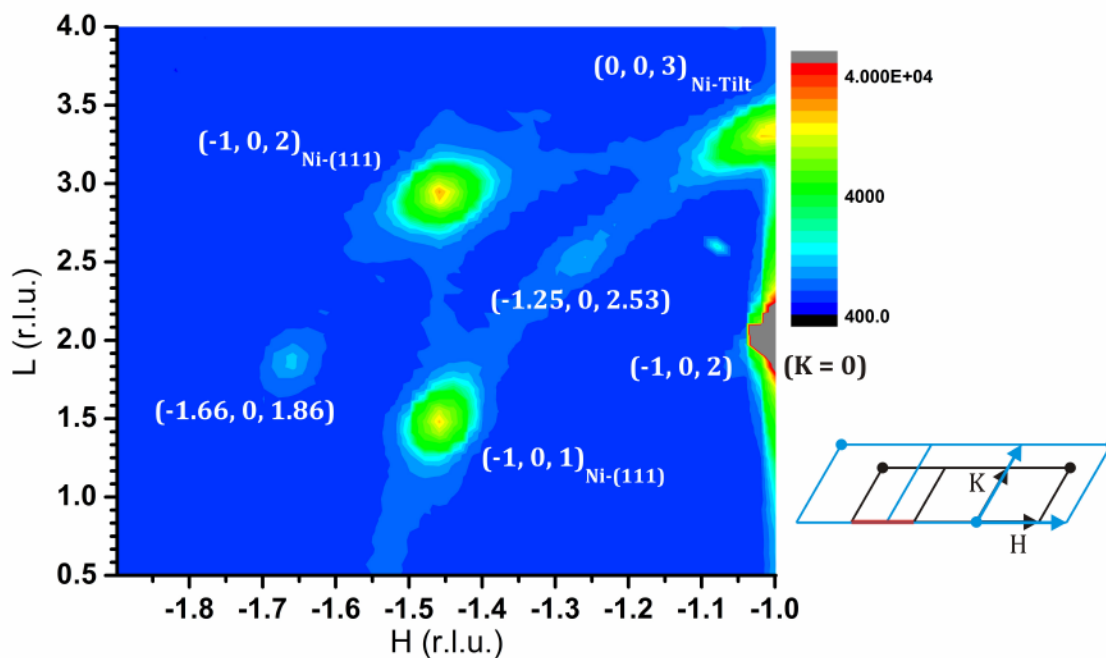

Figure 5.39: Reciprocal H-L map measured after the heat treatment. The detection of the same peaks as before the heat treatment (see Figure 5.33) indicated the existence of the same NP types after this treatment. The average sizes of the particles have changed, however.

compared to 67 Å and 34 Å before the heat treatment. Hence, the average size of the (111)-NPs has grown remarkably.

A similar behavior is observed for the tilted-NPs where the average size considerably grows to a height of

$$\text{Height}_{\text{Tilted}-\text{NP}} = \frac{1}{0.173} \cdot 8.9\ \text{Å} = 51.4\ \text{Å} \pm 3.0\ \text{Å} \tag{5.47}$$

and a width of

$$\text{Width}_{\text{Tilted}-\text{NP}} = \frac{2}{\sqrt{3} \cdot 0.050} \cdot 3.61\ \text{Å} = 83.4\ \text{Å} \pm 5.0\ \text{Å} \tag{5.48}$$

compared to 29.5 Å and 60.4 Å before the heat treatment. The height of both types grows in good agreement with the reflectivity data and remains in the same range
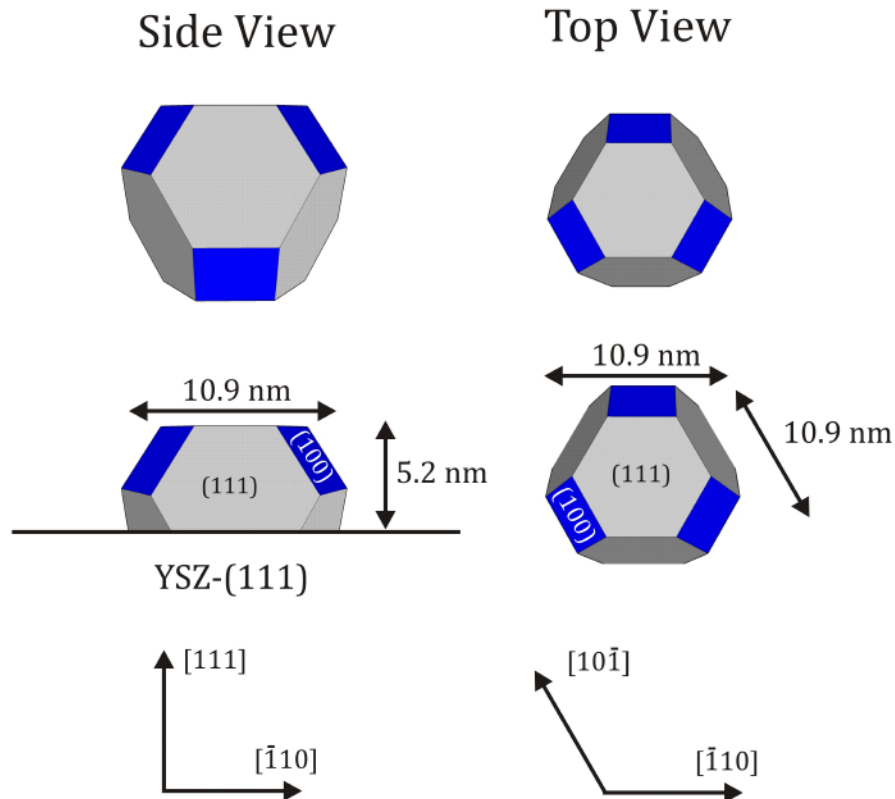

Figure 5.40: Side- and top-view of the (111)-NP after the heat treatment. These particles show no change in shape due to a very similar width-to-height ratio as before, leading to the same work of adhesion. Their size, however, has grown remarkably.

for both types.

Since the amount of nickel atoms must remain constant, the growth of the average size of the NPs together with the decreased coverage is an indication for a decreased number of particles and the growth of the bigger NPs at the expense of the smaller ones. Such a growth might be caused by Ostwald ripening and is often observed for small particles or fluids [189], where bigger particles adsorb smaller particles due to their higher thermodynamic stability [190; 191].

Ostwald ripening takes place because the atoms within bigger particles have lower energies due to their higher ordering compared to smaller particles. The atoms on the surfaces of smaller particle detach to the bigger particles, since the
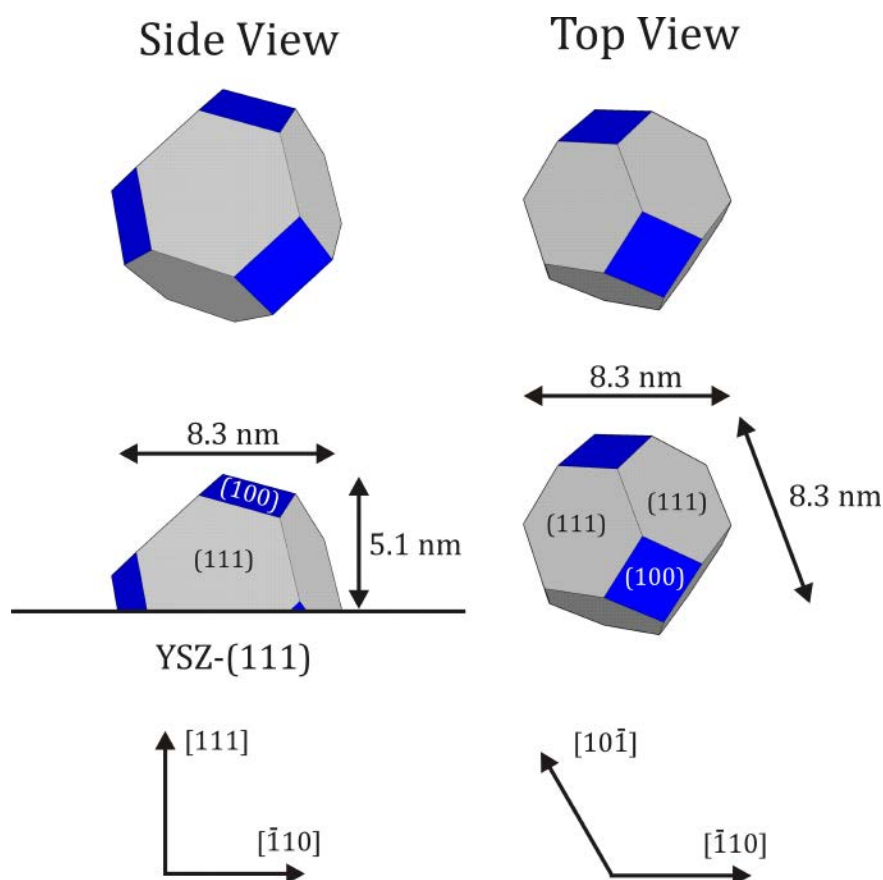

Figure 5.41: : The tilted-NPs show changes in size and shape after the heat treatment. The size grows to average heights and widths of 5.1 nm and 8.3 nm respectively. The (111) facets have thereby increased their area noticeably.

surface to volume ratio and thus the surface energies of the big particles are much lower. Annealing of the NPs in the present case supports the NP atoms with enough kinetic energy and hence the cross-over of the atoms from small particles to bigger particles is possible. The average growth of the NP size can thus be explained by Ostwald ripening.

An alternative mechanism is the coalescence of the NPs which become mobile at high temperatures and "melt" together to form bigger particles. This mechanism has been observed for palladium NP on a TiO_2 surface with STM [192]. A considerable mass transfer can however be concluded regardless the growth mechanism.

The shape of both types can be constructed as done so in the last section. The resulting shape of the (111)-NPs is shown in Figure 5.40. Thus, these particles keep their shapes and grow in size only. This is due to the nearly constant ratio of width to height before and after the heat treatment

$$\frac{\text{Width}_{\text{Before heat}}}{\text{Height}_{\text{Before heat}}} = 1.9 \sim 2.0 = \frac{\text{Width}_{\text{After heat}}}{\text{Height}_{\text{After heat}}} \tag{5.49}$$

and leads to the same effective work of adhesion given in equation (5.41). It can hence be assumed, that the equilibrium shape of the (111)-NPs was achieved before the heat treatment.

The shape of the tilted-NPs on the contrary has changed, leading to the conclusion that the equilibrium shape was not achieved yet. This uncommon shape is shown in Figure 5.41. The NPs are therefore sitting on altering (111)-oriented and (100)-oriented facets with the latter ones touching the surface only with their tips. The size of the (111)-side facets has thereby grown considerably.

5.2.3.2 Methane Treatment

SOFCs great advantage compared to other fuel cells is its ability to use hydrocarbons as fuel. Thus the influence of CH_4 on the shape of nickel NPs were studied here.

At a methane pressure of 10^{-5} mbar and 300°C, no changes of the NPs were observed. Figure 5.42 shows a reciprocal L-scan at (−1.44, 0) where the (−1, 0, 1)$_{\text{Ni(111)}}$ and (−1, 0, 2)$_{\text{Ni(111)}}$ Bragg peaks of (111)-oriented Ni and its twin were
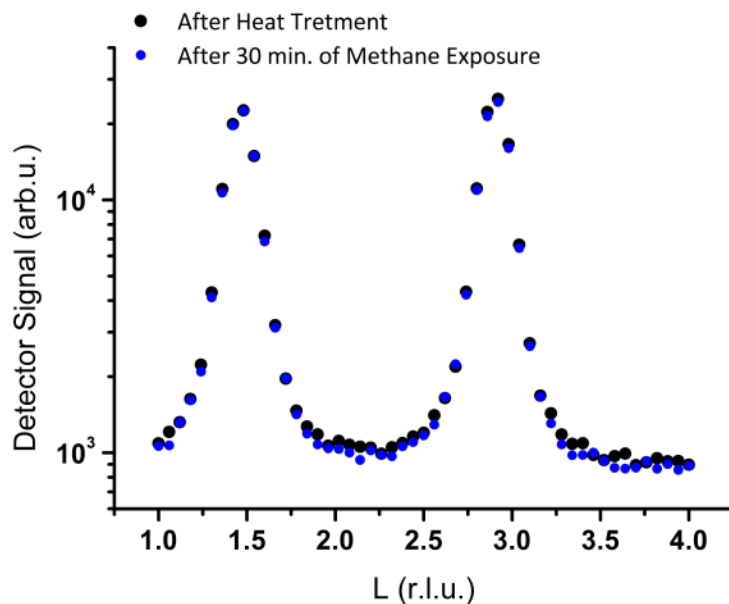
Figure 5.42: Reciprocal L-scans through the $(1, 0, 1)_{Ni(111)}$ and the twin peak $(1, 0, 2)_{Ni(111)}$ of (111)-NPs do not show any change before and after exposure to 10^{-5} mbar methane at 300°C. This together with unchanged reflectivity curves indicate that the NP-shape has not changed upon a possible CH_4 adsorption.

measured before and after methane exposure for 30 minutes. The shape, size and width of the peaks remain unchanged during this treatment. It can thus be concluded that the shape of the NPs is not affected by a possible adsorption of the hydrocarbon on the particles [193]. This statement is supported by the measured reflectivity after 35 minutes of exposure and cooling down the sample. Reflectivity curves measured before and after methane exposure do not show any change either.

5.2.3.3 Oxygen Treatment

The oxidation of nickel on the SOFCs anode is an issue that leads to decreasing efficiencies since NiO is inert in oxidation reactions (see section 2.6). The structural changes of the discovered NP types were therefore studied after an oxygen treatment at 300°C and 10^{-5} mbar O_2 for 35 minutes. Both single crystal facets of the NPs are reported to form NiO at these conditions [194; 195] with oxidation rates proportional to the oxygen pressure. Oxygen is moreover found to penetrate into

the bulk of the single crystals at temperatures above 250°C [15; 16]. CTR measurements did not show any indication of such a treatment to affect the surface structure of the YSZ(111) substrate as shown in Figure 5.24.

We start again with a reflectivity curve measured after this treatment. The curve is plotted in Figure 5.43 and shows changes compared to the ones measured after the evaporation of Ni (Figure 5.26) and after the heat treatment (Figure 5.38). The increased periodicity of the oscillations indicate a thickness growth and hence a height-growth of the NPs. This indication is approved by a fit of the curve that delivers a thickness of

$$d = 53.3 \text{ Å} \tag{5.50}$$

Note that a statement about the coverage of the surface is not possible here since a mixture of Ni and NiO is expected to cover the surface.

Reciprocal L-scans along (−1.44, 0, L) were performed during the oxygen
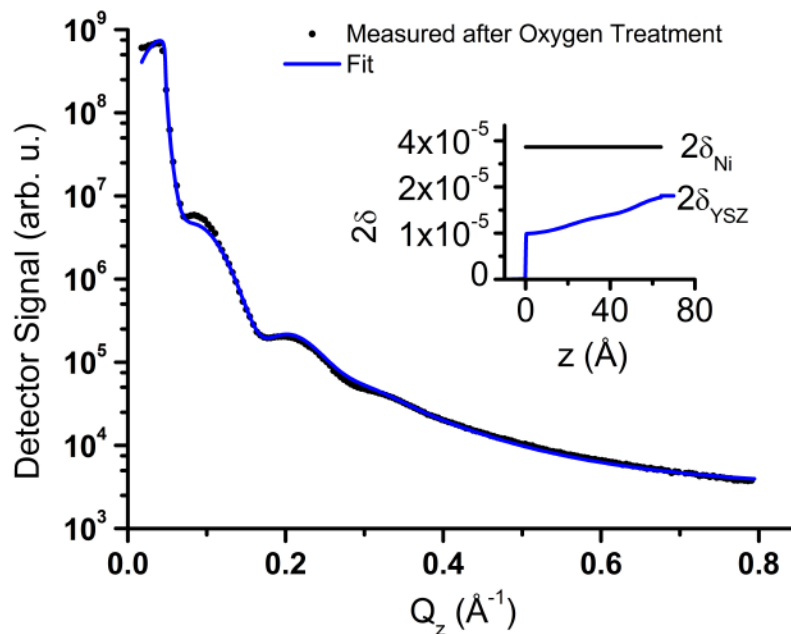

Figure 5.43: Reflectivity curve measured after the oxygen treatment shows a change of its characteristics compared to the curves measured before. The fit of this curve results in a film with a thickness of 53.3 Å.

treatment. At the L positions 2.88 and 1.44 the $(-1, 0, 2)_{Ni(111)}$ and $(-1, 0, 1)_{Ni(111)}$ Bragg peaks are expected. Figure 5.44 shows these scans measured before the treatment, and after one, 20 and 35 minutes of oxygen exposure. It becomes clear that oxygen immediately starts to attenuate the Bragg peaks of the (111)-NP with continues progress. The integrated intensities of the Bragg peaks, thereby, show an exponential decay with a time constant of 18.4±7.2 minutes.

It can thus be assumed that NiO starts to form with an exponential growth. The formation of NiO out of the nickel NPs is proved by the measurement of the same reciprocal map as shown in Figure 5.39 and using the point detector. This map is plotted in Figure 5.45.

Additional peaks appear at $(-1.21, 0, 1.21)$ and $(-1.21, 0, 2.42)$. Considering the lattice constant of NiO to be 4.20 Å (see section 2.6.1) the ratio of the reciprocal

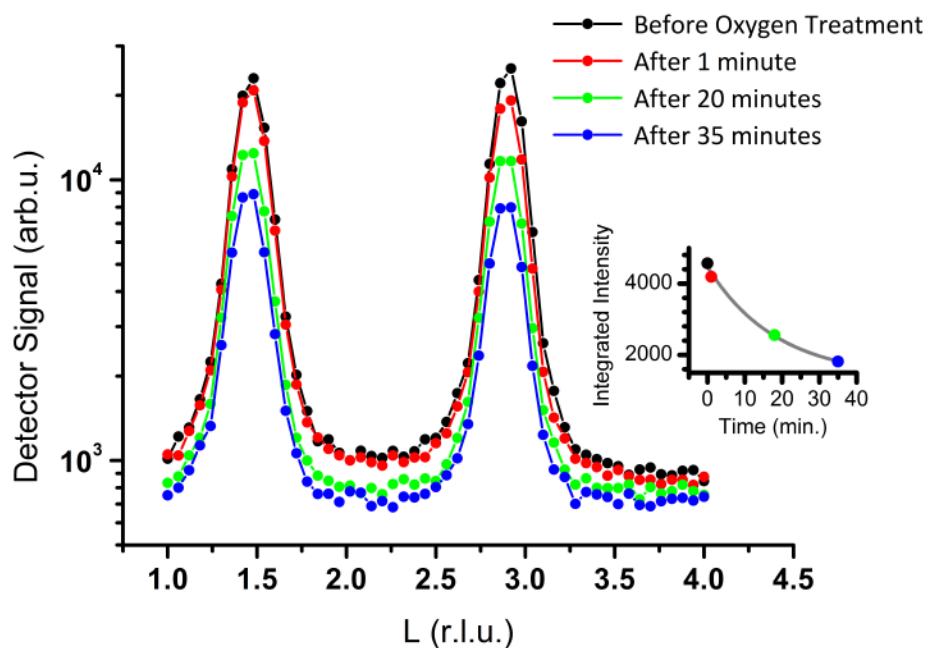**Figure 5.44:** L-scans at $(-1.44, 0, L)$. The peaks at L = 2.88 and 1.44 are the $(-1, 0, 2)_{Ni(111)}$ and the $(-1, 0, 1)_{Ni(111)}$ twin Bragg peaks. Expositing the NP to oxygen results in a decay of the Ni(111) signal. The inset shows integrated intensities of the peaks at $(-1.44, 0, 1.44)$ whit an exponential characteristics and a fitted (grey line) time constant of 18±7 minutes.

substrate axes and the NiO axes is given by

$$\frac{\frac{1}{\sqrt{2}} \cdot 4.20 \text{ Å}}{\frac{1}{3.61 \text{ Å}}} = 1.216 \tag{5.51}$$

The peaks can hence be assigned as the $(0, -1, 2)_{\text{NiO-(111)}}$ and $(0, -1, 1)_{\text{NiO-(111)}}$ Bragg peaks of (111)-oriented NiO and the formation of NiO NPs with the same epitaxy as their preceding unoxidized (111)-NPs is concluded.

The intensities of the nickel NPs have moreover decreased considerably, especially for the internal twins. The peak observed at $(-1.25, 0, 2.53)$ has even disappeared completely.

The dimensions of the single NP types can be calculated as described before. It leads to the dimensions of the (111)-NPs of
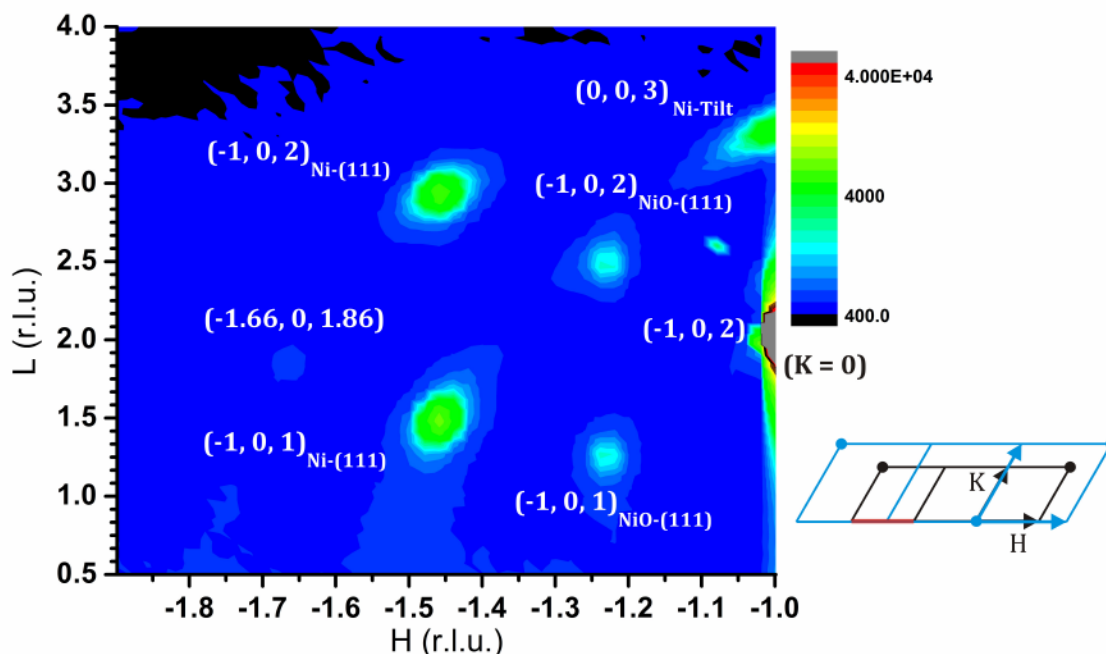

Figure 5.45: Reciprocal H-L map at K = 0 measured with the point detector. NiO(111) peaks appear at $(-1.21, 0, 1.21)$ and $(-1.21, 0, 2.42)$ originating from (111)-oriented NiO NPs which keep the epitaxy of their parent unoxidized NPs. All Ni-NP peaks become weaker after the oxidation and the peaks of the internal twinning almost completely disappear.

$$\text{Width}_{(111)-\text{NP}} = \frac{2}{\sqrt{3} \cdot 0.045} \cdot 3.61 \text{ Å} = 92.3 \text{ Å} \pm 5.5 \text{ Å} \tag{5.52}$$

and

$$\text{Height}_{(111)-\text{NP}} = \frac{1}{0.188} \cdot 8.9 \text{ Å} = 47.5 \text{ Å} \pm 2.9 \text{ Å} \tag{5.53}$$

compared to 95 Å and 52 Å after the heat treatment. Thus, the size of the (111)-NPs has decreased by about 23%. Interestingly, the width-to-height ratio is again 2 and thus the same as the ratios before and leads to the same work of adhesion. The shape of these NPs will thus remain the same and only the size changes, as shown in Figure 5.46. The shape after the unoxidized (111)-oriented NPs is shown in Figure 5.46.
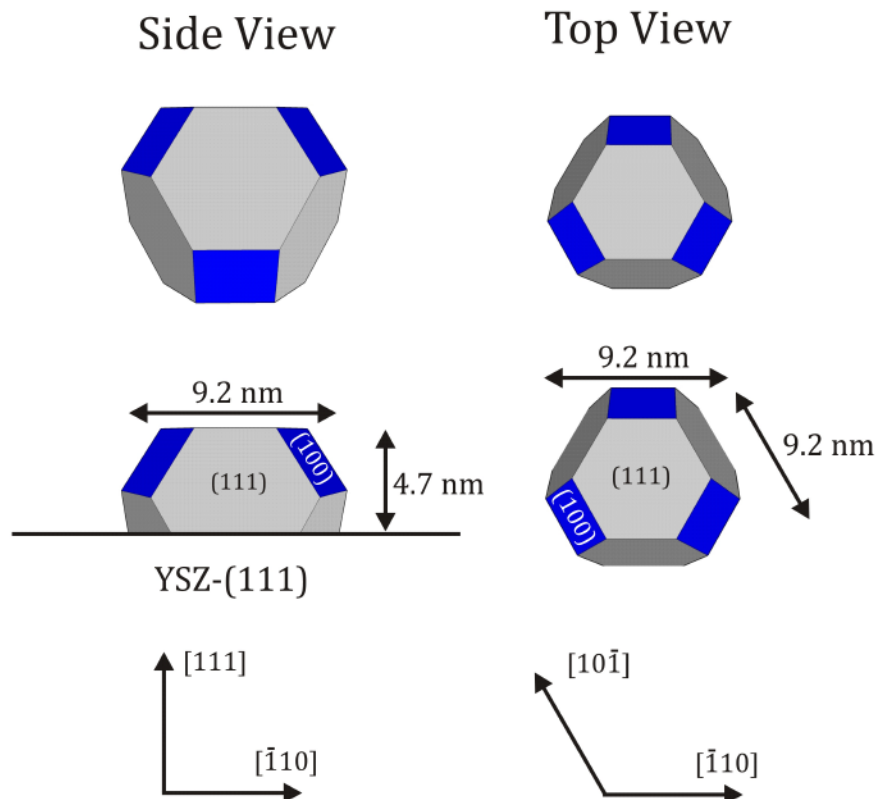

Figure 5.46: Side- and top-view of the (111)-NPs after Oxidation. These particles again show no change in shape. The average size, however, is reduced indicating a random oxidation of all particles.

The size of the NiO-(111) NPs is determined to be

$$\text{Width}_{\text{NiO}-(111)} = \frac{21}{\sqrt{3} \cdot 0.045} \cdot 3.61 \text{ Å} = 92.3 \text{ Å} \pm 5.5 \text{ Å} \qquad (5.54)$$

and

$$\text{Height}_{\text{NiO}-(111)} = \frac{1}{0.218} \cdot 8.9 \text{ Å} = 40.7 \text{ Å} \pm 2.4 \text{ Å} \qquad (5.55)$$

The NiO-(111) NPs and the Ni(111) NPs thus have the same width and slightly differ in height. Note that the formation of NiO causes a 15% increase of the particles width and height ($a_{\text{Ni}}/a_{\text{NiO}}$ = 1.157)

The average size loss of the unoxidized (111)-NPs and their simultaneous shape conservation give hints for a possible oxidation mechanism of these particles. The formation of a 3 nm thick NiO layer on a Ni(111) single crystal surface is reported for the temperatures used for the oxygen treatment here [17]. The oxidation of the NPs is therefore believed to homogenously start on all the facets of the NPs regardless the NP's size. The reported oxide thickness is thus able to oxidize small particles completely and bigger particles partially (see Figure 5.47). The homogenous oxidation from all facets moreover leads to an unchanged shape of the remaining nickel particles and decreases their average heights and widths.
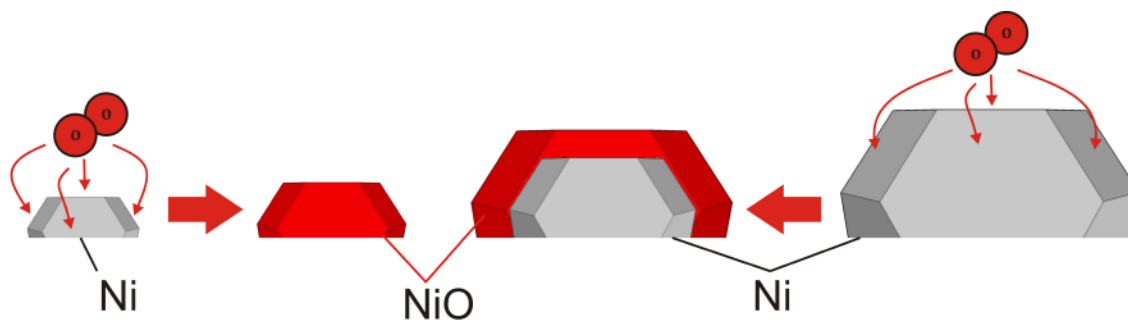
Figure 5.47: Oxidation mechanism of the (111)-NPs: the facets of the nickel NPs (silver) are oxidized homogenously. The oxide saturation thickness on each facet leads to a complete oxidation of small NPs (left side) while big NPs (right side) are partially oxidized.   The big unoxidized NPs before the oxidation are thus converted into particles with nickel cores and oxide shells.

Following this mechanism, big parent nickel NPs result in nickel cores with an oxide shell.

A very interesting fact results from the size of the tilted-NPs. This type has the dimensions of

$$\text{Width}_{\text{Tilted−NP}} = \frac{2}{\sqrt{3} \cdot 0.049} \cdot 3.61 \,\text{Å} = 85.1 \,\text{Å} \tag{5.56}$$

and

$$\text{Height}_{\text{Tilted−NP}} = \frac{1}{0.178} \cdot 8.9 \,\text{Å} = 50.0 \,\text{Å} \tag{5.57}$$

compared to 83.4 Å and 51.4 Å before the oxygen treatment. The average size of the

Figure 5.48: : The shape and average size of the tilted-NPs after the oxygen treatment does not change. The intensity decrease of their Bragg peaks however indicates a strong oxidation of these NPs.

tilted-NPs has thus changed minimally leading to the shape shown in Figure 5.48.

The oxide peaks of the tilted orientation could not be measured due to lack of time during the beamtime. The Bragg signal of the tilted-NPs decreases distinctly however, pointing to a strong oxidation of these particles. The almost constant average size of these particles thereby poi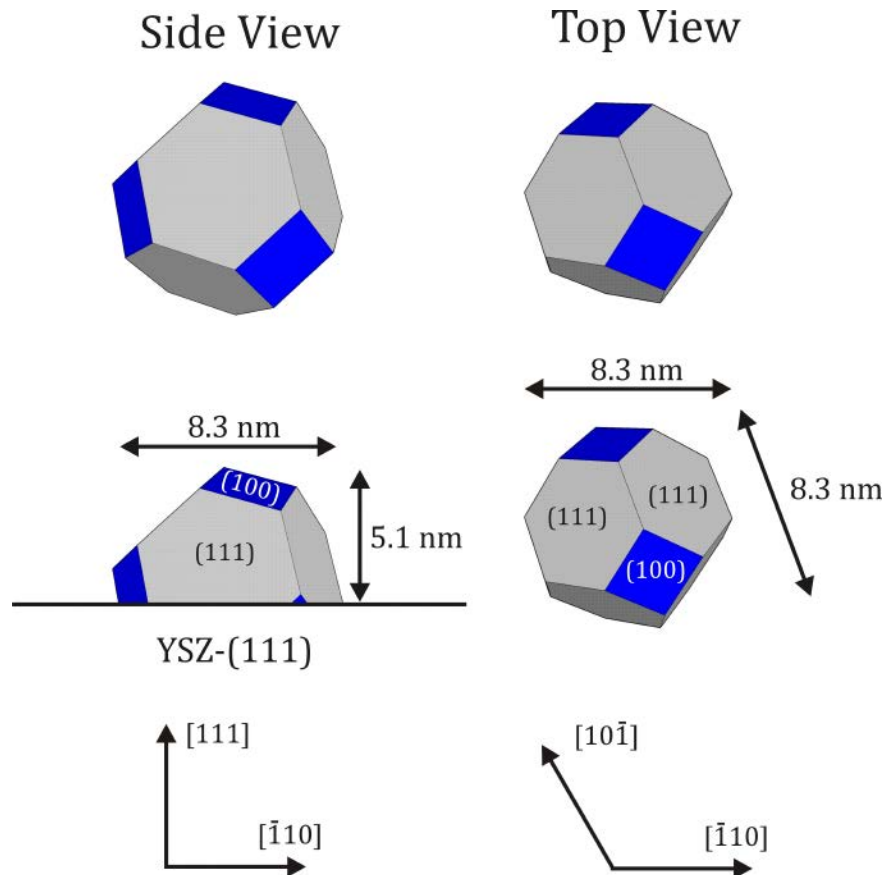nts to a different oxidation procedure as for the (111)-oriented NPs. Such an oxidation could start at the interface with the substrate and oxidize whole NPs independent from their size.

5.2.4 Summary

Surface X-ray diffraction was used to examine the growth of nickel nanoparticles on a freshly prepared YSZ(111) surface and shape changes of these particles after a heat treatment and exposures to methane and oxygen.

Nickel NPs could be grown with the PVD method using an electron beam evaporator with a nominal thickness of 5.7 nm at substrate temperatures of 350°C. AFM images measured *ex-situ* show particles with heights around 3 nm. This value is supported by reflectivity measurements which also reveal a 60% coverage of the surface.

Two different types of interface driven NP-growth were determined using SXRD. The first type are (111)-oriented epitaxially grown NPs (called (111)-NP) with laterally coexisting twins having a lattice mismatch of 4.0%. A small fraction of the particles has also an internal twinning due to stacking inversion. These particles have an average height of 34 Å and a width of 67 Å. The adhesion energy is therefore determined to be 124 meV/Å^2 [102].

The second type of NPs has a 41.33°-tilted (111) orientation (called tilted-NP). This so-called "coherent tilt" is known for the growth of rare earth metals in order to release long-range strain [187] and is an indication for strong interface driven growth. This type of NPs have average heights of 29.5 Å and widths of 60.4 Å. The epitaxy of both NP types suggests a homogenous growth.

The truncated octahedron equilibrium shape of the nickel Wulff-construction can be used to determine the shapes of the NPs [100; 99]. The tilted-NPs thereby show an uncommon round shape.

A heat treatment at 700°C and reductive conditions for 75 minutes leads to shape changes of the two NP types. Both types grow in height and width with the (111)-NPs keeping their shape however. This is an indication for the (111)-NPs to have reached their equilibrium shape before the heat treatment and leads to the same work of adhesion as before the heat treatment. Considering the conservation of mass, the average size growth can be attributed to Ostwald ripening [190; 196] where bigger particles grow at the expense of smaller ones, or the coalescence of mobile small particles to form bigger NPs [192], both leading to a decreased number of particles. This sintering of particle is unbeneficial for catalytic applications since the surface area is reduced.

When the NPs are exposed to 10^{-5} mbar of methane at 300°C for 30 minutes, no change of the NPs is observed. A possible adsorption of the hydrocarbons on the NPs [193] is thus concluded not to affect the structure of the NPs.

The most distinct changes are caused by an oxygen treatment at 10^{-5} mbar O_2 pressure and 300°C for 35 minutes. The intensity of the (111)-NPs Bragg reflections decrease exponentially to form epitaxial (111)-oriented NiO-NPs.

The nickel (111)-NPs shrink to a size of 92 Å in width and 47 Å in height and keep their shape at the same time. The epitaxial (111)-oriented NiO NPs have the same width of 92 Å as the unoxidized NPs and a smaller height of 40 Å. A possible oxidation is a homogeneous NiO formation on each of the NP facets. The reported oxide thicknesses under the oxidation conditions used here [17] are sufficient to oxidize small particles completely and big particles partially which on the other hand leads to a shrinking average width and height of the unoxidized particles. This mechanism moreover predicts the big parent nickel NP to consist of nickel cores and NiO shells after the oxidation.

The tilted nickel NPs keep their average size and shape after the oxidation. Their amount is however reduced as indicated by the decreased intensity of their Bragg

peak. The partial oxidation of these particles can thus be assumed as well. Detailed statements can however not be made due to missing experimental data. The constant average size of these particles however points to a different oxidation mechanism than for the (111)-oriented NPs.

All determined heights from SXRD measurements are in very good agreement with reflectivity measurements. The structure of the YSZ(111) surface was controlled by CTR measurements which did not show indications for a distinct change after the growth of the NPs and the NP treatments.

6 The YSZ(100) Surface

The (100) surface of cubic YSZ is a type-c Tasker surface and thus polar (see section 3.2.3). It has the third lowest surface energy among the low-index orientations and its polarity has motivated both experimental and theoretical studies on this surface. While an experimental study using high-resolution medium-energy ion scattering (HRMEIS) suggests a (1 x 1) reconstruction to compensate the polarity [18], a DFT study predicts this reconstruction to only happen at high yttrium contents at the surface and suggest a 50% oxygen vacancy at the surface to neutralize the polarity as an alternative [12] (see also section 2.5.3).

A systematic atomic structure determination study of the YSZ(100) surface was performed as part of this work using non-anomalous SXRD. CTRs after four different treatments of the surface were measured and analyzed to investigate the contradictorily models mentioned above. The obtained structural and compositional information deliver consistent models for this surface.

The growth of nickel nanoparticles on this surface and their shape changes at different temperatures and after exposure to oxygen were examined to give a complete picture of the structural parts of the three-phase boundary which is of great interest for SOFCs anodes [8].

This chapter takes the same approach to present the results as the previous one. First the models for the YSZ(100) surface under four different conditions are presented. The next part will present the growth and shape change of nickel nanoparticles at several conditions. All experiments were performed *in-situ*, unless explicitly mentioned.

6.1   Surface Structure

6.1.1 Sample Preparation

The single crystal (100)-oriented samples used for the structure determination and the nickel nanoparticle growth were purchased from Crystec GmbH and have miscuts smaller than 0.1°. Since these samples were cut from the same crystal as the (111)-oriented samples, the same preparation was used for the (100) surface (see section 5.1.1).

The 10x10x1 mm samples were mounted on a molybdenum sample holder using tantalum foils for the UHV experiments. They were transparent throughout the whole experiments indicating a stable bulk structure.

The preparation and characterization experiments using AFM, AES and reflectivity are omitted here because of identical results as for the YSZ(111) samples in the previous chapter and the interested reader is referred to section 5.1.1.

6.1.2   Surface X-ray Diffraction Experiments

All SXRD experiments on the YSZ(100) surface were performed under UHV conditions at the MPI-MF beam line at the Ångström-Quelle-Karlsruhe described in section 4.1.4. using an energy of 10keV and an incident angle of $\alpha_i = $ 0.267°, i.e. the critical angle at this energy. The experiments were performed in the dedicated high-temperature UHV mobile chamber and data were collected using the point detector (see section 4.1.4). Crystal truncation rods were measured after four different sample treatments.

- Treatment I:
    - After the sample preparation to get a clean and smooth surface as described in section 5.1.1:
        - T = 400°C
        - $p_{O2} = 10^{-5}$ mbar O_2
        - for 120 minutes
- Treatment II:
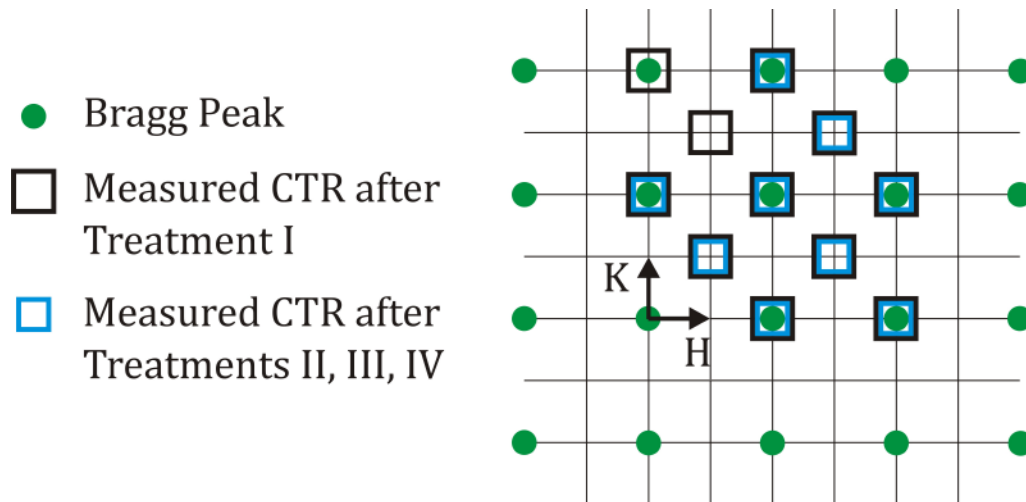
Figure 6.1: In-plane reciprocal map of YSZ(100). Eleven CTRs were measured after the usual cleaning preparation / treatment I, which are marked with black rectangular. Nine CTRs were measured after treatments II, III and IV marked as blue rectangles. The resulting CTRs after averaging are given in **Table 6.1** and Figure 6.2.

- o at a slightly higher temperature and oxidative conditions
    - ▪ T = 600°C
    - ▪ $p_{O2} = 10^{-5}$ mbar
    - ▪ for 120 minutes
- • Treatment III:
    - o after another increase of temperature and oxidative conditions at
        - ▪ T = 900°C
        - ▪ $p_{O2} = 10^{-5}$ mbar
        - ▪ for 120 minutes
- • Treatment IV:
    - o the same temperature but reducing conditions at
        - ▪ T = 900°C
        - ▪ No O2
        - ▪ for 120 minutes

Table 6.1: Total number of datasets available for structure refinements after averaging over symmetry-equivalent structure factors considering the P4mm surface symmetry.

Treatment	# F	#CTR	∅ ΔF
I	219	7	10%
II	217	7	10%
III	208	7	10%
IV	205	7	10%

The data measured after each of the above treatments will be labeled with "Treatment I" to "Treatment IV" hereafter for convenience.

Figure 6.1 shows the reciprocal in-plane map of YSZ(100) using the selection rules given in equation (4.8) with the measured CTRs marked with rectangles. Eleven CTRs were measured after treatment I and nine CTRs after treatments II, III and IV. Integration and averaging of the data was performed using ana and ave (see section 4.1.5). Averaging over symmetry equivalent structure factors using the P4mm symmetry of the surface, results in a huge set of data given in Table 6.1. Hence, there are seven CTRs with very good errors after each treatment available for structure refinements.

These CTRs are shown in Figure 6.2. A closer look reveals that there are no major changes between the CTRs measured after treatment I and II as well as between the CTRs measured after the treatments III and IV. Thus, there is no relevant difference of the surface structure between a treatment at 400°C and 600°C at oxidizing conditions. And more interestingly, no changes in the surface structure are observed between a treatment at 900°C and oxidizing or reductive conditions.

This impression is consolidated by the reflectivity curves measured after each treatment and shown in Figure 6.3. Major differences are seen between the curves measured after treatments I/II and treatments III/IV, only. A fit of these curves (see appendix B for fitting parameters) leads to σ surface roughnesses of 1.2 Å for the surface after treatment I and 1.7 Å for the surface after treatment IV.
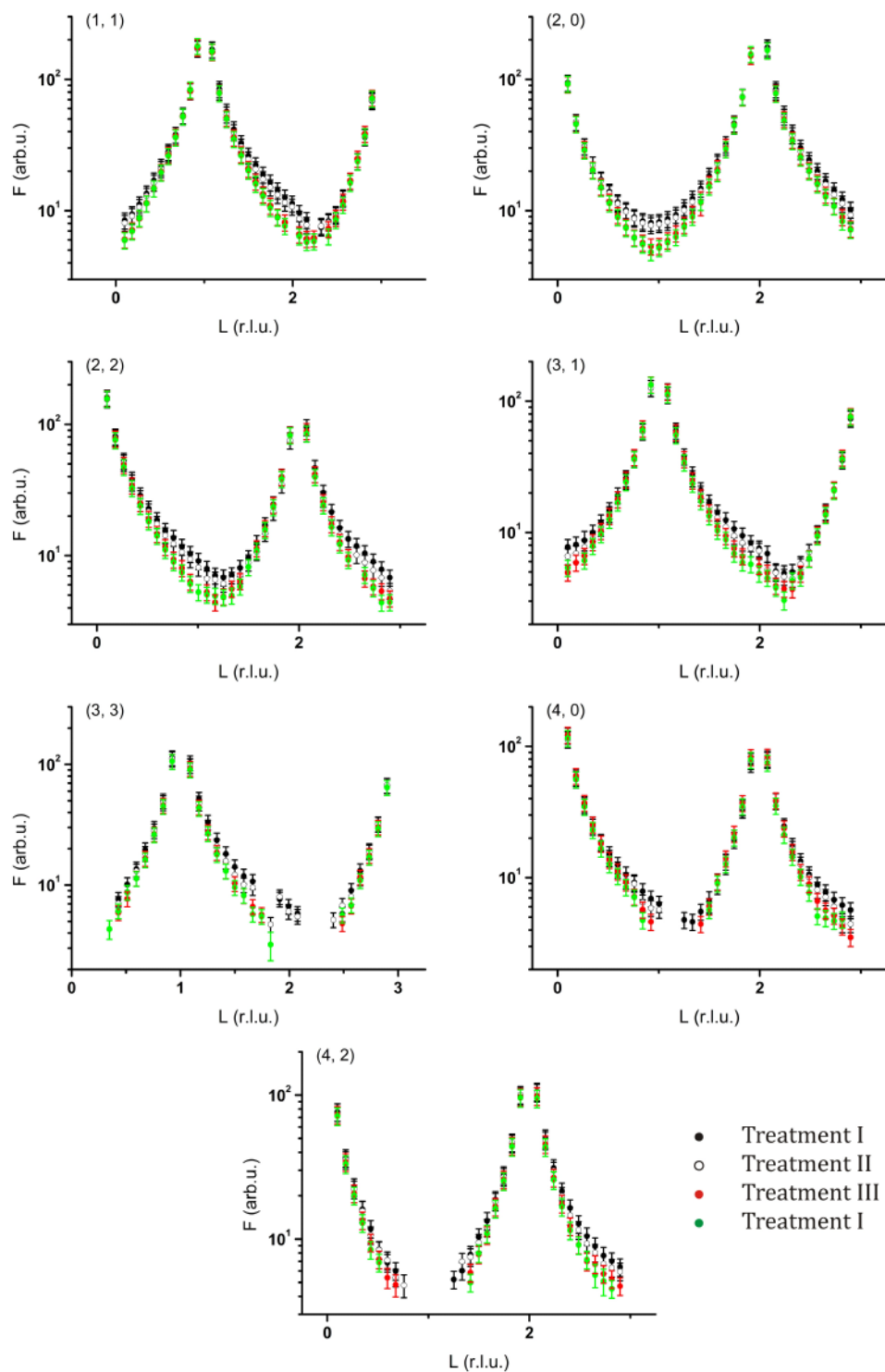
Figure 6.2: Measured CTRs after the four treatments given above and averaging. CTRs only show major differences after the treatments I/II and II/IV.
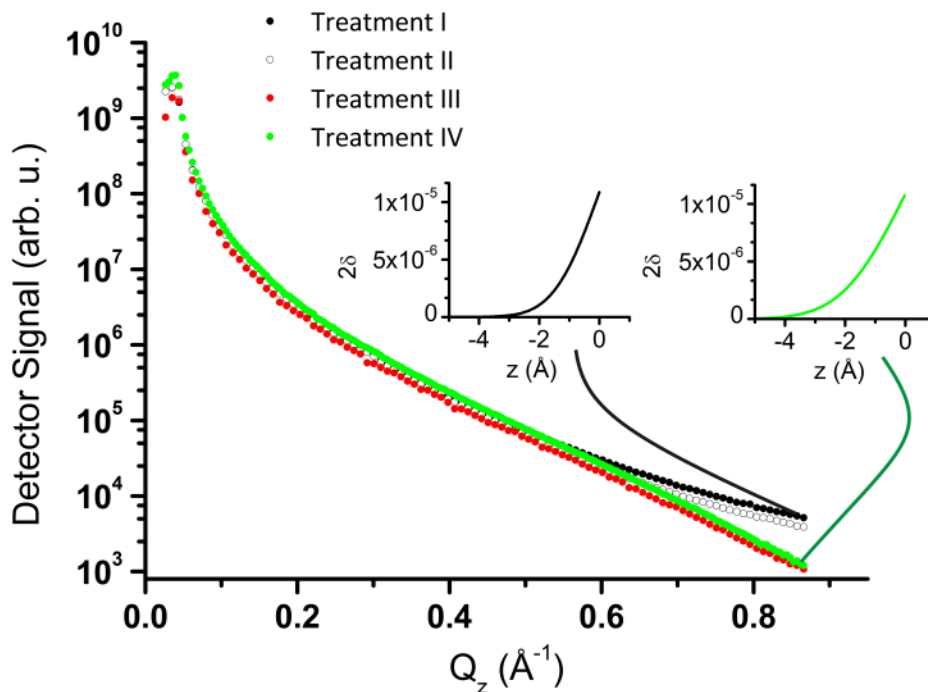
Figure 6.3: Reflectivity curves measured after treatments I to IV. It is clear to see that major differences only occur after treatment II. That is, there is no change between the surface reflectivity after treatments I and II and treatments III and IV. Together with the measured CTRs shown in Figure 6.2, this points to only two considerably different surface structures after these four different conditions. The difference between the curves is given by rms surface roughnesses of 1.2 Å and 1.7 Å after treatment I and IV, respectively. The insets show density profiles resulting from the according fits.

It can Thus be concluded that there are just two different surface structures to handle after the four different treatments. This fact can be attributed to the chemical potentials which do not change considerably between the conditions I/II and III/IV (see [197]).

These considerations lead to the decision to perform surface refinements using either the data measured after treatment I or after treatment IV.

6.1.3 Structure Refinements

The Tasker model introduced in section 3.2 show that the YSZ(100) orientation has a polar surface. Polar surfaces are known to undergo considerable surface

Bulk-like   (1 x 1) reconstructed

Topview

Sideview

- Zr
- O - bulk
- O - surface
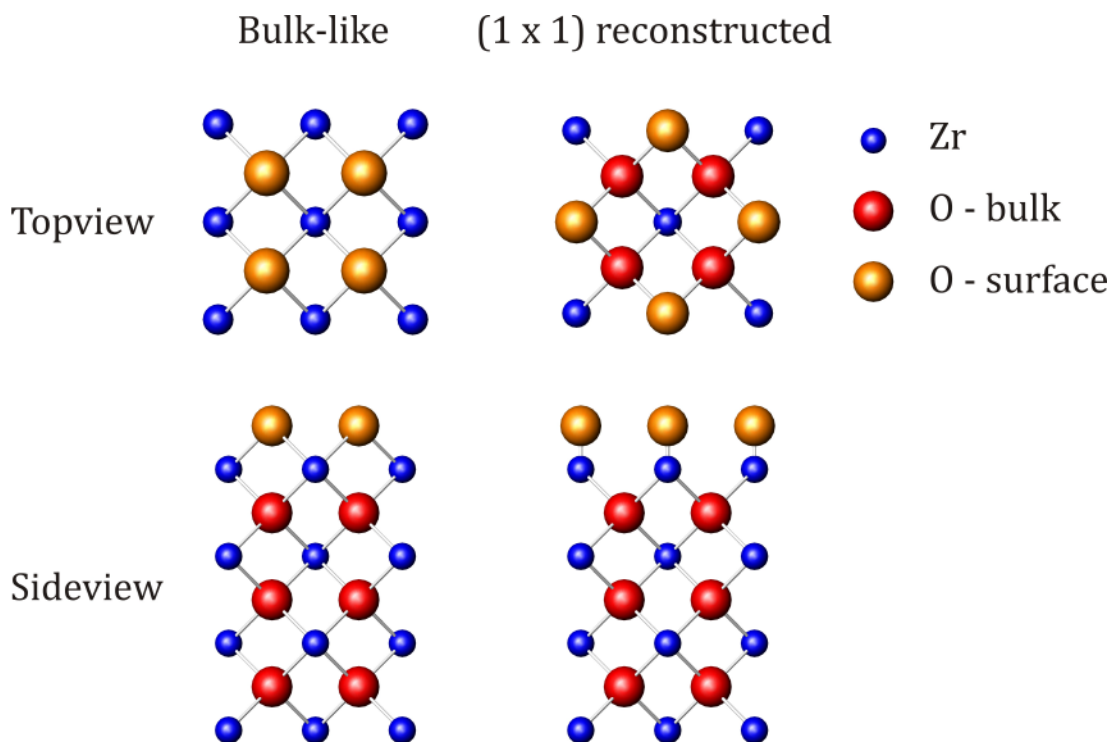
Figure 6.4: (1 x 1) reconstructed surface proposed from ion-scattering experiments [17]. The left part shows a bulk-like, oxygen terminated structure. To construct the reconstruction, the topmost oxygen layer, illustrated as orange balls, are rotated by 45°. The resulting structure is shown in the right part. Here the surface oxygen atoms sit above the underlying metal atoms. These two surfaces were used as starting points for structure refinements.

structure changes in order to neutralize the surface polarity. These changes are often reconstructions of the surface or surface faceting (see [21; 118] and references therein). Since there is an experimental work reporting a (1 x 1) reconstruction of the YSZ(100) surface [18] this model and a bulk-like structure were used as starting points for surface structure refinements.

It is important to emphasize that only non-anomalous / normal SXRD data are available for this surface. A direct distinguishing between Zr and Y is hence not possible, as described in section 4.1.3. This inability makes the use of the Zr-shift model difficult since an interpretation of the resulting models will be ambiguous.

The refinement results presented here are thus restricted to the fluorite model. Therefore only oxygen and metals will be distinguished and all metals are restricted

to be Zr. This is a proper assumption because the difference of one electron between Y and Zr cannot be resolved. The approach is to use two oxygen terminated fluorite surfaces as a starting point (see section 3.2.3) for the refinements and compare the results to find out proper surface structure models for the different conditions.

Refinements were done as described in section 4.1.5.4 using a cubic unit cell with the lattice constant

$$a = 5.14 \, \text{Å} \qquad\qquad (6.1)$$

according an yttria concentration of 9.5% [71].

The static DW-factors were taken from Table 2.1 and the „Robach extension" in rod was used in order to account for oxygen vacancies created by yttria doping. Each metal (4a) fluorite site is fully occupied and each oxygen (8c) fluorite site is occupied 95.25% according the chemical composition $Y_{0.19}Zr_{0.81}O_{1.905}$.

The (1 x 1) reconstructed surface model [18] was constructed by placing the topmost oxygen atoms above the underlying Zr atoms as described in section 2.5.3 and shown in Figure 6.4. The oxygen atoms are set to a distance of 1.26 Å to the underlying Zr atoms which is the {100}-layer distance of the bulk.

The bulk-like oxygen termination without a reconstruction is constructed by a truncation of the bulk above an oxygen layer and is shown in the left part of Figure 6.4.

6.1.3.1 Structure after Treatment I

Using the surfaces described above with the Bulk DW-factors lead to agreement factors of

$$\chi_N^2(1 \text{ x } 1) = 12.0 \qquad\qquad (6.2)$$

for the reconstructed surface and

$$\chi_N^2 = 10.3 \qquad\qquad (6.3)$$

for the bulk-like structure using equation (4.25) and showing both surfaces similar agreements. The resulting CTRs are shown in Figure 6.5.
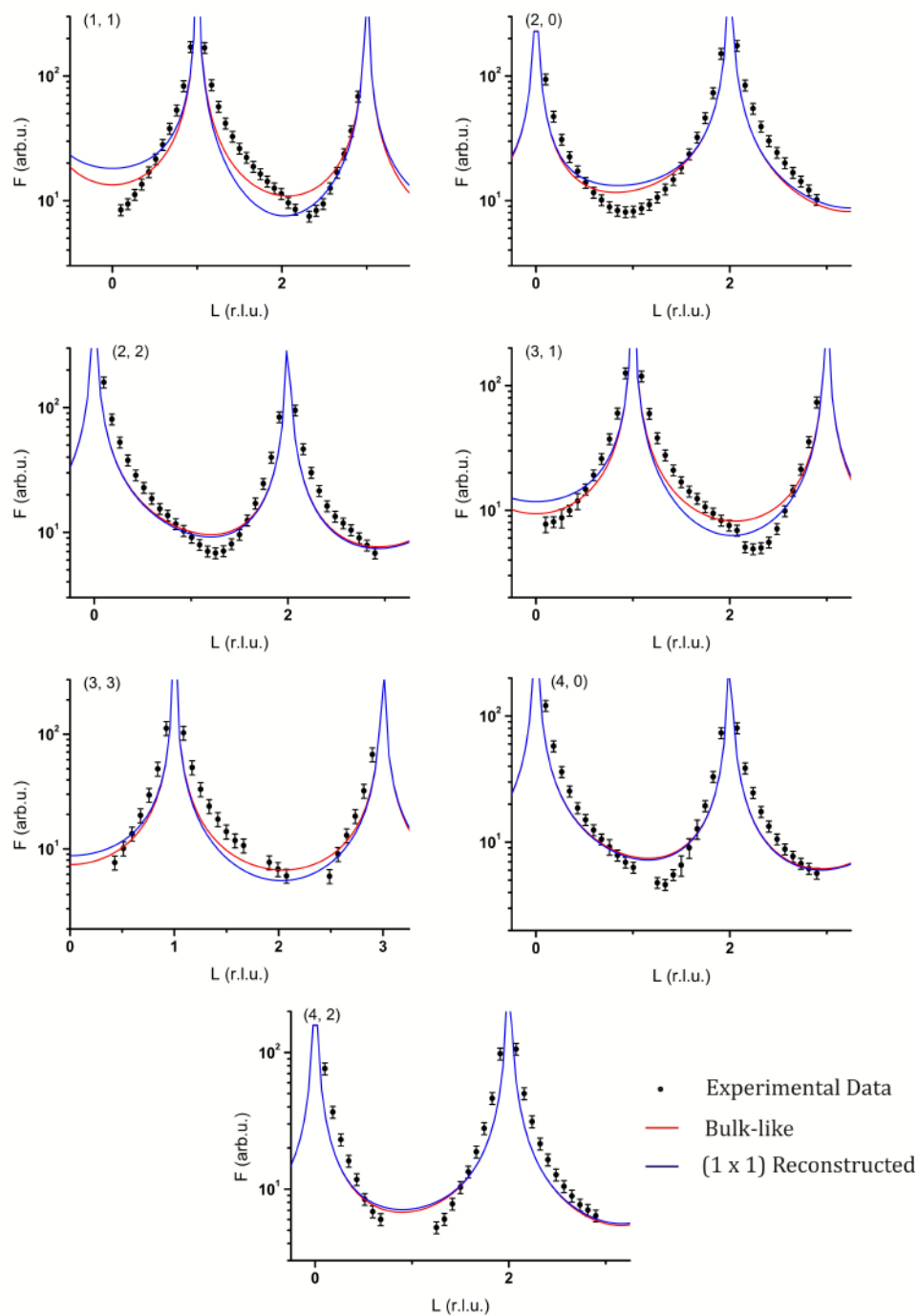
Figure 6.5: Experimental data measured after treatment I (black points) and resulting CTRs from the unreconstructed (red lines) and reconstructed (blue lines) surfaces before the refinement leading to normalized agreement factors of 5.2 and 6.2, respectively.

As a first fitting attempt, the two topmost layers were allowed to displace out-of-plane and the static Debye-Waller factor of Zr was refined as well. The DW of oxygen turned out to have no influence on the fit. These parameters together with a β-roughness parameter lead to the agreement factors 2.2 and 1.4 for the (1 x 1) reconstructed and the unreconstructed surface, respectively. However, both fits do not show a satisfying shape agreement with the experimental data.

The best fitting results were achieved by allowing out-of-plane displacements of the two topmost layers - that is one oxygen and one zirconium layer - and their occupancies with the resulting CTRs shown in Figure 6.7. The resulting parameters are shown in Figure 6.6 and Table 6.2. Five parameters were thus used for this fits:

- one scaling parameter
- two out-of-plane displacement parameters for the topmost oxygen and metallic layer
- two occupancy parameters for these layers.

The reconstructed surface is showing noticeable displacements of the oxygen and metal layer. While the oxygen layer is moving away from the bulk by 0.73 Å, the metal layer is pushed towards the bulk by 0.20 Å. These displacements lead to a total distance of the topmost layers of 2.19 Å.

The concentration of both, oxygen and Zr atoms are decreased dramatically to 19% and 32% respectively which together with the displacements lead to a very good normalized agreement factor of

$$\chi_N^2(1 \text{ x } 1) = 1.5 \tag{6.4}$$

Table 6.2: Concentration of the topmost Zr and O layer resulting from structure refinements starting with a (1 x 1) reconstructed and a bulk-like model. The values for the different models are very similar.

	(1x1)-reconstructed	Bulk-like
O Concentration	18.7±0.1%	11±2%
Zr Concentration	31.80±0.01%	31.96±0.01%

Starting with the unreconstructed surface and using the same parameters leads to a similar agreement factor of

$$\chi_N^2 = 1.5 \qquad\qquad (6.5)$$

In this fit all resulting parameters but the oxygen displacement show very similar values as for the fit using the (1 x 1) structure. Zr atoms are shifted 0.19 Å towards the bulk while oxygen atoms virtually remain at their bulk positions. At the same time the concentration of the atoms shows drastic changes. The Zr concentration is reduced to 32% and the oxygen concentration heavily drops to 11%.

Both resulting models point to a displacement of the topmost Zr atoms towards the bulk, while having a huge oxygen vacancy concentration at the surface. Such a behavior is consistent since the Zr atoms are attracted more strongly by the underlying oxygen layer due to a depletion of binding to the topmost layer.

Note that a DFT study predicts a (1 x 1) reconstruction for yttria enriched surfaces only [12]. In this study, the topmost oxygen atoms of the (1 x 1) reconstructed surface are calculated to shift 0.59 Å away from the bulk which is in
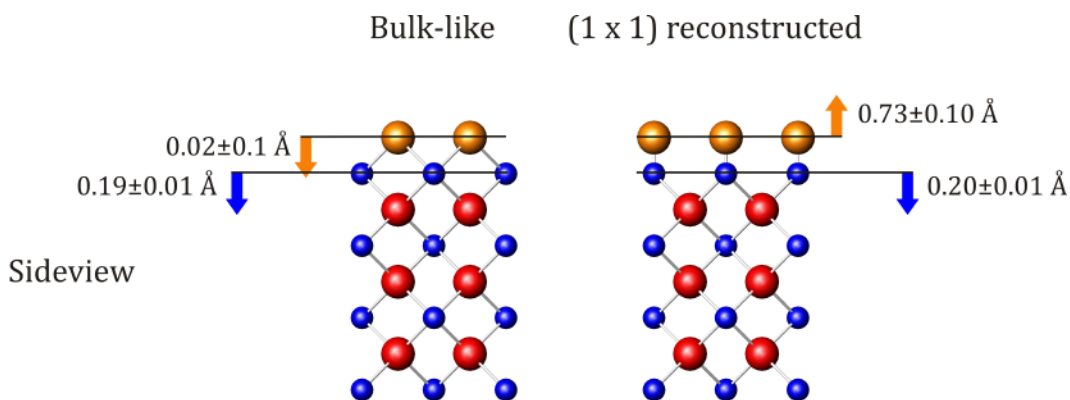
Figure 6.6: Starting from a bulk-like and a (1 x 1) reconstructed surface, very good agreement factors are achieved by refining the out-of-plane displacements of the two topmost layers and their occupancies. In both cases, Zr atoms (blue) show very similar displacements into the bulk, caused by a high oxygen vacancy concentration in the topmost layer. The oxygen displacement and vacancies resulting from the reconstructed surface are in a very good agreement with DFT calculations (occupancies are given in Table 6.2). This structure is therefore suggested for the surface after treatment I implying a Y-enriched surface. Displacements are given with respect to bulk positions.

Figure 6.7: Structure refinements using the data after treatment I and either a (1 x 1) reconstructed (blue lines) or a bulk-like surface (red lines) as starting points. Both fits deliver very good and similar agreement factors.

very good agreement with the value resulting from the fit of this work.

In spite of the excellent agreements of both fits with the experimental data, this fact points the structure of the studied surface to be (1 x 1) reconst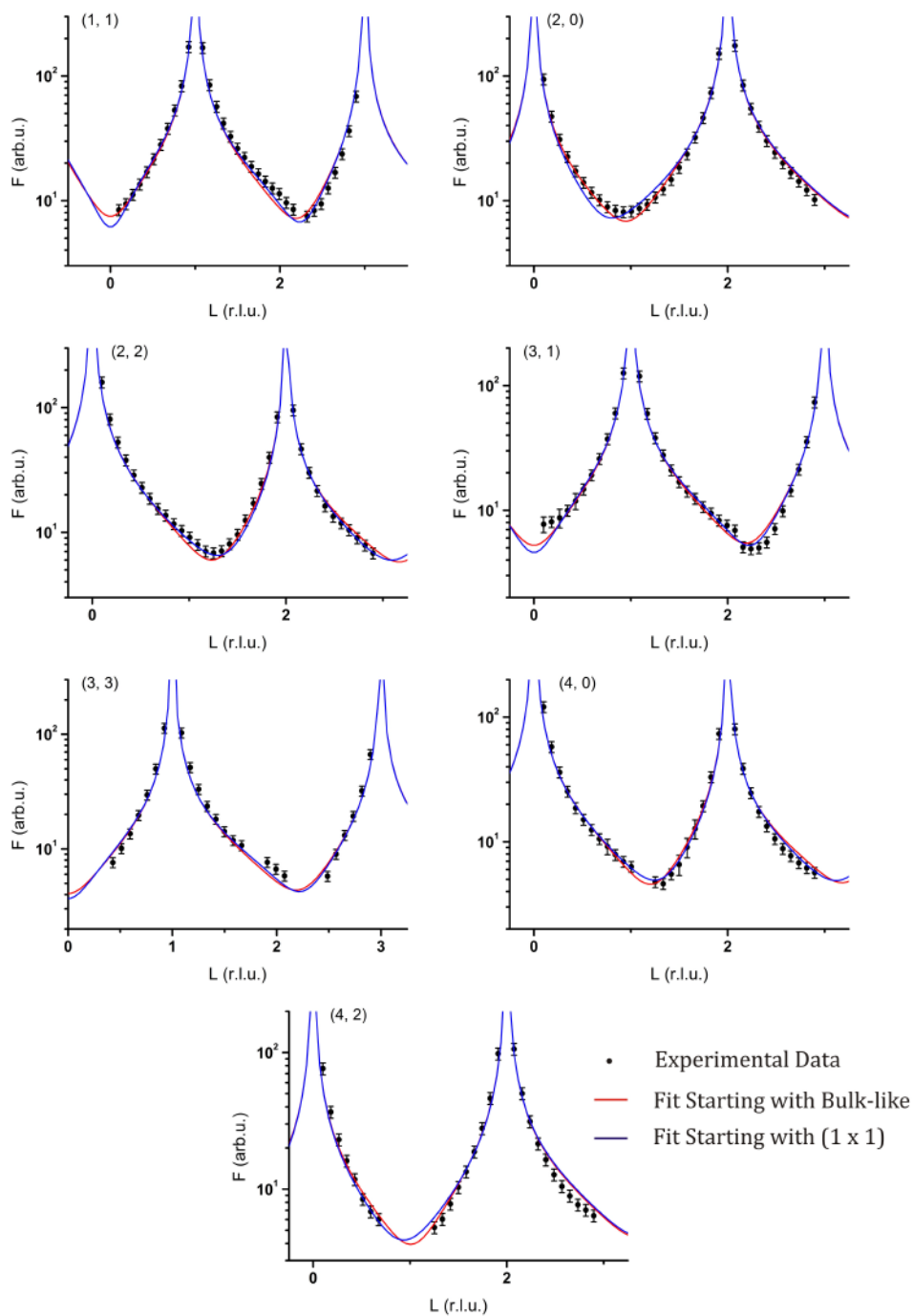ructed. It can therefore be concluded that the surface is yttria enriched after treatment I. It is however important to notice that the surface is highly defective. Although the experimentally reported oxygen vacancy concentration of 10% [18] is far below the value derived here, the DFT calculations agree with the high number of defects due to a high concentration of Y [12] (see also section 2.4.2 for the creation of O vacancies through Y doping). The model derived here is thus in better agreement with the DFT calculations as the formally proposed structure.

6.1.3.2   Structure after Treatment IV

A clear result regarding the surface reconstruction is obtained after a treatment at 900°C. Note that at this temperature reducing and oxidative conditions lead to a similar structure, as discussed in the previous sections.

Both unrefined surfaces again show similar agreement with the experimental data of

$$\chi_N^2(1 \ x \ 1) = 17.3 \qquad\qquad (6.6)$$

for the reconstructed surface and

$$\chi_N^2 = 15.1 \qquad\qquad (6.7)$$

for the bulk-like surface using equation (4.25) both poorer than the agreement with the data measured after treatment I, however. The resulting CTRs are shown in Figure 6.8.

The best refinements for the (1 x 1) reconstructed surface were achieved when using the same fitting parameters as for the previous fit. In contrast to the fits for the structure after treatment I, the oxygen concentration of the topmost layer was immediately fitted to be 0 even when the Zr-shift model was used as a starting point tentatively. This is a clear evidence for the surface not to be reconstructed after treatment IV. The reason therefore will become clear in the following.
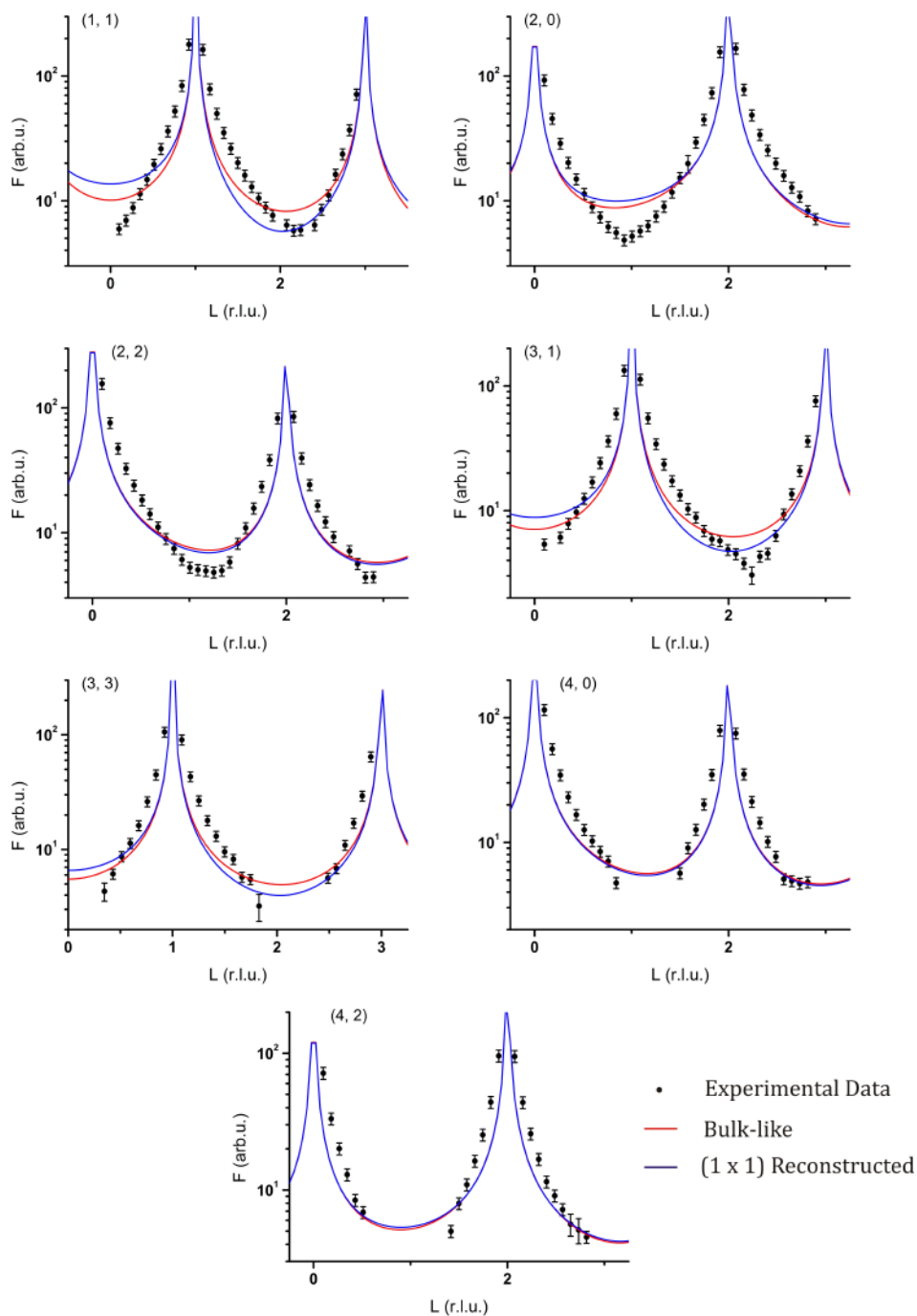
Figure 6.8: Agreement of the unrefined (1 x 1) reconstructed (blue lines) and the bulk-like (red-lines) surface with the CTRs measured after treatment IV showing similar behavior. The agreements are, however, poorer than with the data measured after treatment I.

Table 6.3: Concentration of the topmost O layer and the two topmost Zr layers Zr1 and Zr2 (see Figure 6.9).

	Bulk-like
O Concentration	53 ±2%
Zr1 Concentration	56.7±0.6%
Zr2 Concentration	89.4±0.5%

In order to get satisfying refinement results for the bulk-like surface, the concentration of one additional metal layer had to be refined. The contribution of a second layer to the CTRs is also indicated in the smooth oscillations of the measured data. This leads to a total of six fitting parameters:

- ones scaling factor
- two displacement parameters for the two topmost layers
- two occupancy parameters for each of these layers
- one additional occupancy parameter for the second topmost metal layer

The topmost Zr layer will be called Zr1 and the second topmost Zr layer denoted Zr2 in order to distinguish them.

The resulting displacements and concentrations are shown in Figure 6.9 and Table 6.3. The fit delivers displacements of the topmost oxygen and metal layer towards the bulk by 0.11 Å and 0.05 Å, respectively. These shifts are less distinct than for the state after treatment I but both show to the same direction.

The reason for the less enhanced shifts of the topmost layers is given by the occupancy of the atoms in the two topmost layers which strongly increase compared to the state before, to have values of 53% for oxygen and 57% for Zr1. The topmost metallic layer thus has a more balanced binding environment and the displacements become smaller. The content of the second Zr layer (Zr2) is somewhat reduced to 89%.

Since the (1 x 1) reconstruction which requires an yttria enriched surface vanishes, a treatment at 900°C can be concluded to cause Zr segregation to the

surface. This segregation can moreover be expected to originate from subsurface layers due to the decrease of the second Zr layer (Zr2) concentration.

 The resulting fit parameters lead to an excellent agreement of the according CTRs shown in Figure 6.10 with the experimental data, even at unusually looking positions like the flat minimum around (2, 2, 1) and the dip around (1, 1, 2.25). The very good agreement is also represented by a normalized agreement factor of

$$\chi_N^2 = 1.2 \tag{6.8}$$

A 1:2 ratio of the oxygen to metal concentrations proposed for the compensation of the surface polarity [12], does not result from the model here. Moreover the (1 x 1) reconstruction can be excluded at this state. A possible stabilization mechanism for this surface is thus the creation of defects in subsurface layers as resulting from the fit of the Zr2 atoms.
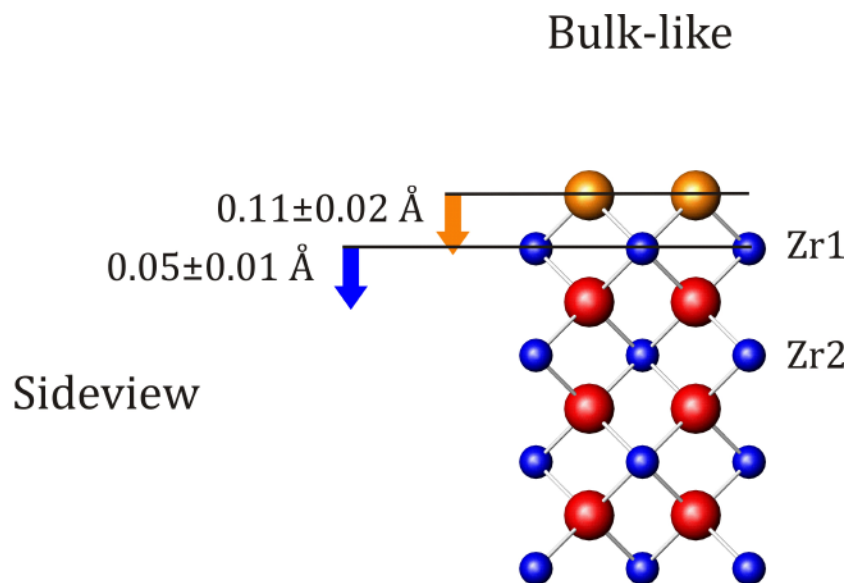
Figure 6.9: Displacements of the two topmost atom layers with respect to bulk positions for the state after treatment IV. Both layers are shifted into the bulk. The topmost oxygen layer is thereby displaced more pronounced than the Zr layer. The small shift of the Zr layer can be attributed to the more balanced number of bindings to the surrounding layers compared to the state after treatment I. Satisfactory agreement is achieved by refining the concentration of the two topmost Zr layers, called Zr1 and Zr2 respectively.
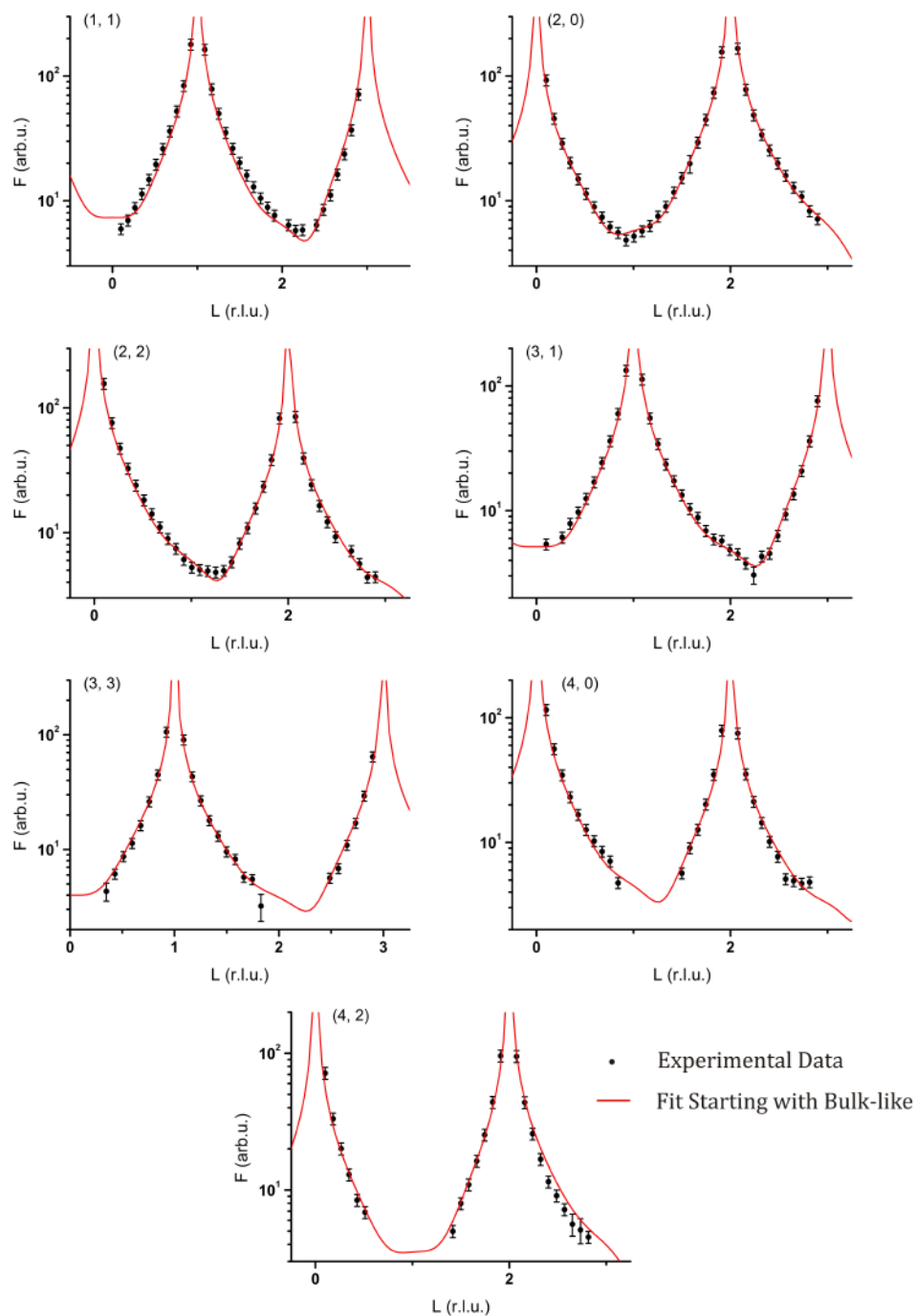
Figure 6.10: Agreement of the refined bulk-like structure (red lines) with the experimental data black dots. Very good agreement is observed even at unusually looking CTR positions.

6.1.4   Summary

The atomic structure of the polar YSZ(100) surface was studies systematically after four different treatments. A comparison of the measured CTRs and reflectivity curves shows that the surface does not considerably change between temperatures of 400°C and 600°C at oxidative conditions. It also turns out that there is no major structural change between an oxidative and reductive treatment at 900°C. This behavior is attributed to the predominant influence of the temperature on the chemical potential at high temperatures.

Since only non-anomalous/normal SXRD data are available for this surface which do not allow distinguishing between Zr and Y, the fluorite model was used as a starting point for structure refinements including intrinsic oxygen vacancies, however. A (1 x 1) reconstruction of this surface was reported recently [18], which motivated the use of a (1 x 1)- and a bulk-like oxygen-terminated surface as starting points.

The best refinement results using the dataset measured at oxidative conditions at 400°C were achieved fitting out-of-plane displacements of the topmost oxygen and metallic layers and the concentration of their atoms. Both, the (1 x 1) reconstructed and the unreconstructed surfaces deliver very good agreements with the measured data after this refinement.

The reconstructed surface, however, shows very good agreement with a theoretical study [12]. In this DFT investigation, the (1 x 1) reconstruction is predicted for an yttria enriched surface where the topmost oxygen atoms are displaced outwards by 0.59 Å, compared to 0.73 Å (±0.10 Å) in the fit. An yttria enriched surface for the surface studied at the condition here is thus concluded. The $(1\ x\ 1)$ reconstruction is moreover in line with an ion scattering study [18].

The proposed model after this treatment contains a huge number of surface vacancies. Only 18% of the oxygen and 32% of the metal sites are occupied. The high number of oxygen vacancies in the topmost layer causes a depletion of binding partners for the underlying metallic layer. This leads to a stronger attraction of this atomic layer by deeper layers and displaces it towards the bulk by 0.20Å.

The structure of the surface after a treatment at 900°C changes significantly. Using the same fitting parameters, the concentration of the (1 x 1) reconstructed oxygen atoms is determined to be 0, even if using the Zr-shift model. There is therefore no reconstructed surface after such a treatment. Best refinements were achieved when the concentration of an additional metallic layer was fitted in the bulk-like model.

Here, the topmost oxygen and metallic layer are shifted towards the bulk by 0.11 Å and 0.05 Å, respectively. The less distinct shift of the metallic layers is due to a strongly increased occupancy of the topmost oxygen layer to 57%, which leads to a more balanced binding situation of the topmost metallic layer and thus a smaller shift of it.

The concentration of the topmost metallic layer increases to 53% which together with the lift of the (1 x 1) reconstruction and the requirement of an yttria enriched surface for such a reconstruction [12] lead to the conclusion that Zr is segregating to the surface. The concentration of the additional metallic layer is determined to be 89% indicating the segregated Zr atoms to originate from subsurface layers.

Both suggested models for a polarity neutralization of the YSZ(100) surface – a (1 x 1) reconstruction or an oxygen to metal ratio of 1:2 in the topmost layers – are not resulting from the model proposed for the state after the heat treatment. A possible way to neutralize the polarity of the surface at this state is thus the creation of defects in subsurface layers, indicated by the decreased concentration of the second highest metallic layer.

The segregation of zirconia to the surface and the increased oxygen concentration there can be explained by considering basic properties of YSZ. At high temperatures, oxygen atoms become mobile and can segregate to the surface. At the same time, the high metal vacancy concentration at the surface leads to a decreased strain attracting Zr atoms to occupy sites here. At high temperatures, Zr atoms have enough mobility and segregate to these energetically more favorable sites at the surface.

6.2   Growth and Shape Change of Nickel Nanoparticles

This section presents the growth of Ni on the YSZ(100) surface under UHV conditions. The resulting shape of the nanoparticles (NP) studied with SXRD will be the topic of a subsequent section. Following the path of the previous chapter, the effect of a heat- and an oxygen- treatment will be discussed as well. These conditions are of importance for this system, due to the operating conditions of SOFCs at high temperatures and reductive conditions. The oxygen treatment is of interest since a prevention of NP oxidation is an important task in state-of-the-art SOFCs.

6.2.1 Growth

The nickel-growth experiments were performed on the very same sample that was used for the surface structure determination without being taken out of UHV-conditions. That is, the structure of the substrate surface is known from section 6.1.3.2. The SXRD experiments were performed at X-ray energies of 10 keV and a point detector was used for all measurements. The particles were characterized after the sample cooled down to room temperature and the according gases were pumped out in order to prevent structural changes of the NPs during the characterization.

As for the growth of Ni on YSZ(111), an electron beam evaporator was used for the physical vapor deposition (PVD) (see section 4.3)

Following parameters were applied for the nickel growth:

- Substrate temperature: T = 550°C
- Evaporation time: 30 minutes
- Flux current: ~25 nA
- Growth rate: ~0.19 nm/minute

A higher substrate temperature than in the case of Ni growth on the YSZ(111) surface was hence chosen. With this elevated temperature a single type of epitaxial growth of Ni was aimed to be achieved.

6.2.2 Particle Shape

Figure 6.11 shows an AFM image measured *ex-situ* after the evaporation where NPs on top of the substrate are observed. This image was measured using a different AFM machine than for the NPs on the YSZ(111) surface which leads to a lower resolved image. Profile scans along the NPs indicate particles with heights around 3
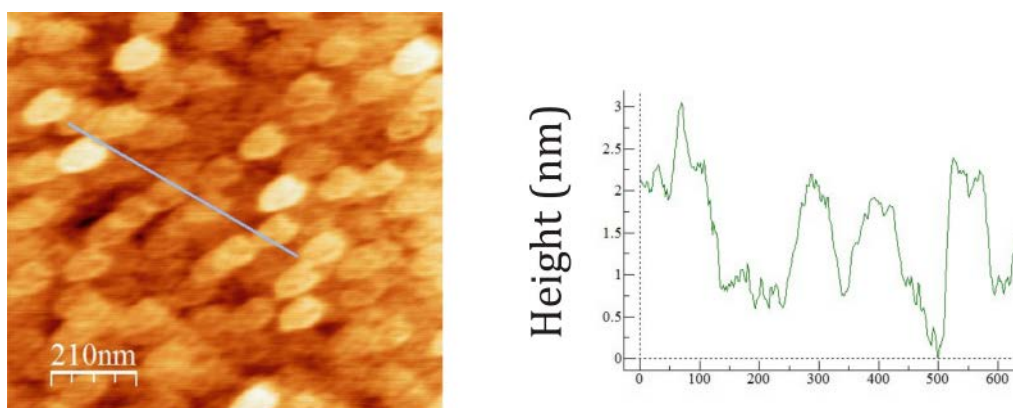
Figure 6.11: Left: AFM image of the Ni-evaporated substrate measured *ex-situ*. It shows homogenously distributed nanoparticles. Right: a profile scan along the NPs (indicated with a grey line in the left part) reveals the particles to have heights around 3 nm.

nm.

A reflectivity curve measured *in-situ* after the evaporation and cool down of the system is shown in Figure 6.12. Oscillations clearly point to an additional layer on the single-crystal YSZ(100) surface. The curve can be fitted with a layer of the thickness

$$d = 40.0 \text{ Å} \tag{6.9}$$

and thus in a good agreement with the AFM image within its resolution (see appendix B for all reflectivity fitting parameters).
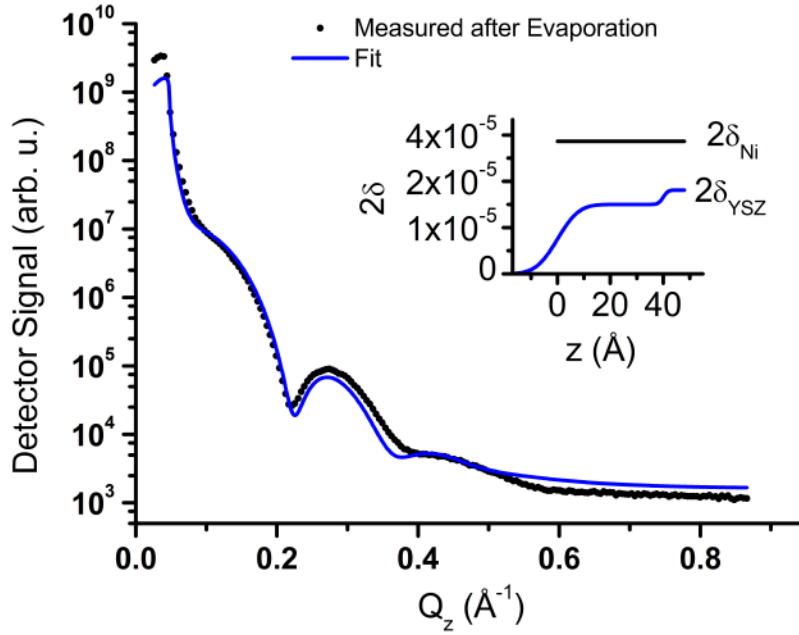
Figure 6.12: Reflectivity curve measured directly after the evaporation and cool down. A fit results in the density profile shown in the inset and delivers the height of the NPs to be 40 Å. The coverage of the surface is derived from the electron density and is determined to be 52%.

In order to determine the coverage of the surface, the electron density of this layer was fitted as well resulting to a 2δ value of

$$2\delta_{\mathrm{Fit}} = 1.8 \cdot 10^{-5} \tag{6.10}$$

compared to a $2\delta_{\mathrm{Ni}}$ of $3.44 \cdot 10^{-5}$ (at 10 keV). The resulting coverage is thus calculated to be (see also section 5.2.2)

$$\Theta = \frac{2\delta_{\mathrm{Fit}}}{2\delta_{\mathrm{Ni}}} = 0.52 \triangleq 52\% \tag{6.11}$$

The lattice constants of Ni and YSZ of

$$a_{\mathrm{Ni}} = 3.54 \text{ Å} \tag{6.12}$$

and

$$a_{\mathrm{YSZ}} = 5.14 \text{ Å} \tag{6.13}$$
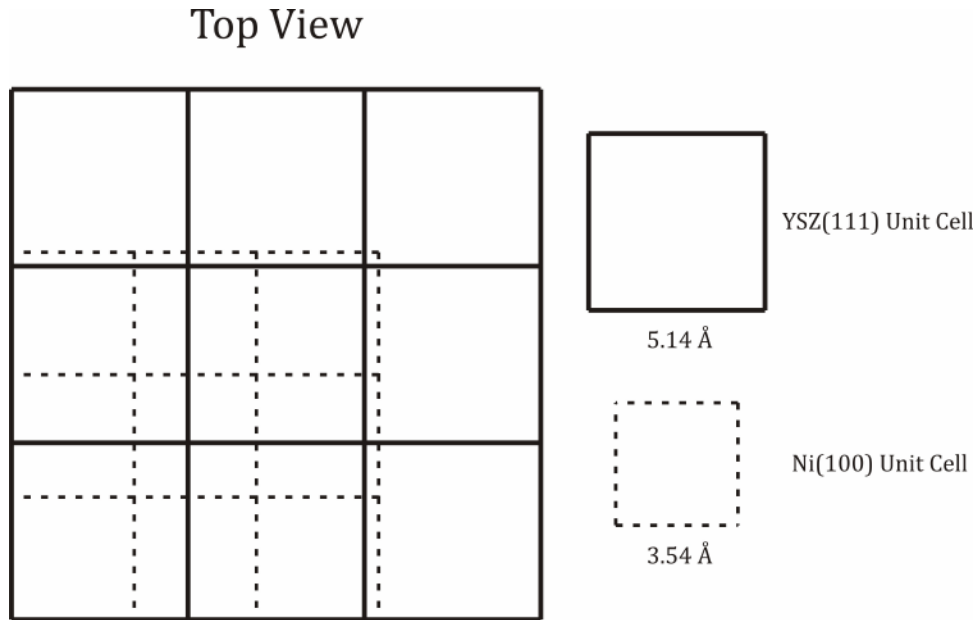
Figure 6.13: Cube on cube epitaxy of Ni(100) growth on YSZ(100). The lattice constants of 3.54 Å and 5.14 Å, respectively, lead to a mismatch of 4% when three Ni unit cells are set on top of two YSZ unit cells.

suggest two types of cube on cube epitaxial growth of (100)-oriented nickel NPs on the YSZ(100) surface. The first type is depicted in Figure 6.13 and gives the arrangement of the Ni lattice along the YSZ lattice. Hence, three Ni unit cells fit on two YSZ unit cells with the mismatch

$$\text{Mismatch}_{\text{cube/cube}} = \frac{2 \cdot 5.14\,\text{Å}}{3 \cdot 3.54\,\text{Å}} = 0.039 \sim 3.9\% \qquad (6.14)$$

The second possible epitaxy is 45° in-plane rotated cubic Ni unit cells. This means a diagonal arrangement of the Ni unit cell with respect to the substrate unit cell as illustrated in Figure 6.14. Such an epitaxy leads to an even lower mismatch at the substrate and suggests a growth such that two diagonal Ni unit cells fit on one substrate unit cell. The mismatch can thus be determined as

$$\text{Mismatch}_{45°\text{cube/cube}} = \frac{2 \cdot \cos(45°) \cdot 3.54\,\text{Å}}{5.14\,\text{Å}} = 0.020 \triangleq 2.0\% \qquad (6.15)$$

The latter epitaxy is thus more probably to grow than the first one.
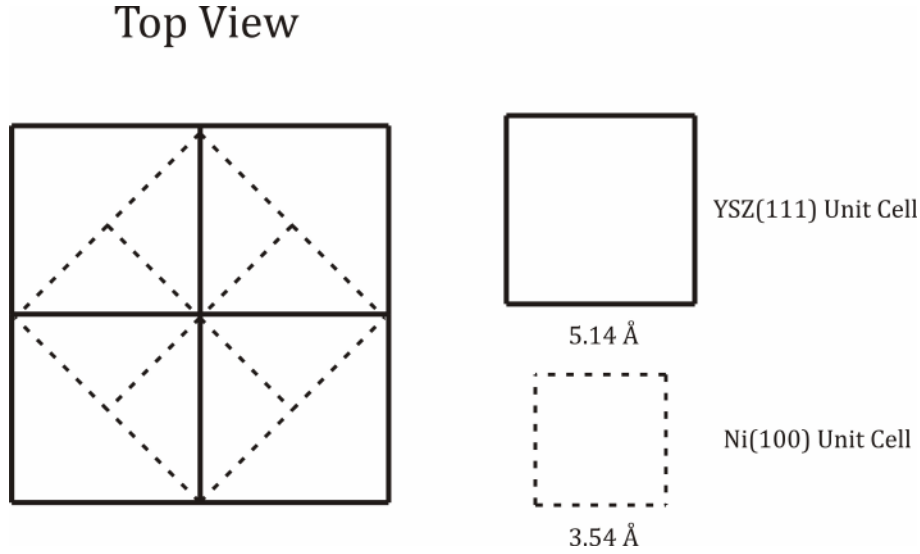
Figure 6.14: 45°-rotated cube on cube epitaxy of Ni(100) on YSZ(100). A mismatch of 2% results when two Ni unit cells are diagonally arranged on the YSZ(100) unit cell. This small mismatch indicates this epitaxy to be favored, which is however not observed.

Subscriptions of the following reciprocal coordinates will be used to allow an easy identification of the respective peaks.

- "substr" gives the reciprocal coordinates of the YSZ(100) substrate
- "bul" is used as a subscription for reciprocal bulk Ni coordinates

In order to observe the growth of the two growth types, scans were performed during the evaporation. The first type of scans were reciprocal $(H, 0, 0)_{substr}$-scans where the Ni $(2, 0, 0)_{bul}$ bulk Bragg peak is expected at the substrate $H_{substr} = 2.98$ (see Figure 6.16 c) for reciprocal-coordinates subscriptions) due to

$$\frac{2 \cdot 1/a_{Ni}}{1/a_{YSZ}} = \frac{2 \cdot 1/3.54\,\text{Å}}{1/5.14\,\text{Å}} = 2.98 \tag{6.16}$$

The seconds type of scans were performed along the $(H_{substr}, K_{substr}=H_{substr}, 0)$ direction where the $(4, 0, 0)_{bul}$ bulk Bragg peak of the diagonal orientation is expected at $(4.08, 4.08, 0)$ since

$$\frac{\cos(45°) \cdot 4 \cdot 1/a_{Ni}}{1/a_{YSZ}} = 4.08 \tag{6.17}$$
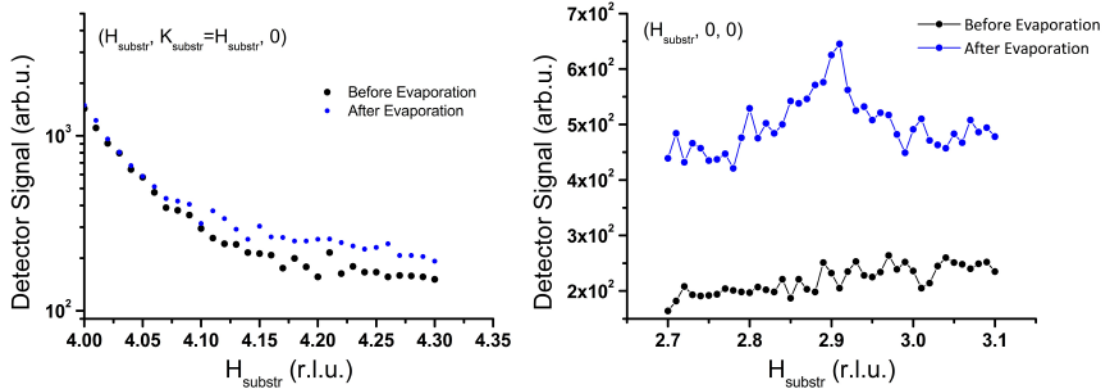
Figure 6.15: Left: a peak is expected at H_{substr} = 4.08 for the rotated cube on cube epitaxy. But there is no change visible before and after the deposition of Ni meaning that this orientation does not grow. Right: the small peak appearing at H_{substr} = 2.98 indicates the cube on cube growth of nickel on YSZ-(100). The weak intensity however, points to a rather small amount to have this orientation.

Both of these scans measured before and after the evaporation are shown in Figure 6.15. They indicate that the rotated cube on cube orientation is not detectable in spite of the very good lattice mismatch (the allover signal increase in this scan is due to fluorescence of Ni at 10 keV). The cube on cube epitaxy shows a weak $(2, 0, 0)_{bul}$ Bragg peak at $(2.98, 0, 0)$ $_{substr}$ pointing to a rather small fraction of the particles to have a (100) orientation.

Instead a Ni $(2, 0, 0)_{bul}$ Bragg peak was found at $(2.9, 2.9, 0)_{substr}$ and another one at $(2.9, 2.9, 2.5)_{substr}$ as shown in Figure 6.16 a). The L_{substr}-distance between these peaks is in a very good agreement with (111)-oriented Ni since

$$\frac{c^*_{Ni-(111)}}{a^*_{YSZ}} = \frac{\frac{1}{\sqrt{3} \cdot a_{Ni}}}{1/a_{YSZ}} = 0.836 \tag{6.18}$$

and

$$3 \cdot 0.836 = 2.508 \tag{6.19}$$

indicating the existence of (111)-oriented NPs.

When a rocking scan was performed around the peak at $(2.9, 2.9, 0)_{substr}$, peaks were detected each 30° as shown in Figure 6.16 b). Six of these peaks are numerated
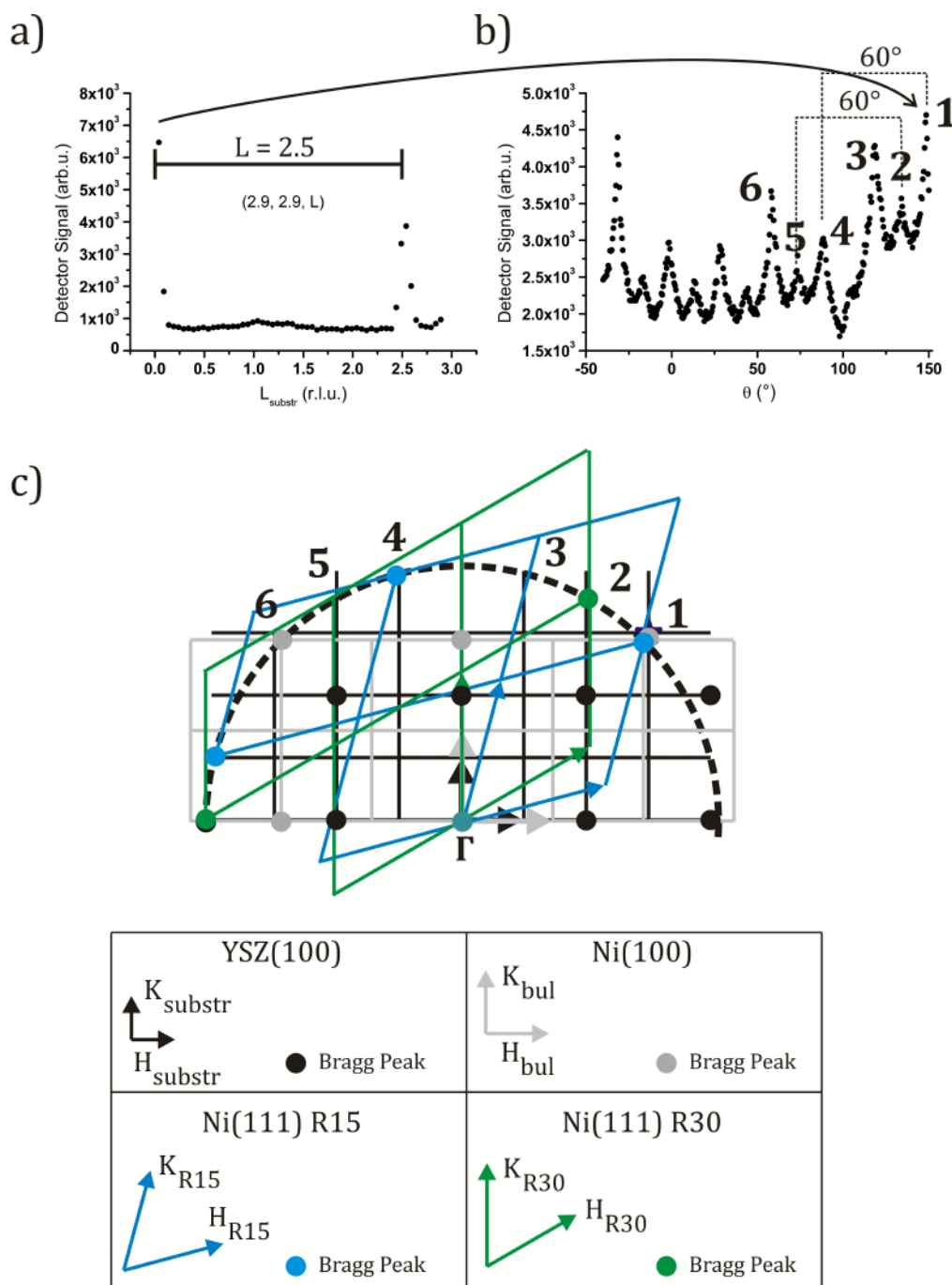
Figure 6.16: a) Reciprocal $(2.9, 2.9, L)_{substr}$ scans show peaks at an L-distance of 2.5 indicating a (111) orientation of Ni. When rocking scans were performed around this peak denoted 1 in b), peaks were observed at distances of 30°. The 60° symmetry of the hexagonal (111) orientation is discovered using the reciprocal map in c). Here Peaks 1 to 6 of the scan in b) are drawn as well and can be identified using the reciprocal unit cells of the substrate, (100)-oriented Ni and 15° as well as 30° in-plane-rotated (111)-oriented Ni.

and can be identified using the in-plane reciprocal map illustrated in Figure 6.16 c). Peaks with a distance of 60° can thus indeed be assigned to (111)-oriented Ni. However, the reciprocal unit cells are rotated in-plane by angles of 15° and 30° with respect to the substrate. These orientations are appointed "Ni-R15" and "Ni-R30" hereafter for convenience.

Introducing two new subscriptions:

- "R15" for the reciprocal coordinates of the (111)-oriented and 15° in-plane rotated Ni coordinates and
- "R30" as a subscription for the (111)-oriented and 30° in-plane rotated reciprocal Ni coordinates,

the six peaks can be assigned as follows (see Figure 6.16 c):

- Peak 1: $(1, 1, 0)_{R15}$ Bragg peak of Ni-R15
- Peak 2: $(1, 1, 0)_{R30}$ Bragg peak of Ni-R30
- Peak 3: $(1, 1, 0)_{R-15}$ Bragg peak of -15° in-plane rotated and (111)-oriented Ni. This orientation exists due to symmetry reasons.
- Peak 4: $(-1, 2, 0)_{R15}$ Bragg peak of Ni-R15
- Peak 5: $(-1, 2, 0)_{R30}$ Bragg peak of Ni-R30
- Peak 6: $(-2, 2, 0)_{bul}$ Bragg peak of (100)-oriented Ni

We have hence three different types of growth orientations:

- (100)-oriented cube on cube growth
- (111)- oriented and 15° rotated (Ni-R15)
- (111)-oriented and 30° rotated (Ni-R30)

These growth orientations of Ni on YSZ(100) are in line with former studies on Ni films and island on this substrates [19; 20] (see also section 2.6.3).

The existence of the rotated Ni-R15 particles is also supported by the measurements of reciprocal maps. Figure 6.17 shows a $(H, L)_{substr}$ -map at $K_{substr} = 2.9$. Three peaks are observed in this map: a peak at $(3, 2.9, 1)$ which is the tail of the substrates $(3, 3, 1)$ Bragg peak. Two other peaks are found at $(2.9, 2.9, 2.5)_{substr}$ which is identified as the $(1, 1, 3)_{R15}$ Bragg peak of the Ni-R15 orientation. The remaining peak starts to appear around $(2.9, 2.9, 0)_{substr}$ which is identified as the (1,
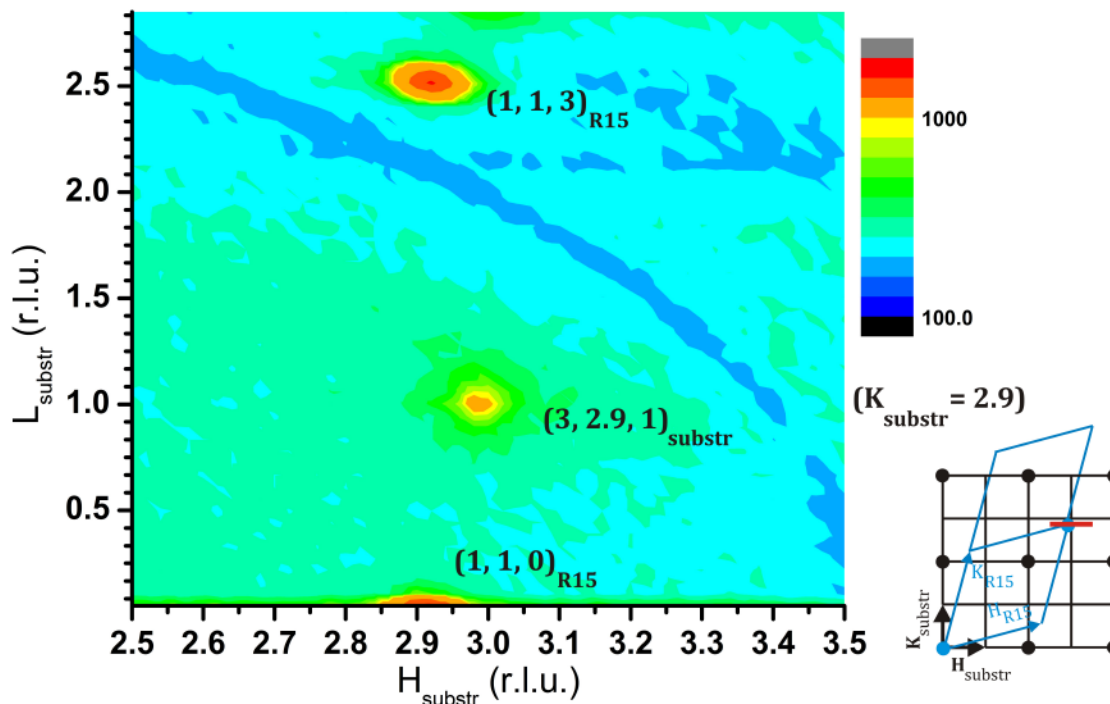
Figure 6.17: Reciprocal (H-L)$_{substr}$ map at K$_{substr}$=2.9. The red line in the sketch shown in the lower right part illustrates the scanned area. Peaks appearing can clearly be assigned to the substrates Bragg peak tail (3, 2.9, 1)$_{substr}$ and 15° in-plane rotated (111)-oriented Ni at (1, 1, 0)$_{R15}$ and (1, 1, 3)$_{R15}$.

1, 0)$_{R15}$ Bragg peak of the Ni-R15 orientation. It should be mentioned that although no signal of a twinning in the (111)-growth is observed in this map, other scans along the reciprocal L-directions proved the existence of laterally coexisting twins (see for instance Figure 6.23).

The cube on cube epitaxy and mismatch of the (100)-oriented NPs were illustrated in Figure 6.13. Figure 6.18 shows the epitaxial relationships of the rotated Ni(111) orientations. It is clear to see that while both types have reasonable mismatches in one direction, the mismatch in the other direction is rather large.

In case of the Ni-R30 NPs shown in the right part of Figure 6.18, a huge mismatch along the direction called "x" results when two Ni(111) unit cells are projected on one YSZ(100) unit cell and thus
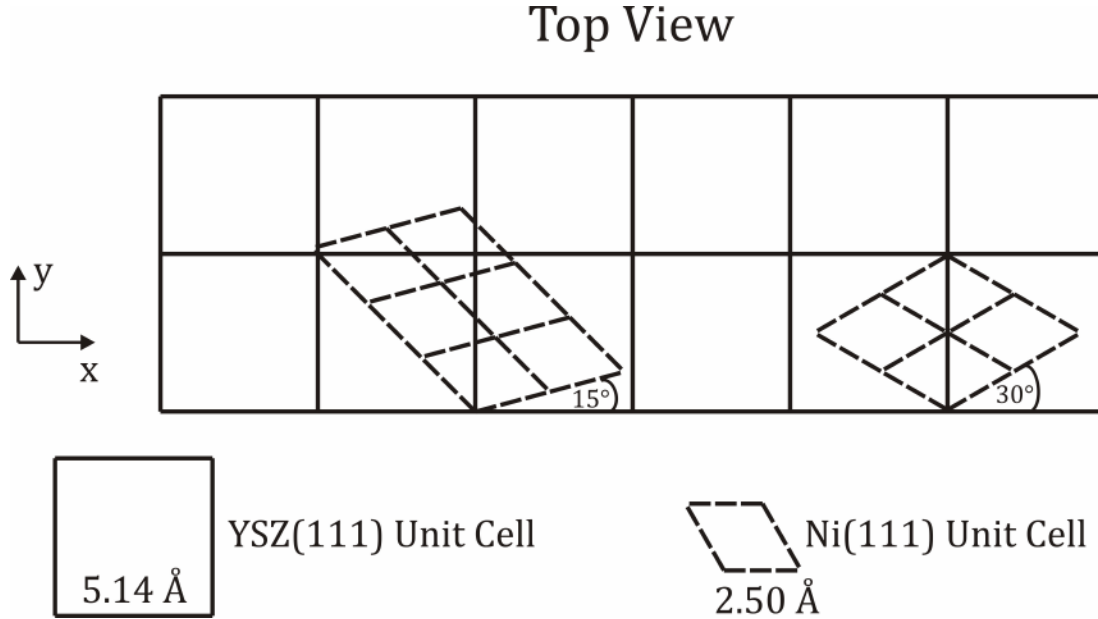
Figure 6.18: Epitaxial relations of the rotated nickel NPs on the YSZ-(100) substrate. While the Ni-R15 show reasonable lattice mismatches along both in-plane directions as illustrated on the left side, the Ni-R30 NPs have a good mismatch along the direction called y and a huge mismatch along the other direction.

$$\text{Mismatch}_{R30,x} = \frac{2 \cdot \cos(30°) \cdot 2.50\,\text{Å}}{5.14\,\text{Å}} \triangleq 15.3\% \qquad (6.20)$$

A much lower mismatch results along the other direction, when two Ni(111) unit cells are set on top of one YSZ(100) unit cell

$$\text{Mismatch}_{R30,y} = \frac{4 \cdot \cos(60°) \cdot 2.50\,\text{Å}}{5.14\,\text{Å}} \triangleq 2.2\% \qquad (6.21)$$

The mismatches for the Ni-R15 NPs behave just the opposite way with less distinct differences, however:

$$\text{Mismatch}_{R15,x} = \frac{2 \cdot \cos(15°) \cdot 2.50\,\text{Å}}{5.14\,\text{Å}} \triangleq 5.5\% \qquad (6.22)$$

and

$$\text{Mismatch}_{R15,y} = \frac{3 \cdot \cos(45°) \cdot 2.50\,\text{Å}}{5.14\,\text{Å}} \triangleq 3.8\% \qquad (6.23)$$

according the left part of Figure 6.18.
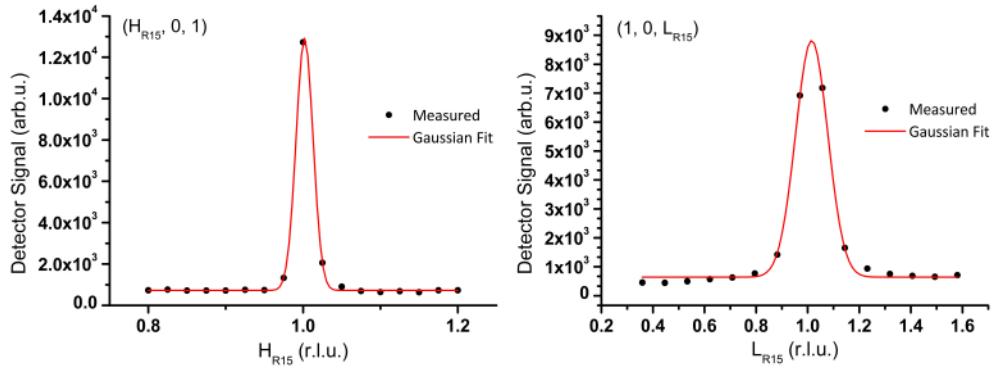
Figure 6.19: Reciprocal H_{R15}- and L_{R15}- scans through the $(1, 0, 1)_{R15}$ Bragg peak of Ni-R15 NPs using the Ni-R15 coordinates. FHWM of Gaussian fits are used to determined ΔH and ΔL. These values are then used to determine the average size of the Ni-R15 NPs and point to a very flat shape.

These mismatches are an indication for a nickel surface energy driven growth of the NPs, since the (111) facet of nickel has the lowest surface energy (see Table 2.4).

The size of each NP type can be derived by determining the width of the Bragg peaks assigned to these types. As explained in section 5.2.2, the Bragg peaks are fitted assuming a Gaussian shape. The FWHM value is than taken as ΔL or ΔH to determine the average dimension of the particles in the according direction.

Figure 6.19 shows H and L-scans through the $(1, 0, 1)_{R15}$ Bragg peak of the Ni-R15 NPs using the Ni-R15 coordinates. The Gaussian fit delivers $FWHM_H$ and $FWHM_L$ values of 0.0258 and 0.1472. The width is thus determined to be

$$\text{Width}_{Ni-R15} = \frac{2}{\sqrt{3} \cdot 0.0258} \cdot 2.50 \text{ Å} = 112.0 \text{ Å} \pm 12.0 \text{ Å} \qquad (6.24)$$

where 2.50 Å is the in-plane unit cell length of (111)-oriented Ni and $2/\sqrt{3}$ due to its hexagonal shape. The height is determined accordingly

$$\text{Height}_{Ni-R15} = \frac{1}{0.1472} \cdot 6.13 \text{ Å} = 41.6 \text{ Å} \pm 4.2 \text{ Å} \qquad (6.25)$$

with 6.13 Å as the height of a (111)-oriented Ni unit cell. The Ni-R15 NPs thus have a very flat shape with a width-to-height ratio of 2.7. Using the Ni surface energies

given in Table 2.4, the work of adhesion W_{adh} for these particles is calculated to be [102]:

$$W_{adh} = 2 \cdot 94 \frac{meV}{\text{Å}^2} - \sqrt{\frac{3}{2} \cdot \frac{41\,\text{Å}}{112\,\text{Å}}} \cdot 103 \frac{meV}{\text{Å}^2} = 142 \frac{meV}{\text{Å}^2}$$

$$= 2.27 \frac{J}{m^2}$$

(6.26)

and thus higher as 1.99 J/m² for the (111) surface (see equation (5.41)) but still much lower than a value of 9.8 J/m² derived from contact angle measurements and assuming a spherical shape of the particles [188]. The derived work of adhesion for these particles is however in the same range as Pd NPs grown on Al_2O_3 on NiAl-(110) (2.8 J/m²) [102].

Analogous scans were used to determine the dimensions of the (100)-oriented NPs with the following results (note that all measurements used for the particle size

Figure 6.20: Shape of the rotated (111)-oriented NPs derived from the Wulff-construction shown in the top. The dimensions lead to a rather flat shape with (111) side facets. Note that the NPs are rotated in-plane. Crystal directions are not given since the substrate unit cell is cubic.

determinations are given in appendix C and not shown here). The height of these particles were derived to be

$$\text{Height}_{\text{Ni}-(100)} = 37.6 \,\text{Å} \pm 2.3 \,\text{Å} \tag{6.27}$$

and thus in the same range as the rotated Ni(111) particles and in a good agreement with the reflectivity result. The width was rather difficult to determine due to the high background signal in the performed scans and was thus estimated to be

$$\text{Width}_{\text{Ni}-(100)} = 62 \,\text{Å} \pm 20 \,\text{Å} \tag{6.28}$$

The shape of the respective NPs can be illustrated using the equilibrium shape of the Wulff-construction as given in section 2.6.2. The NPs shape is constructed as described in section 5.2.2 regarding the dimensions of the particles [101].

The shape of the rotated (111)-oriented NPs is given in Figure 6.20. Starting from the equilibrium shape illustrated in the top part, results in the NPs given in the bottom part of. Note that crystal directions are not given here due to two reasons.

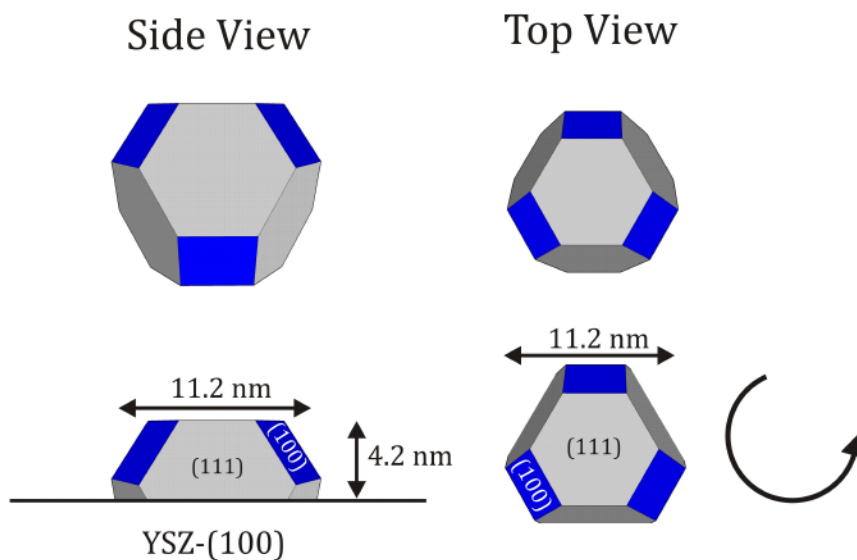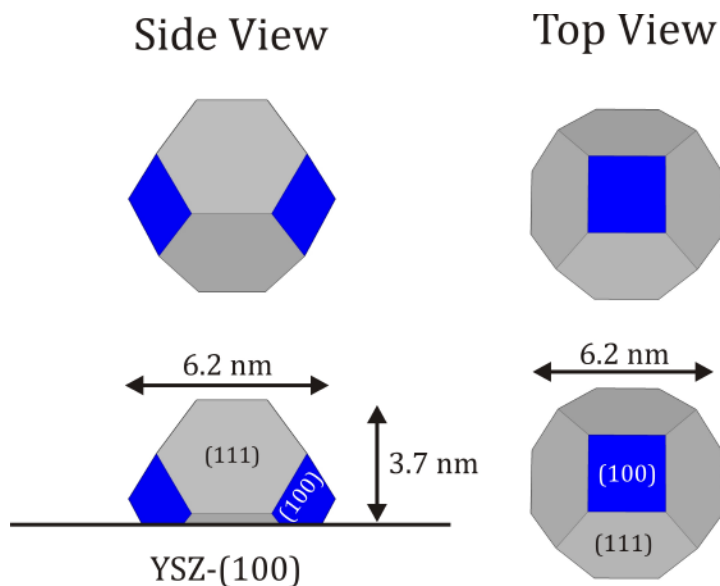**Figure 6.21:** Shape of the (100)-oriented NPs derived from the Wulff-construction shown in the top. The dimensions lead to a higher shape compared to the (111)-oriented particles. This shape is however unreliable due to the error of its width.

First, the particles have to be rotated by 15° or 30° with respect to the in-plane lattice of the substrate and second, the substrate has a cubic unit cell which makes both in-plane directions equivalent. There are hence particles with an in-plane rotation of -15° and -30° as well.

An analogous procedure leads to the comparably high shape of the Ni-(100) NPs as shown in Figure 6.21. Note that the error of this NP types dimensions lead to according uncertainties of their shape and makes the calculation of the respective work of adhesion unreliable.

The intensity of the Bragg peaks of the rotated Ni(111) NPs and the (100)-oriented NPs can be used to estimate the relative amount of each type and lead to the conclusion that most of the surface is covered with the (111)-oriented NPs. This result is in a very good agreement with previous observations using TEM [20]. Growing Ni islands on a YSZ(100) substrate, it was found that Ni grows predominantly (111)-oriented with a small fraction of (100) orientation. The in-plane rotations could not be detected in this study, however.

6.2.3 Shape Changes

Shape changes of NPs at conditions relevant for SOFCs were investigated and are presented in the following. Since SOFCs are operated at temperatures above 600°C and reductive conditions, the NPs were studied after a heat treatment under reducing conditions. Oxidation of Ni leading to a reduced activity of the NPs is an important issue in state-of-the-art SOFCs. The influence of an oxygen treatment on the NPs was therefore examined as well.

6.2.3.1 Heat Treatment

The low amount of (100)-oriented NPs covering the surface suggests a preferential (111)-oriented growth of the NPs. In order to remove (100)-oriented particles, the sample was

- annealed at T = 750°C
- for 45 minutes
- under reductive conditions.

The rocking scan shown in Figure 6.16 b) was repeated to observe changes of the NP-types and showed exactly the same peaks as before annealing the sample leading to the conclusion that all NP types are still present.

The sample was hence

- subsequently annealed to T = 850°C

- for further 25 minutes

- under reductive conditions

After this heat treatment the sample was cooled down and the NPs were characterized. The results are presented in this section.

A reflectivity curve measured after this treatment is plotted in Figure 6.22 together with the curve measured after the evaporation and shown in Figure 6.12. It becomes obvious, that the curve has virtually not changed and hence the same
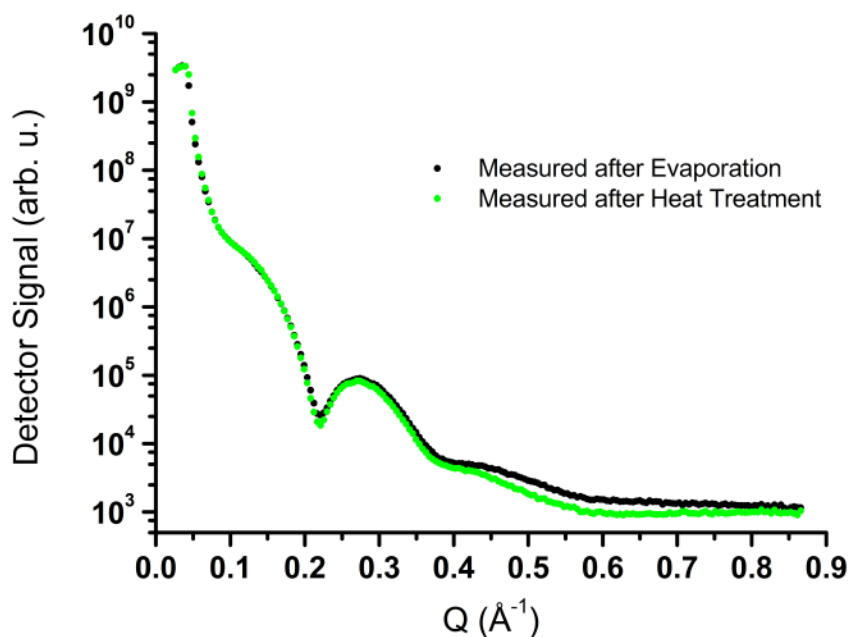
Figure 6.22: Reflectivity curve measured after the heat treatment does not show major differences to the curve measured after the evaporation. Hence, the height of the NPs and the coverage of the surface can be assumed to have not changed, keeping the values of 40 Å and 52%, respectively.

thickness and coverage of 40 Å and 52% respectively remain.

Reciprocal maps were measured in order to investigate shape changes of the respective NP types. A H-L map at K_{substr} = 2.91-H_{substr} using the substrate coordinates is shown in Figure 6.23. Several peaks are observed here. The peak at $(1.44, 1.44, 1.44)_{substr}$ can be assigned to the $(1, 1, 1)_{bul}$ Bragg peak of (100)-oriented Ni regarding the lattice relations given in equation (6.16).

The peaks at $(0.63, 2.28, 1.68)_{substr}$, $(2.28, 0.63, 1.68)_{substr}$, $(0.63, 2.28, 0.84)_{substr}$ and $(2.28, 0.63, 0.84)_{substr}$ are identified as the $(0, 1, 2)_{R15}$, and $(1, 0, 1)_{R15}$ Bragg peaks of Ni-R15 and the peaks of their laterally coexisting twins respecting equation (6.18) and the 15° rotation. The CTR of the Ni NPs and the signal of the NP's (111) facets are also visible in this map.

In addition to these, two peaks are observed at $(1.18, 1.73, 1.40)_{substr}$ and $(1.73,$
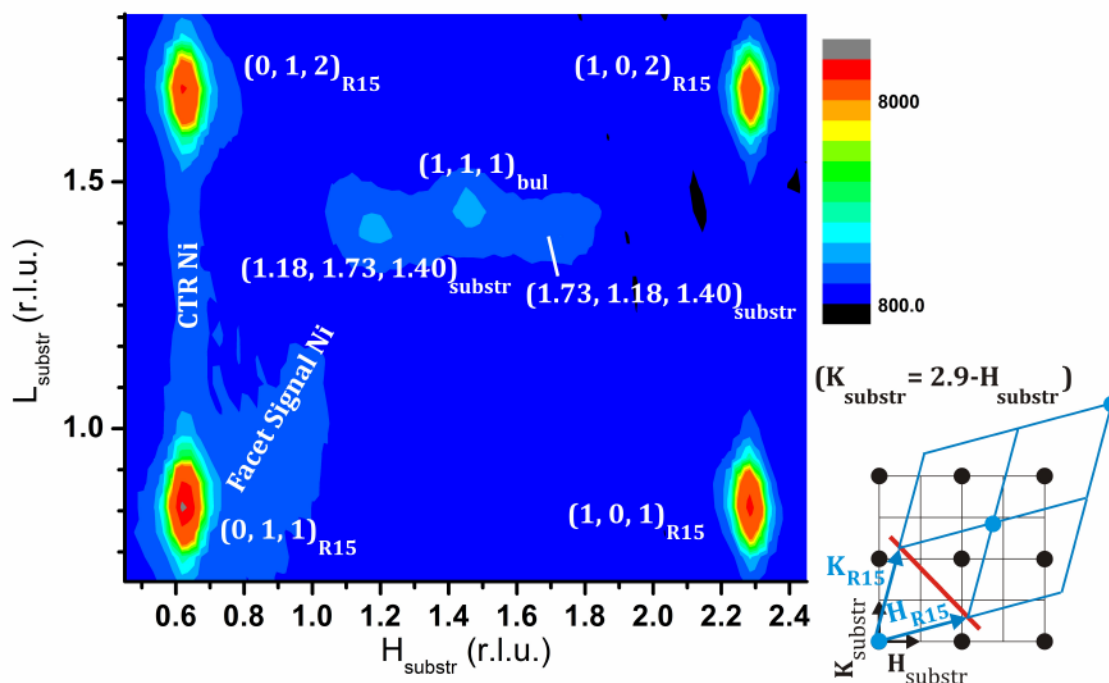
Figure 6.23: Reciprocal (H-L)$_{substr}$ map at K_{substr}=2.91-H_{substr} measured after the heat treatment. The appearing peaks can be identified as Bragg peaks of the Ni-R15 and (100)-oriented NPs. The latter type, however, has a lower intensity pointing to a small fraction of the substrate to be covered with them.

1.18, 1.40)$_{substr}$. They originate from an internal stacking inversion within the Ni-R15 and show that both laterally coexisting twins are having internal twinnings as well.

An interesting property of the (111)-oriented NPs was discovered, when an in-plane reciprocal map at L_{R15} = 1.1 was measured. Two peaks from the CTR signals of the Ni-R15 and Ni-R30 NPs are expected in this map which is plotted in Figure 6.24. It shows a ring with altering intensity, however with intensity maxima at the expected positions. It is also clear to see that the signal of the ring is above the background signal. It can thus be concluded that the signal within the whole ring is originating from NPs, and that the stronger signal at the expected position is not superposed on a background signal. The ring moreover lies on a circle sector with the origin in the Γ point. It thus originates from (111)-oriented NPs having arbitrary in-plane rotations.

Since the reflectivity curve remains similar after the treatment and the size of the
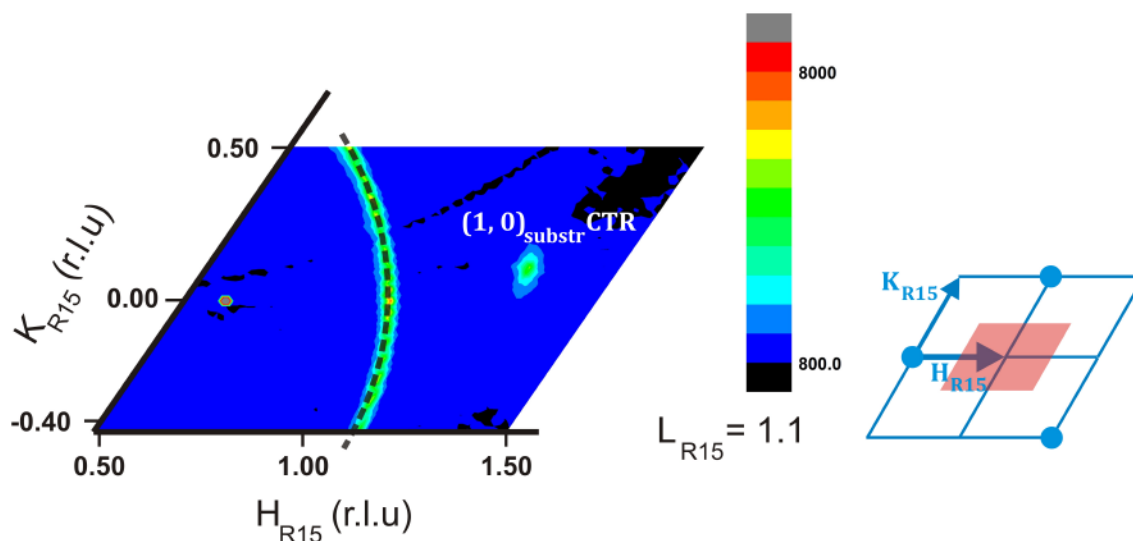
Figure 6.24: An in-plane reciprocal map around the peaks of Ni-R15 and Ni-R30 shows a ring that lies on a circle centered at Γ. Since the peaks of the Ni-R15 and Ni-R30 lay on this circle, a textured growth of the (111)-oriented NPs is followed. Ni-R15 and Ni-R30 are more favored in- plane rotations however. The peak at (1.28, 0.1, 1.1)$_{R15}$ is the (1, 0) substrate CTR signal.

NPs are found not to have changes considerably in the following, it is concluded that all of these orientations existed before annealing the sample, as well.

These different in-plane rotations indicate a textured growth of the NPs, where the Ni NPs grow (111)-oriented, but the in-plane orientation is arbitrary with a preference of the Ni-R15 and Ni-R30, however. Since a major part of the NPs is (111)-oriented, with the (111) orientation of Ni having the lowest surface energy, it can be concluded that the growth is purely surface energy driven for the majority of the NPs and only interface driven for the minority of the (100)-oriented, cube on cube NPs.

Summarizing the results, there are two types of NPs:

- Textured (111)-oriented NPs, with a preferential 15° and 30° in-plane rotation having laterally coexisting twins and a small fraction of internal twinnings.
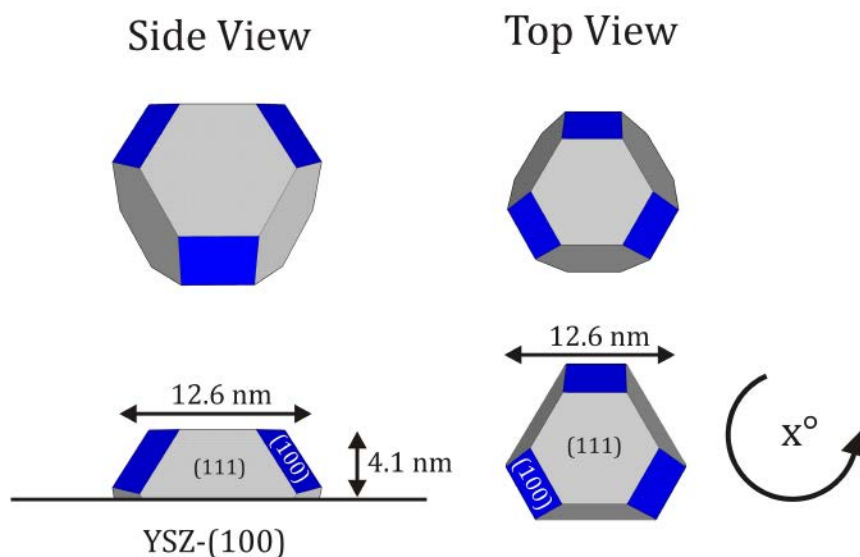
Figure 6.25: Shape of the rotated (111)-oriented NPs after the heat treatment. This treatment leads to a flatter shape of these NPs. The (111)-oriented NPs have an arbitrary in-plane rotation due to a textured growth. This together with the flat shape indicates the growth of (111)-oriented Ni films upon higher evaporation.

- A minority of (100)-oriented cube on cube epitaxial grown NPs.

The characterization of the NPs will thus be restricted to the Ni-R15 NPs and (100)-oriented NPs hereafter. The sizes of the NPs are determined as before and are

$$\text{Height}_{\text{Ni-R15}} = 41.4 \text{ Å} \pm 2.5 \text{ Å} \tag{6.29}$$

in agreement with the result of the reflectivity curve and

$$\text{Width}_{\text{Ni-111}} = 126.2 \text{ Å} \pm 7.6 \text{ Å} \tag{6.30}$$

The textured NPs have thus become slightly flatter as shown in Figure 6.25. The work of adhesion consequently becomes bigger

$$W_{\text{adh}} = 2 \cdot 94 \frac{\text{meV}}{\text{Å}^2} - \sqrt{\frac{3}{2}} \cdot \frac{41 \text{ Å}}{126 \text{ Å}} \cdot 103 \frac{\text{meV}}{\text{Å}^2} = 147 \frac{\text{meV}}{\text{Å}^2}$$

$$= 2.35 \frac{\text{J}}{\text{m}^2} \tag{6.31}$$
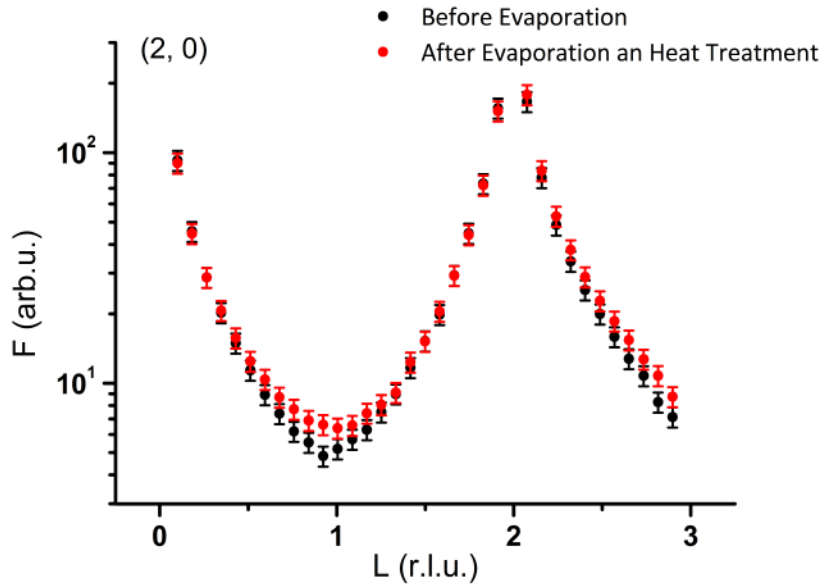
Figure 6.26: (2, 0) CTR of the substrate indicates structure changes of the YSZ(100) surface after the evaporation of nickel and the heat treatment. The data can be fitted by either an increase of Zr at the surface due to the heat treatment or the occupation of vacant surface sites by Ni.

compared to 2.27 J/m² before the heat treatment.

The dimensions of the (100)-oriented NPs after the heat treatment are

$$\text{Height}_{Ni-(100)} = 38.7 \text{ Å} \pm 2.3 \text{ Å} \tag{6.32}$$

and

$$\text{Width}_{Ni-(100)} = 60 \text{ Å} \pm 20 \text{ Å} \tag{6.33}$$

where the big error is again due to a bad background to signal ratio. The shape of these NPs has thus not changes distinctively within the errors and an illustration is left out.

The surface of the substrate was checked after the heat treatment by measuring CTRs. Figure 6.26 shows the (2, 0) CTR before and after the treatment indicating a change of the surface. A fit of these data was successful by either assuming an increased Zr concentration at the surface due to the heat treatment which is in line with results of section 6.1.3.2, or the occupation of vacant Zr sites at the interface with Ni.

6.2.3.2 Oxygen Treatment

The influence of oxygen on the NPs at operating temperatures of SOFCs is of interest for the efficiency, since NiO is inert for oxidative reactions. The NPs were thus treated with oxygen as follows:

- at T = 850°C
- and an oxygen pressure of $p_{O2} = 10^{-7}$ mbar
- for 12 minutes

and subsequently

- at oxygen pressures of $p_{O2} = 10^{-6}$ mbar
- for 13 minutes

The oxygen treatment at this high temperature is reported to lead to a high oxidation rate of both single crystal facets of the NPs with oxygen penetrations depths into the bulk in the range of μm [15; 16].

In order to observe the changes caused by this treatment, reciprocal L-scans were performed across the Ni-R15 (1, 0, 1)$_{R15}$ Bragg peak during the oxygen treatment. The resulting scans before and after five, 13, 14 and 17 minutes of oxygen treatment are shown in Figure 6.27. The integrated intensities and the FWHM values are plotted in the insets of this figure using Gaussian fits of the measured scans. Different behaviors are observed for the oxygen pressures 10^{-7} and
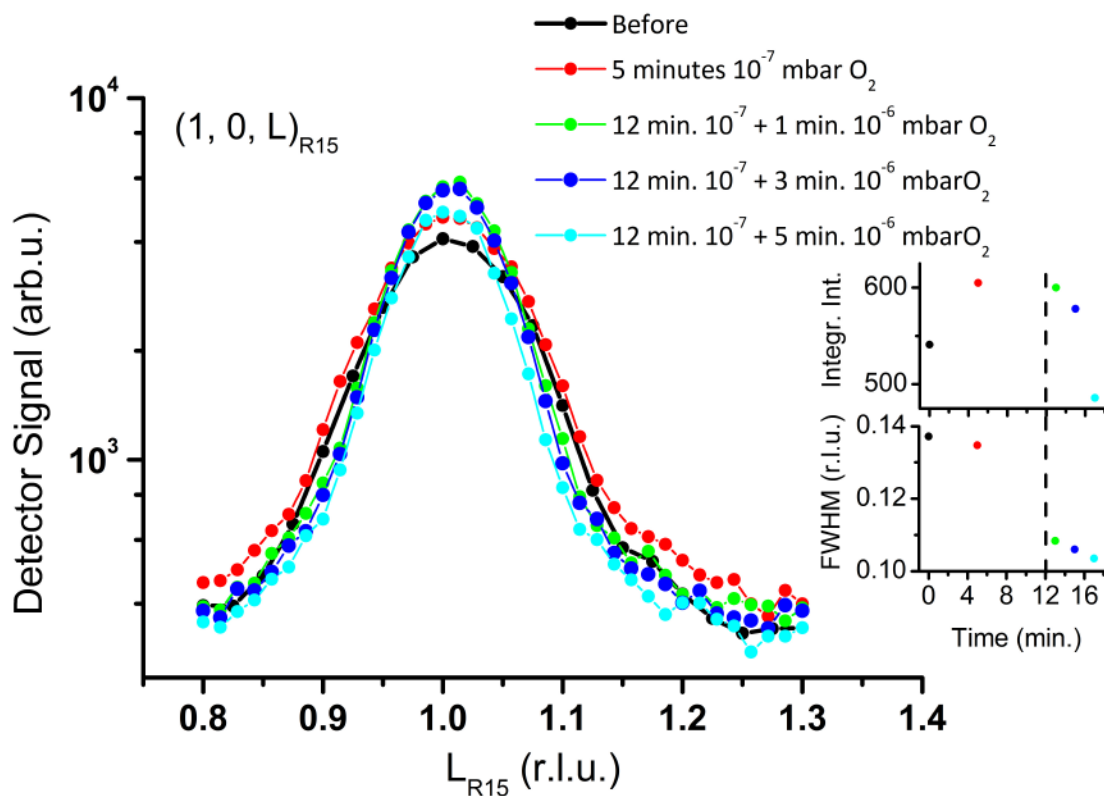
Figure 6.27: Reciprocal L$_{R15}$-scans at (1, 0, L)$_{R15}$ using the Ni-R15 coordinates. The insets show the development of the integrated intensities and the FWHM of the peaks. The continuous decrease of FWHM points to a steady growth of the NPs height to 62.4 Å, due to considerable oxygen induced mass transfer at 850°C. The decrease of the integrated intensities at 10^{-6} mbar show that the higher oxygen pressure leads to higher oxidation rates of the particles.

10^{-6} mbar. For the lower oxygen pressure, the integrated intensity increases, while the measured peak becomes slightly narrower. At the higher pressure, however, the integrated intensity decreases rapidly while the FHWMs drop is more distinct compared to the values at the lower pressure.

The initial increase of the integrated intensities at 10^{-7} mbar O_2 pressure might originate from an activation time of the oxidation. Following the results from the previous section, the high temperature leads to an average size growth of the NPs before the oxidation starts.

The continuous decrease of the $FWHM_L$ value is an indication for a height growth of the NPs even during the oxidation and L scans after the oxygen treatment indeed lead to a considerable height growth of the particles to

$$\text{Height}_{\text{Ni}-\text{R15}} = 62.4 \text{ Å} \pm 3.7 \text{ Å} \tag{6.34}$$

compared to a value of 41.4 Å before this treatment, which means a growth of 21 Å.
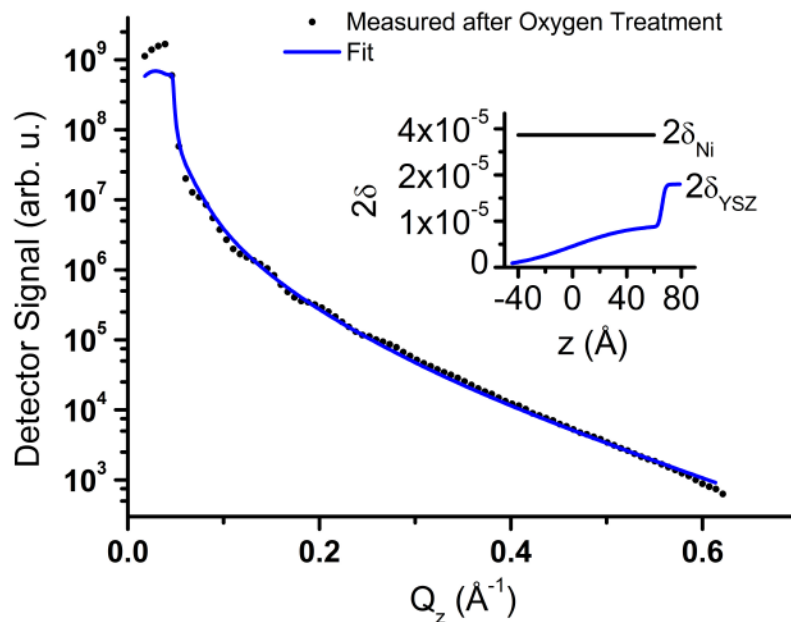
Figure 6.28: Reflectivity curve measured after the oxygen treatment show major differences to the curve measured after the heat treatment indicating a considerable change of the NPs. A fit of this curve results to a 65.8 Å thick film.

The heat treatment at reducing conditions and the same temperature leads to a comparably small increase of the height (see equation (6.29)). The shape change observed here is therefore oxygen induced. The simultaneous decrease of the integrated intensity points to an oxidation of the NPs at the same time.

The growth of the NPs height is supported by the reflectivity curve measured after the treatment and shown in Figure 6.28. Beside the changed periodicity of the oscillations leading to a height of

$$d = 65.8 \, \text{Å} \tag{6.35}$$

in good agreement with the value derived above, the curve shows a clear decrease of intensity arising from a rougher surface. The oscillations are thus less distinct and a fit more difficult leading to less reliable results.

The formation of NiO NPs is confirmed by the results of reciprocal map measurements after the oxygen treatment. Figure 6.29 shows an H_{R15}-L_{R15}
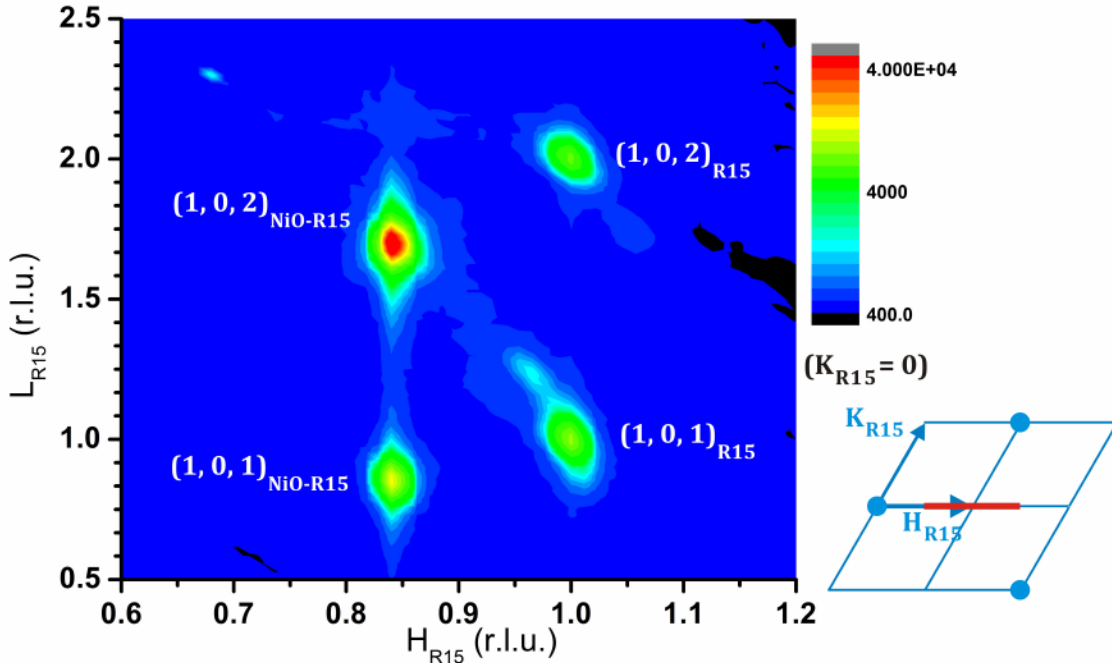
Figure 6.29: Reciprocal H_{R15}-L_{R15} map at $K_{R15} = 0$ using the Ni-R15 coordinates. Two new peaks beside the known Ni-R15 Bragg peak and its twin show up which can be identified as the $(1, 0, 1)_{NiO-R15}$ and $(1, 0, 2)_{NiO-R15}$ Bragg peaks of NiO-R15.

reciprocal map at $K_{R15}=0$. Beside the peaks appearing at $(1, 0, 1)_{R15}$ and $(1, 0, 2)_{R15}$ belonging to the respective Bragg peaks of the Ni-R15 and its twin, two other peaks are detected at $(0.84, 0, 0.84)_{R15}$ and $(0.84, 0, 1.68)_{R15}$. The relation between the reciprocal unit cells of (111)-oriented Ni and NiO is given by

$$\frac{a^*_{NiO-(111)}}{a^*_{Ni-(111)}} = \frac{b^*_{NiO-(111)}}{b^*_{Ni-(111)}} = \frac{c^*_{NiO-(111)}}{c^*_{Ni-(111)}} = \frac{\frac{1}{\sqrt{3}\cdot a_{NiO}}}{\frac{1}{\sqrt{3}\cdot a_{Ni}}} = 0.84 \tag{6.36}$$

with a_{NiO} = 4.20 Å. These peaks are thus identified as the $(1, 0, 1)_{NiO\text{-}R15}$ and $(1, 0, 2)_{NiO\text{-}R15}$ Bragg peaks of NiO-R15. The formed NiO NPs are therefore concluded to retain the epitaxy of their parent Ni NPs.

The reference map shown in Figure 6.23 was measured after the oxidation as
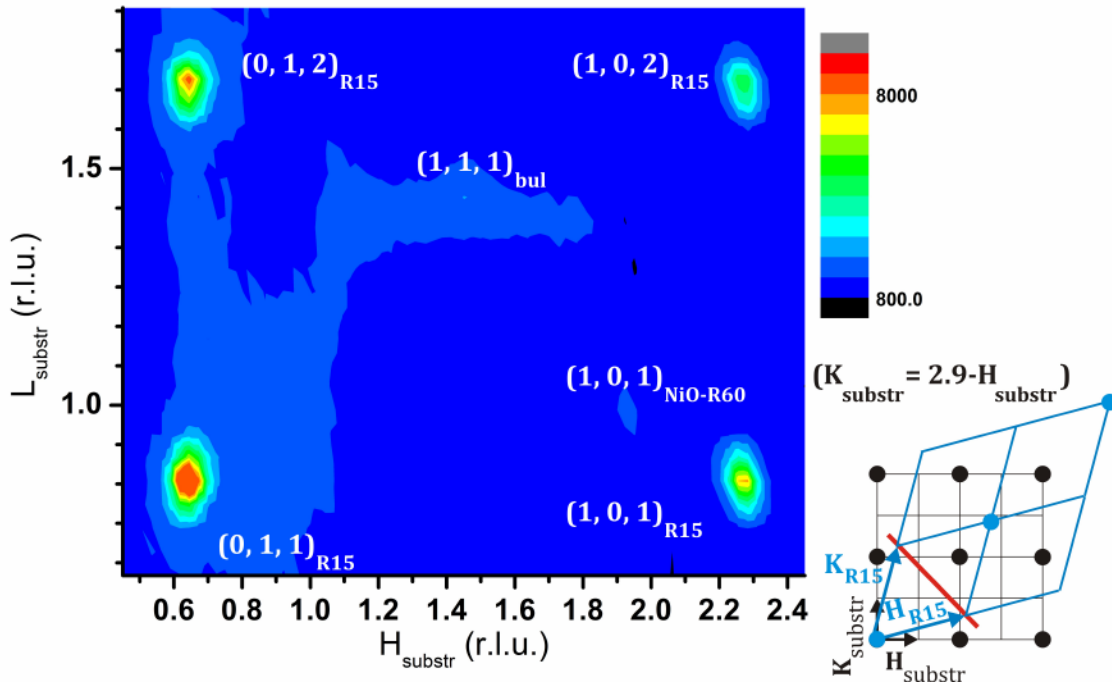
Figure 6.30: Reciprocal (H-L)$_{substr}$ map at K_{substr} = 2-91-H$_{substr}$ using the substrate coordinates. The (1, 1, 1)$_{bul}$ Bragg peak of the (100)-oriented NPs has become considerably weaker most probably due to the formation of (100)-oriented NiO NPs. The Bragg peaks of the Ni-R15 have become distinctly weaker too. The peak appearing at (1.96, 0.98, 0.98)$_{substr}$ is identified at the (1, 0, 1)$_{NiO\text{-}R60}$ Bragg peak of (111)-oriented and 60° in-plane rotated NiO NPs.

well. This map is plotted in Figure 6.30 and points to distinctive changes of the NPs. All peaks arising from unoxidized particles have lost a considerable amount of their intensity. The $(1, 1, 1)_{bul}$ Bragg peak of the (100)-oriented Ni NPs has turned into a negligible spot indicating an almost complete oxidation of this particle type. Moreover the signals arising from the internal twins are not detectable and have disappeared. The peak found at $(1.96, 0.98, 0.98)_{substr}$ can be identified as the $(1, 0, 1)_{NiO\text{-}R60}$ Bragg peak of (111)-oriented and 60° in-plane rotated NiO NPs pointing to an conversion of the parent particles epitaxy once again.

The size of the (111)-oriented Ni and NiO NPs is determined to be

$$\text{Width}_{Ni-R15} = 130.42\,\text{Å} \pm 7.8\,\text{Å} \qquad (6.37)$$

compared to 126.2 Å before. Considering the height increase of 21 Å resulting from equation (6.34), this means that the unoxidized NPs have become much higher as shown in Figure 6.31 which leads to a decrease of the work of adhesion to
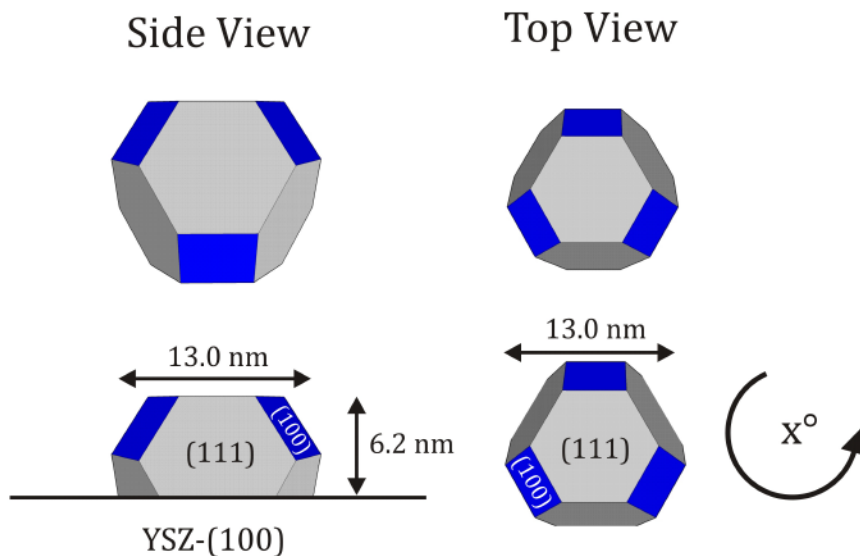
Figure 6.31: Shape of the rotated (111)-oriented NPs after the oxygen treatment. This treatment leads to a more distinct growth in height than in width leading to a less flat shape. The amount of these NPs is however reduced by oxidation.

$$W_{adh} = 2 \cdot 94 \frac{meV}{\mathring{A}^2} - \sqrt{\frac{3}{2} \cdot \frac{62\,\mathring{A}}{130\,\mathring{A}} \cdot 103 \frac{meV}{\mathring{A}^2}} = 127 \frac{meV}{\mathring{A}^2}$$

(6.38)

$$= 2.03 \frac{J}{m^2}$$

The formed NiO-R15 NPs dimensions are determined to be

$$\text{Height}_{NiO-R15} = 54.4\,\mathring{A} \pm 3.3\,\mathring{A}$$

(6.39)

and

$$\text{Width}_{NiO-R15} = 158.4\,\mathring{A} \pm 9.5\,\mathring{A}$$

(6.40)

The oxidized NPs are thus broader, but lower than the Ni-R15 NPs, which means that they are even flatter than the particles before the oxidation.

Note that the formation of NiO out of Ni leads to a volume increase that is given by a 16% increase of the crystal axis ($a_{NiO}/a_{Ni} = 1.157$). This increase is in a fairly good agreement with the ratio of the width and height of the R15-NPs with the resulting NiO NPs within the errors since

$$126.2\,\mathring{A} \cdot 1.16 = 146.4\,\mathring{A} \simeq 158.5\,\mathring{A}$$

(6.41)

and
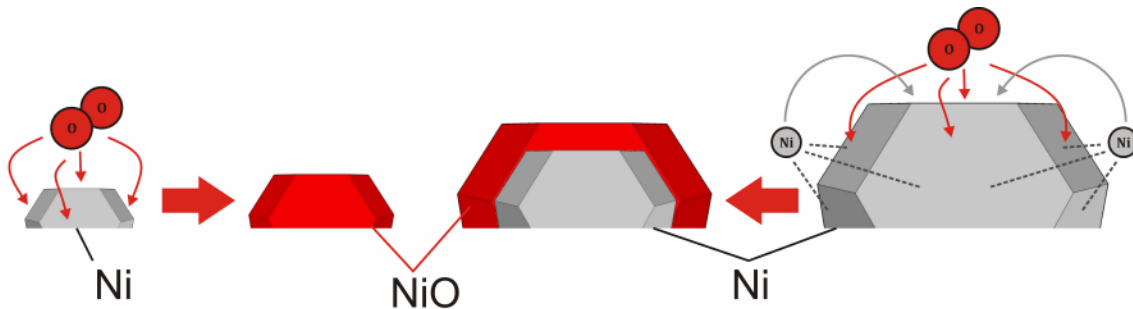
Figure 6.32: The shape change of the Ni-R15 NPs and the formation of textured NiO NPs can be explained by an oxidation mechanism, where all facets of the NPs are homogenously oxidized. This leads to the total oxidation of small NPs (left side). Bigger nickel particles are partially oxidized and the high mass transfer at 850°C leads to a simultaneous height growth (right side). Such a mechanism implies the coexistence of particles with Ni cores and NiO shells.

$$41.4 \, \text{Å} \cdot 1.16 = 48.0 \, \text{Å} \simeq 54.4 \, \text{Å} \qquad\qquad (6.42)$$

The dimension changes of the nickel NPs and the size of the NiO NPs point to a oxidation mechanism similar to that of the (111)-oriented nickel NPs on the YSZ(111) surface. While at the high temperature used for the oxidation here massive mass transport occurs additionally to change the shape of the unoxidized NPs, the facets of the nickel particles are homogenously oxidized. This leads to a complete oxidation of small NPs and a partial oxidation of bigger particles which grow in height un addition (see Figure 6.32). This mechanism implies the coexistence of particles with a Ni core and a NiO shell.

The high oxidation temperature moreover causes a rapid oxidation of the particles which leads to the formation of NiO in the expense of a majority of the unoxidized NPs as a comparison of the nickel Bragg peaks in Figure 6.27 and Figure 6.23 but also the intensity relation of the NiO and Ni Bragg peaks in Figure 6.29 reveal.
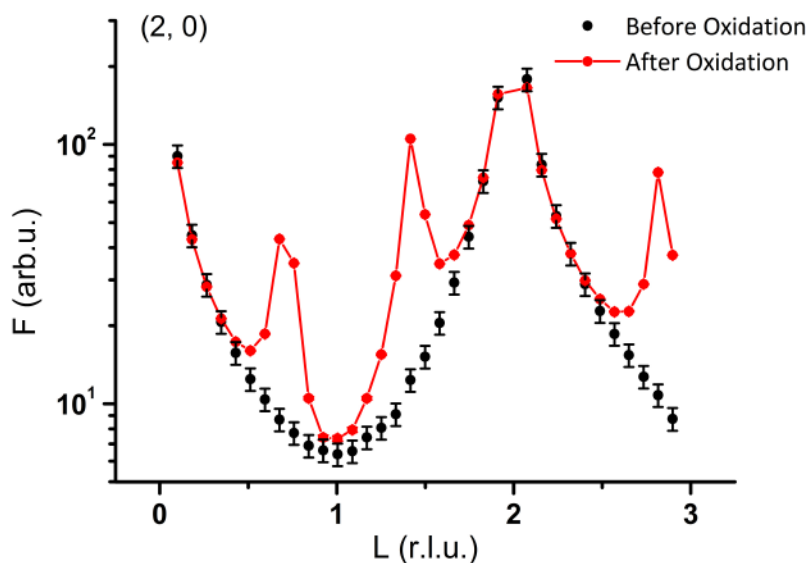
Figure 6.33: (2, 0) CTR of the substrate show modulated peaks at 0.7, 1.4 and 2.8. These peaks arise from the Bragg peak tails of (111)-oriented NiO NPs with an in-plane rotation of 0°.

An interesting effect is observed when measuring the (2, 2) CTR of the substrate. This CTR is plotted in Figure 6.33 and shows additional modulations on the CTRs. The additional peaks on the CTRs are detected at the L values 0.7, 1.4 and 2.8. Considering the reciprocal ratio of (111)-oriented NiO and the substrate

$$\frac{\frac{1}{\sqrt{3} \cdot a_{\text{NiO}}}}{\frac{1}{a_{YSZ}}} = 0.7 \tag{6.43}$$

these peaks can be identified as Bragg peak tails of (111)-oriented and textured NiO NPs.

6.2.4 Summary

Nickel was grown on the YSZ(100) surface after the heat treatment described in section 6.1.3.2. An electron beam evaporator was used to deposit Ni on the substrate at 550°C with a nominal thickness of 5.7 nm. The existence of NPs was checked and proved by AFM and reflectivity revealing a 52% coverage of the substrate. SXRD was applied to characterize the NPs.

In contrast to the expected cube on cube epitaxy favored by the lattice mismatches of Ni and YSZ, only a small fraction of the NPs show such a growth with average widths of 6.2 nm and heights of 3.7 nm.

The majority of the NPs grow (111)-oriented with laterally coexisting twins in agreement with other studies [19; 108; 110]. These particles are textured with an arbitrary in-plane rotation, favoring a 15° or 30° rotation however. Both types contain a small fraction of internal stacking inversions leading to a twinning of these NPs. The textured NPs have average heights and widths of 4.2 nm and 11.2 nm, respectively, leading to rather flat shapes. The work of adhesion for the growth of the (111)-oriented NP on YSZ(100) is determined to be 2.27 J/m^2.

The predominant (111)-oriented textured growth points to a surface energy driven growth of most of the particles, since the lattice mismatches of these particles with the substrate are substantial and the (111) facet of nickel has the lowest surface energy.

After a heat treatment at reductive conditions and 750°C for 45 minutes and subsequently at 850°C for 25 minutes, the textured NPs become slightly flatter due to an increased average width to 12.6 nm while keeping their height. The (100)-oriented NPs shape is not influenced by such a treatment. The reflectivity keeps its characteristics and the small shape changes caused by these high temperatures points to a high stability of the NPs.

Major changes are caused by the oxidation of the NPs at 850°C and 10^{-7} mbar O_2 for 12 minutes and subsequently 10^{-6} mbar O_2 for 12 minutes. The (100)-oriented nickel NPs virtually vanish completely while a considerable amount of the textured nickel NPs are converted into textured NiO NPs. The high present temperature moreover lead to a considerable oxygen induced shape change of the textured nickel NPs with average widths and heights of 13 nm and 6.2 nm and leading to a decreased work of adhesion of 2.03 J/m². The average size of the NiO NPs is 15.8 nm in width and 5.4 nm in height pointing to flat particles.

An oxidation mechanism where all NP facets are homogenously oxidized is thus suggested. This mechanism leads to the complete oxidation of small NPs and. Bigger NPs are partially oxidized and grow in height due to the high oxygen induced masstransfer.

The dimensions of the NPs determined with the SXRD data are in very good agreement with reflectivity data. The surface of the substrate was checked after the heat treatment and showed a noticeable change. This change can be attributed to an increase of Zr at the surface or the incorporation of Ni in vacancy sites at the interface. A characterization of the interface after the oxidation was not possible due to the superposition of the substrate CTR and textured NiO Bragg peaks.

7 Summary, Discussions and Outlook

7.1 Summary

The goal of this work was to deliver knowledge about the two structural components of the three-phase boundary of the most used SOFC anode cermet at the pristine state and after simulated SOFC operating conditions. The three-phase boundary plays a predominant role in the efficiency enhancement and improved design of future fuel cells [8; 9; 32].

These two components are the YSZ surface and Ni nanoparticles [1; 2; 8]. The lowest energy (111) surface and thus the most common facet [12], and the polar (100) surface were chosen to be studied therefore experimentally using surface X-ray diffraction. Consistent atomic structures for both surfaces with sub-Ångström resolution were found and the growth, shape and shape changes of nickel NPs on these surfaces under operating conditions were determined.

The atomic structure of the (111) surface was studied extensively by making use of a combination of anomalous and non-anomalous SXRD to enable the discrimination between Y and Zr within the derived models. The highly sensitive data allows proposing very exact atomic structure models using the "Zr-shift" bulk structure as starting points. At the pristine state, this surface was found to be yttrium enriched agreeing with recent publications [49; 80]. A large number of metal and oxygen vacancies result in a highly defective surface being highly distorted due to distinct displacements of Zr atoms from their bulk positions. These finding are supported by a number of experimental and theoretical investigations [52; 49; 53; 80]. After a treatment at 1000°C and reductive conditions simulating SOFC anode operating environments, Zr and O atoms segregate to the surface while the Y content remains constant. The majority of Zr surface atoms, thereby, occupy

ideal fluorite positions which together with the decreased vacancy, leads to a less defective and disordered surface structure.

The NPs grown on this surface show either an epitaxial (111) orientation or coherent tilts. While the first growth type has been reported before [14; 107], the second type has been unknown for nickel NPs on this substrate. Both NP types indicate a highly interface driven growth of Ni. The (111)-oriented particles coexist with lateral twins both having internal twinning as well. These NPs have a flat shape while the coherent tilted particles shape is rather round.

After a treatment at 700°C and reductive conditions, the average size of both NP types start to grow due to Ostwald ripening or coalescence of small particles. The particles were additionally exposed to 10^{-6} mbar oxygen at 300°C for 35 minutes, to investigate the oxidation present at startup and shut-down cycles of SOFCs. After this treatment NiO-NPs with the same epitaxy as their parent unoxidized NPs start to grow. The facets of the (111)-oriented nickel NPs are believed to be oxidized homogenously leading to a complete oxidation of small NPs and partial oxidation of bigger NPs. The tilted nickel NPs show a different oxidation behavior, where the penetration of O_2 through the interface could result in a complete oxidation of the nickel NPs regardless their initial size.

The surface of the substrate is not influenced by the growth of nickel or by any of the above NP treatments.

The atomic structure of the (100) surface was investigated using non-anomalous SXRD. The model for the pristine state of this facet basing on the fluorite-like model of the bulk was found to be (1 x 1) reconstructed in agreement with a former experimental work [18] and implying an yttria enriched surface according DFT calculations [12]. A huge number of vacancy sites and distinct displacements at the surface lead to a highly defective and distorted structure. After a heat treatment at 900°C and reductive conditions simulating SOFC anodes operating conditions, the reconstruction is lifted, most likely due to the segregation of Zr from subsurface layers. The oxygen concentration at the surface is increased as well, both leading to a less defective and more ordered structure.

The majority of the particles are flat, textured and (111)-oriented in agreement with previous studies [19; 110; 20] and pointing to a nickel surface energy driven growth. Only an insignificant fraction of the nickel NPs grown on the YSZ(100) surface shows a (100)-oriented cube on cube epitaxy.

After a heat treatment at 850°C and reductive conditions the (100)-oriented NPs are stable while the textured particles become flatter and the average size increases. The particles were oxidized at 850°C and 10^{-7} mbar oxygen for 12 minutes and subsequently at 10^{-6} mbar oxygen for 13 minutes. While the (100)-oriented NPs are oxidized completely, a major fraction of the textured Ni NPs is transformed into textured NiO NPs. At these high temperatures, a combined oxygen-induced mass transfer and homogenous oxidation of all facets causes the textured Ni NPs to become higher. The structure of the substrate changes after the heat treatment of the NPs, due to Zr segregation or the implementation of Ni atoms at vacant surface sites.

7.2   Discussions and Outlook

 The structures of both studied surfaces are highly defective and disordered at the pristine state. After the treatment at high temperatures and reductive conditions simulating SOFC-anode environments, the structures become less defective and more ordered. Assuming the presence of defects and a disordered structure at the surface to be beneficial for the surface activity of oxides [21; 198] and the oxygen ion exchange at the three-phase boundary, operating conditions can be concluded to decrease the efficiency of the anode. Controlling these defects and preventing Zr segregation are thus keys for enhanced anode efficiencies.

Considering yttria at the surface to be responsible for these defects and the disorder, an yttria enriched surface even at operating conditions could be a possible solution for increased efficiencies of the SOFC anode. Indeed, a very recent study showed the improvement of the anode cermets performance when a highly yttrium-enriched layer was deposited on the YSZ surface [22].

There are two types of NPs growing on each of the studied surfaces. This is a possible hint for locally different configurations of the substrate surfaces which are also present in the bulk [24; 25]. Note that diffraction always gives a statistically averaged structure and such local differences cannot be distinguished. The different NP types might as well be caused by other circumstances as the particle sizes [199]. The large oxygen vacancy concentration on both substrates is likely to result in surfaces with oxygen and metal termination which could explain the two different growth types as well. A complementary study on the local composition of the substrates under the respective conditions should be a future goal to deliver additional insight.

The SXRD results of this work do now allow to determine the size- and angular distribution of the single NP types. Transmission electron microscopy is thus a possible tool to supplement and confirm the results of this work and should be addressed in a future work.

At operating conditions, NPs on both substrates start to grow at the expense of small particles. In both cases, this development leads to a decrease of Ni surface area which is destructive for the efficiency. Preventing the sintering of the NPs at operating conditions will thus be another key for the design of future anode materials.

It can thus be summarized that the operating environment of an SOFC anode is not beneficial for its efficiency from a structural point of view. It should however be mentioned that the processing of hydrocarbons on the anode might as well have beneficial or detrimental influence on the anode structure. This aspect was not part of this work but is an interesting topic for upcoming studies based on the results found here.

The oxygen treatment at elevated temperatures of the NPs on both studied substrates reveals the strong oxidation of all NP types with different oxidation mechanisms. However, the operating conditions of the anode at high temperatures and reductive conditions might transform NiO NPs back to unoxidized particles as

observed for nickel single crystals [16; 200], which is a further topic for a future study relevant for SOFC anodes.

In conclusion, this work delivers fundamental insight into the structure of the most used SOFC anode cermet at two relevant states. The results serve as a base for continuative investigations leading to a molecular understanding of the processes on an SOFC anode and the theoretical modeling of them.

Appendix

A   Unit Cells

Construction of a Zr-shift Unit Cell

The Zr-shift model was proposed for the bulk of YSZ using a combination of non-anomalous and anomalous X-ray diffraction [35] and used in this work as a starting point for the refinements including anomalous data.

In this model, all Zr atoms within the fluorite structure are displaced along [111] directions by 0.19 Å, while there are two types of oxygen atoms. Type one is called O1 and is shifted along [100] directions by 0.31 Å and type to is called O2 and remains at the (8c) sites of the Fm3M symmetry group [55]. The yttrium atoms occupy ideal (4a) sites.

The construction of a Zr-shift unit cell can thus be done as follows. We start with an ideal model, where all metal occupy (4a) and all oxygen atoms occupy (8c) positions with the fractional coordinates.

Atom	x	y	z
Y	0	0	0
Y	0.5	0.5	0
Y	0	0.5	0.5
Y	0.5	0	0.5
Zr	0	0	0
Zr	0.5	0.5	0
Zr	0	0.5	0.5
Zr	0.5	0	0.5
O	0.25	0.25	0.25
O	0.75	0.75	0.25
O	0.25	0.75	0.75
O	0.75	0.75	0.75
O	0.25	0.25	0.75
O	0.75	0.25	0.25

O	0.25	0.75	0.25
O	0.75	0.25	0.75

While the Y atoms remain at the same coordinates, each Zr atom is shifted along eight symmetry equivalent [111] direction by 0.19 Å. Assuming a lattice constant of 5.14 Å, this means a shift change of the fractional coordinates of

$$\frac{0.19\,\text{Å}}{\sqrt{3}\cdot 5.14\,\text{Å}} = 0.0213$$

along the $\pm[111]$, $\pm[\bar{1}11]$, $\pm[\bar{1}\bar{1}1]$ and $\pm[1\bar{1}1]$ directions resulting in eight Zr atoms surrounding each Y atom.

In case of the oxygen atoms, the O2 type keep the above given ideal positions. The fractional displacement of the O1 types are done along the $\pm[001]$, $\pm[100]$ and $\pm[010]$ direction by

$$\frac{0.31\,\text{Å}}{5.14\,\text{Å}} = 0.0603$$

ending up with six O2 atoms surrounding each O1 atoms.

The fractional coordinates of the Zr-shift model are thus

Atom	x	y	z
Y	0	0	0
Y	0.5	0.5	0
Y	0	0.5	0.5
Y	0.5	0	0.5
O2	0.25	0.25	0.25
O2	0.75	0.75	0.25
O2	0.25	0.75	0.75
O2	0.75	0.75	0.75
O2	0.25	0.25	0.75
O2	0.75	0.25	0.25
O2	0.25	0.75	0.25
O2	0.75	0.25	0.75
Zr	0.02134174	0.02134174	0.02134174
Zr	0.52134174	0.52134174	0.02134174
Zr	0.02134174	0.52134174	0.52134174
Zr	0.52134174	0.02134174	0.52134174
Zr	-0.02134174	-0.02134174	-0.02134174
Zr	0.47865826	0.47865826	-0.02134174
Zr	-0.02134174	0.47865826	0.47865826

Zr	0.47865826	-0.02134174	0.47865826
Zr	-0.02134174	0.02134174	0.02134174
Zr	0.47865826	0.52134174	0.02134174
Zr	-0.02134174	0.52134174	0.52134174
Zr	0.47865826	0.02134174	0.52134174
Zr	0.02134174	-0.02134174	-0.02134174
Zr	0.52134174	0.47865826	-0.02134174
Zr	0.02134174	0.47865826	0.47865826
Zr	0.52134174	-0.02134174	0.47865826
Zr	-0.02134174	-0.02134174	0.02134174
Zr	0.47865826	0.47865826	0.02134174
Zr	-0.02134174	0.47865826	0.52134174
Zr	0.47865826	-0.02134174	0.52134174
Zr	0.02134174	0.02134174	-0.02134174
Zr	0.52134174	0.52134174	-0.02134174
Zr	0.02134174	0.52134174	0.47865826
Zr	0.52134174	0.02134174	0.47865826
Zr	0.02134174	-0.02134174	0.02134174
Zr	0.52134174	0.47865826	0.02134174
Zr	0.02134174	0.47865826	0.52134174
Zr	0.52134174	-0.02134174	0.52134174
Zr	-0.02134174	0.02134174	-0.02134174
Zr	0.47865826	0.52134174	-0.02134174
Zr	-0.02134174	0.52134174	0.47865826
Zr	0.47865826	0.02134174	0.47865826
O1	0.25	0.25	0.31031128
O1	0.75	0.75	0.31031128
O1	0.25	0.75	0.81031128
O1	0.75	0.75	0.81031128
O1	0.25	0.25	0.81031128
O1	0.75	0.25	0.31031128
O1	0.25	0.75	0.31031128
O1	0.75	0.25	0.81031128
O1	0.25	0.25	0.18968872
O1	0.75	0.75	0.18968872
O1	0.25	0.75	0.68968872
O1	0.75	0.75	0.68968872
O1	0.25	0.25	0.68968872
O1	0.75	0.25	0.18968872
O1	0.25	0.75	0.18968872
O1	0.75	0.25	0.68968872
O1	0.31031128	0.25	0.25

O1	0.81031128	0.75	0.25
O1	0.31031128	0.75	0.75
O1	0.81031128	0.75	0.75
O1	0.31031128	0.25	0.75
O1	0.81031128	0.25	0.25
O1	0.31031128	0.75	0.25
O1	0.81031128	0.25	0.75
O1	0.18968872	0.25	0.25
O1	0.68968872	0.75	0.25
O1	0.18968872	0.75	0.75
O1	0.68968872	0.75	0.75
O1	0.18968872	0.25	0.75
O1	0.68968872	0.25	0.25
O1	0.18968872	0.75	0.25
O1	0.68968872	0.25	0.75
O1	0.25	0.31031128	0.25
O1	0.75	0.81031128	0.25
O1	0.25	0.81031128	0.75
O1	0.75	0.81031128	0.75
O1	0.25	0.31031128	0.75
O1	0.75	0.31031128	0.25
O1	0.25	0.81031128	0.25
O1	0.75	0.31031128	0.75
O1	0.25	0.18968872	0.25
O1	0.75	0.68968872	0.25
O1	0.25	0.68968872	0.75
O1	0.75	0.68968872	0.75
O1	0.25	0.18968872	0.75
O1	0.75	0.18968872	0.25
O1	0.25	0.68968872	0.25
O1	0.75	0.18968872	0.75

This unit cell hence contains 92 atoms. However, none of the positions if fully occupied.

(111)-Oriented Zr-shift Unit Cell

The transformation from a cubic unit cell into a hexagonal, (111)-oriented unit cell is given by the transformation matrix

$$\mathcal{M} = \begin{pmatrix} 1/2 & 0 & -1/2 \\ -1/2 & 1/2 & 0 \\ 1 & 1 & 1 \end{pmatrix}$$

with a determinant of 0.75. The (111)-unit cell is thus 0.75 times the size of the cubic unit cell and will contain 69 atoms.

The unit cell is constructed by transforming the coordinates of the cubic Zr-shift unit cell given above using the matrix [185]

$$\mathcal{H} = (\mathcal{M}^T)^{-1} = \begin{pmatrix} 2/3 & 2/3 & -4/3 \\ -2/3 & 4/3 & -2/3 \\ 1/3 & 1/3 & 1/3 \end{pmatrix}$$

with

$$\begin{pmatrix} x_s \\ y_s \\ z_s \end{pmatrix} = \mathcal{H} \cdot \begin{pmatrix} x \\ y \\ z \end{pmatrix}$$

This results in the following fractional coordinates

Atom	x_s	y_s	z_s
Y	0.33333333	0.66666667	0.66666667
Y	0.66666667	0.33333333	0.33333333
Y	0	0	0
O2	0.33333333	0.66666667	0.91666667
O2	0	0	0.75
O2	0.66666667	0.33333333	0.58333333
O2	0.33333333	0.66666667	0.41666667
O2	0	0	0.25
O2	0.66666667	0.33333333	0.08333
Zr	0.02800004	0.97199996	0.99299999
Zr	0.94399993	0.97199996	0.99299999
Zr	0.02800004	0.05600007	0.99299999
Zr	0	0	0.97899997
Zr	0.33333333	0.66666667	0.68766669
Zr	0.30533332	0.69466668	0.67366669
Zr	0.38933337	0.69466668	0.67366669
Zr	0.3053333	0.61066659	0.67366668
Zr	0.36133335	0.7226667	0.65966668
Zr	0.27733328	0.63866661	0.65966667

Zr	0.36133333	0.63866661	0.65966667
Zr	0.33333331	0.66666663	0.64566666
Zr	0.6666667	0.33333335	0.35433335
Zr	0.7226667	0.36133335	0.34033335
Zr	0.63866669	0.36133337	0.34033334
Zr	0.63866669	0.27733332	0.34033334
Zr	0.69466669	0.38933337	0.32633334
Zr	0.69466669	0.30533332	0.32633334
Zr	0.61066667	0.30533333	0.32633333
Zr	0.66666667	0.33333333	0.31233333
Zr	0	0	0.021
Zr	0.97199996	0.02799998	0.00700001
Zr	0.97199996	0.94399998	0.00700001
Zr	0.056	0.028	0.007
O1	0.37399999	0.62600001	0.937
O1	0.37399999	0.74799999	0.937
O1	0.25200001	0.62600001	0.937
O1	0.29266667	0.58533335	0.89633334
O1	0.41466665	0.70733333	0.89633334
O1	0.29266667	0.70733333	0.89633334
O1	0.04066666	0.08133332	0.77033333
O1	0.91866668	0.95933334	0.77033333
O1	0.04066666	0.95933334	0.77033333
O1	0.08133332	0.04066666	0.72966667
O1	0.95933334	0.91866668	0.72966667
O1	0.95933334	0.04066666	0.72966667
O1	0.70733333	0.29266667	0.60366666
O1	0.70733333	0.41466665	0.60366666
O1	0.58533335	0.29266667	0.60366666
O1	0.74799999	0.37399999	0.563
O1	0.62600001	0.25200001	0.563
O1	0.62600001	0.37399999	0.563
O1	0.37399999	0.74799999	0.437
O1	0.37399999	0.62600001	0.437
O1	0.25200001	0.62600001	0.437
O1	0.29266667	0.58533335	0.39633334
O1	0.29266667	0.70733333	0.39633334
O1	0.41466665	0.70733333	0.39633334
O1	0.04066666	0.95933334	0.27033333
O1	0.91866668	0.95933334	0.27033333
O1	0.04066666	0.08133332	0.27033333
O1	0.08133332	0.04066666	0.22966667

O1	0.95933334	0.91866668	0.22966667
O1	0.95933334	0.04066666	0.22966667
O1	0.58533335	0.29266667	0.10366666
O1	0.70733333	0.41466665	0.10366666
O1	0.70733333	0.29266667	0.10366666
O1	0.62600001	0.25200001	0.063
O1	0.62600001	0.37399999	0.063
O1	0.74799999	0.37399999	0.063

B   Reflectivity Fitting Parameters

The reflectivity data was fitted using the program fewlay [168]. The following gives the parameter files of this program after the according fits. These files are constructed as follows

- First line: Used Energy. anka = 10keV, Mo = 17.50keV
- Following lines until "xx" line: used layer system.
    - Each layer system has four fittable parameters
        - Thickness d
        - Roughness σ
        - 2δ
        - 2β
    - The numbers before the materials indicate whether the parameters were used for the fit or not
        - 0 = not used for the fit
        - 1 = used for fit
- The lines after the "xx" lines are
- They are built up as
    - First: fitted value
    - Second: lower limit
    - Third: upper limit
- The four first lines after "xx" are the optical values
    - Incoming intensity
    - Constant background
    - A-takeoff (geometry parameter)
- The following lines correspond to the fitting parameters of the layer system.

YSZ(111) Surface

Unprepared Surface

Mo
1111 h20
1100 ZrO2
0100 ZrO2
   xx
5.59648324315007E+0008 1.00000000000000E+0003 1.00000000000000E+0011
1.17010061954537E+0002 1.00000000000000E+0000 1.00000000000000E+0003
1.00000020447675E-0006 1.00000000000000E-0006 1.00000000000000E+0000
3.32886271819989E+0000 1.00000000000000E-0001 1.00000000000000E+0002
1.02479534678092E+0001 1.00000000000000E+0000 2.00000000000000E+0001
2.08607120774680E+0000 1.00000000000000E+0000 2.00000000000000E+0001
5.12451799568779E-0006 1.00000000000000E-0006 2.00000000000000E-0005
1.66715143028203E-0007 5.00000000000000E-0008 2.00000000000000E-0007
1.00000052587738E+0005 1.00000000000000E+0005 1.10000000000000E+0005
3.31840221612548E+0000 1.00000000000000E+0000 8.00000000000000E+0001
1.00000352588196E+0000 1.00000000000000E+0000 1.80000000000000E+0000

Prepared Surface

anka
1100 ZrO2
0100 ZrO2
   xx
4.65711037543186E+0009 1.00000000000000E+0003 1.00000000000000E+0011
9.99999632268683E+0002 1.00000000000000E+0000 1.00000000000000E+0003
1.00000078213223E-0006 1.00000000000000E-0006 1.00000000000000E+0000
6.66124969240123E+0000 1.00000000000000E-0001 1.00000000000000E+0002
1.00000052587738E+0005 1.00000000000000E+0005 1.10000000000000E+0005
1.76600898322017E+0000 1.00000000000000E+0000 8.00000000000000E+0001
1.00000352588196E+0000 1.00000000000000E+0000 1.80000000000000E+0000

Nickel Nanoparticles on YSZ(111) Surface

After Evaporation

anka

1111 nix2

1111 nix

0100 ZrO2

xx

1.52876088115974E+0010 1.00000000000000E+0003 1.00000000000000E+0012

1.09699111921171E+0002 1.00000000000000E+0001 1.10000000000000E+0002

9.99999393670269E-0004 1.00000000000000E-0011 1.00000000000000E-0003

1.00005711670981E-0006 1.00000000000000E-0006 9.00000000000000E+0001

1.22254712812598E+0001 1.00000000000000E+0000 1.00000000000000E+0002

1.00000041149712E-0001 1.00000000000000E-0001 2.00000000000000E+0001

9.02930158368659E-0006 5.00000000000000E-0006 3.50000000000000E-0005

9.99999522634042E-0007 1.00000000000000E-0007 1.00000000000000E-0006

2.41351161251111E+0001 1.00000000000000E+0000 1.00000000000000E+0002

7.56718499408075E+0000 1.00000000000000E-0003 2.00000000000000E+0001

2.63692345910245E-0005 2.00000000000000E-0006 3.50000000000000E-0005

2.99999912092098E-0006 1.00000000000000E-0007 3.00000000000000E-0006

3.69603855073500E+0000 1.00000000000000E-0006 2.00000000000000E+0001

The total density of the two Ni layer is calculated as follows:

$$2\delta_{Fit} = \frac{(2\delta_{\text{Film1}} \cdot d_1) + (2\delta_{\text{Film2}} \cdot d_2)}{d_1 + d_2}$$

Where $2\delta_{\text{Film1}}$ and $2\delta_{\text{Film2}}$ are the resulting 2δ values for the first and second Ni layer with d_1 and d_2 as the respective layer thicknesses.

The coverage Θ is thus determined as

$$\Theta = \frac{\dfrac{\left(9.03 * 10^{-6} \cdot 12.2 \text{ Å}\right) + (2.64 \cdot 10^{-5} * 24.1 \text{ Å})}{36.3 \text{ Å}}}{2\delta_{Ni} = 3.44 * 10^{-5}}$$

After Heat Treatment

anka

1111 nix2

1111 nix

0100 ZrO2

  xx

3.85959869923654E+0009 1.00000000000000E+0003 1.00000000000000E+0012

1.09999907368135E+0002 1.00000000000000E+0001 1.10000000000000E+0002

1.00117116609244E-0011 1.00000000000000E-0011 1.00000000000000E-0003

1.00044471208891E-0006 1.00000000000000E-0006 9.00000000000000E+0001

2.25968256777739E+0001 1.00000000000000E+0000 1.00000000000000E+0002

1.00000041149712E-0001 1.00000000000000E-0001 2.00000000000000E+0001

1.12888313989402E-0005 5.00000000000000E-0006 3.50000000000000E-0005

9.99999522634042E-0007 1.00000000000000E-0007 1.00000000000000E-0006

2.55198212738907E+0001 1.00000000000000E+0000 1.00000000000000E+0002

1.99999951173358E+0001 1.00000000000000E-0003 2.00000000000000E+0001

1.77871624712906E-0005 2.00000000000000E-0006 3.50000000000000E-0005

2.99999912092098E-0006 1.00000000000000E-0007 3.00000000000000E-0006

5.30006153115164E+0000 1.00000000000000E-0006 2.00000000000000E+0001

After Oxygen Treatment

anka

1111 nix2

1111 nix

0100 ZrO2

  xx

4.87451171875000E+0009 1.00000000000000E+0003 1.00000000000000E+0012

2.86990433961153E+0003 1.00000000000000E+0001 1.00000000000000E+0004

9.99999984878452E-0004 1.00000000000000E-0011 1.00000000000000E-0003

1.65016955930097E-0006 1.00000000000000E-0006 9.00000000000000E+0001

2.16107656228069E+0001 1.00000000000000E+0000 1.00000000000000E+0002

1.00000041149712E-0001 1.00000000000000E-0001 2.00000000000000E+0001

1.16806705006789E-0005 5.00000000000000E-0006 3.50000000000000E-0005

1.00000085777745E-0007 1.00000000000000E-0007 1.00000000000000E-0006

3.17132932970195E+0001 1.00000000000000E+0000 1.00000000000000E+0002
1.15177819442130E+0001 1.00000000000000E-0003 2.00000000000000E+0001
1.67979083410799E-0005 2.00000000000000E-0006 3.50000000000000E-0005
2.99999912092098E-0006 1.00000000000000E-0007 3.00000000000000E-0006
7.95220161523974E+0000 1.00000000000000E-0006 2.00000000000000E+0001

YSZ(100) Surface

After Treatment I

anka

0100 ZrO2

  xx

2.06635839299540E+0010 1.00000000000000E+0003 1.00000000000000E+0012
9.75387476385499E+0002 1.00000000000000E+0001 1.00000000000000E+0005
1.00117116452278E-0011 1.00000000000000E-0011 1.00000000000000E-0003
1.00006002422641E-0007 1.00000000000000E-0007 9.00000000000000E+0001
1.20173991923690E+0000 1.00000000000000E-0003 2.00000000000000E+0001

After Treatment IV

anka

0100 ZrO2

  xx

2.52946199550382E+0010 1.00000000000000E+0003 1.00000000000000E+0012
1.00000076641303E-0001 1.00000000000000E-0001 1.10000000000000E+0003
9.99999393670269E-0004 1.00000000000000E-0011 1.00000000000000E-0003
1.00014676101633E-0007 1.00000000000000E-0007 9.00000000000000E+0001
1.68090470432547E+0000 1.00000000000000E-0006 2.00000000000000E+0001

Nickel nanoparticles on YSZ(100) Surface

After Evaporation

anka

1111 nix

0100 ZrO2

  xx

1.20000000000000E+0010 1.00000000000000E+0010 1.00000000000000E+0011

1.61211138150583E+0003 1.00000000000000E-0011 1.00000000000000E+0004

1.00117116609240E-0011 1.00000000000000E-0011 1.00000000000000E-0003

1.02893333304967E-0006 1.00000000000000E-0006 9.00000000000000E+0001

4.00000000000000E+0001 1.00000000000000E-0001 1.00000000000000E+0002

6.40000000000000E+0000 1.00000000000000E-0001 1.00000000000000E+0002

1.80000000000000E-0005 2.00000000000000E-0006 3.50000000000000E-0005

3.00000000000000E-0006 1.00000000000000E-0007 3.00000000000000E-0006

1.48450891353013E+0000 1.00000000000000E-0006 1.00000000000000E+0001

After Oxygen Treatment

anka

1111 nix

0100 ZrO2

  xx

6.89707031250000E+0009 1.00000000000000E+0009 1.00000000000000E+0011

2.80000000000000E+0000 1.00000000000000E-0011 1.00000000000000E+0004

2.95834065526311E-0008 1.00000000000000E-0011 1.00000000000000E-0003

1.00059747368248E-0006 1.00000000000000E-0006 9.00000000000000E+0001

6.58125000000000E+0001 1.00000000000000E-0001 1.00000000000000E+0002

3.44000000000000E+0001 1.00000000000000E-0001 1.00000000000000E+0002

1.09413281250000E-0005 2.00000000000000E-0006 3.50000000000000E-0005

2.98125000000000E-0006 1.00000000000000E-0007 3.00000000000000E-0006

1.95189726677439E+0000 1.00000000000000E-0006 1.00000000000000E+0001
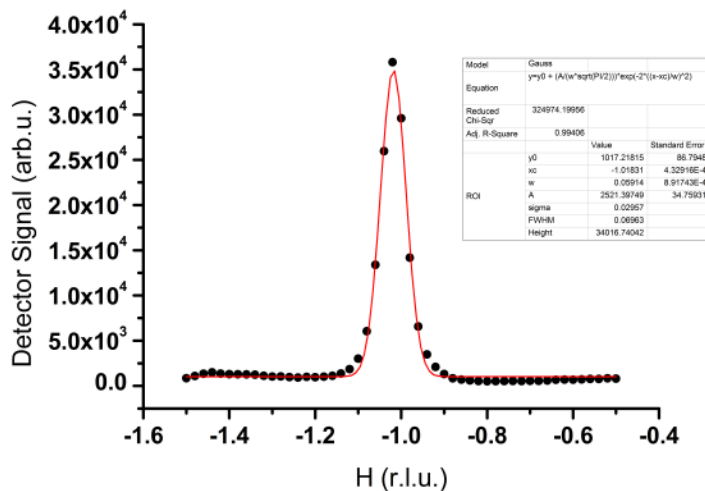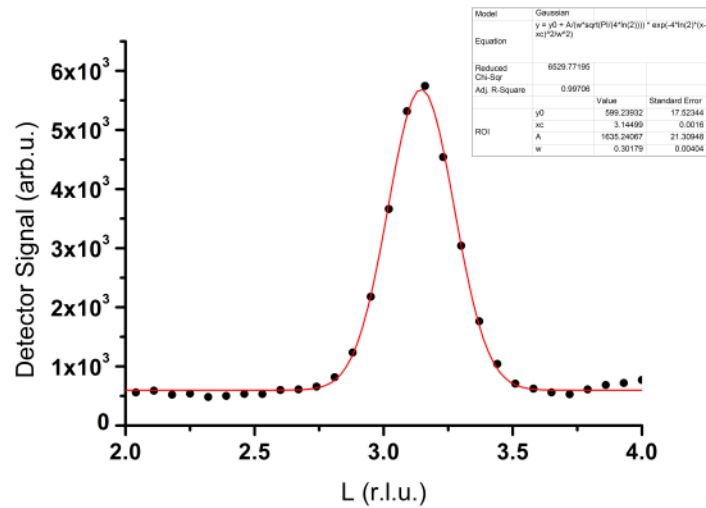
C Scans for Nanoparticle Size Determination

This part of the appendix gives the scans used to determine the size of the NPs. The results of the Gaussian fits with the respective FWHM values are always given in a table in the inset of the plots.
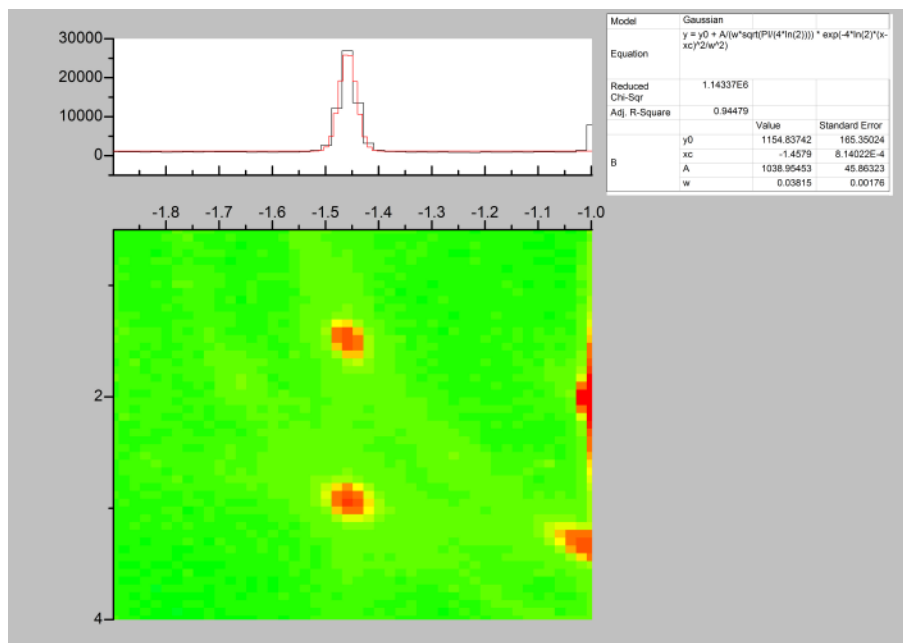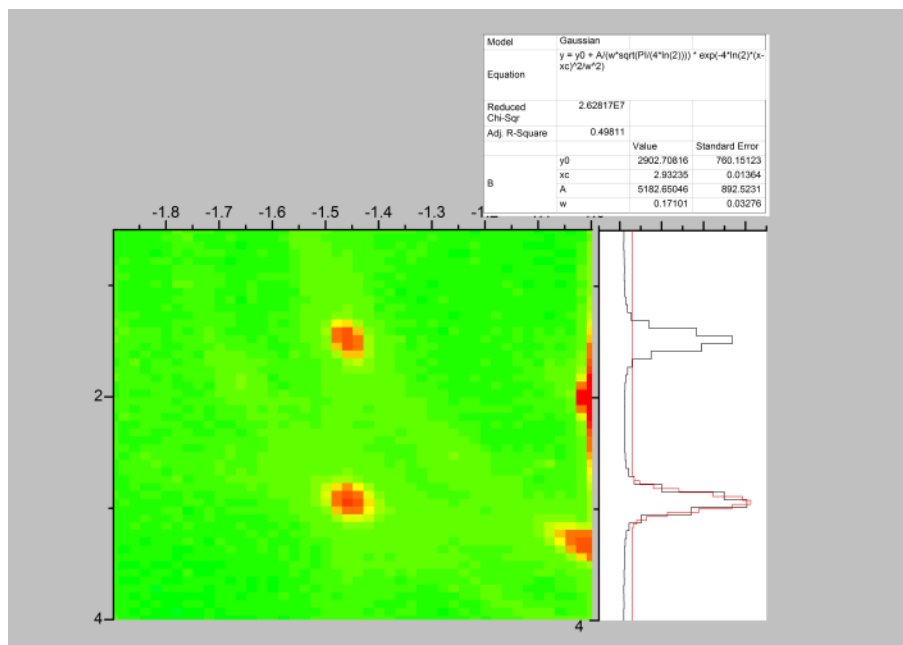
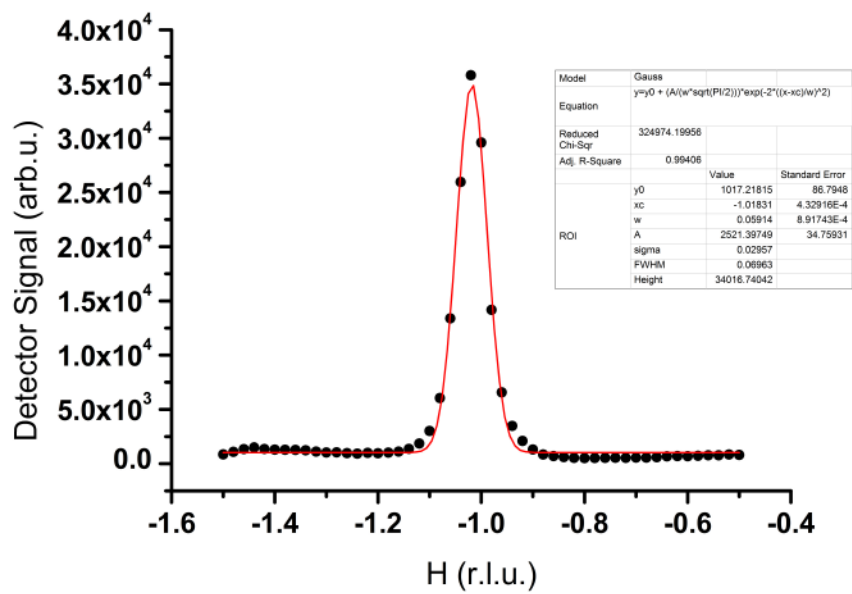## Nickel Nanoparticles on YSZ(111) Surface

After Evaporation

Tilted-NPs

After Heat Treatment

(111)-NPs

Tilted-NPs

Model	Gauss	
Equation	y=y0 + (A/(w*sqrt(PI/2)))*exp(-2*((x-xc)/w)^2)	
Reduced Chi-Sqr	324974.19956	
Adj. R-Square	0.99406	
	Value	Standard Error
y0	1017.21815	86.7948
xc	-1.01831	4.32916E-4
w	0.05914	8.91743E-4
ROI A	2521.39749	34.75931
sigma	0.02957	
FWHM	0.06963	
Height	34016.74042	

After Oxygen Treatment

(111)-NPs

Model	Gauss		
Equation	y=y0 + (A/(w*sqrt(PI/2)))*exp(-2*((x-xc)/w)^2)		
Reduced Chi-Sqr	125129.49018		
Adj. R-Square	0.99013		
		Value	Standard Error
	y0	1140.97997	55.29401
	xc	-1.45602	3.88887E-4
	w	0.03835	7.84757E-4
B	A	910.6415	16.89451
	sigma	0.01917	
	FWHM	0.04515	
	Height	18947.10016	

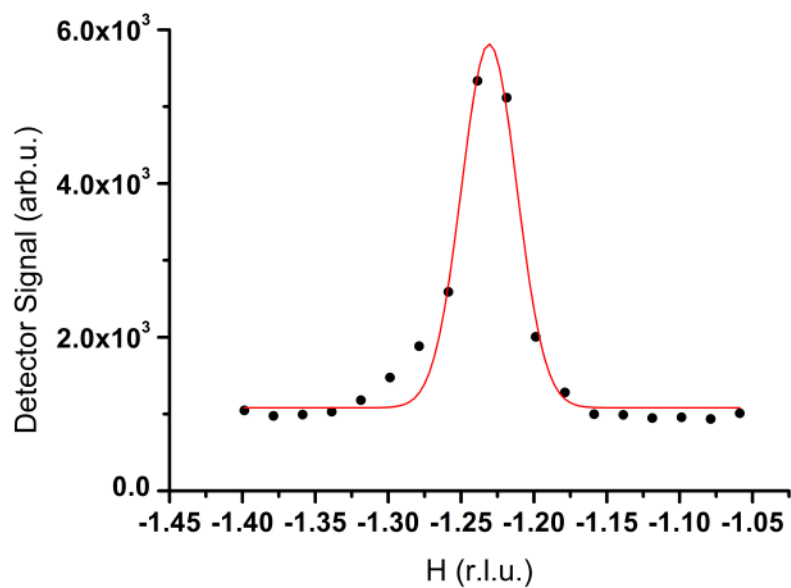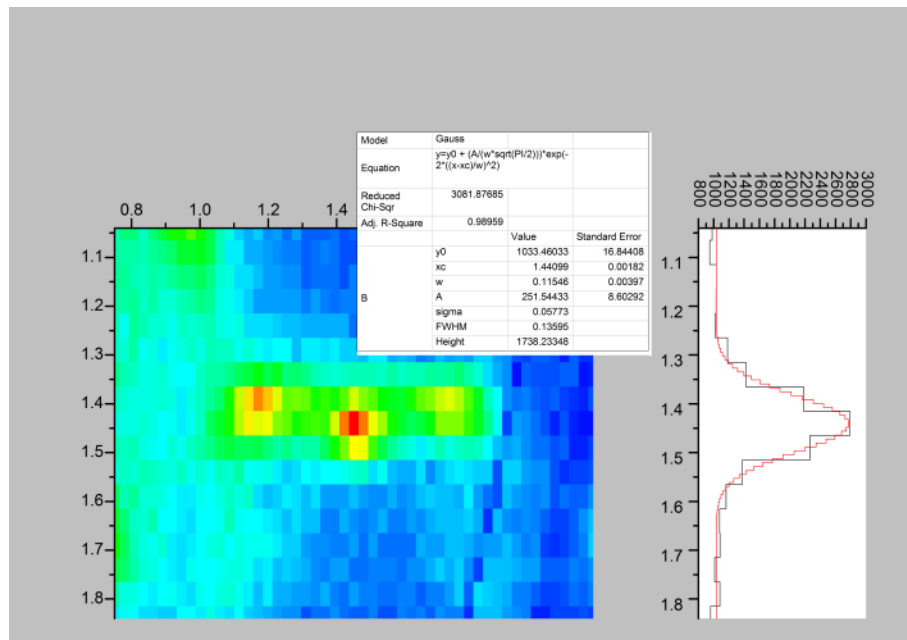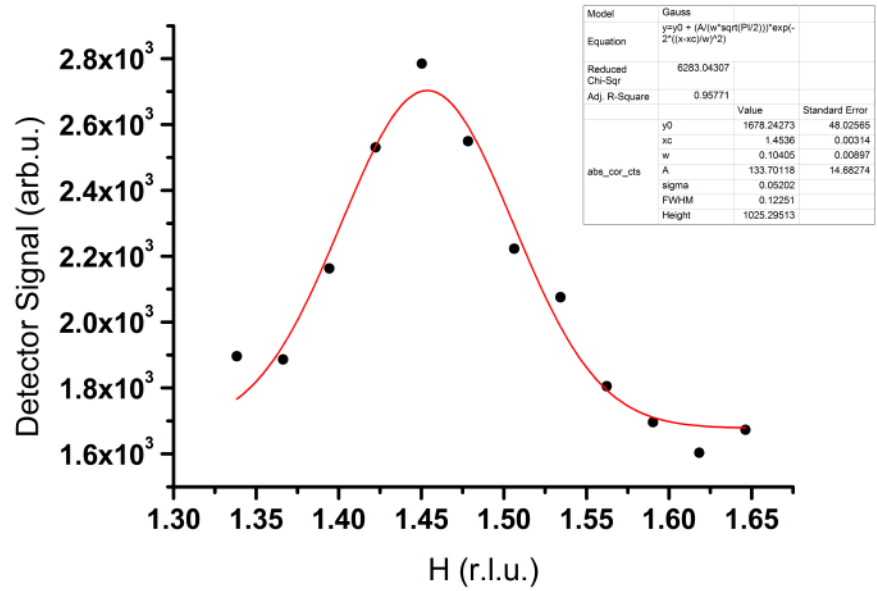| Model	Gauss		
Equation	y=y0 + (A/(w*sqrt(PI/2)))*exp(-2*((x-xc)/w)^2)		
Reduced Chi-Sqr	1.49308E7		
Adj. R-Square	0.58683		
		Value	Standard Error
	y0	2624.62679	576.3335
	xc	1.48599	0.01257
	w	0.15933	0.02567
B	A	4870.66779	708.6223
	sigma	0.07967	
	FWHM	0.1876	
	Height	24390.59721	

Tilted-NPs

(111)-NiO NPs

Nickel Nanoparticles on YSZ(100) Surface

After Evaporation

Ni-(100)

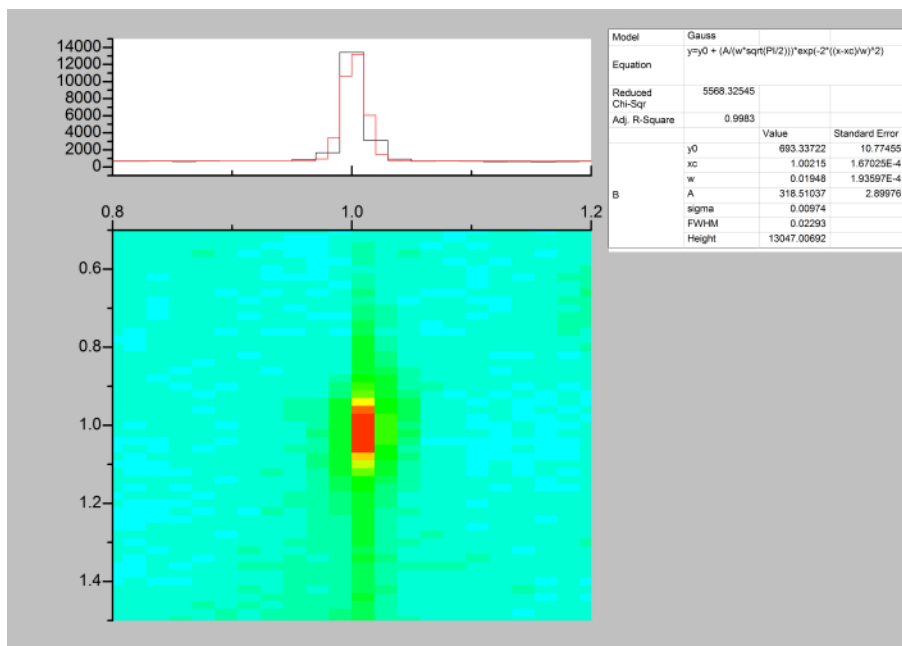| Model	Gauss	
Equation	y=y0 + (A/(w*sqrt(PI/2)))*exp(-2*((x-xc)/w)^2)	
Reduced Chi-Sqr	6263.04307	
Adj. R-Square	0.95771	
	Value	Standard Error
y0	1678.24273	48.02565
xc	1.4536	0.00314
w	0.10405	0.00897
abs_cor_cts A	133.70118	14.68274
sigma	0.05202	
FWHM	0.12251	
Height	1025.29513	

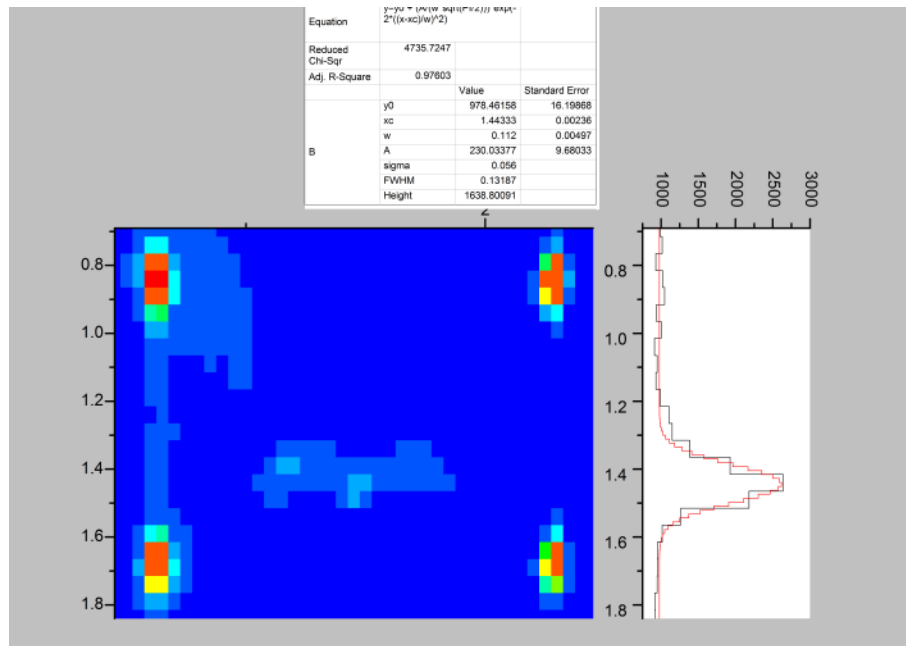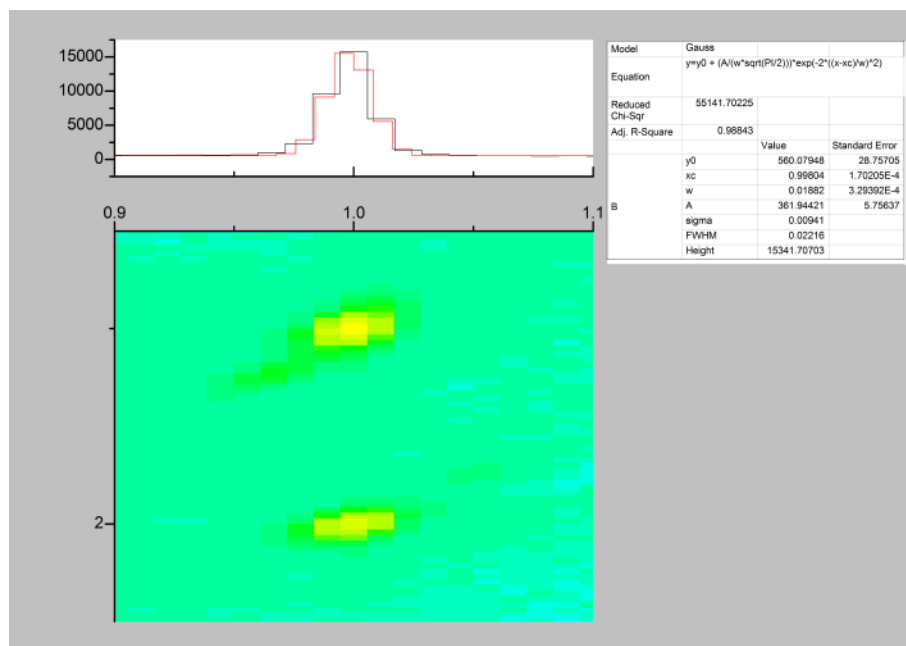| Model	Gauss	
Equation	y=y0 + (A/(w*sqrt(PI/2)))*exp(-2*((x-xc)/w)^2)	
Reduced Chi-Sqr	3061.87685	
Adj. R-Square	0.98959	
	Value	Standard Error
y0	1033.46033	16.84408
xc	1.44099	0.00182
w	0.11546	0.00397
B A	251.54433	8.60292
sigma	0.05773	
FWHM	0.13595	
Height	1738.23348	

After Heat Treatment

Ni-R15

(100)-Ni

After Oxygen Treatment

Ni-R15

NiO-R15

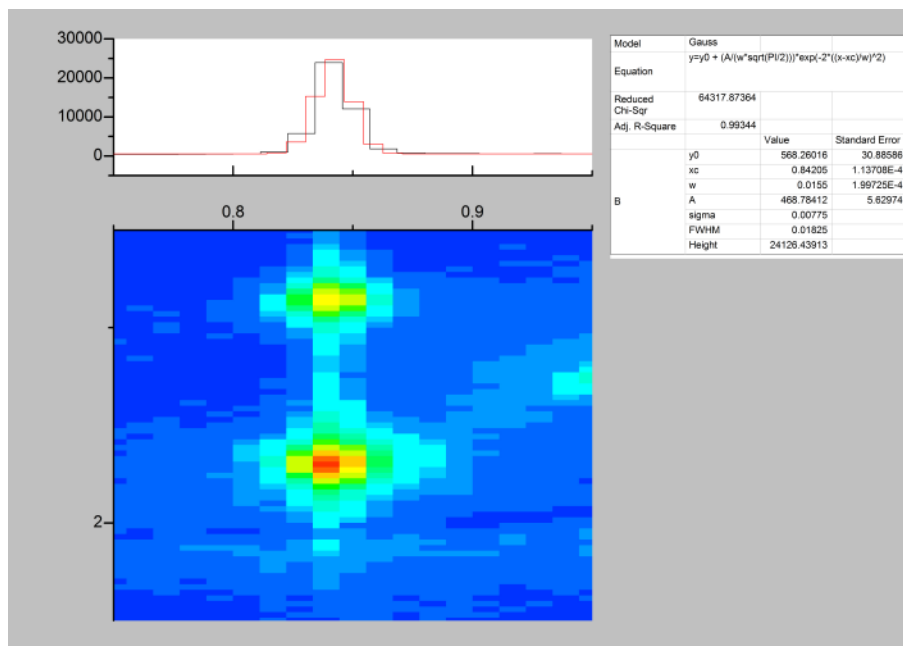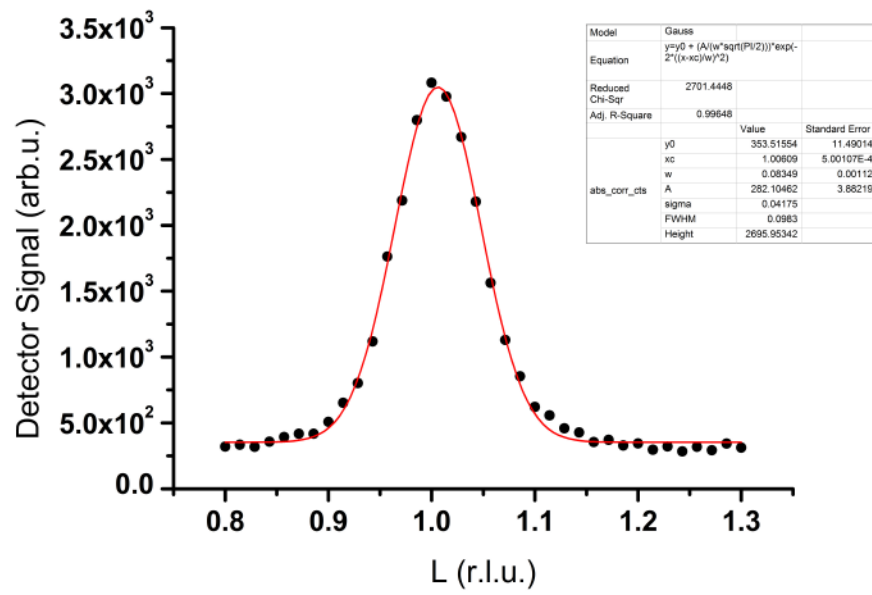| Model	Gauss		
Equation	y=y0 + (A/(w*sqrt(PI/2)))*exp(-2*((x-xc)/w)^2)		
Reduced Chi-Sqr	2701.4448		
Adj. R-Square	0.99648		
		Value	Standard Error
abs_corr_cts	y0	353.51554	11.49014
	xc	1.00609	5.00107E-4
	w	0.08349	0.00112
	A	282.10462	3.88219
	sigma	0.04175	
	FWHM	0.0983	
	Height	2695.95342	
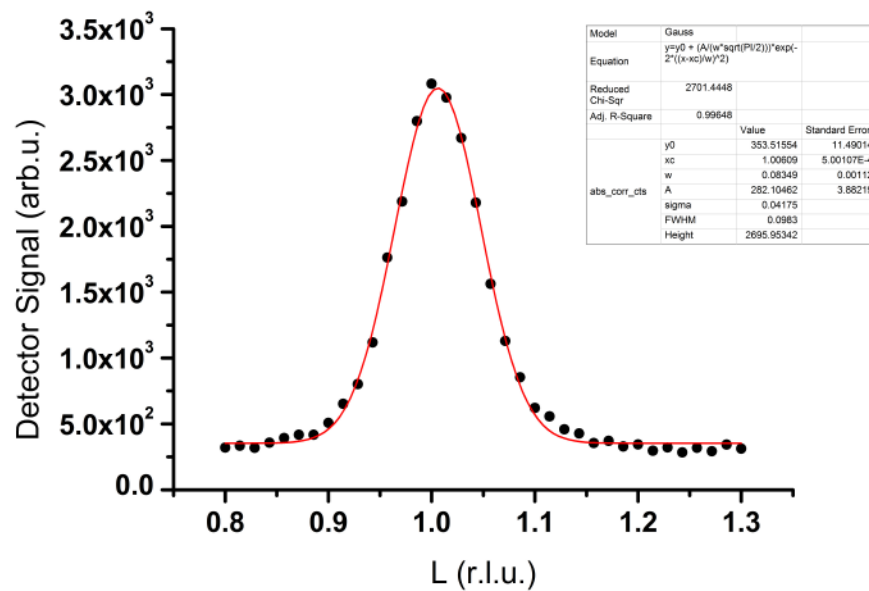
Bibliography

1. **Steele, B. and Heinzel, A.** Materials for fuel-cell technologies. *Nature.* 2001, Vol. 414, pp. 345 - 352.

2. **Minh, N.** Ceramic Fuel Cells. *Journal of the American Ceramics Society.* 1993, Vol. 76, pp. 563 - 588.

3. **Song, C.** Fuel processing for low-temperature and high-temperature fuel cells. Challenges, and opportunities for sustainable development in the 21st century. *Catalysis Today.* 2002, Vol. 77, pp. 17 - 49.

4. **BMW Group.** *Veröffentlichte Artikel.* [Online] 2003. www.bmwgroup.com/d/nav/index.html?http://www.bmwgroup.com/d/0_0_www _bmwgroup_com/forschung_entwicklung/science_club/veroeffentlichte_artikel/20 03/news200322.html.

5. *Die Brennstoffzelle als Stein der Weisen.* **Frankfurter Allgemeine Zeitung.** 10. 06 2010.

6. *Das Comeback der Brennstoffzelle.* **Handelsblatt.** 14. 08 2010.

7. **Bundesministerium für Wirtschaft und Arbeit.** *Strategiepapier zum Forschungsbedaf in der Wasserstoff-Energietechnologie.* 2010.

8. **Atkins, A., et al.** Advanced anodes for high-temperature fuel cells. *Nature Materials.* 2004, Vol. 3, pp. 17 - 27.

9. **Vogler, M., et al.** Modelling Study of Surface Reactions, Diffusion, and Spillover at a Ni/YSZ Patterned Anode. *Journal of The Electrochemical Society.* 2009, Vol. 156, pp. B663 - B672.

10. **Nolte, P.** *In situe Oxidation Study of Supported Rh and Pd Nanoparticles (Dissertation).* Stuttgart : Universität Stuttgart, 2009.

11. **Kasper, N., et al.** In situ oxidation study of MgO(100) supported Pd nanoparticles. *Surface Science.* 2006, Vol. 600, pp. 2860 - 2867.

12. **Ballabio, G., et al.** Ab initio study of yttria-stabilized cubic zirconia surfaces. *Physical Review B.* 2004, Vol. 70, pp. 75417 - 75423.

13. **Christensen, A. and Carter, E.** First-principles study of the surfaces of zirconia. *Physical Review B.* 1998, Vol. 58, pp. 8050 - 8064.

14. **Sasaki, T., et al.** Atomic and Electronic Structure of Ni/YSZ(111) Interface. *Materials Transactions.* 2004, Vol. 45, pp. 2137 - 2143.

15. **Deckers, S., Habraken, F. and Weg, W. van der.** Oxidatio of clean and Pt-covered Ni(111). *Applied Surface Science.* 1990, Vol. 45, pp. 207 - 220.

16. **Bokx, P. de, et al.** The Interaction of Oxygen with Ni(100) and the Reduction of the Surface Oxide by Hydrogen. *Applied Surface Science.* 1980, Vol. 5, p. 321.

17. **Koll, T.** *Diffusion oder Oxidation? Der Sauerstoff und die Ni(111)-Oberfläche (Dissertation).* Bochum : Shaker Verlag, 1998.

18. **Nishimura, T., et al.** Surface structure of Y2O3(9.5 mol%)-stabilized ZrO2(001) determined by high-resolution medium-energy ion scattering. *Physical Review B.* 2001, Vol. 64, pp. 73404 - 73408.

19. **Dickey, E., et al.** Prefered Crystallographic Orientation of Nickel Films deposited on (100) Cubic-Zirconia Substrates. *Thin Solid Films.* 2000, Vol. 372, pp. 37 - 44.

20. **Wagner, T., Duscher, G. and Kirchheim, R.** Decomposition of the ZrO2 Electrolyte in Contact with Ni: Struture and Chemical Composition of the Ni-electrolyte Interface. *Journal of Materials Research.* 1999, Vol. 14, pp. 3340 - 3345.

21. **Heinrich, V. and Cox, P.** *The Surface Science of Metal Oxides.* Cambridge : Cambridge University Press, 1994.

22. **Chao, C., Kim, Y. and Prinz, F.** Surface Modification of Yttria-Stabilized Zirconia Electrolyte by Atomic Layer Deposition. *Nano Letters.* 2009, Vol. 10, pp. 3626 - 3628.

23. **Vreeburg, R., et al.** A comparison between the reduction kinetics of oxidized Ni(111) and Ni(100) surfaces by hydrogen and deuterium. *Surface Science.* 1992, Vol. 272, pp. 294 - 298.

24. **Goff, J., et al.** Defect structure of yttria-stabilized zirconia and its influence on the ionic conductivity at elevated temperatures. *Physical Review B.* 1999, Vol. 59, pp. 14202 - 14219.

25. **Hull, S.** Superionics: crystal structures and conduction processes. *Reports on Progress in Physics.* 2004, Vol. 67, pp. 1285 - 1288.

26. *Toyota Plans 6 New Hybrids for 2012.* **The New York Times.** 2010.

27. *Fuel Cell Cars: Where Are They Now?* **The Wall Street Journal.** 2010.

28. **UK Fuel Cells.** [Online] 2006. www.fuelcellsuk.org/the-industry/.

29. **Rosi, N., et al.** Hydrogen Storage in Microporous Metal-Organic Frameworks. *Science.* 2003, Vol. 300, pp. 1127 - 1129.

30. **Crabtree, G., Dresselhaus, M. and Buchanan, M.** The Hydrogen Economy. *Physics Today.* 2004, Vol. December, p. 39.

31. **Spacil, H.** *Electrical Device Including Nickel-Containing Stabilized Zirconia Electrode. 3,558,360* US Patent, 1970.

32. **Shihkin, M. and Ziegler, T.** Oxidation of H2, CH4, and CO Molecules at the Interface between Nickel and Yttria-Stabilized Zirconia: A Theoretical Study Based on DFT. *Journal of Physical Chemistry C.* 2009, Vol. 113, pp. 21667 – 21678.

33. **Official Website of the Nobel Prize.** *The Nobel Prize in Chemistry 2007.* [Online] http://nobelprize.org/nobel_prizes/chemistry/laureates/2007/.

34. —. *The Nobel Prize in Physics 1986.* [Online] http://nobelprize.org/nobel_prizes/physics/laureates/1986/.

35. **Ishizawa, N., et al.** Synchrotron radiation study of yttria-stabilized zirconia, Zr0.758Y0.242O1.879. *Acta Crystallographica.* 1999, Vol. B55, pp. 726 - 735.

36. **Stierle, A., et al.** A surface x-ray study of the structure and morphology of the oxidized Pd(001) surface. *Journal of Chemical Physics.* 2005, Vol. 122, pp. 44706 - 44710.

37. **Stierle, A.** Oxidation of Palladium: from single crystal surfaces towards nanoparticles. *Zeitschrift für Metallkunde: International Journal of Materials Research.* 2009, Vol. 100, p. 10.

38. **Schmid, M., et al.** Structure of Ag(111)-p(4 x 4)-O: no silver oxide. *Physical Review Letters.* 2006, Vol. 96, pp. 1461021 - 14610214 .

39. **Gong, X., et al.** The (2x1) Reconstruction of the Rutile TiO2(011) Surface: a Combined Density Functional Theory, X-ray Diffraction, and Scanning Tunneling Microscopy Study. *Surface Science.* 2009, Vol. 603, pp. 138 - 144.

40. **Stierle, A. and Molenbroek, A.** Novel in-situ techniques for nano catalysis. *MRS Bulletin.* 2007, Vol. 32, pp. 1001 - 1050.

41. **Nolte, P., et al.** Shape Changes of Supported Rh Nanoparticles During Oxidation and Reduction Cycles. *Science.* 2009, Vol. 321, pp. 1654 - 1658.

42. **Nolte, P., et al.** Carbon Incorporation and Deactivation of MgO(001) supported Pd Nanoparticles during CO Oxidation. *Catalysis Today.* 2009, Vol. 145, p. 243.

43. **Nernst, W.** Über die elektrolytische Leitung fester Körper bei sehr hohen Temperaturen. *Zeitschrift für Elektrochemie.* 1899, Bd. 6, S. 41 - 43.

44. **Padture, N., Gell, M. and Jordan, E.** Thermal Barrier Coatings for Gas-Turbine Engine Applications. *Science.* 2002, Vol. 296, pp. 280 - 284.

45. **Cairney, J., et al.** Phase stability of thermal barrier oxides: A comperative study of Y and Yb additions. *International Journal of Materials Research.* 2007, Vol. 12, pp. 1177 - 1187.

46. **S.Jiang and S.Chan.** A review of anode materials development in solid oxide fuel cells. *Journal of Materials Science.* 2004, Vol. 37, pp. 4405 - 4439.

47. **Jamsak, W., et al.** Performance of ethanol-fuelled solid oxide fuel cells: Proton and oxygen ion conductors. *Chemical Engineering Journal.* 2007, Vol. 133, pp. 187 - 194.

48. **Shishkin, M. and Ziegler, T.** The Oxidation of H2 and CH4 on an Oxygen-Enriched Yttria-Stabilized Zirconia Surface: A Theoretical Study Based on Density Functional Theory. *Journal of Physical Chemistry C.* 2008, Vol. 112, pp. 19662 - 19669.

49. **Wang, X.** Yttrium segregation and surface phases of yttria-stabilized zirconia (111) surface. *Surface Science.* 2008, Vol. 602, pp. L5 - L9.

50. **Bernasik, A., Kowalski, K. and Sadowski, A.** Surface segregation in yttria-stabilized zirconia by means of angle resolved X-ray photoelectron spectroscopy. *Journal of Physicy and Chemistry of Solids.* 2002, Vol. 63, pp. 233 - 239.

51. **Pomfret, M., et al.** Structural and Compositional Characterization of Yttria-Stabilized Zirconia: Evidence of Surface-Stabilized, Low-Valence Metal Species. *Analytical Chemistry.* 2005, Vol. 77, pp. 1791 - 1795.

52. **Morrow, S., et al.** High temperature scanning tunneling microscopy of purely ion conducting yttria-stabilized zirconia (YSZ). *Surface Science.* 2009, Vol. 603, pp. L78 - L81.

53. **Eichler, A. and Kresse, G.** First-principles calculations for the surface termination of pure and yttria-doped zirconia surfaces. *Physical Review B.* 2004, Vol. 69, pp. 45402 - 45418.

54. **Wyckoff, R.** *Crystal Structures.* Florida, USA : Krieger Publishing Company, 1982.

55. *International Tables for Crystallography.* s.l. : Kluwer academic publishers, 1995. Vol. A.

56. **Teufer, G.** The crystal structure of tetragonal ZrO2. *Acta Crystallographica.* 1962, Vol. 15, p. 1187.

57. **McCullough, J. and Trueblood, K.** The Crystal Structure of Baddeleyite (Monoclinic ZrO2). *Acta Crystallographica.* 1959, Vol. 12, pp. 507 - 511.

58. **Dixon, J., et al.** Electrical Resistivity of Stabilized Zirconia at Elevated Temperatures. *Journal of the Electrochemical Society.* 1963, Vol. 110, pp. 276 - 280.

59. **Ioffe, A., Rutman, D. and Karpachov, S.** On the nature of the conductivity maximum in zirconia-based solid electrolytes. *Elelctrochimica Acta.* 1978, Vol. 23, pp. 141 - 142.

60. **Morterra, C., et al.** Surface characterization of tetragonal ZrO2. *Applied Surface Science.* 1993, Vols. 65-66, pp. 257 - 264.

61. **Orlando, R., et al.** Ab initio study of the bare and hydrated (001) surface of tetragonal zirconia. *Surface Science.* 1992, Vol. 275, pp. 482 - 492.

62. **Haase, F. and Sauer, J.** The Surface Structure of Sulfated Zirconia: Periodic ab Initio Study of Sulfuric Acid Adsorbed on ZrO2(101) and ZrO2(001). *Journal of the American Chemical Society.* 1998, Vol. 120, pp. 13503 - 13512.

63. **Eichler, A.** Tetragonal Y-doped zirconia: Structure and ion conductivity. *Physical Review B.* 2001, Vol. 64, pp. 174103 - 174111.

64. **Garvie, R. and Nicholson, P.** Structure and Thermomechanical Properties of Partially Stabilized Zirconia in the CaO-ZrO2 System. *Journal of the American Ceramic Society.* 1972, Vol. 55, pp. 152 - 157.

65. **Stefanovich, E., Shluger, A. and Catlow, C.** Theoretical Study of the Stabilization of Cubic-Phase ZrO2 by Impurities. *Physical Review B.* 1994, Vol. 49, pp. 11560 - 11571.

66. **Hohnke, D.** Ionic conduction in doped oxides with the fluorite structure. *Solid State Ionics.* 1981, Vol. 5, pp. 531 - 534.

67. **Witthemore, O. and Ault, O.** Thermal Expansion of Various Ceramic Materials to 1500 C. *Journal of the American Ceramic Society.* 1956, Vol. 39, pp. 443 - 444.

68. **Karaulov, A., Grebenyuk, A. and I. Rudyak.** Effect of Phase Composition of Zirconium Dioxide on Spalling Resistance. *Izv. Akad. Nauk SSSR, Neorganicheskie Materialy.* 1967, Vol. 3, pp. 1101 - 1103.

69. **King, A. and Yavorsky, P.** Stress Relief Mechanisms in Magnesia- and Yttria-Stabilized Zirconia. *Journal of the American Ceramic Society.* 1968, Vol. 51, pp. 38 - 42.

70. **Krishnan, V., Heislbetz, S. and Bertagnolli, H.** Structural Investigations on Nanocomposite Mixed Metal Oxide Powders Used in Surface Catalysis. *Zeitschrift für Physikalische Chemie.* 2008, Vol. 222, pp. 1023 - 1038.

71. **Yashima, M., Ishizawa, N. and Yoshimura, M.** Application of an Ion-Packing Model Based on Defect Clusters to Zirconia Solid Solutions: II, Applicability of Vegard's law. *Journal of the American Ceramic Society.* 1992, Vol. 75, pp. 1550 - 1557.

72. **Faber, J., Mueller, M. and Cooper, B.** Neutron-diffraction study of Zr(Ca,Y)O(2-x): Evidence of differing mechanisms for internal and external distortions. *Physical Review B.* 1978, Vol. 17, pp. 4884 - 4888.

73. **Horiuchi, H., et al.** Time-of-Flight Neutron Diffraction Study of a Single Crystal of Yttria-Stabilized Zirconia, Zr(Y)O1.862, at High Temperature and in an Applied Electrical Field. *Acta Crystallographica.* 1984, Vol. B40, pp. 367 - 372.

74. **Morinaga, M. and Cohen, J.** X-ray Diffraction Study of Zr(Ca,Y)O2_ x.I. The Average Structure. *Acta Crystallographica.* 1979, Vol. A35, pp. 789 - 795.

75. **Moroney, L., Thompson, T. and Cox, D.** ADPD: a new approach to shared-site problems in crystallography. *Journal of Applied Crystallography.* 1988, Vol. 21, pp. 206 - 208.

76. **Steele, D. and Fener, B.** The structure of cubic ZrO2 : YO, .5 solid solutions by neutron scattering. *Journal of Physics C.* 1973, Vol. 7, pp. 1 - 11.

77. **Suzuki, S., Tanaka, M. and Ishigame, M.** Structural studies on the Zr0,-Y,O, system by electron diffraction and electron microscopy I1. *Journal of Physics C.* 1987, Vol. 20, pp. 2963 - 2972.

78. **Welberry, T., et al.** Diffuse Scattering in Yttria-Stabilized Cubic Zirconia. *Journal of Solid State Chemistry.* 1992, Vol. 100, pp. 71 - 89.

79. **Welberry, T., et al.** A 3D Model for the Diffuse Scattering in Cubic Stabilized Zirconias. *Journal of Solid State Chemistry.* 1993, Vol. 106, pp. 461 - 475.

80. **Mayernick, A., et al.** A reactive force-field (ReaxFF) Monte Carlo study of surface enrichment and step structure on yttria-stabilized zirconia. *Surface Science.* 2010, Vol. 604, pp. 1438 - 1444.

81. **Kresse, G. and Hafner, J.** First-principles study of the adsorption of atomic H on Ni (111), (100) and (110). *Surface Science.* 2000, Vol. 459, pp. 287 - 302.

82. **Christmann, K., et al.** Adsorption of hydrogen on nickel single crystal surfaces. *Journal of Chemical Physics.* 1974, Vol. 60, pp. 4528 - 7540.

83. **Christmann, K., et al.** Chemisorption geometry of hydrogen on Ni(111): Order and disorder. *Journal of Chemical Physics.* 1979, Vol. 70, pp. 4168 - 4184.

84. **Bychkov, V., et al.** Nonlinear behaviour during methane and ethane oxidation over Ni, Co and Pd catalysts. *Surface Science.* 2009, Vol. 603, pp. 1680 - 1689.

85. **Demuth, J. and Eastman, D.** Photoemission Observation of Pi-d Bonding and Surface Reactions of Adsorbed Hydrocarbons on Ni(111). *Physical Review Letters.* 1974, Vol. 32, pp. 1123 - 1127.

86. **Stroscio, J., Bare, S. and Ho, W.** The Chemisorption and Decomposition of Ethylene and Acetylene on Ni(110). *Surface Science.* 1984, Vol. 148, pp. 499 - 525.

87. **Hambourger, M. and Moore, T.** Nailing Down Nickel for Electrocatalysis. *Science.* 2009, Vol. 326, pp. 1355 - 1356.

88. **Wever, F. und Ruetten, P.** Walzstruktur kubisch krystallisierender Metalle. *Annalen der Physik.* 1925, Bd. 76, S. 476.

89. **Clark, G., Asbury, W. and Wick, R.** An Application of X-ray Crystallometry to the Structure of Nickel Catalysts. *Journal of the American Chemical Society.* 1925, Vol. 47, pp. 2661 - 2671.

90. **Warren, B.** *X-ray Diffraction.* New York : Dover Publications Inc., 1990.

91. **Krishna, P. and Pandey, D.** Close-Packed Structures. *International Union of Crystallography Commission on Crystallographic Teaching.* Cardiff : University College Cardiff Press, 1981.

92. **Waal, B. van de.** Cross-twinning model of fcc crystal growth. *Journal of Crystal Growth.* 1996, Vol. 158, pp. 153 - 165.

93.

94. **Christmann, K., et al.** Adsorption of hydrogen on Nickel Single Crystal Surfaces. *Journal of Chemical Physics.* 1974, Vol. 60, pp. 4528 - 4540.

95. **Stroscio, J., Bare, S. and Ho, W.** The Chemisorption and Decomposition of Ethylene and Acetylene on Ni(110). *Surface Science.* 1984, Vol. 148, pp. 499 - 525.

96. **Wedler, G.** *Adsorption.* Weinheim : Verlag Chemie, 1970.

97. **Ertl, G. und Küppers, D.** Wechselwirkung von Wasserstoff mit einer Nickel (110)-Oberfläche. *Berichte der Bunsen-Gesellschaft.* 1971, Bd. 75, S. 1017 - 1025.

98. **Foiles, S., Baskes, M. and Daw, M.** Embedded-atom-method functions for the fcc metals Cu, Ag, Au, Ni, Pd, and their alloys. *Physical Review B.* 1986, Vol. 33, pp. 7983 - 7991.

99. **Cleveland, C. and Landman, U.** The energetics and structure of nickel clusters: Size dependence. *Journal of Chemical Physics.* 1991, Vol. 94, pp. 7376 - 7396.

100. **Wulff, G.** Zur Frage der Geschwindigkeit des Wachsthums und der Auflösung der Krystallflächen. *Zeitschrift für Krystallographie und Mineralogie.* 1901, Bd. 34, S. 449 - 530.

101. **Winterbottom, W.** Equilibrium shape of a small particle in contact with a foreign substrate. *Acta Metallurgica.* 1967, Vol. 15, pp. 303 - 310.

102. **Hansen, K. Højrup, et al.** Palladium Nanocrystals on Al2O3: Structure and Adhesion Energy. *Physical Review Letters.* 1999, Vol. 83, pp. 4120 - 4123.

103. **Henry, C.** Surface studies of supported model catalysts. *Surface Science Reports.* 1998, Vol. 31, pp. 231 - 325.

104. **Bäumer, M. and Freund, H.** Metal deposits on well-ordered oxide Films. *Progress in Surface Science.* 1999, Vol. 61, pp. 127 - 198.

105. **Barbier, A., Renaud, G. and Robach, O.** Growth, Annealing and Oxidation of the Ni/MgO (001) Interface Studied by Grazing Incidence X-ray Scattering. *Journal of Applied Physics.* 1998, Vol. 84, pp. 4259 - 4267.

106. **Dickey, E., Fan, X. and Pennycook, S.** Direct atomic-scale imaging of ceramic interfaces. *Acta Metallurgica.* 1999, Vol. 47, pp. 4061 - 4068.

107. **Christensen, A. and Carter, E.** Adhesion of ultrathin ZrO2(111) films on Ni(111) from first principles. *Journal of Chemical Physics.* 2001, Vol. 114, pp. 5816 - 5831.

108. **Han, X., et al.** Electronic Structure and Bonding Properties of ZrO2/Ni Interface. *Key Engineering Materials.* 2002, Vols. 224-226, pp. 335 - 358.

109. **Beltrán, J., et al.** Bond formation at the Ni/ZrO2 interface. *Physical Review B.* 2003, Vol. 68, p. 75401.

110. **Beltrán, J., et al.** Bond formation at the Ni/c-ZrO2 interface. *Journal of the European Ceramic Society.* 2003, Vol. 23, pp. 2737 - 2740.

111. **Chirsey, D. and Hubler, G.** *Pulsed Laser Deposition of Thin Films.* New York : John Wiley & Sons, 1994.

112. **Mantl, S. and Bay, H.** New method for epitaxial heterostructure layer growth. *Applied Physics Letters.* 1992, Vol. 61, pp. 267 - 267.

113. **Cox, P.** *Transition Metal Oxides: An Introduction to Their Electronic Structure and Properties.* Oxford : Oxford University Press, 2010.

114. **Johnson, B.** *Some Thermodynamic Aspects of Inorganic Chemistry.* Cambridge : Cambridge University Press, 1982.

115. **Wendt, S., et al.** The Role of Interstitial Sites in the Ti3d Defect State in the Band Gap of Titania. *Science.* 2008, Vol. 320, pp. 1755 - 1759.

116. **Tilley, R.** *Defect Crystal Chemistry.* Glasgow : Blackie, 1987.

117. **Kohn, W. and Sham, L.** Self-Consistent Equations Including Exchange and Correlation Effects. *Physical Review.* 1965, Vol. 140, pp. A1133 - 1138.

118. **Diebold, U.** The Surface Science of Titanium Dioxide. *Surface Science Reports.* 2003, Vol. 48, pp. 53 - 229.

119. **Freund, H.** Oxide Surfaces. *Faraday Disscussions.* 1999, Vol. 114, pp. 1 - 31.

120. **Al-Abadleh, H. and Grassian, V.** Oxide Surfaces as Enviromental Interfaces. *Surface Science Reports.* 2003, Vol. 52, pp. 63 - 161.

121. **Tasker, P.** The Stability of Ionic Surfaces. *Journal of Physics C.* 1979, Vol. 12, pp. 4977 - 4984.

122. **LaFemina, J.** Total Energy Computations of Oxide Surface Reconstructions. *Critical Reviews in Surface Chemistry.* 1994, Vol. 3, pp. 297 - 386.

123. **Gerlach, R., et al.** Structure and dynamics of CO/MgO(001): a helium atom scattering study. *Surface Science.* 1995, Vols. 331 - 333, pp. 1490 - 1495.

124. **Heidberg, J., et al.** The monolayer CO adsorbed on MgO(100)detected by polarization infrared spectroscopy. *Surface Science.* 1995, Vols. 331 - 333, pp. 1467 - 1472.

125. **Over, H., et al.** Atomic-Scale Structure and Catalytic Reactivity of the RuO2(110) Surface. *Science.* 2000, Vol. 287, pp. 1474 - 1476.

126. **Dulub, O., et al.** Electron-Induced Oxygen Desorption from the TiO2(011)-2×1 Surface Leads to Self-Organized Vacancies. *Science.* 2007, Vol. 317, pp. 1052 - 1056.

127. **Dulub, O., et al.** Structure, defects, and impurities at the rutile TiO2(011)-(2 x 1) surface: A scanning tunneling microscopy study. *Surface Science.* 2006, Vol. 600, pp. 4407 - 4417.

128. **Müller, P. and Saúl, A.** Elastic effects on surface physics. *Surface Science Reports.* 2004, Vol. 54, pp. 157 - 258.

129. **Somorjai, G.** The Evolution of Surface Chemistry. A Personal View of Building the Future on Past and Present Accomplishments. *Journal of Pysical Chemistry B.* 2002, Vol. 106, pp. 9201 - 9213.

130. **Cowley, J.** *Diffraction Physics.* New York : American Elsevier, 1975.

131. **Als-Nielsen, J.** *Elements of Modern X-Ray Physics.* West Sussex : John Wiley & Sons Ltd., 2001.

132. **Dosch, H.** *Critical Phenomena at Surfaces and Interfaces: Evenescent X-Ray and Neutron Scattering.* Berlin : Springer-Verlag, 1992.

133. **Robinson, I. and Tweet, D.** Surface x-ray diffraction. *Reports on Progress in Physics.* 1992, Vol. 55, pp. 599 - 651.

134. **Feidenhans'l, R.** Surface determination by X-ray diffraction. *Surface Science Reports.* 1989, Vol. 10, pp. 105 - 188.

135. **Robinson, I.** Crystal truncation rods and surface roughness. *Physical Review B.* 1986, Vol. 33, pp. 3830 - 3836.

136. **Bragg, W. L.** The analysis of crystals by the X-ray spectrometer. *Proceedings of the Royal Society of London, Series A.* 1914, Vol. 89, pp. 468 - 489.

137. **Offical website of the Nobel Prize.** *The Nobel Prize in Physics 1915.* [Online] http://nobelprize.org/nobel_prizes/physics/laureates/1915/index.html.

138. **Vineyard, G.** Grazing-incidence diffraction and the distorted-wave approximation for the study of surfaces. *Physical Review B.* 1982, Vol. 26, pp. 4146 - 4159.

139. **Kittel, C.** *Introduction to Solid State Physics.* New York : Kohn Wiley & Sons, 19995.

140. **Debye, P.** Interferenz von Röntgenstrahlen und Wärmebewegung. *Annalen der Physik.* 1913, Bd. 348, S. 49 - 92.

141. **Waller, I.** Zur Frage der Einwirkung der Wärmebewegung auf die Interferenz von Röntgenstrahlen. *Zeitschrift für Physik A.* 1923, Bd. 17, S. 398 - 408.

142. **National Institute of Standards and Technology.** Physical Reference Data. *http://physics.nist.gov/PhysRefData/FFast/html/form.html.* [Online] [Cited: March 25, 2010.]

143. **Stierle, A., et al.** Dedicated Max-Planck beamline for the in situ investigation of interfaces and thin films. *Review of Scientific Instruments.* 2004, Vol. 75, pp. 5302 - 5307.

144. **Huber Diffraction and Positioning Equipment.** Official Huber webpage. *www.xhuber.com.* [Online]

145. **Vlieg, E.** Integrated Intensities Using a Six-Circle Surface X-ray Diffractometer. *Journal of Applied Crystallography.* 1997, Vol. 30, pp. 532 - 543.

146. **SPEC, Official webpage of.** *http://www.certif.com/spec.html.* [Online]

147. **Lohmeier, M. and Vlieg, E.** Angle Calculations for a Six-Circle Surface X-ray Diffractometer. *Journal of Applied Crystallography.* 1993, Vol. 26, pp. 706 - 716.

148. **Henrich, B., et al.** PILATUS:AsinglephotoncountingpixeldetectorforX-rayapplications. *Nuclear Instruments and Methods in Physics Research A.* 2009, Vol. 607, pp. 247 - 249.

149. **Patterson, B., et al.** The materials science beamline at the Swiss Light Source: design and realization. *Nuclear Instruments and Methods in Physics Research A.* 2005, Vol. 540, pp. 42 - 67.

150. **Newport.** Ofiicial webpage of Newport. *www.newport.com.* [Online]

151. **Swiss Light Source at PSI.** Webpage of the materials science beamline at SLS. *http://sls.web.psi.ch/view.php/beamlines/ms/index.html.* [Online]

152. **Vlieg, E.** From beam time to structure factors. [Introduction]. 2001. available at: www.esrf.eu/computing/scientific/joint_projects/ANA-ROD/.

153. **Ana-Rod.** Webpage of Ana-Rod at esrf.eu. *http://www.esrf.eu/computing/scientific/joint_projects/ANA-ROD/index.htm.* [Online] March 2010.

154. **IDL.** Webpage of IDL at ITTVIS. [Online] www.ittvis.com/ProductServices/IDL.aspx.

155. **Vlieg, E.** A concise ROD manual. *available at: www.esrf.eu.* 2001.

156. **Robach, O.** Appendix to the manual of the ROD program (experimental version): Robach's extension. *available at: www.esrf.eu.* 2007.

157. **Levenberg, K.** A Method for the Solution of Certain Problems in Least Squares. *Quarterly of Applied Mathematics.* 1944, Vol. 2, pp. 164 - 168.

158. **Marquardt, D.** An Algorithm for Least-Squares Estimation of Nonlinear Parameters. *SIAM Journal on Applied Mathematics.* 1963, Vol. 11, pp. 431 - 441.

159. **Freeman, D.** A meeting with Enrico Fermi. *Nature.* 2004, Vol. 427, p. 297.

160. **Vonk, V.** An Extension to "rod" for Simultaneous Use of Non-anomalous and Anomalous Data for Fits. To be Published Soon.

161. **Mezger, M., et al.** Molecular Layering of Fluorinated Ionic Liquids at a Charged Sapphire (0001) Surface. *Science.* 2008, Vol. 322, pp. 424 - 428.

162. **Stierle, A., et al.** High resolution x-ray characterization of Co films on Al2O3. *Journal of Applied Physics.* 1993, Vol. 73, pp. 4808 - 4814.

163. **Zabel, H.** X-ray and neutron reflectivity analysis of thin films and superlattices. *Applied Physics A.* 1994, Vol. 58, pp. 159 - 168.

164. **Tolan, M.** *X-Ray Scattering from Soft-Matter Thin Films.* Berlin : Springer, 1999.

165. **Jackson, J.** *Classical Electrodynamics.* New York : John Wiley & Sons, 1999.

166. **Parratt, L.** Surface Studies of Solids by Total Reflection X-Rays. *Physical Review.* 1954, Vol. 95, pp. 359 - 369.

167. **Névot, L. and Croce, P.** Caractérisation des surfaces par réflexion rasante de rayons X. Application à l'étude du polissage de quelques verres silicates. *Revue de Physique Appliquée.* 1980, Vol. 15, pp. 761 - 779.

168. **Stierle, A.** Obtainable from stierle@mf.mpg.de.

169. **Meyer, G. and Amer, N.** Simultaneous measurement of lateral and normal forces with an optical-beam-deflectlon atomic force microscope. *Applied Physics Letters.* 1990, Vol. 57, pp. 2089 - 2091.

170. **Stifter, T., Marti, O. and Bhushan, B.** Theoretical investigation of the distance dependence of capillary and van der Waals forces in scanning force microscopy. *Physical Review B.* 2000, Vol. 20, pp. 13667 - 13673.

171. **Loos, J.** The Art of SPM: Scanning Probe Microscopy in Material Science. *Advanced Materials.* 2005, Vol. 17, pp. 1821 - 1833.

172. **Lee, S., Hesse, D. and Gösele, U.** Influence of miscut Y2O3-stabilized ZrO2 substrates on the azimuthal domain structure and ferroelectric properties of epitaxial La-substituted Bi4Ti3O12 films. *Journal of Applied Physics.* 2006, Vol. 100, pp. 64101 - 64108.

173. **Green, R., Barré, L. and Giorgi, B.** Nano-structures in YSZ(100) surfaces: Implications for metal deposition experiments. *Surface Science.* 2007, Vol. 601, pp. 792 - 802.

174. **Voichovsky, K., et al.** Direct mapping of the solid–liquid adhesion energy with subnanometre resolution. *Nature Nanotechnology.* 2010, Vol. 5, pp. 401 - 405.

175. **Lauritsen, J. and Reichling, M.** Atomic resolution non-contact atomic force microscopy of clean metal oxide surfaces. *Journal of Physics: Condensed Matter.* 2010, Vol. 22, p. 263001.

176. **Bhushan, B.** *Springer Handbook of Nanotechnology.* Berlin : Springer, 2004.

177. **Horcas, I., et al.** WSXM: A software for scanning probe microscopy and a tool for nanotechnology. *Review of Scientific Instruments.* 2007, Vol. 78, pp. 13705 - 13713 .

178. **Auger, P.** Sur les rayons β secondaires produits dans un gaz par des rayons X. *Comptes Rendus de l'Académie des sciences.* 1923, Vol. 177, pp. 169 - 171.

179. **Chung, M. and Jenkins, L.** Auger Electron Energies of the Outer Shell Electrons. *Surface Science.* 1970, Vol. 22, pp. 479 - 485.

180. **Larkins, F.** Semiemperical Auger-Electron Energies for Elements 10 < Z < 100. *Atomic Data and Nuclear Data Tables.* 1977, Vol. 20, pp. 311 - 387.

181. **Briggs, D. and Grant, J.** *Surface Analysis by Auger and x-Ray Photoelectron Spectroscopy.* West Sussex : IM Publications LLP, 2003.

182. **Mattox, D.** *The Foundations of Vacuum Coating Technology.* Norwich : Noyes Publications, 2003.

183. **Diebold, U., et al.** The Relationship Between Bulk and Surface Properties of Rutile TiO2(110). *Surface Review and Letters.* 2000, Vol. 7, pp. 613 - 617.

184. **Tomita, M., Tanabe, A. and S.Imoto.** An AES Study of Surface Oxidation of Zirconium. *Surface Science.* 1989, Vol. 209, pp. 173 - 182.

185. **Sands, D.** *Vectors and Tensors in Crystallography.* New York : Dover Publications, 1995.

186. **Vielstich, W., Lamm, A. and Gasteiger, H.** *Handbook of Fuel Cells: Fundamentals, Technology, Applications.* Hoboken : Wiley & Sons, 2003. Vol. 4.

187. **Du, R. and Flynn, C.** Asymmetric Coherent Tilt Boundaries Formed by Molecular Beam Epitaxy. *Journal of Physics: Condensed Matter.* 1990, Vol. 2, pp. 1335 - 1341.

188. **Humenik, M. and Kingery, W.** Metal-Ceramic Interactions: 111, Surface Tension and Wetta bility of Metal-Ceramic Systems. *Journal of The American Ceramic Society.* 1954, Vol. 37, pp. 18 - 23.

189. **Vece, M. Di, et al.** Hydrogen-induced Ostwald ripening at room temperature in a Pd nanocluster film. *Physical Review Letters.* 2008, Vol. 100, pp. 236105 - 236109.

190. **Ostwald, W.** Über die vermeintliche Isometrie des roten und gelben Quecksilberoxyds und die Oberflächenspannung fester Körper. *Zeitschrift für physikalische Chemie.* 1900, Bd. 34, S. 495 - 503.

191. **Lifshitz, I. and Sloyozov, V.** The kinetics of precipitation from supersaturated solid solutions. *Journal of Physics and Chemistry of Solids.* 1961, Vol. 19, pp. 35 - 50.

192. **Jak, M., et al.** Scanning tunnelling microscopy study of the growth of small palladium particles on TiO2(110). *Surface Science.* 200, Vol. 457, pp. 295 - 310.

193. **Weaver, J., Carlsson, A. and Madix, R.** The adsorption and reaction of low molecular weight alkanes on metallic single crystal surfaces. *Surface Science Reports.* 2003, Vol. 50, pp. 107 - 199.

194. **Barbier, A., et al.** Stability and stoichiometry of (polar) oxide surfaces for varying oxygen chemical potential. *Journal of Physics: Condensed Matter.* 2008, Vol. 20, pp. 184014 - .

195. **Besenbacher, F. and Norskov, K.** Oxygen chemisorption on metal surfaces: General trends for Cu, Ni and Ag. *Progress in Surface Science.* 1993, Vol. 44, pp. 5 - 66.

196. **Ostwald, W.** *Lehrbuch der Allgemeinen Chemie.* Leipzig : Engelmann, 1893.

197. **Reuter, K. and Scheffler, M.** Composition, structure, and stability of RuO2(110) as a function of oxygen pressure. *Physical Review B.* 2001, Vol. 65, p. 035406.

198. **Diebold, U. and S. Li, M. Schmid.** Oxide Surface Science. *Annual Review of Physical Chemistry.* 2010, Vol. 61, pp. 129 - 148.

199. **Olander, J., et al.** Size- and temperature-dependent epitaxy for a strong film-substrate mismatch: The case of Pt/MgO(001). *Physical Review B.* 2007, Vol. 76, p. 075409.

200. **Tongeren, R. Vreenburg P. van, Gijzeman, O. and Geus, J.** A comparison between the reduction kinetics of oxidized Ni(111) and Ni(100) surfaces by hydrogen and deuterium. *Surface Science.* 1992, Vol. 272, pp. 294 - 298.

Acknowledgments. Danksagung

This work would not have been possible without the diverse help and support of many people. I would like to sincerely thank all of them and mention some of the most important contributors in the following and ask those who feel forgotten and disregarded for pardon.

Ohne den Zuspruch von zahlreichen Helfern, die mich während meiner Promotion auf vielfältige Weise unterstützt haben, wäre diese Arbeit unvorstellbar gewesen. Ich möchte ihnen allen aufrichtig danken und einige wichtige Mitwirkende nachkommend hervorheben. Mögen mir alle, die sich vernachlässigt und vergessen fühlen verzeihen.

Prof. Dr. Helmut Dosch war auch unter am Ende der Dissertation etwas erschwerten Bedingungen stets ein Unterstützer meiner Arbeit und ein hervorragender Motivator. Vielen Dank, dass Sie an mich geglaubt haben und sich immer wieder die Zeit nahmen, nach dem Rechten zu sehen.

Prof. Dr. Andreas Stierle bin ich für seine geduldigen Erklärungen und die vielzähligen wissenschaftlichen Beiträge zum tiefsten Dank verpflichtet. Er war mir allzeit ein großartiger Mentor und die zahlreichen Treffen mit ihm waren immer sehr hilfreich und produktiv.

Prof. Dr. Michler danke ich herzlichst für das Übernehmen des Mitberichtes meiner Doktorarbeit sowie seine äußert freundliche und reibungslose Hilfe. Ebenso möchte ich **Prof. Dr. Wunner** für den Vorsitz der mündlichen Prüfung und eine sehr angenehme Unterstützung danken.

Die wissenschaftlichen und nichtwissenschaftlichen Beiträge von **Dr. Vedran Vonk** und **Dr. Claus Ellinger** kann ich nicht hoch genug einschätzen. Sie waren mir bei all meinen Synchrotron-Experimenten sowie deren Vorbereitung und Auswertung von unschätzbarer Hilfe und haben auch durch zahlreiche physikalische und nichtphysikalische Diskussionen wesentlich zu einer schönen und erfolgreichen Zeit meiner Promotion beigetragen. Vielen Dank. Veel dank.

Meine Mutter verdient es hier besonders hervorgehoben zu werden. Es fehlen mir die Worte meine Dankbarkeit für alles, was sie für mich getan und geopfert hat auszudrucken. Deshalb sage ich einfach danke. Danke aus den tiefsten Tiefen meines Herzens. Danke für alles. مرسی

Last but not least möchte ich mich bei meiner **Viola** bedanken. Vielen Dank für Deine Unterstützung und das Verständnis besonders während der letzten Monate meiner Doktorarbeit. Danke auch für die Ablenkung von der Arbeit und die Motivation. Und danke, dass Du für mich da bist.